In-situ Environmental TEM Studies

For Developing Structure-Activity Relationship in Supported Metal Catalyst

by

Santhosh Chenna

A Dissertation Presented in Partial Fulfillment
of the Requirements for the Degree
Doctor of Philosophy

Approved October 2011 by the
Graduate Supervisory Committee:

Peter A. Crozier, Chair
Ray Carpenter
Karl Sieradzki
William Petuskey

ARIZONA STATE UNIVERSITY

December 2011

ABSTRACT

In-situ environmental transmission electron microscopy (ETEM) is a powerful tool for following the evolution of supported metal nanoparticles under different reacting gas conditions at elevated temperatures. The ability to observe the events in real time under reacting gas conditions can provide significant information on the fundamental processes taking place in catalytic materials, from which the performance of the catalyst can be understood.

The first part of this dissertation presents the application of *in-situ* ETEM studies in developing structure-activity relationship in supported metal nanoparticles. *In-situ* ETEM studies on nanostructures in parallel with *ex-situ* reactor studies of conversions and selectivities were performed for partial oxidation of methane (POM) to syngas ($CO+H_2$) on Ni/SiO_2, Ru/SiO_2 and $NiRu/SiO_2$ catalysts. During POM, the gas composition varies along the catalyst bed with increasing temperature. It is important to consider these variations in gas composition in order to design experiments for *in-situ* ETEM.

In-situ ETEM experiments were performed under three different reacting gas conditions. First in the presence of H_2, this represents the state of the fresh catalyst for the catalytic reaction. Later in the presence of CH_4 and O_2 in 2:1 ratio, this is the composition of the reacting gases for the POM reaction and this composition acts as an oxidizing environment. Finally in the presence of CH_4, this is the reducing gas. Oxidation and reduction behavior of Ni, Ru and NiRu nanoparticles were followed in an *in-situ* ETEM under reacting gas conditions

and the observations were correlated with the performance of the catalyst for POM.

The later part of the dissertation presents a technique for determining the gas compositional analysis inside the *in-situ* ETEM using electron energy-loss spectroscopy. Techniques were developed to identify the gas composition using both inner-shell and low-loss spectroscopy of EELS. Using EELS, an "*operando* TEM" technique was successfully developed for detecting the gas phase catalysis inside the ETEM. Overall this research demonstrates the importance of *in-situ* ETEM studies in understanding the structure-activity relationship in supported-metal catalysts for heterogeneous catalysis application.

DEDICATION

This thesis is dedicated to my parents, my brothers, my sisters, my friends for their support and encouragement.

ACKNOWLEDGMENTS

I thank my advisor, Dr. Peter A. Crozier, for providing me the opportunity and challenge to sharpen my skills under his guidance. Without his encouragement, valuable suggestions and constant assistant, this research would have been impossible. I am very grateful for all his support throughout my Ph.D.

I would like to thank my committee members, Dr. Karl Sieradzki, Dr. Ray Carpenter, Dr. William Petuskey, for their valuable suggestions. I would like to thank all the Crozier group members for making the work place enjoyable. I would also like to thank Ben K. Miller for his help in calibrating the energy the energy-loss peaks. I am grateful to Karl Weiss and Zhenquian Liu for training me on the TEM.

The financial support provided by the National Science Foundation NSF-CBET-0553445 and Department of Energy DE-FG02-07ER46442 are also gratefully acknowledged. The use of TEM at the John M. Cowley Center for High Resolution Microscopy at Arizona State University is gratefully acknowledged.

Finally, I would like to thank my best friend Ms. Sanjiarani Santra, my parents, brothers and sisters for their support. I specially want to thank my elder brothers Hari Krishna and Mahesh for providing me the financial support to come to Arizona State University.

TABLE OF CONTENTS

Page

CHAPTER Page

CHAPTER Page

CHAPTER Page

LIST OF TABLES

LIST OF FIGURES

Figure Page

Figure Page

Figure Page

Figure Page

Figure Page

Figure Page

Figure Page

Figure Page

Figure Page

Figure Page

Figure Page

Figure Page

Figure Page

Chapter 1

GENERAL INTRODUCTION

1.1. Introduction to catalysis

Catalysis plays a major role in our life and livelihood. The word “Catalysis” came from Greek meaning “down” or “to loosen” [1]. Catalysis is the change in rate of a chemical reaction due to the participation of a catalyst. Nature has developed some of the most efficient catalytic processes like photosynthesis in leafs where chlorophyll in leafs is a type of photocatalyst and converts carbon dioxide and water to glucose and oxygen in the presence of sun light [2]. Enzymes are catalysts that present in biological cells which control the rate of chemical reactions sufficient for life [3]. Catalysts are also important for modern technology impacting areas such as energy, health, environmental control and food industry. More than 90% of commercially produced chemicals involve catalysts at some stage in the processes of their manufacture [4]. The global demand on catalysts was estimated at US$29.5 billion in 2010 which will increase further with rapid recovery in automotive and chemical industries [5].

Catalysts increase the reaction rate by providing an alternative reaction path way by lowering the activation energy. Figure 1.1 shows the energy diagram for a chemical reaction A and B converting to C and D. In the absence of catalyst, reaction proceeds along a reaction pathway indicated by the solid curve. The presence of a catalyst lowers the activation energy by changing the reaction pathway as shown by the dotted curve. The final products and the overall

thermodynamics of the reaction remain the same, only the rate of the reaction is affected by the presence of the catalyst.

Most industrial catalysts are heterogeneous catalysts with supported metal particles. In a heterogeneous catalyst, the phase of the catalyst is different from the reactants. In most of energy related applications, the catalyst is in a solid phase with reactants in the gas or liquid phase. In this thesis, the reactants are in the gas phase. Figure 1.2, schematically illustrates the reaction mechanism and fundamental steps taking place for a reaction conducted on the surface of a heterogeneous catalysts. One or more gaseous species (reactants) adsorb onto the surface of the catalyst, dissociate, diffuse on to the surface, and combined to form product molecules which then desorb giving products. Poisoning of the catalyst can take place if the desorption does not occur. During these gas-solid interactions, the phase and morphology of the catalyst can significantly change which can influence the catalytic properties of the material. The catalyst structure after the reaction may not be a true representative of the active phase that exists during the reaction. One of the challenges is to characterize the catalytic material at high temperatures and pressures that typically exist in the reactor. Hence, these structural changes must be studied under reacting gas conditions using *in-situ* techniques.

1.2. *In-situ* environmental transmission electron microscopy

1.2.1 Literature

Since the invention of transmission electron microscope (TEM) by Ernst Ruska in 1939 [6], electron microscopy has become a key technique for obtaining the atomic scale structural and chemical information of the materials. One of the earliest applications of electron microscopy studies of catalysts was done by John Turkevich in 1945 [7]; electron micrographs of several industrial catalysts were presented in this paper. Since then, electron microscopy has become vital tool for studying the catalytic materials to obtain information on particle size and shape, and atomic structure information of the catalyst surfaces [8,9]. Analytical electron microscopy can provide much more information than just particle size and shape. Information such as, oxidation state of the catalyst, elemental distributions in bimetallic catalysts can be obtained from analytical microscopy studies [10,11]. TEM has been extensively used for studying heterogeneous catalysts, several works and reviews can be found in the literature on the use of TEM for studying these catalytic materials [12-16]. Although *ex-situ* TEM provides significant information on the catalyst structure and composition, the observations may not be representative of the catalyst in its working state. A fresh catalyst may undergo significant changes during a reaction (such as phase transformation, morphological changes, etc.) based on the surrounding gas environment which may affect its catalytic properties. *In-situ* techniques have to be applied for understanding the dynamic nanoscale changes of the catalysts under reacting gas conditions, which is the main focus of this thesis.

The word "*in-situ*" came from Latin which means "in the place". The technique *in-situ* transmission electron microscopy (TEM) refers to the observations of dynamic responses of the material to an externally applied stimulus. The ability to observe the events in real time is what *in-situ* TEM offers to the world of materials science research. Researchers have developed several *in-situ* TEM techniques to understand the fundamental processes in materials under different external stimuli. The electron microscopes or microscope holders can be modified to introduce external stimuli such as, heating, cooling, mechanical straining, electric or magnetic fields, gas environments, and light [17-19]. Nanostructural changes observed under these controlled conditions can then be correlated with the properties of the materials. In this thesis, *in-situ* environmental TEM (ETEM) studies were performed on supported metal catalysts under reacting gas conditions at elevated temperatures for developing structure-activity relationship.

In-situ ETEM is a powerful tool that allows materials to be studied under dynamic reacting conditions at high spatial resolutions. From these dynamic observations, information on intermediate phases/structure can be determined which can provide scientific information on the mechanisms of phase transformations, shape changes etc and their effect on the catalyst performance. This kind of information on transitional forms may be difficult or impossible to obtain from *ex-situ* studies of used catalysts. Moreover, *ex-situ* studies may not provide a representative picture of the catalyst structure and composition in its working condition. Scanning probe microscopy (STM/AFM) can also be used to

study the dynamic gas-solid interactions at very high spatial resolutions, but these are limited to study only the model flat surfaces [20]. *In-situ* ETEM is an ideal tool for studying the high surface area nanomaterials that are often employed as catalysts in industry.

The history of *in-situ* environmental TEM dates back to 1950's. Ito et al., in 1958 first developed a specimen reaction device for the electron microscope to observe the sample during the reaction [21]. Hasimoto and group in 1968 have constructed a gas reaction chamber for an electron microscope that can be heated up to 1000^{o}C at gas pressures of 300 Torr [22]. Baker et al., used the design developed by Hasimoto for performing controlled atmosphere electron microscopy studies and the dynamic changes were recorded continuously on a videotape with the help of a camera [23]. Baker and co-workers were the first to apply *in-situ* ETEM studies for heterogeneous catalysis. Baker et al., followed the carbon deposition and growth of filamentous carbon on different metal particles and were able to measure the activation energy of the reaction [24-27]. Gai et al, has applied atomic resolution ETEM for probing gas-solid interactions at atomic level under controlled reacting gas conditions [28]. Creemer et al., have performed atomic scale electron microscopy at ambient pressure by using a nonreactor made of MEMS technology [29].

Many groups also have shown the power of ETEM for studying dynamic gas-solid reactions in catalytic materials [30-31]. At Arizona State University, *in-situ* ETEM has been used for many years to understand the fundamental processes that take place at the nanoscale under controlled gas environments. For example,

Li et al., performed *in-situ* studies to understand the fundamental process that takes place during the synthesis of supported mono-metallic and bi-metallic catalysts [32-34]. Wang et al., performed *in-situ* studies of dynamic changes that take place in the ceria-based oxides during redox process for solid oxide fuel cell application [35,36].

1.2.2. *In-situ* environmental cell

An environmental cell in the *in-situ* ETEM is a chamber around a TEM specimen into which a controlled amount of desired gas can be introduced. In general TEM's are used under high vacuum conditions (10^{-6} to 10^{-10} Torr) in order to avoid scattering from gas molecules and increase the life of electron source. By the introduction of gases into the TEM, the vacuum conditions are disturbed and the electron gun life time can be degraded. The main requirement for building *in-situ* ETEM is to confine the gases within the environmental cell so that the vacuum of the column and the gun region remains undisturbed.

There are three possible ways the gas can be introduced into the sample region without disturbing the microscope vacuum. One type of environmental cell is the gas-injection system that is equipped with the TEM holder [36,37], the pressure near the sample region is determined by the flow rate of the gas. The advantage of this is it is easy to operate, but very low pressures can be achieved by this technique (only about 10^{-5} Torr). The other technique that is used for achieving gas environments near the sample region are by the use of windowed cells [29,38]. In a windowed cell, two electron transparent membranes were used

above and below the sample to confine the gas environments near the sample region. The gases are introduced through the fine tubes inside the specimen holder rod. By this technique gas pressures of up to 1 atm can be achieved, however the spatial resolution obtained by this method is rather low due to the presence of membrane windows above and below the sample. One more disadvantage is the reliability of the windows, once the membrane of the cell is broken during the operation, it can give serious problems to the microscope and recovery from which can take long times. A major advantage of windowed cells is that, any conventional microscope can be turned into an ETEM just by building a windowed cell holder for that specific microscope.

The differential pumping system is the other technique with which reasonable gas pressures can be achieved near the sample region without disturbing the microscope vacuum and the electron gun [31-35,39,40]. In this thesis, a differential pumping system was used for performing *in-situ* ETEM studies. Gas was introduced into the environmental cell and was pumped at different levels. Gas was confined near the sample region with the help of apertures, gas pressures of up to few Torr can be achieved by this technique. The gas pressure inside the cell is limited by the choice of aperture size, pumping speed, and distance between apertures. Detailed information of this technique is discussed in chapter 2, section 2.4.2. The spatial resolution that can be obtained by using this technique is in general much better. With recent developments in aberration correctors, information can be obtained at sub-angstrom resolution under dynamic conditions [28]. The major disadvantage of this technique is a

dedicated microscope has to be specially built for performing *in-situ* ETEM studies, which can be very expensive.

1.2.3. Heating holders

Several heating holders are available in the market depending on the application [41,42]. The material used for making the holder should be compatible with the TEM sample grid, reacting gases and reaction temperature used for the reaction. For example heating holder made of Ta furnace will corrode when heated to high temperatures in the presence of oxygen. A major challenge in obtaining *in-situ* ETEM high resolution imaging is associated with the sample drift when the holder is heated to high temperatures. It will take about 30 to 60 minutes for the drift to stabilize for obtaining high resolution imaging. Recently heating holders are built with MEMS technology, where small area of the holder near the sample region is heated, which will stabilize very quickly. By using these holders, high resolution imaging is possible within few minutes of reaching the desired temperature.

1.2.4. Support considerations

One of the challenges in following the evolution of supported metal catalysts under reacting gas conditions relates to the inherent complexity that is often present in the nanostructure and composition of real working catalysts. Even under *ex-situ* conditions, many “simple” heterogeneous catalysts show a variety of structures and morphologies between and within individual nanograins. Many

common high surface area supports may be composed of nanocrystals possessing multiple crystal facets and complex surface defect structures. For example, Li et al., found that in Ni supported on TiO_2, the nature of the metal-support interaction depended on whether the metal nucleated on anatase or rutile grains and on the particular crystal facet of these two different titanias [43]. The complexity of high surface area support structures can lead to significant heterogeneity in the microstructure of supported monometallic catalyst and provide rich but complex nanostructure in bimetallic systems [32,33]. For *in-situ* work in which dynamic structural changes take place during reaction conditions, this structural complexity greatly complicates the interpretation of the TEM data. For this reason amorphous SiO_2 spheres have been chosen as a simple model system on which metal nanoparticles were dispersed. The surface of the SiO_2 spheres is relatively homogenous, which implies that the interaction of the support with the nanoparticles is similar everywhere for the catalyst. Moreover the simple geometry of this support is ideal for observing and interpreting changes in metal particle size, shape and composition during *in-situ* ETEM studies.

1.3. Partial oxidation of methane

Partial oxidation of methane (POM) was considered as a model reaction. Methane is the predominant gas component of natural gas, which is found abundantly in many locations around the world. The product gas ratio (H_2/CO=2) obtained from partial oxidation of methane is suitable as input for Fisher-Tropsch synthesis [44,45]. POM is an important reaction for syngas production because of its slight

exothermic nature [46-48], and the POM may also be useful for other energy related process such as fuel reforming for high temperature fuel cell applications [49].

The catalytic partial oxidation of methane was first reported in 1946 by Prettre et al, where methane and oxygen was fed stoichiometrically (in 2:1 ratio) over Ni catalyst [50]. It was found that the Ni catalyst deactivated by the carbon formation. Ashcroft and co-workers showed that methane could be converted to high conversions and selectivities to synthesis gas without coke formation over noble metal catalysts like Rh, Ru, and Ir [51, 52]. Several monometallic and bimetallic catalysts on variety of supports were studied for this reaction [53]. Figure 1.3 shows the thermodynamic equilibrium conversions of CH_4 and O_2 and their selectivity towards CO_2 and CO at different temperatures at 1 atm, calculated using Factsage program [54]. These thermodynamic limits set the maximum achievable catalytic activity that can be obtained for this reaction. A best catalyst will reach the thermodynamic equilibrium values very quickly.

For partial oxidation of methane under high conversion conditions, the gas composition in the reactor changes along the catalyst bed changes from 100% reactant gas at the entrance of the bed to close to 100 % product gas at the exit, with intermediate gas products in the middle (Figure 1.4). The gas composition across the reactor is influenced by the reaction pathway for syngas formation. Two main reaction mechanisms have been proposed for the POM reaction [Eq. 1 below]. One is the indirect POM, where the reaction proceeds through complete combustion of methane to CO_2 and H_2O [Eq. 2] followed by carbon dioxide and

steam reforming [Eq. 3 and 4] [55,56]. The other is direct POM to syngas without the formation of CO_2 and H_2O.

$$CH_4 + ½O_2 \rightarrow CO + 2H_2 \qquad \Delta H^o_{298} = -36 \text{ kJ mol}^{-1} \qquad (1)$$

$$CH_4 + 2O_2 \rightarrow CO_2 + 2H_2O \qquad \Delta H^o_{298} = -802 \text{ kJ mol}^{-1} \qquad (2)$$

$$CH_4 + CO_2 \rightarrow 2CO + 2H_2 \qquad \Delta H^o_{298} = +247 \text{ kJ mol}^{-1} \qquad (3)$$

$$CH_4 + H_2O \rightarrow CO + 3H_2 \qquad \Delta H^o_{298} = +206 \text{ kJ mol}^{-1} \qquad (4)$$

Most experimental findings support that CO_2 and H_2O are the products that form initially at low temperatures by complete combustion during the temperature ramp-up in CH_4 and O_2 and syngas forms at high temperatures [46,53, 55,]. Thus the gas composition present in the reactor will involve gas mixtures of CH_4, O_2, CO_2, CO, H_2O and H_2 with the exact composition depending on the location and temperature on the reactor bed. Moreover, during the reactor ramp-up, the catalyst structure and activity will change with temperature leading to further changes in the ambient gas composition. Thus during ramp-up, the "reactor condition" varies in time and space and it is important to take this into account in the design and interpretation of environmental TEM experiments.

There are several groups that perform catalytic activity measurements on supported metal catalysts and there are several groups that have been using *in-situ* ETEM studies to understand the fundamental process during gas-solid interactions. This thesis is focused in bridging these two fields by performing catalytic activity measurements externally in a reactor or in the TEM and performing *in-situ* ETEM studies under reacting gas conditions to get

nanostructural information. *In-situ* ETEM observations are correlated with the catalytic performance to get the structure-activity relationship.

Structure-activity relationship studies were performed on pure Ni and pure Ru supported on SiO_2 spheres. Ni was considered as a cheap catalyst and Ru is a noble metal and efficient catalyst for POM reaction. The difference in the phase and morphological changes were studied under reacting gas conditions that are relevant to POM and their affect on the catalyst performance is discussed. After understanding the behavior of two metals a NiRu bimetallic catalyst was prepared and similar experiments were performed on NiRu to that of Ni and Ru. *In-situ* ETEM experiments were performed under different gas environments to understand the interactions between Ni and Ru and these observations were correlated with the catalyst performance.

1.4. Outline

Chapter 2 introduces to the material synthesis procedures and the instrumentation used in this thesis. Chapter 3 and 4 shows the *in-situ* phase transformations in supported Ni and Ru nanoparticle respectively under reacting gas conditions and their effect on the catalytic performance is discussed. In chapter 5 both Ni and Ru were mixed together to get bimetallic NiRu nanoparticles and *in-situ* ETEM experiments are performed under reacting gas conditions to follow the changes in compositional distributions in individual nanoparticles. These changes in nanoparticle composition are then correlated with the catalytic performance for POM reaction. Chapter 6 discusses about the electron energy-loss spectroscopy

(EELS) technique for determining the gas composition in the environmental cell in the ETEM. In chapter 7, "*Operando* TEM" technique will be discussed, where EELS has been used to detect the gas phase catalysis inside the environmental cell in a TEM. Chapter 8 summarizes the conclusions from this work and will finish with some future directions on this project.

References

1. van Santen, R. A., van Leeuwen, P. W. N. M., Moulijn, J. A., & Averill, B. A. (1999). *Catalysis: An integrated approach* (123). Elsevier.

2. Ke, B. (2001). *Photosynthesis photobiochemistry and photobiophysics* (10). Kluwer Academic Publishers.

3. Grisham, C. M., & Garrett, R. H. (1999). *Biochemistry*. Philadelphia: Saunders College Publishers.("Retrieved from http://en.wikipedia.org/wiki/Enzyme")

4. Ertl, G., Knozinger, H., & Weitkamp, J. (1997). *Handbook of heterogeneous catalysis* (Vol 1).

5. Market Report. (2011). *Global Catalyst Market* (2nd Edition). Acmite Market Intelligence.

6. Knoll, M., & Ruska, E. (1932). Das Elektronenmikroskop. *Zeitschrift fuer Physik*, 78, 318-339.
7. Turkevich, J. (1945). Electron Microscopy of Catalysts, *The Journal of Chemical Physics*, 13(6), 235-239.

8. Ozkaya, D. (2008). Particle size analysis of supported platinum catalysts by TEM. *Platinum Metal Review*, 5(1), 61-62.

9. Marks, L. D., & Smith, D. J. (1983). Direct surface imaging in small metal particles. *Nature*, 303, 316-317.

10. Garvie, L. A. J., & Buseck, P.R. (1998). Ratios of ferrous to ferric iron from nanometre-sized areas in minerals. *Nature*, 396, 667-670.

11. Jing, Y., Sun, K., Liu, J., Nag, N., & Browning, N. (2003). Atomic Scale Spectroscopy of Supported Pd-Cu/γ-Al_2O_3 Bimetallic Catalysts, Microscopy & Microanalysis, 9(2), 406-407.

12. Lyman, C. E. (1983). Microanalysis of Catalysis by analytical electron microscopy. *Journal of Molecular Catalysis*, 20, 357-368.

13. Sattler, M. L., & Ross, P. N. (1986). The surface structure of Pt crystallites supported on carbon black. *Ultramicroscopy*, 20, 21-28.

14. Pennycook, S. J., & Howie, A. (1983) Characterization of supported catalysts by high-resolution STEM. *Journal of Molecular Catalysis*, 20, 345-355.

15. Yacaman, M. J., Diaz, G., & Gomez, A. (1995). Electron microscopy of catalysts; the present, the future and the hopes. *Catalysis Today*, 23(3), 161-199.

16. Datye, A. K. (2003). Electron microscopy of catalysts: recent achievements and future prospects. *Journal of Catalysis*, 216(1-2), 144-154.

17. Wang, C. W., Xu, W., Liu, J., Choi, D. W., Arey, B., Saraf, L. V., Zhang, J. G., Yang, Z. G., Thevuthasan, S., Baer, D. R., & Salmon, N. (2010). In situ transmission electron microscopy and spectroscopy studies of interfaces in Li ion batteries: Challenges and opportunities. *Journal of Materials Research*, 25(8), 1541-1547. s

18. Minor, A. M., Asif, S. A. S., Shan, Z. W., Stach, E. A., Cyrankowski, E., Wyrobek, T. J., & Warren, O. L. (2006). A new view of the onset of plasticity during the nanoindentation of aluminium. *Nature Materials*, 5, 697–702.

19. Shindo, D., Takahashi, k., Murakami, Y., Yamazaki, K., Deguchi, S., Suga, H., & Kondo, Y. (2009). Development of a multifunctional TEM specimen holder equipped with a piezodriving probe and a laser irradiation port. *Journal of Electron Microscopy*, 58(4), 245-249.

20. Iwasawa, Y., Onishi, H., & Fukui, K. (2001). *In-situ* STM study of surface catalytic reactions on TiO_2 (110) relevant to catalyst design. *Topics in Catalysis*, 14(1-4), 163-172.

21. Ito, T., & Hiziya, H. (1958). A specimen reaction device for the electron microscope and its applications. *Journal of Electronmicroscopy*, 6(1), 4-11.

22. Hashimoto, H., Naiki, T., Eto, T., & Fujiwara, K. (1968). High temperature gas reaction specimen chamber for an electron microscope. *Japanese Journal of Applied Physics*, 7(8), 946-952.

23. Baker, R. T. K., & Harros, P. S. (1972). Controlled atmosphere electron microscope. *Journal of Physics. E: Scientific Instruments*, 5, 793-797.

24. Baker, R. T. K., Chludzinski, J. J. (1986). *In-situ* electron microscopy studies of the behavior of supported ruthenium particles. *Journal of Physical Chemistry*, 90, 4734-4738.

25. Baker, R. T. K. (1995) A review of *in-situ* electron microscopy studies of metal/metal oxide-graphite interactions. *Journal of Adhesion*, 52, 13-40.

26. Baker, R. T. K., & Chludzinski, J. J. (1980). Filamentous carbon growth on nickel-iron surfaces-effect of various oxide additives. *Journal of Catalysis*, 64, 464–478.

27. Baker, R. T. K., Chludzinski, J. J., & Lund C. R. F. (1987). Further studies of the formation of filamentous carbon from the interaction of supported iron particles with acetylene. *Carbon* 25, 295–303.

28. Gai, P., Boyes, E. D. (2009). Advances in atomic resolution *in-situ* environmental transmission electron microscopy and $1A^{o}$ aberration corrected *in-situ* electron microscopy. *Microscopy Research and Technique*, 72, 153-164.

29. Creemer, J. F., Helveg, S., Hoveling, G. H., Ullmann, S., Molenbroek, A. M., Sarro, P. M., & Zandbergen, H. W. (2008). Atomic-scale electron microscopy at ambient pressure. *Ultramicroscopy*, 108, 993-998.

30. Hansen, P. L., Wagner, J. B., Helveg, S., Rostrup-Nielsen, J. R., Clausen, B. S. & Topsoe, H. (2002). Atom-resolved imaging of dynamic shape changes in supported copper nanocrystals. *Science*, 295, 2053-2055.

31. Hansen, T. W., Wagner, J. B., Hansen, P. L., Dahl, S., Topsoe, H., & Jacobson, C. J. H. (2001). Atomic-resolution *in-situ* transmission electron microscopy of a promoter of a heterogeneous catalyst. *Science*, 294, 1508-1510. Li, P., Liu, J., Nag, N., & Crozier, P. A. (2005). Atomic-scale study of *in-situ* metal nanoparticle synthesis in a Ni/TiO_2 system. *Journal of Physical Chemistry B*, 109(29), 13883-13890.

32. Li, P., Liu, J., Nag, N., & Crozier, P. A. (2006). *In-situ* synthesis and characterization of Ru promoted Co/Al_2O_3 Fischer–Tropsch catalysts. *Applied Catalysis A: General*, 307, 212-221.

33. Li, P., Liu, J., Nag, N., & Crozier, P. A. (2009). *In-situ* preparation of $Ni-Cu/TiO_2$ bimetallic catalysts. *Journal of Catalysis*, 262, 73-82.

34. Wang, R., Crozier, P. A., Sharma, R., & Adams, J.B. (2008). Measuring the redox activity of individual catalytic nanoparticles in cerium-based oxides. *Nano Letters*, 8(3), 962-967.

35. Wang, R., Crozier, P. A., & Sharma, R. (2009). Structural transformation in ceria nanoparticles during redox processes. *Journal of Physical Chemistry C*, 113(14), 5700–5704.

36. Takeo, K., Toshie, Y., Mitsuru, K., Akira, W., Marukawa, T., Mima, T., Kuroda, K., Saka, H., Arai, S., Makino, H., Suzuki, Y., & Kishita, K. (2005).

Development of a gas injection/specimen heating holder for use with transmission electron microscope. *Journal of Electron Microscopy*, 54(6), 497–503.

37. Takeo, K., Toshie, Y., Mitsuru, K., Akira, W., & Yasuhira, N. (2006). Development of a specimen heating holder with an evaporator and gas injector and its application for catalyst. *Journal of Electron Microscopy*, 55(5), 245–252.

38. Giorgio, S., Sao Joao, S., Nitsche, S., Chaudanson, D., Sitja, G., & Henry, C. R. (2006). Environmental electron microscopy (ETEM) for catalysts with a closed E-cell with carbon windows. *Ultramicroscopy*, 106, 503-507.

39. Sharma, R. (2009). Kinetic measurements from *in-situ* TEM observations. *Microscopy Research and Technique*, 72, 144-152.

40. Sharma, R. (2005). An environmental transmission electron microscope for *in-situ* synthesis and characterization of nanomaterials. *Journal of Materials Research*, 20(7), 1695-1707.

41. Gatan (from http://www.gatan.com/products/specimen_holders).

42. Protochips (from http://www.protochips.com/en/technology.html).

43. Li, P., Liu, J., Nag, N., & Crozier, P. A. (2006). Dynamic nucleation and growth of Ni nanoparticles on high-surface area titania. *Surface* Science, 600(3), 693-702.

44. Van Der Laan, G. P., & Beenackers, A. A. C. M. (1999). Kinetics and selectivity of the fischer-tropsch synthesis: A literature review. *Catalysis Review: Science & Engineering*, 41(3&4), 255-318.

45. Bart, J. C. J., & Sneeden, R. P. A. (1987). Copper-zinc oxide-alumina methanol catalysts revisited. *Catalysis Today*, 2(1), 1-124.

46. Tsang, S. C., Claridge, J. B., Green, M. L. H. (1995). Recent advances in the conversion of methane to synthesis gas. *Catalysis Today*, 23, 3-15.

47. York, A. P. E., Xiao, T., & Green, M. L. H. (2003). Brief overview of the partial oxidation of methane to synthesis gas. *Topics in Catalysis*, 2003, 22(3-4), 345-358.

48. Wang, J.X., & Lunsford, J. H. (1986). Characterization of [Li+O] centers in lithium-doped magnesium oxide catalysts. *Journal of Physical Chemistry*, 90(22), 5883-5887.

49. Prettre, M., Eichner, C. H., & Perrin, M. (1945). The catalytic oxidation of methane to carbonmonoxide and hydrogen. *Transactions of the Faraday Society*, 42, 335-339.

50. Cabezas, M. D., Lamas, D. G., Bellino, M. G., Fuentes, R. O., Walsoe de Reca, N. E., & Larrondo, S.A. (2009). Catalytic behavior of PdO/NiO/SDC composites for partial oxidation of methane: Application as anodes of single-chamber IT-SOFCs. *Electrochemical and Solid-State Letters*, 12(3), B34-B37.

51. Ashcroft A. T., Cheetham, A. K., Foord, J. S., Green, M. L. H., Grey, C. P., Murrell, A. J., & Vernon, P. D. F. (1990). Selective oxidation of methane to synthesis gas using transition metal catalysts. *Nature*, 344, 319-321.

52. Ashcroft A. T., Cheetham, Green, M. L. H., & Vernon, P. D. F. (1990). Partial oxidation of methane to synthesis gas using carbon dioxide. *Nature*, 352, 225-226.

53. Enger, B. C., Lodeng, R., & Holmen, A. (2008). A review of catalytic partial oxidation of methane to synthesis gas with emphasis on reaction mechanisms over transition metal catalysts. *Applied Catalysis A: General*, 346, 1-27.

54. Bale, C. W., Chartrand, P., Degterov, S. A., Eriksson, G., Hack, K., Ben Mahfound, R., Melancon, J., Pelton, A. D., & Petersen, S. (2002). Factsage thermochemical software and databases. Calphad, 26(2), 189-228.

55. Torniainen, P. M., Chu, X., & Schmidt, L. D. (1994). Comparison of monolith-supported metals for the direct oxidation of methane to syngas. *Journal of Catalysis*, 146(1), 1-10.

56. Dissanayake, D., Rosynek, M. P., Kharas, K. C., Lunsford, J. H. (1991). Partial oxidation of methane to carbon monoxide and hydrogen over a Ni/Al_2O_3 catalyst. *Journal of Catalysis*, 132(1), 117-127.

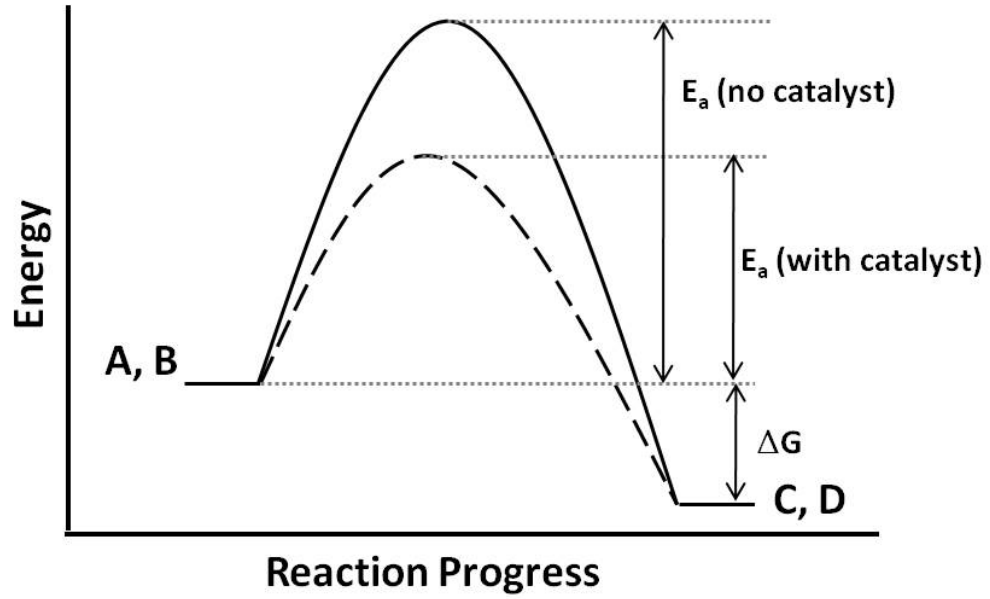

Figure 1.1. Energy diagram showing the effect of catalyst on the reaction path.

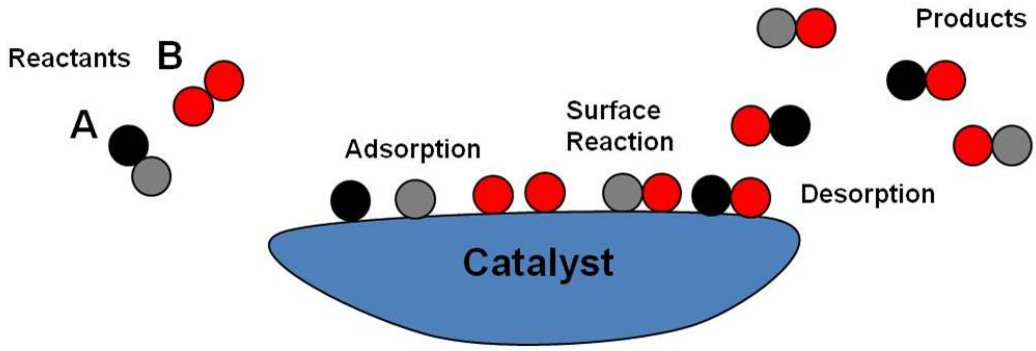

Figure 1.2. Schematic showing the principle of heterogeneous catalysis.

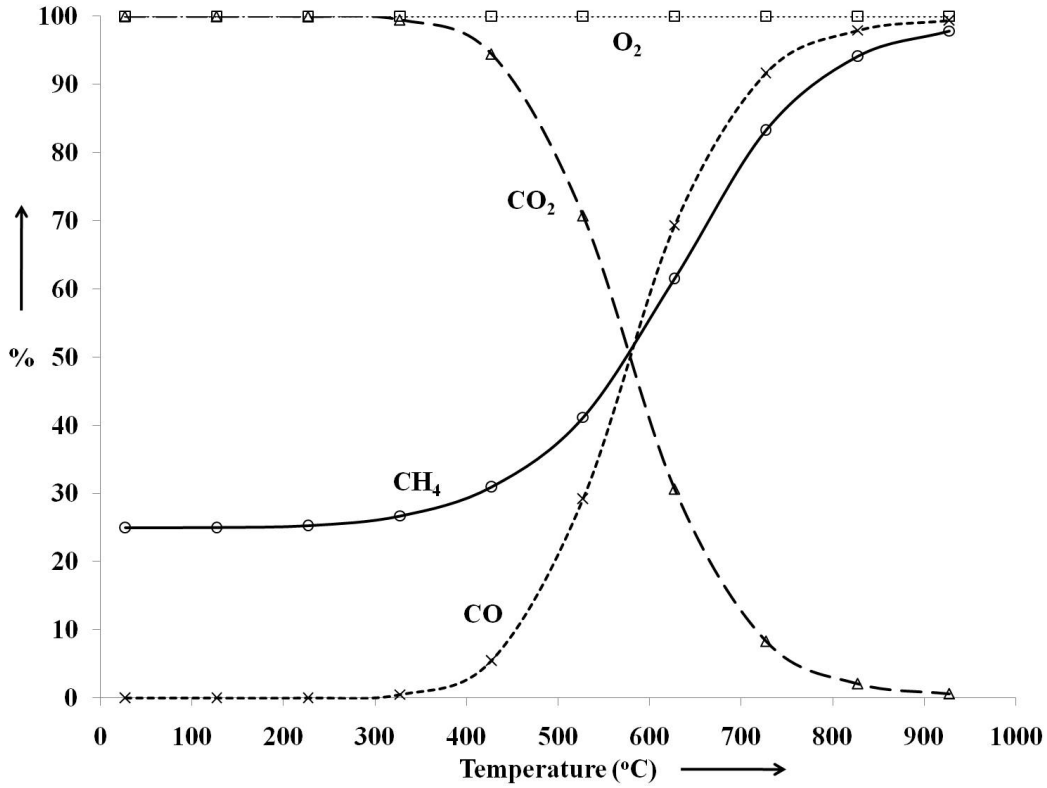

Figure 1.3. Plot showing the thermodynamic equilibrium conversions of CH_4 and O_2 and there selectivity towards CO_2 and CO at 1 atmosphere, calculated using Factsage program [54].

Figure 1.4. Schematic representation of reactor under high catalytic conversions and selectivity for partial oxidation of methane reaction.

Chapter 2

INSTRUMENTATION AND EXPERIMENTAL METHODS

2.1. Introduction

This chapter introduces to the synthesis procedures and characterization techniques used in this dissertation. First the introduction of the catalyst support, SiO_2, its synthesis will be described followed by incipient impregnation procedures to get metal dispersions onto the support. The ISRI RIG 150 reactor was used to perform the catalytic reactions and a Varian 3900 Gas Chromatography was used to measure the catalytic activity. *Ex-situ* TEM nanoscale structural characterization was performed in an analytical JEOL JEM 2010 F and *in-situ* environmental transmission electron microscopy (ETEM) studies under reacting gas conditions were performed in an FEI Tecnai F20. Several TEM techniques such as high resolution electron microscopy, scanning transmission electron microscope, electron diffraction, energy dispersive x-ray spectroscopy, electron energy loss spectroscopy were used to obtain the nanoscale structural and chemical information.

2.2. Catalyst synthesis procedure

2.2.1 Catalyst support: SiO_2 spheres

SiO_2 spheres of uniform size were prepared using Stober's method [1]. Stober et al., developed a system of chemical reactions that control the uniform growth of SiO_2 spheres by means of hydrolysis of alky silicates in the presence of alcohol. Chemicals used for this reaction are ethanol (100% pure), ammonium hydroxide

(29% ammonia), deionized water and tetraethoxyorthosilicate (TEOS, 99.999% from Sigma Aldrich) as a source for silica. Typical synthesis procedures involve mixing a known amount of ethanol, deionized water and ammonium hydroxide in a beaker and heating on a hot plate while stirring. Once the desired temperature is reached, TEOS is added to this mixture and the reaction was left for 2 hours. After 2 hours reaction was stopped and the remaining chemicals were evaporated by heating to 100^{o}C. SiO_2 spheres were collected and heat treated at 500^{o}C in air for 2 hours.

Figure 2.1a shows the silica spheres prepared by Stober's method. From the image it is clear that the SiO_2 sphere have a well-defined morphology which gives a great advantage in following the nanoparticle evolution under dynamic gas reacting conditions in the *in-situ* TEM. Figure 2.1b shows the particle size distribution of these spheres. The average size of the spheres measured from TEM images is 305 nm +/- 23 nm with a specific surface area 7.5 m^2/gm (determined from TEM).

2.2.2. Metal/SiO_2 synthesis

The incipient wetness method was chosen for impregnation of metal precursors on to the SiO_2 support. In this method, metal salt solution of know concentration was added to the support, the amount of precursor solution added is equivalent to the pore volume of the support [2]. For determining the pore volume of the silica spheres, precursor solution was added slowly drop by drop until the powder turned damp. The amount of precursor solution added till the powder turned damp

gave the approximate pore volume of the silica spheres. The specific pore volume for silica spheres obtained by this method is about 500 μl/gm.

The impregnation procedure was performed according to the method outlined by Banerjee et al [3]. Ethanol was used as a solvent for preparing precursor solution because of its lower surface tension than water, this helps in better spreading of the precursor over the support [4]. The surface tension of ethanol and water at 20^{o}C in air are 22.5 mN/m and 72.8 mN/m respectively. Incipient wetness impregnation was carried out in a mortar by drop wise addition of nickel nitrate solution (ethanol solvent) equivalent to the pore volume of the SiO_2 in a saturated ethanol atmosphere while mixing for 10 min. Saturated ethanol vapor ambient prevents the drying of ethanol solvent from precursor solution during mixing, this provides a better mixing between the precursor solution and the support giving a better metal dispersions. To achieve a saturated ethanol atmosphere, impregnation was performed in a glove bag containing a beaker with alcohol and the alcohol was stirred using a magnetic stirrer. After a couple of hours the glove bag was saturated with alcohol. Figure 2.2 shows the glow bag set up established for performing incipient wetness impregnation. After impregnation, the sample was dried at 120^{o}C for 2 hours followed by reduction in 5% H_2/Ar atmosphere at 400^{o}C for 3 hours. The conventional calcination step was avoided to give improved metal dispersions in this case [5].

2.3. Catalytic Measurements

2.3.1. ISRI RIG-150 Microreactor

The *in-situ* research instruments (ISRI) RIG-150 microreactor (figure 2.3) is a very convenient tool for catalyst synthesis and characterization. The capabilities of RIG-150 are: 1) It provides computerized control of the gas flows through the reactor, which can be used to run either steady state or transient reactions that require a repeated number of different flow sequences. 2) To run temperature programmed reactions such as temperature programmed reduction (TPR), temperature programmed oxidation (TPO) and temperature programmed desorption (TPD). The unit collects and stores both temperature and thermal conductivity cell data as per the user instructions. 3) To perform pulse adsorption experiments, this involves pulsing of single gas or gas mixtures at specific time intervals. 4) To perform BET surface area measurements.

The microreactor is equipped with mass flow controllers to provide computerized control of the gas flows into the reactor. Various gases can be used with the given mass flow controllers by adjusting the flow calibration values. All the mass flow controllers are calibrated for the gases of interest by matching the gas flow from the exit of the reactor with that of the value entered in the program. Gas flow from the exit of the reactor was measured by using a digital mass flow meter. It is also equipped with a thermal conductivity detector (TCD) used for measuring the gas composition based on the thermal conductivity of gas. More details about the TCD will be discussed in the next section.

Catalytic reactions were performed in a reactor containing a quartz tubular fix-bed flow furnace, with an internal diameter of 10 mm. A K-type thermo-couple is placed at the top of the catalyst bed for measuring the temperature of the bed, as shown in figure 2.4. The effluent gas from the reactor outlet was analyzed by using a Varian 3900 gas chromatography system.

2.3.2 Varian 3900 Gas Chromatography

The gas chromatography (GC) is a chemical analysis instrument that enables the separation of different components in a gas mixture based on the chromatographic separation principles. It consists of two phases, a mobile phase (or moving phase) and a stationary phase. The mobile phase is a carrier gas, usually an inert gas such as He, Ar or a nonreactive gas like N_2. The stationary phase is usually a layer of polymer or an inert solid support (usually porous) packed inside a piece of metal tubing called the column [6]. The column is the heart of the gas chromatography that enables the separation of the components in a gas mixture. As the gas stream enters into the column, the individual components are separated at different rates depending on its adsorption affinity towards the material used in the stationary phase. Gas with relatively high affinity to the stationary phase will move slower compare to the one with lower affinity and thus migrates slowly through the column. This difference in the migration velocity leads to the separation of individual components in the gas mixtures [7]. The column can also be heated to higher temperatures to facilitate faster migration of the gases to elute at lower times. However, this will degrade the peak resolution in the chromatogram.

The specific model of gas chromatography used for measuring gas composition is Varian 3900 GC is shown in figure 2.5. This system is equipped with a parallel setup of 2 Porous Layer Open Tube (PLOT) columns for separation of permanent gases in short time. PLOT columns have the inner surface coated with a porous layer of solid support or adsorbent. The sample is injected via a normal injection port and is split into the parallel setup of 2 columns. A short CP-Molsieve is used to separate the few gases (O_2 N_2, CH_4 and CO) before the first peak (composite peak of all inert gases) elutes from the CP-PoraBOND Q PLOT column. After the first peak, the CH_4 and CO_2 elute from the CP-PoraBOND Q column (if water is present, it will also be seen from the CP-PoraBond). The CO_2 and eventually water that enters the Molsieve column will be adsorbed. As CH_4 elutes from both systems, the split ratio between the two columns can be calculated by the ratio of the methane peaks of CP-Molsieve 5 A and CP-PoraBOND Q. Baking of the column at 250^{o}C for 24 hours is done frequently to remove any moisture that has been adsorbed onto the surface of the stationary phase.

The gases that elute from the column will flow into the detector. There are many types of detectors that can be used, such as thermal conductivity detector (TCD), flame ionization detector (FID), mass spectrometer (MS) etc. The gas chromatography employed for the experiments is equipped with TCD, which is sensitive to the difference in the thermal conductivity of the gas components and the carrier gas. The TCD has two sides, a sample side and a reference side. The sensors on each side of the cell are two delicate filaments, total of four; these filaments form a Wheatstone bridge [8]. In order for the filaments to give a

balanced signal, the same composition of gases must be flowing on both sides of the cell at all times. As the composition of the gases change on the sample side with respect to the reference side, this will give a change in the TCD signal. Thermal conductivities of different gases are mentioned in table 2.1 [9]. He was chosen as a carrier gas to get the high sensitivity detection for different gases. With He as a carrier gas, chromatography can detect all the gases of our interest except H_2 because of smaller difference in the thermal conductivities between He and H_2. If H_2 needs to be detected then N_2 or Ar should be used as a carrier gas.

Figure 2.6 shows an example of gas chromatograph, the x-axis represents the time scale at which the each gas component is eluted from the column and detect by the TCD. The y-axis is the intensity of each peak given in micro volts; the intensity of the peak depends on the amount of the component that is present in the gas stream. Ratios of areas under the peaks will give the relative gas composition ratio in the gas stream. Peak positions for individual gases (CH_4, O_2, CO_2, and CO) relevant to partial oxidation of methane are calibrated by flowing pure gases. It is important to calibrate the correction factors for relative areas under the peaks for determining the gas compositions, because two gases of the same concentration with different thermal conductivities can give different peak intensities. The intensity of the peak also depends on the differences in the thermal conductivity of the gas component and the carrier gas. The larger the thermal conductivity difference between the carrier gas and the sample gas the larger the signal intensity of sample gas. A correction factor for each set of gas mixtures was calibrated by flowing equal amounts of gases into the GC and

taking the ratio of the areas under the peaks. Conversions and selectivities for the reaction are calculated from the gas chromatography signal and an example for partial oxidation of methane is shown below:

CH_4 and O_2 conversions along with CO_2 and CO selectivities were calculated by using the following equations:

$$CH_4 \text{ Conversion: } (CH_{4,in}\text{-}CH_{4,out})/CH_{4,in} \quad (1)$$

$$O_2 \text{ Conversion: } (O_{2,in}\text{-}O_{2,out})/O_{2,in} \quad (2)$$

$$CO_2 \text{ Selectivity: } CO_{2,out}/(CH_{4,in}\text{-}CH4_{,out}) \quad (3)$$

$$\text{CO Selectivity: 100- } CO_2 \text{ Selectivity} \quad (4)$$

where $CH_{4,in}$, $CH_{4,out}$ are the amount of methane gas going in and coming out of the reactor respectively, similarly for O_2. $CO_{2,out}$ is the amount of carbon dioxide and carbon monoxide coming out of the reactor.

2.4. Nanoscale Characterization

2.4.1. TEM and STEM imaging

The transmission electron microscope (TEM) is a powerful tool to obtain atomic scale information on materials. It uses a beam of electrons to illuminate the specimen and a magnified image is produced with the transmitted electrons with the help of lenses. A basic TEM consists of an illumination system, image forming system, transfer lens and a viewing screen or recording device. The illumination system consists of an electron source to provide an intense beam of high energy electron and condenser lenses (magnetic lenses) to transfer the

electrons to the specimen giving either a broad beam or a focused beam. The image forming system consists of objective lens, intermediate lens and projector lens. The role of the objective lens is to form the first intermediate image or diffraction pattern which are then magnified and projected onto the viewing screen by the intermediate and projector lenses [10]. The image and diffraction pattern are then magnified and projected onto the viewing screen by the intermediate and projector lenses [10]. Figure 2.7 shows the ray diagram for forming images (figure 2.7a) and diffraction patterns (figure 2.7b) in the TEM. Low magnification TEM images will provide information about the particle size, particle morphology, and metal dispersions on support [11,12]. High resolution TEM images can provide atomic-scale information on interplanar spacing from which the structural information of the nanoparticles can be obtained [13]. Defects, surface structures, interface interactions, information on core-shell structures can also be obtained from high resolution TEM images [14-18].

In scanning transmission electron microscopy (STEM) mode, a focused, convergent beam of electrons is focused and scanned across the specimen, electrons scattered at different angles are collected by a detector to form an image. Scanning of the beam is accomplished by using two pairs of scanning coils located between the condenser lens and the objective pole piece. One function of the scanning coils is to keep the beam parallel to the optic axis while it scans across the specimen [10]. The STEM signal generated at each point on the specimen is detected, amplified, and proportional signal is displayed at an equivalent point on the detector. The image builds up as the scanning takes place.

In STEM imaging, serial recording is done instead of parallel recording which is the case in TEM imaging.

Two types of STEM images can be obtained depending on whether the signal is collected from the beam which includes the direct beam or only the scattered electrons. If the direct beam is detected it is called bright-field STEM imaging. If annular detector is used to collect the scattered electrons, it is called annular dark-field. Figure 2.8 shows the schematic diagram illustrating the formation of Z-contrast image in STEM mode. The integrated intensity formed on the detector is roughly proportional to the square of the atomic number ($Z^{1.7}$) [19]. Qualitative elemental distribution at atomic level can be obtained from Z-contrast images as the difference in atomic numbers will have different intensities. However it is not easy to differentiate between the two elements if they have similar atomic number. The advantage of STEM mode over TEM mode is the precise control on the position of the beam on the area of interest, which can be used to get local chemical information by using energy dispersive x-ray spectrometer (EDX) or electron energy-loss spectrometer (EELS) detectors.

Ex-situ TEM characterization is performed on a JEOL JEM 2010 operated at 200keV (shown in figure 2.9). This microscope has a point to point resolution of 0.19 nm and an information limit of 0.14 nm. This microscope is equipped with angle annular dark-field (ADF) detector for STEM imaging. TEM samples were prepared by dispersing catalyst powder onto a holy carbon film supported on a copper grid.

2.4.2. *In-situ* environmental TEM characterization

In-situ environmental TEM (ETEM) is a powerful tool for following the dynamic gas-solid interactions on the surface of the catalyst [20-22]. It helps in studying the catalyst under reacting gas conditions and can provide information on nanoscale changes taking place in the catalyst. This kind of information can provide several fundamental insights into the gas-solid interactions, mechanisms of phase transformation, sintering mechanisms, evolution of nanoparticles under reacting gas conditions, growth kinetics etc [23-25]. Performing *in-situ* ETEM experiments under reacting gas conditions will give information on the active phases of the catalyst during catalysis. This kind of information helps in correlating the nanostructures with the catalytic performance.

In-situ ETEM experiments were performed in an FEI Tecnai F20 field emission TEM (figure 2.10) operating at 200kV with a point resolution of 0.24 nm and an information limit of 0.14 nm [26,27]. This instrument is capable of performing both TEM and STEM under reacting gas conditions. It is equipped with Gatan imaging filter, this allows us to follow *in-situ* nanoscale chemical changes using electron energy loss spectroscopy.

Figure 2.11, shows the external gas handling system connected to the TEM. The gas handling system consists of a mixing tank, from which gas flows along the stainless tube and a leak valve is used to control the amount of gas flowing into the microscope column. Figure 2.12 shows the schematic of gas handling arrangement. The mixing tank allows gases of arbitrary composition to be mixed from up to 4 different gases. Gases were combined by injecting

appropriate pressures into a mixing tank assuming Dalton's law (molar ratios = ratio of partial pressures). Dalton's law applies only to ideal gases not for real gases which are composed of interacting gas molecules [28]. However, in this case, the pressures are equal to or less than one atmosphere where the compressibilities are close to unity giving errors in molar ratios of less than a few percent. All gases (except lab air) used for our experiments are 99.999% pure.

This microscope is equipped with a differential pumping system for holding gas pressures near the sample region of the microscope and at the same time protects the electron gun from damage because of exposure to high gas pressures [27]. Figure 2.13 shows the schematic of the differential pumping system, this system is capable of handling gas pressures of up to 8 Torr. Gas is introduced in the sample area through the leak valve and the escape rate into the rest of the TEM column is restricted by small differential pumping apertures of 100 μm in size. Gas leaked through these apertures is pumped at different levels using turbo molecular pump (1^{st} level of pumping) and molecular drag pump (2^{nd} level of pumping). The small opening of the differential pumping apertures helps in holding high gas pressures near the sample region of the microscope [27].

Heating the samples was performed using a Gatan heating holder with a furnace body made of inconel. This holder is capable of going up to 900^{o}C in vacuum and the maximum temperature it can go in presence of gases depends on the type of gas and its pressure. The amount of current required to heat the furnace to a certain temperature is different in the presence of gas compared to that of in vacuum, which depends on the thermal conductivity (table 2.1) and the

pressure of the gas. It requires relatively higher currents in the presence of H_2 and He gas than the other gas components to maintain the same temperature. Since the maximum current that can be passed through the holder is limited, the highest temperature the holder can reach in the presence of gas will depend on the type of gas and its pressure. The heating holder is equipped with thermocouple to read the temperature of the furnace. It is also equipped with a water cooling system to keep the temperature low at the O-ring region when the furnace is heated to temperatures above 500^{o}C. Temperature of the holder is adjusted by changing the current flow into the furnace. The error in determining local sample temperature was +/- 25^{o}C.

TEM samples for *in-situ* ETEM experiments were prepared by gently crushing the catalyst sample between glass microscope slides and dispersing them onto a platinum (Pt) grid. The Pt grids were made by punching 3 mm grids from Pt gauze (99.9% pure, 100 mesh woven from 0.0762 mm diameter wire) obtained from Alfa Aesar. Pt grids were chosen because of its chemical inertness even at high temperatures. The operating temperatures are well below the Tamman temperature of Pt, this keeps the diffusion of Pt atoms extremely low and the likelihood of Pt interacting with the sample is very small. Pt is one of the best catalysts for most of the reactions, during *in-situ* environmental studies under reacting gas conditions, Pt can catalyze the reaction and can change the gas composition inside the environmental cell. The extent of catalysis on the Pt grid will vary depending on the reaction. The volume of reacting gas inside the cell is very large compared to the amount of Pt available for catalysis. Though there is a

catalytic reaction taking place due to the presence of Pt, the amount of product gas formation will be negligible compared to the amount of reactant gases. Moreover electron energy loss-spectroscopy can be used to monitor any change in the gas composition during *in-situ* ETEM experiments. To make sure the platinum grid is placed firmly onto the holder, two inconel washers were used on both sides of the grid and secured with a hexring, both washers and the hexring are made of inconel. Figure 2.14 shows the schematic of loading the sample onto the heating holder.

2.4.3. Chemical analysis using EDX and EELS

Analytical transmission electron microscopy is capable of providing chemical analysis at high spatial resolutions [30]. When a fast moving electron hits the sample there are several interactions that take place between the electron and the sample. Some are elastic interactions, where there is no change in the electron energy after the interaction with the atoms in the sample and some are inelastic interactions, where a high energy electron can lose energy to an atom. Spectroscopy takes advantage of these inelastic interactions to identify the chemical species in the material.

In the process of loosing energy, the primary electron generates x-rays which are detected by the energy dispersive x-ray (EDX) spectrometry. An incident electron can ionizes the atom by removing one of the bound electrons leaving the atom in an excited state. For example, suppose a K-shell electron is removed by the incident electron (as show in figure 2.15); this will leave a

vacancy in the K-shell. The ion can lower its energy by filling the vacancy with an electron from the outer shell and the excess energy is radiated as a characteristic X-ray. This characteristic X-ray energy is unique to the specific atom which can be used to identify the elements present in the sample. The main component of the EDX is the x-ray detection unit which is made of semiconductor material. X-rays from the sample hit the detector generating electron-hole pairs; the number of electron-hole pairs generated is proportional to the energy of the x-rays. The number of electron-hole pairs is detected by the detector and converted into a signal. The detector is cooled to liquid nitrogen temperature to deactivate the electron-hole pair generation due to thermal energy; this will help in keeping the noise levels very low while detecting the x-ray signal.

EDX can detect all the elements above lithium. EDX can be used for both qualitative and quantitative analysis. The position of the peak on the energy scale can be used to identify the elements present in the sample. Quantitative analysis in EDX can be performed using Cliff-Lorimer equation [30]. For example, the elemental ratio in a bimetallic nanoparticle can be determined by using the following Cliff-Lorimer equation [30]:

$$C_A/C_B = k * I_A/I_B$$

where C_A and C_B are the concentrations of elements A and B respectively in the sample and I_A and I_B are the intensities of the characteristic peaks from elements A and B respectively. ‘k’ is a sensitivity factor that depends on the atomic number correction factor, x-ray absorption within the sample, and x-ray fluorescence within the sample. By assuming that the nanoparticles are very small any

absorption or fluorescence within the sample can be ignored, and hence k depends only on the atomic number correction factor. ‘k’ factor can be obtained by taking the EDX spectrum from known sample composition or can be calculated from the theoretical cross-sections [30]. EDX was used to determine the elemental ratio in individual bimetallic nanoparticles, the detailed procedure of EDX analysis will be discussed in chapter 5. EDX analysis of bimetallic nanoparticles was performed on a JEOL JEM 2010F TEM equipped with a EDAX EDX detector with an energy resolution of 130 eV.

In electron energy-loss spectrometry (EELS), the inelastically scattered electrons are transmitted through the sample and are detected by the EELS detector. Electrons enter into the spectrometer through a variable entrance aperture and travel through the drift tube where these electrons are deflected by the magnetic field. Electrons with greater energy loss are deflected further than the zero loss electrons. A spectrum is thus formed in the dispersion plane which consists of a distribution of electron counts. Electrons that have undergone similar energy losses are focused onto a same point on the dispersion place. The object plane of the spectrometer is usually the back focal plane of the projector lens of the TEM.

The EELS spectrum can be divided into two energy-loss regions, valence loss and core loss. The valence-loss spectrum is formed by the energy loss of the electrons due to the excitation of valence electrons. The core-loss spectrum is formed by the energy loss due to the ionization of the inner-shell electrons in an atom. EELS can be used for elemental identification, to determine elemental

composition, oxidation state, atomic bonding state and optical properties [31-33]. In this dissertation, EELS was used to determine the oxidation state of surface layers (Chapter 4) and STEM-EELS line scans to determine the elemental distribution in bimetallic nanoparticles (Chapter 5). In chapter 6, EELS was used to determine the gas composition inside the environmental TEM for *in-situ* studies. EELS was also used to measure the catalytic product formed during gas phase catalysis for heterogeneous catalysis application (Chapter 7).

References

1. Stober, W., Fink, A., & Bohn, E. (1968). Controlled Growth of Monodisperse Silica Spheres in the Micron Size Range. *Journal of Colloid and Interface Science*, 26, 62-69.

2. Ertl, G., Knozinger, H., & Weitkamp, J. (1997). *Handbook of heterogeneous catalysis* (Vol 1).

3. Banerjee, R., & Crozier, P.A. (2011). *In-situ* synthesis and evolution of support metal catalyst: Ni on silica. *Journal of Physical Chemistry*, (in press).

4. Cadamson, A. W., & Gast, A. P. (1997). *Physical Chemistry of* Surface. Wiley (6^{th} Ed). ("Retrieved from http://en.wikipedia.org/wiki/Surface_tension_values").

5. Bartholomew, C. H. (2001). Mechanisms of catalyst deactivation. *Applied Catalysis A: General*, 212(1-2), 17-60.

6. Grant, D. W. (1996). Capillary gas chromatography. John Wiley & Sons.

7. Jonsson, J. A. (1987). Chromatographic theory and basic principles (38). Marcel Dekker.

8. Grob, R. L. (1997). *Modern Pracrice of Gas Chromotography*. John Wiley & Sons. ("Retrieved from http://en.wikipedia.org/wiki/Thermal_conductivity_detector").

9. Tennet, R.M. (1971). Science Data Book. Oliver & Boyd.

10. Williams, D. W., & Carter, C. B. (1996). Transmission electron microscopy. New York: Springer.

11. Ozkaya, D. (2008). Particle size analysis of supported platinum catalysts by TEM. *Platinum Metal Review*, 5(1), 61-62.

12. Hansen, P. L., Wagner, J. B., Helveg, S., Rostrup-Nielsen, J. R., Clausen, B. S. & Topsoe, H. (2002). Atom-resolved imaging of dynamic shape changes in supported copper nanocrystals. Science, 295, 2053-2055.

13. Yao, M. H., Smith, D. J., & Datye, A.K. (1993). Comparative study of supported catalyst particles by electron microscopy methods. *Ultramicroscopy*, 52, 282-288

14. Howie, A., Marks, L.D., & Pennycook, S.J. (1982). New imaging methods for catalyst particles. *Ultramicroscopy*, 8, 163-174.

15. Wang, R., Crozier, P. A., & Sharma, R. (2009). Structural transformation in ceria nanoparticles during redox processes. *Journal of Physical Chemistry C*, 113(14), 5700–5704.

16. Sattler, M. L., & Ross, P.N. (1986). The surface structure of Pt crystallites supported on carbon black. *Ultramicorscopy*, 20, 21-28.

17. Datye, A.K., Logan, A.D. Blankenburg, K. J., & Smith, D. J. (1990). Characterization of surface structure in heterogeneous catalysts by high-resolution transmission electron microscopy. *Ultramicroscopy*, 34, 47-53.

18. Logan, A. D., Braunschweig, E. J., Datye, A. K., & Smith, D.J. (1989). The oxidation of small rhodium metal particles. *Ultramicroscopy*, 31, 132-137.

19. Kirkland, E. J., Loane, R. F., & Silcox, J. (1987). Simulation of annular dark field stem images using a modified multislice method. *Ultramicroscopy*, 23, 77-96.

20. Baker, R. T. K., Chludzinski, J. J. (1986). *In-situ* electron microscopy studies of the behavior of supported ruthenium particles. *Journal of Physical Chemistry*, 90, 4734-4738.

21. Baker, R. T. K., & Rodriguez, N. M. (1994). A review of the use of *in-situ* electron microscopy techniques for the study of iron-based catalysts for coal conversion processes. *Energy & Fuels*, 8(2), 330-340.

22. Gai, P.L. (2002). Developments in *in-situ* environmental cell high-resolution electron microscopy and applications to catalysis. *Topics in Catalysis*, 21(4), 161-173.

23. Chenna, S., Banerjee, R., & Crozier, P. A. (2011). Atomic scale observation of the Ni activation process for partial oxidation of methane using *in-situ* environmental TEM. *Chemcatchem*, 3, 1051-1059.

24. Simonsen, S.B., Chorkendorff, Ib., Dahl, S., Skoglundh, M., Sehested, J., & Helveg, S. (2010). *Journal of American Chemical Society*, 132, 7968-7975.

25. Li, P., Liu, J., Nag, N., & Crozier, P. A. (2005). Atomic-scale study of *in-situ* metal nanoparticle synthesis in a Ni/TiO2 system. Journal of Physical Chemistry B, 109(29), 13883-13890.

26. Sharma, R. (2009). Kinetic measurements from *in-situ* TEM observations. *Microscopy Research and Technique*, 72, 144-152.

27. Sharma, R. (2005). An environmental transmission electron microscope for *in-situ* synthesis and characterization of nanomaterials. *Journal of Materials Research*, 20(7), 1695-1707.

28. Atkins, P., & de Paula, J. (2002). *Physical Chemistry*. New York: W.H. Freeman and Company.

29. Sigle, W. (2005). Analytical transmission electron microscopy. *Annual Review Materials Research*, 35, 239-314.

30. Garratt-Reed A. J., & Bell, D.C. (2003) *Energy-dispersive X-ray analysis in the electron microscope*. BIOS Scientific Publication: Limited.

31. Egerton, R.F. (1996). *Electron energy-loss spectroscopy in the electron microscope* (2nd ed.). New York, BY: Plenum Press.

32. Alexander, D. T. L., Crozier, P. A., & Anderson, J. R. (2008). Brown carbon spheres in East Asian outflow and their optical properties. *Science*, 321, 833-836.

33. Garvie, L. A. J., & Buseck, P.R. (1998). Ratios of ferrous to ferric iron from nanometre-sized areas in minerals. *Nature*, 396, 667-670.

Table 2.1. Thermal conductivity of gases

Gas	**Thermal Conductivity ($Wm^{-1}K^{-1)}$**
Hydrogen	1684
Helium	1415
Nitrogen	243
Argon	162
Methane	302
Oxygen	244
Carbon monoxide	232
Carbon dioxide	145
Water vapor	158

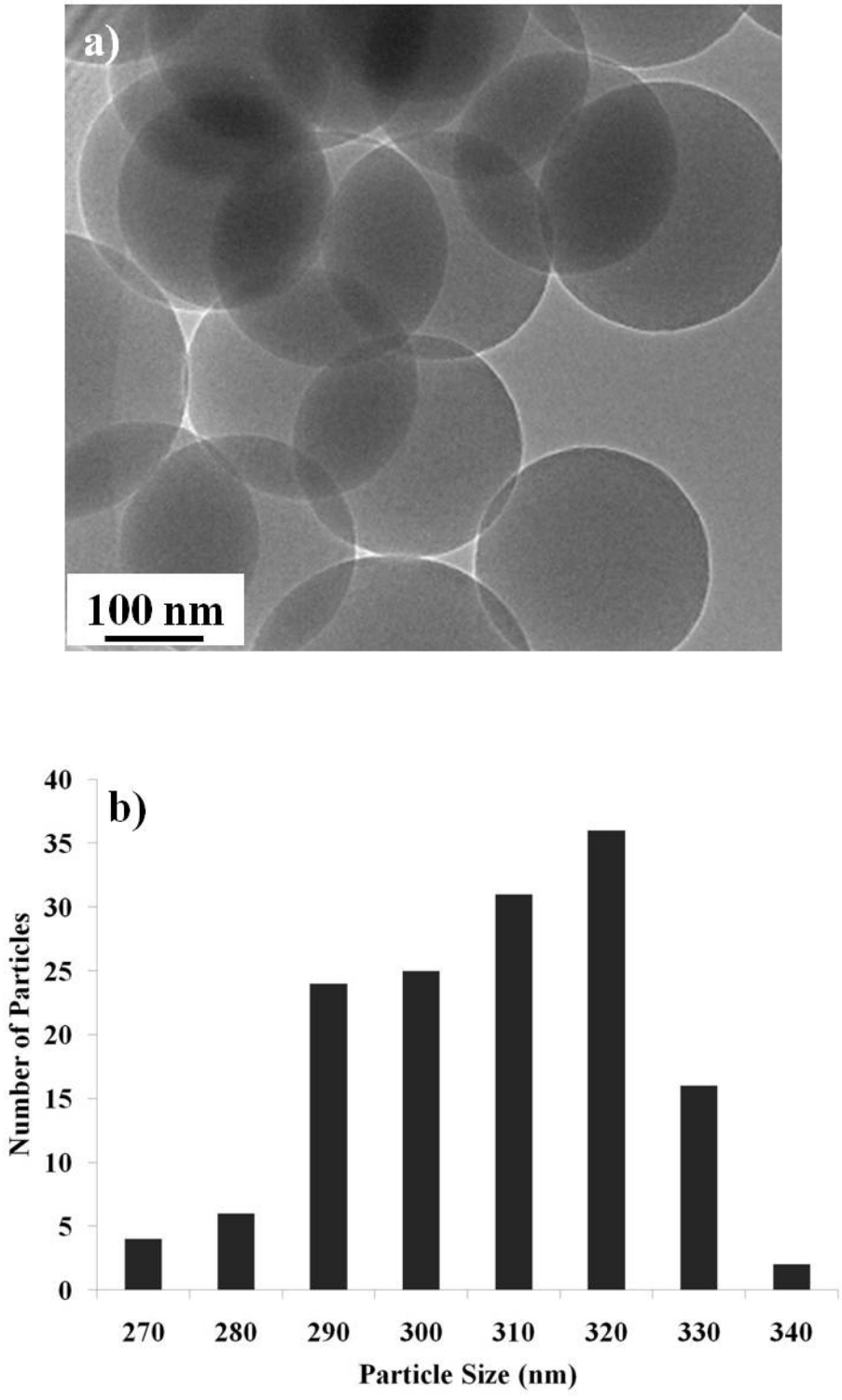

Figure 2.1. a) TEM image of SiO_2 spheres, b) SiO_2 spheres size distribution.

Figure 2.2. Glove bag set up used for incipient impregnation.

Figure 2.3. ISRI RIG-150 microreactor unit.

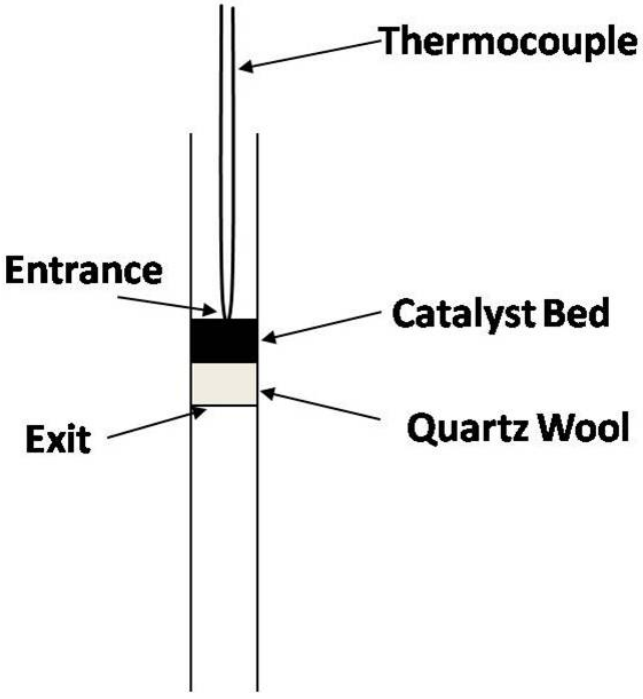

Figure 2.4. Schematic of reactor tube.

Figure 2.5. Varian 3900 Gas Chromatograph unit.

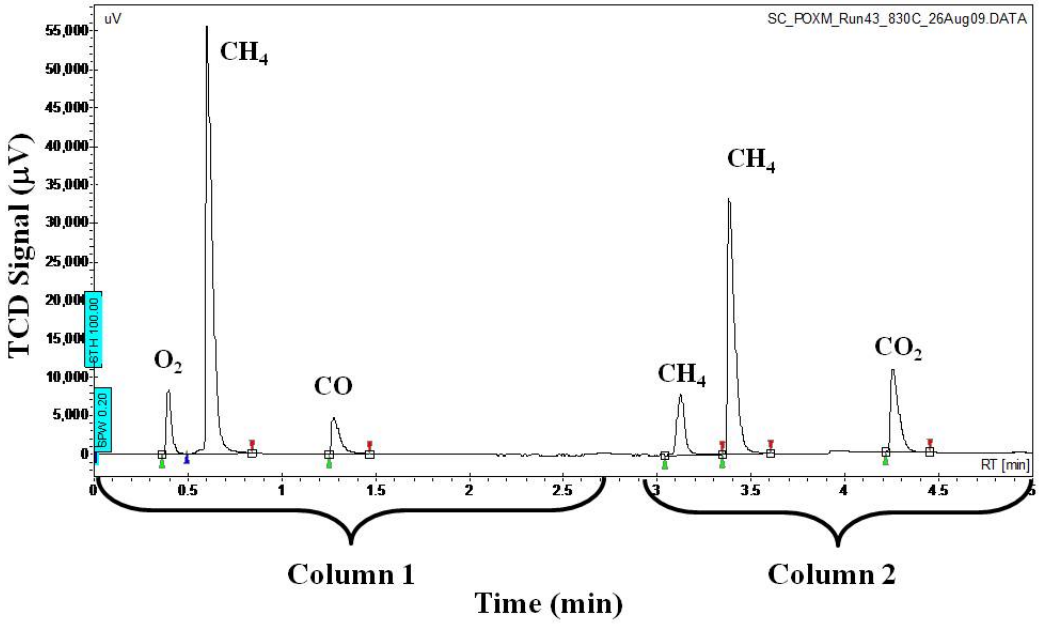

Figure 2.6. Plot showing the schematic of typical gas chromatogram.

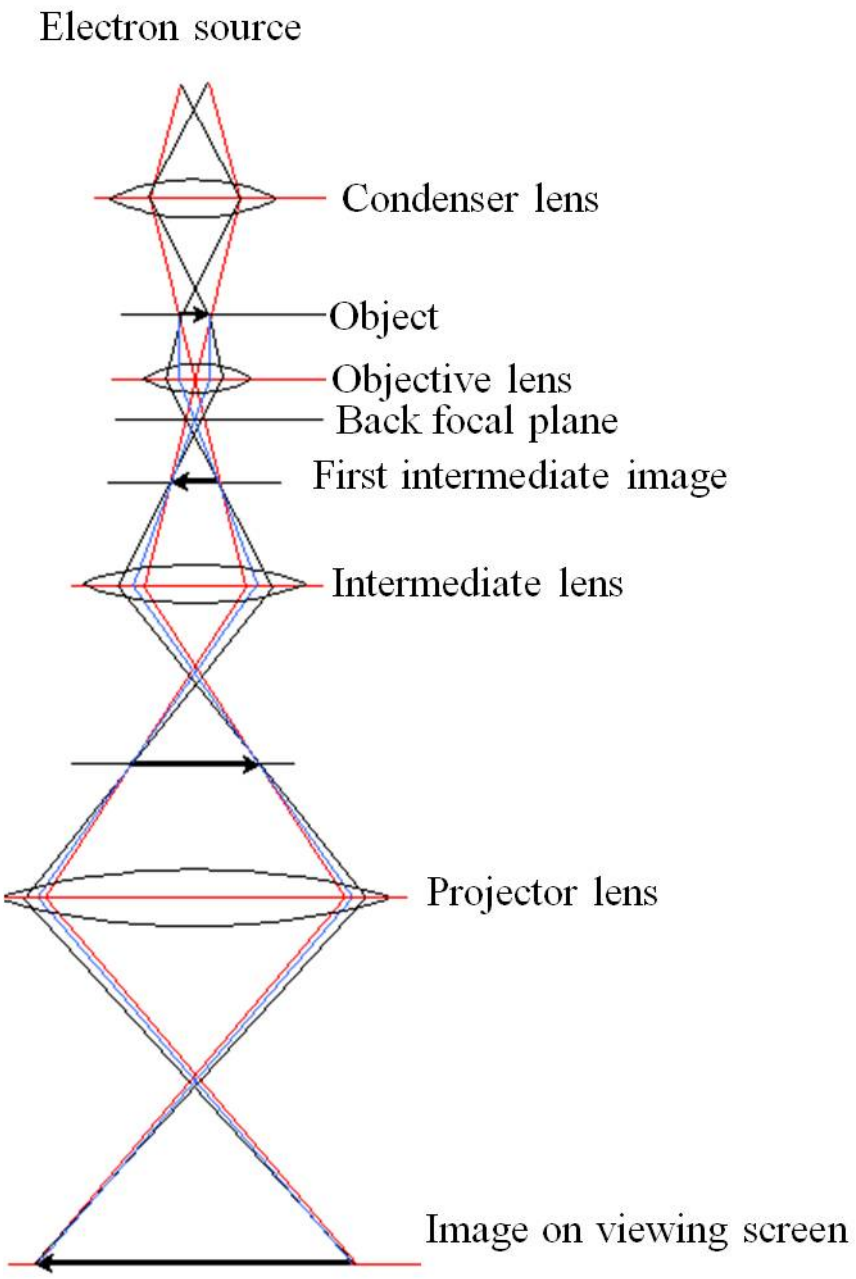

Figure 2.7. Ray diagram showing a) image formation and b) diffraction formation (contd.) [10].

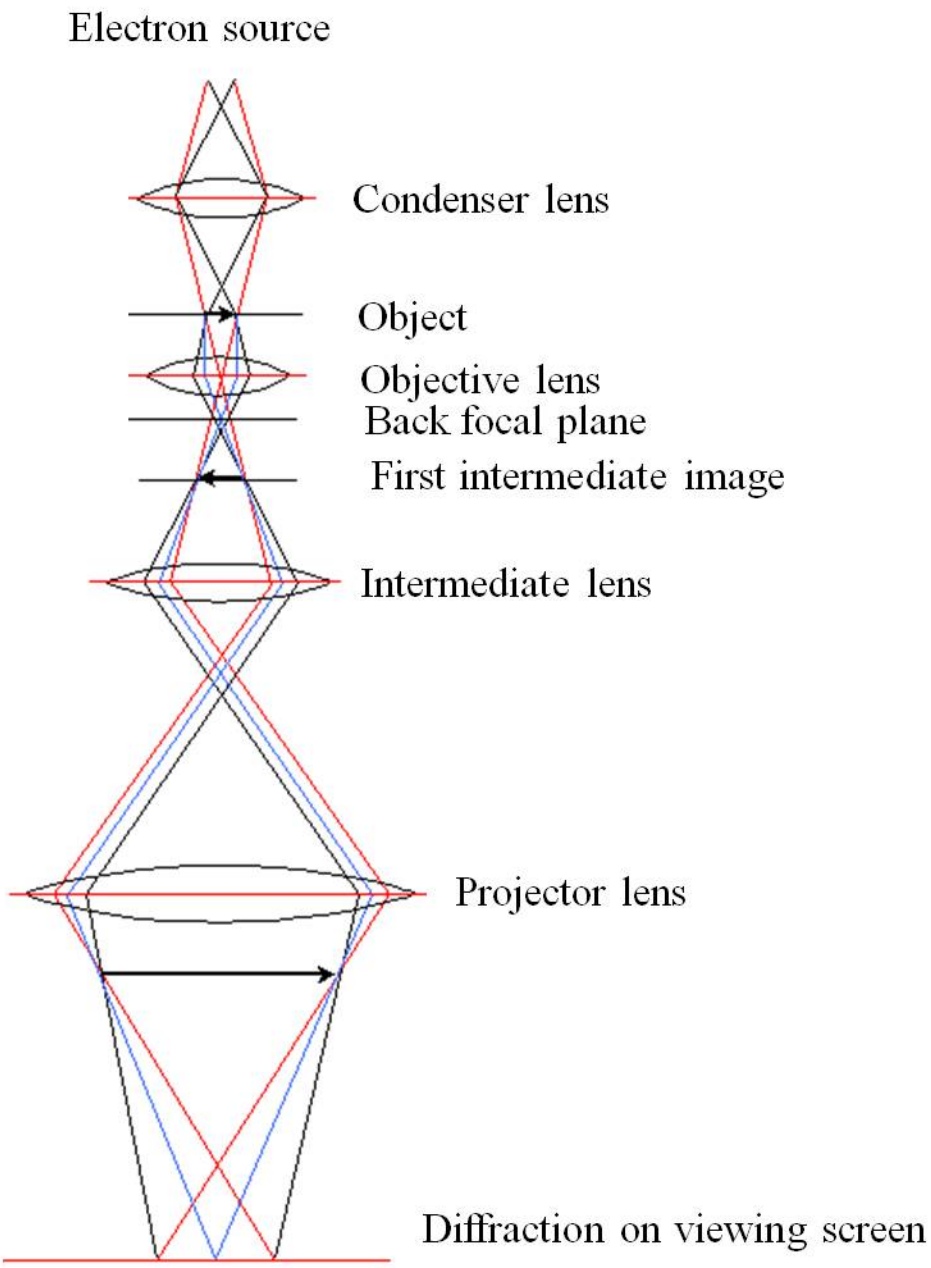
Electron source
Condenser lens
Object
Objective lens
Back focal plane
First intermediate image
Intermediate lens
Projector lens
Diffraction on viewing screen

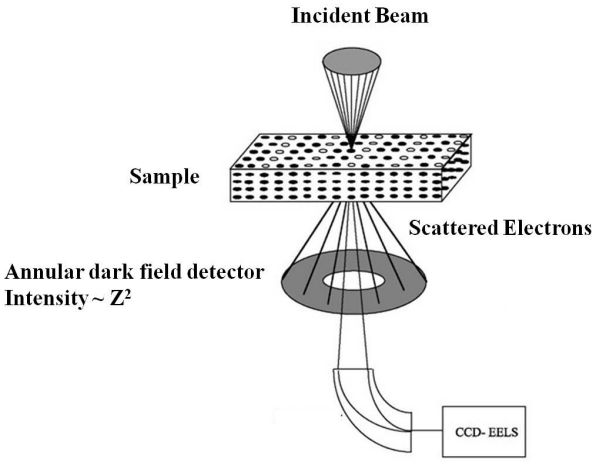

Figure 2.8. Schematic diagram showing the formation of Z-contrast STEM image [10].

Figure 2.9. JEOL JEM 2010 transmission electron microscope at Arizona State University.

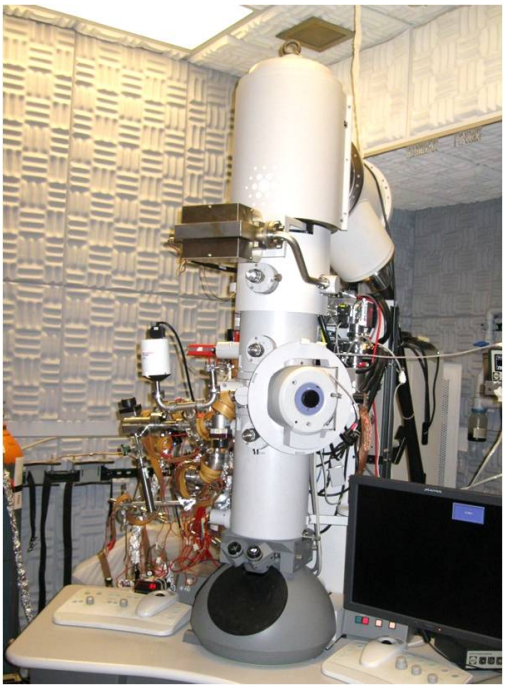

Figure 2.10. FEI Tecnai F20 *in-situ* environmental transmission electron microscope at Arizona State University.

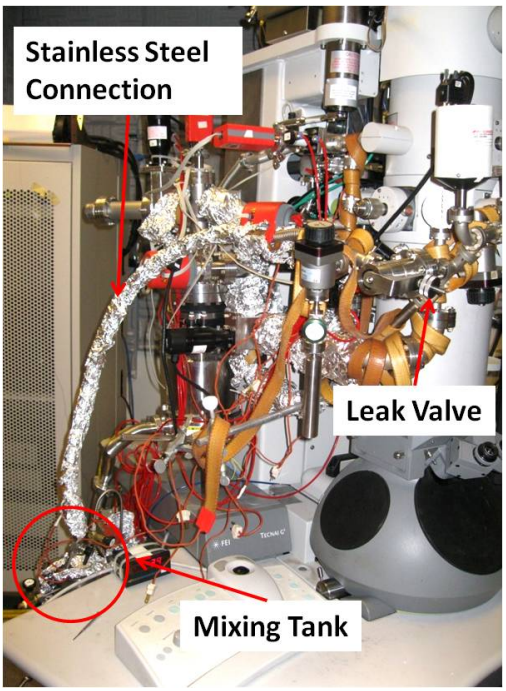

Figure 2.11. External gas handling system connected to the Tecnai F20 TEM column.

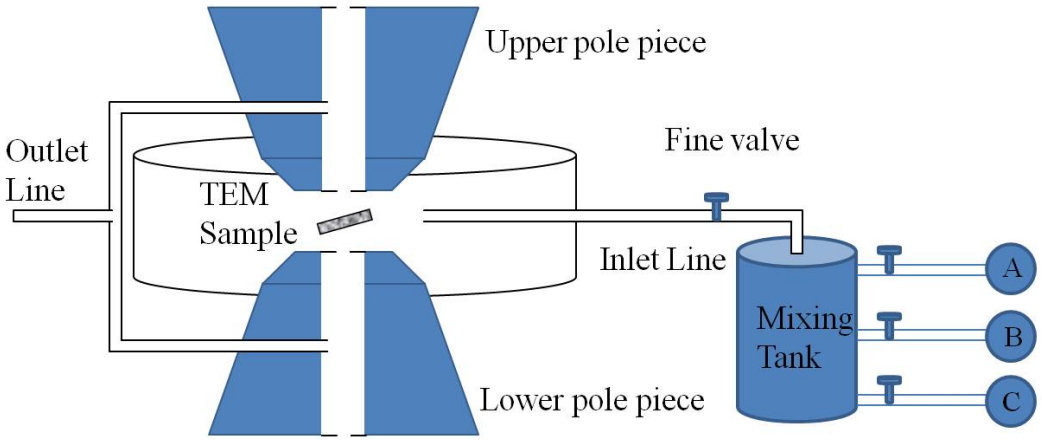

Figure 2.12. Schematic diagram showing the mixing tank setup and its connection to the environmental cell in the ETEM, the mixing tank is approximately 1 m from the cell.

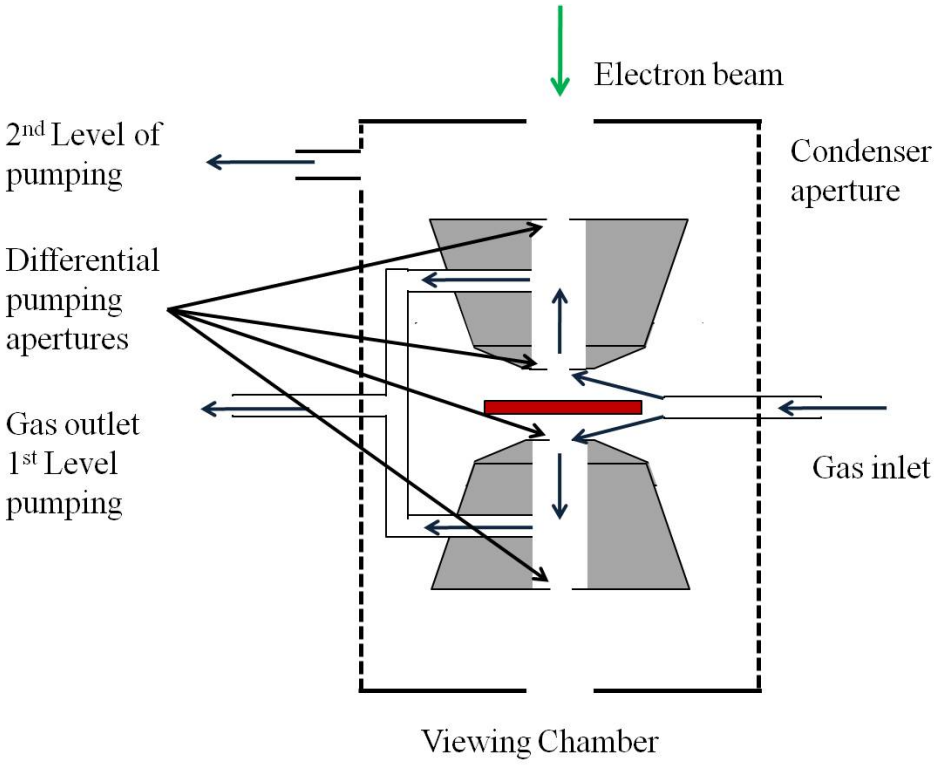

Figure 2.13. Schematic of environmental cell in the ETEM, showing different levels of pumping [27].

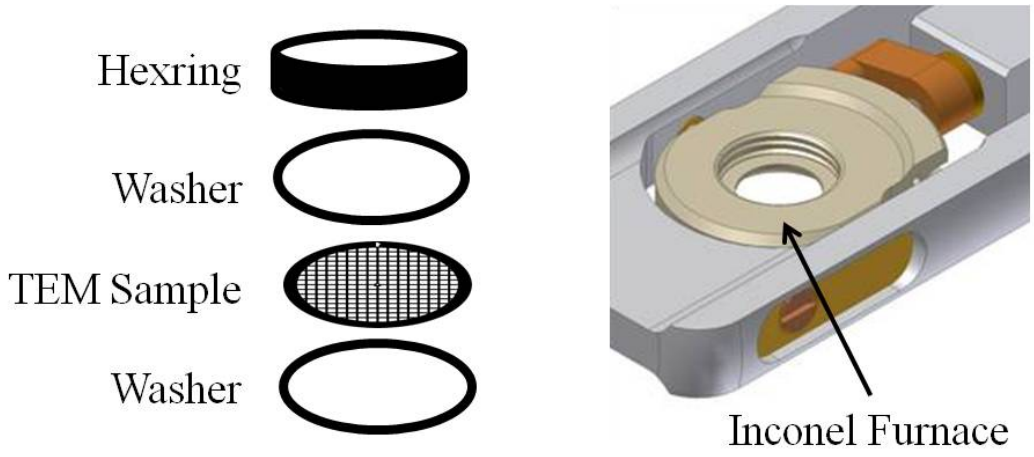

Figure 2.14. Schematic of TEM sample loading on to a Gatan inconel hot stage.

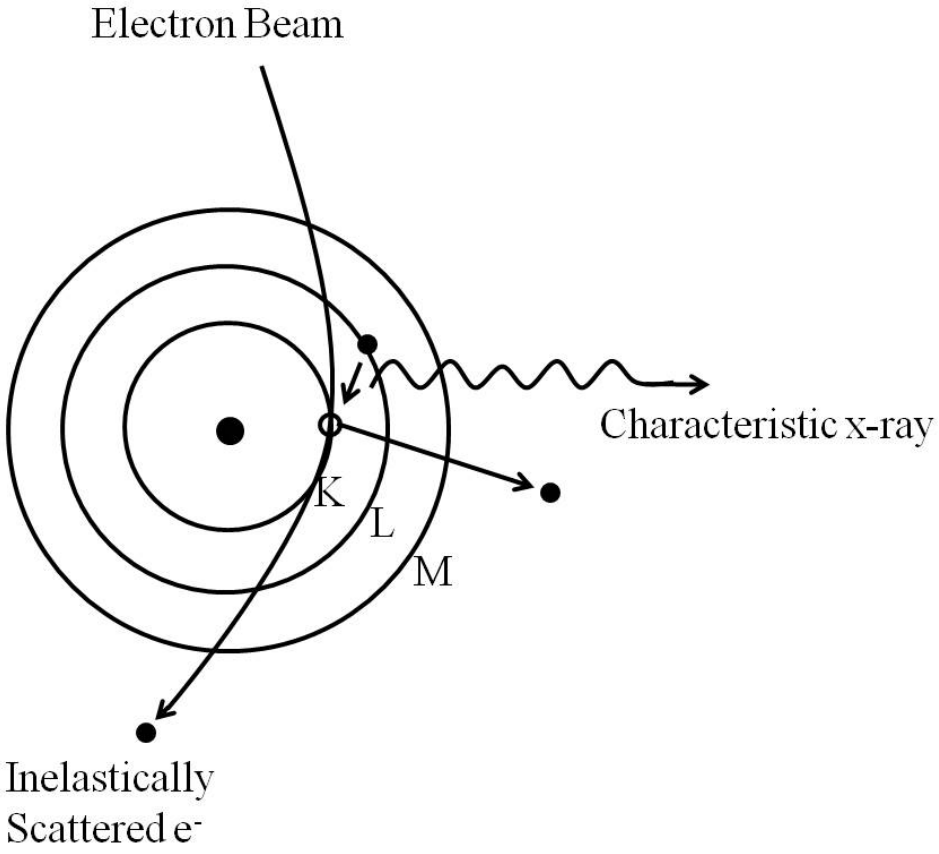

Figure 2.15. Schematic showing the basic principle of x-ray generation by a primary electron [30].

Chapter 3

STRUCTURE-ACTIVITY RELATIONSHIP IN NI CATALYST FOR PARTIAL OXIDATION OF METHANE

3.1. Introduction

The goal of this chapter is to understand the structure-activity relationship in SiO_2 supported Ni catalysts for partial oxidation of methane. Catalytic activity measurements in parallel with *in-situ* nanoscale structure characterization were performed to develop structure-activity relationship in Ni/SiO_2 catalyst. Noble metals are very efficient and stable for converting methane to syngas, [1-6] with Ru and Rh being among the fastest for reaching thermodynamic equilibrium conversions, but noble metals are costly for large scale applications. Supported Ni catalysts have also been studied as less expensive options for partial oxidation of methane. Ni catalysts show high conversion efficiencies at low cost [1,2,7] although deactivation by coke forming and sintering can be problematic.

For partial oxidation of methane at high catalytic conversions, the entrance of the catalyst bed sees mostly reacting gases (mixture of CH_4 and O_2 in 2:1 ratio) and the exit of the catalyst bed sees mostly product gases (mixture of CO and H_2 in 1:2 ratio). The gas composition along the catalyst bed changes from an oxidizing (with O_2 as the oxidation gas) to a reducing environment (with CH_4, CO and H_2 as reduction gases) changing the oxidation state of the Ni nanoparticles. Moreover, during the reactor ramp-up, the catalyst structure and activity will change with temperature leading to further changes in the ambient gas composition. Thus during ramp-up, the “reactor condition” varies in time and

space and it is important to take this into account in the design and interpretation of ETEM experiments. *In-situ* ETEM experiments under oxidizing and reducing gas environments that are relevant to partial oxidation of methane were performed to follow the oxidation and reduction process in supported Ni nanoparticles.

3.2. Ni/SiO_2 catalyst preparation

A 2.5 wt% Ni/SiO_2 catalyst was prepared by impregnating SiO_2 spheres with nickel nitrate hexahydrate ($Ni[NO_3]_2.6H_2O$) solution using incipient wetness techniques. Nickel nitrate hexahydrate solution was prepared by dissolving a known amount of 99.999% $Ni[NO_3]_2.6H_2O$ (obtained from Sigma Aldrich) using ethanol as a solvent. Incipient wetness impregnation was carried out in a mortar by drop wise addition of nickel nitrate solution equivalent to the pore volume of the SiO_2 in a saturated ethanol atmosphere while mixing for 10 min. After impregnation, the sample was dried at 120^oC followed by reduction in 5%H_2/Ar atmosphere at 400^oC for 3 hours. The conventional calcination step was avoided to get improved metal dispersions in this case [8]. Figure 3.1 shows the Ni particle size distribution after the reduction step.

3.3. Ni/SiO_2 catalyst performance

The activity and selectivity of the catalyst was determined with an *In-situ* Research Instruments RIG 150 reactor. For a typical reaction, 10 mg of catalyst was loaded into the reactor and initially reduced at 400^oC in 5% H_2/Ar. Reactions were typically performed using a feed mixture of CH_4:O_2:He = 8:4:50 with a total

flow rate of 62 cc min^{-1}. (Partial pressures of CH_4 and O_2 in the gas feed were 98 Torr and 49 Torr respectively). A typical run would involve ramp-up rates of about 4^oC per minute. The effluent gas from the reactor outlet was analyzed with a Varian 3900 gas chromatography. As He is used as a carrier gas, H_2 was not directly detected; hence CO formation was taken as the reference for measuring the activity of the catalyst for syngas ($CO+H_2$) formation. Conversion and selectivities were calculated according to the details mentioned in section 2.3.2 of chapter 2.

Figures 3.2 (a-d), shows the measured catalytic conversion of CH_4 and O_2 and their selectivity towards CO_2 and CO on Ni/SiO_2 during partial oxidation of methane. During the temperature ramp up, no catalytic conversion of CH_4 take place at temperatures below 300^oC. Complete combustion of up to 24% of CH_4 takes place in the temperature regime of 300^oC to 750^oC giving CO_2 and H_2O in 1:2 ratio with 100% O_2 consumption at 750^oC. A further increase in temperature to 775^oC resulted in a sudden increase of CH_4 conversion from 24% to 97% with almost all the CH_4 being converted to CO and H_2 on 1:2 ratio. A slight increase in CH_4 conversion and CO selectivity was observed with a further stepwise increase in temperature to 900^oC. A dramatic difference in the conversions and selectivity's compared to temperature ramp-up was observed when the reactor temperature was gradually decreased from 900^oC to 400^oC. CH_4 conversion decreases gradually with decrease in temperature while the O_2 conversion remains at 100% down to 500^oC and drops to 5% at 400^oC. Interestingly, on ramp down, significant CO selectivity was observed down to a temperature of 450^oC, in

contrast with the ramp-up data which showed negligible CO selectivity until 775^{o}C. No gas reactions were detected below 400^{o}C.

Figure 3.3 schematically illustrates the possible variation in gas composition along the catalyst bed for three different temperature regimes. The catalyst bed was divided into three regions (not necessarily equal). At temperatures below 300^{o}C, all regions of the bed are exposed to a mixture of CH_4 and O_2 (2:1). In the temperature range of 300^{o}C to 750^{o}C, region I at the front of the bed sees a reactant mixture of mostly CH_4 and O_2 whereas regions II and III are exposed to mixtures containing CH_4, O_2, CO_2 and H_2O. With increasing temperature, the CO_2 and H_2O concentration will increase in region II and III of the bed at the expense of CH_4 and O_2 consumption. Above 750^{o}C, region II is exposed mostly to a mixture of CH_4, CO_2, and H_2O since now most of the O_2 has been consumed during complete combustion of CH_4 in region I. Reforming of methane with CO_2 and H_2O takes place in region II and region III is exposed mostly to a mixture of CO and H_2 (in 1:2 ratio). In reality there is a continuous change in the gas composition across the bed and figure 3.3 simply illustrates the dominant compositions present at different locations and temperatures in order to facilitate the design of appropriate ETEM experiments.

3.4. Dynamic nanoscale evolution under reacting gas conditions

3.4.1. *In-situ* environmental TEM characterization

In-situ environmental TEM was performed on an FEI Tecnai F20 under gas pressures of about 1 Torr. The samples were reduced *in-situ* in the presence of H_2

at 400^{o}C before exposing them to the various gas mixtures of relevance for partial oxidation of methane. To investigate the structure of the catalysts at different points along the reactor bed at different temperatures, a series of ETEM experiments were undertaken in gas mixtures corresponding to the various gas compositions shown in figure 3.3. The ETEM conditions were labelled A - H and are defined in table 3.1. Conditions A and B are always run in sequence at the beginning of each experiment to mimic the initial start-up procedures in the RIG 150 reactor (i.e. experiments exploring conditions C to H are always preceded by A and B). The gases for each experiment were pre-mixed in a mixing tank in the desired ratios before admission into the cell. *In-situ* reactions were carried out at pressures of 0.1 to 0.8 Torr. The Ni/SiO_2 samples were gently crushed between glass microscope slides, loaded onto platinum grids and placed onto a Gatan Inconel heating holder. Electron beam damage effects were minimized by using low-dose image conditions and blanking the beam during the temperature ramp. Furthermore, to check that electron beam effects were not important, the irradiated areas were compared with the non-irradiated areas to make sure that the phase transformations were identical between the two areas.

3.4.2. Initial stage of ramp-up: NiO formation

A typical low magnification image of SiO_2 supported Ni nanoparticles in presence of 0.8 Torr of H_2 at 400^{o}C (Condition A) is shown in figure 3.4a, and diffraction pattern (figure 3.4b) confirming the fcc Ni. Ni nanoparticles are de-wetting the SiO_2 in the presence of H_2 atmosphere. In the presence of a 0.8 Torr mixture of

CH_4 and O_2 in 2:1 ratio at 400^oC (Condition B), the Ni nanoparticles transform to a structure showing a void-like morphology that wets the silica surface, as shown in figure 3.4c. Electron diffraction shows the nanoparticles are now fcc NiO, figure 3.4d. Figure 3.5 (a-e) shows the sequential images of void formation in NiO in the presence of CH_4 and O_2 mixture at 400^oC. This kind of information is not easy to obtain during the *in-situ* studies because of the thermal drift associated with the holder when the reacting gases are introduced into the environmental cell. The sequential images in figure 3.5 were obtained from a video taken at 15 frames per second during the reaction. Drift in the image is corrected by using statistically determined spatial drift package (SDSD) [9] and the images of individual frames are obtained after the drift correction. To reduce the noise, 20 individual frames were averaged to get the single image. From the sequential images it is clear that the void nucleates at the interface of the Ni/SiO_2 and grows away from the interface until the Ni oxidation is complete. Figure 3.6 shows a high resolution *in-situ* ETEM image of void structured NiO particle at 400^oC in the presence of CH_4 and O_2 mixture 60 minutes into the reaction. The high resolution image shows multiple grains with restricted long-range ordering suggesting the presence of defects in the nanoparticle.

It was initially somewhat surprised to see the formation of NiO, since the gas composition was rich in reducing gas (CH_4). To check the gas composition in the environmental cell, electron energy-loss spectroscopy of gases was performed in the environmental cell [10]. Figure 3.7 is a background subtracted energy-loss spectrum from a mixture of CH_4 and O_2 in 2:1 pressure ratio during the *in-situ*

studies, showing C K-edge and O K-edge from CH_4 and O_2 respectively. The background was extrapolated beyond the edge, the K-edges integrated over a 100 eV range and the signal ratio converted to elemental ratios using Hartree Slater cross sections. The result from quantification gave an average value for the O/C ratio of 1.14±0.01. These values lie within about 15% of the nominal value of 1.0 that would be expected based on ratios of the two gases in the mixing tank. This confirms that the Ni to NiO transformation takes place even though the gas composition is rich in CH_4. More details on EELS of gases will be discussed in chapter 6.

As a further check on the validity of the *in-situ* observations, several samples were analyzed from the *ex-situ* reactor at an equivalent point in the ramp-up. After the initial reduction step, the catalyst was heated to 400^{o}C in the *ex-situ* reactor in the presence of CH_4 and O_2 in a 2:1 ratio. The sample was then cooled to room temperature and immediately transferred into a TEM for observation. Figure 3.8, shows a typical image and diffraction pattern from the *ex-situ* sample and confirms both the formation of the void structured morphology and the complete conversion of the Ni to NiO. This shows that the void structure is an intermediate phase formed in the catalyst during ramp-up. Nanoparticle evolution was followed in the presence of the CH_4 and O_2 mixture up to 800^{o}C and electron diffraction confirmed that Ni existed as NiO even at this high temperature.
In the ETEM experiment, the phase transformation of Ni to NiO is caused by the high partial pressure of O_2, about 0.27 Torr, in the gas flow. In the *ex-situ* reactor, the catalyst bed is also exposed to a high oxygen partial pressure at temperatures

up to 700^{o}C. At these oxygen pressures, there is a strong thermodynamic driving force for oxide formation [11]. The presence of the reducing agent CH_4 does not significantly affect the phase transformation because of the higher chemisorption energy of O_2 on the Ni surface compared to CH_4 (chemisorption energies for the Ni (111) surface are 481 kJ mol^{-1} for the O-adatom, and 192.28 kJ mol^{-1} for CH_3^- adsorption) [12,13]. Consequently, the surface is mostly covered by O-adatoms making initial NiO formation kinetically as well as thermodynamically favoured.

Figure 3.9a and 3.9b show the *in-situ* ETEM images of Ni/SiO_2 and NiO/SiO_2 from the same area in presence of H_2 and $2CH_4 + O_2$ at 400^{o}C respectively (Condition B). Superposition of figures 3.9a and 3.9b shows that the void size is almost equivalent to the initial Ni particle size (Figure 3.9c). This suggests a Kirkendall type processes [14] where Ni cations diffuse faster than the O-anions through the NiO. After the initial oxidation of the Ni surface, there are two possible mechanisms by which complete particle oxidation can take place, either by the diffusion of O-anions through NiO to oxidize subsurface Ni or by the diffusion of Ni-cations through NiO shell to react with dissociated oxygen on the surface. The dominant mechanism depends on the rate of diffusion of Ni or O in NiO. Diffusion process can take place via the bulk diffusion or along easy diffusion paths like grain boundaries or other extended defects. Figures 3.6 shows that the NiO particles are composed of more than one grain and that many grains appear to show a high concentration of defects and restricted long-range order. These defects may act as easy diffusion paths during the oxidation process. The diffusion coefficient of Ni-cations and O-anions along the NiO grain boundaries

at 400^{o}C are 10^{-13} cm^2/sec and 10^{-21} cm^2/sec respectively [15-17]. Thus it can be seen that the diffusion coefficient of Ni in NiO along the grain boundaries is eight orders of magnitude greater than that for O. Diffusion of Ni through the NiO creates vacancies inside the metal particle which migrate towards the metal/SiO_2 interface and coalesce to form a void. The void formation process in NiO nanoparticles is depicted schematically in figure 3.10. Similar morphologies have been observed by Railsback et al., and Nakumara et al., where they studied the oxidation behaviour of Ni nanoparticles in the presence of pure oxygen [18,19].

Smaller Ni particles (those less than 4 nm) do not seem to undergo oxidation via this mechanism. For these particles, the diffusion distances are very short and it becomes kinetically possible for the oxide particles to achieve their thermodynamic equilibrium shape of a solid particle. (The void morphology is not the equilibrium shape because of the larger total surface energy associated with the internal surface of the void). In this particular case, these smaller particles represent a minor component of the surface area associated with the catalyst. From the particle size distributions of figure 3.1, the total fraction of surface area associated with Ni particles of different size can be determined simply by assuming that each particle is a sphere (a good approximation in this case). This analysis is given in figure 3.11 and shows that the percentage of surface area associated with particle sizes less than 4 nm is 7% for 2.5wt% Ni/SiO_2 catalyst. Thus for these particular model catalysts, the oxidations (and reduction) mechanisms associated with the larger particles will dominate the overall catalytic activity.

3.4.3. Final stage of ramp-up: NiO reduction and syngas formation

NiO is not an active phase for syngas production. For syngas production, Ni metal must be present on the surface so the NiO must eventually transform back to Ni metal at some later point in the ramp-up process. From the reactor data, as the temperature increases, the gas mixture in region II and region III (figure 3.3) of the catalyst bed becomes more reducing (as O_2 is consumed). Eventually it becomes thermodynamically favourable for the oxide to transform back to metal and at this point, the surface of the oxide will start to reduce.

In-situ reduction was performed under different gas environments in order to understand the NiO reduction process. Initial reduction experiments were performed in a mixture of CO and H_2 (in 1: 2 ratio) which is relevant to the product gas ratio that forms during the partial oxidation of methane. Figure 3.12, shows a selected area electron diffraction pattern recorded during the intermediate stage of reduction of NiO to Ni in presence of 0.1 Torr of CO and H_2 in 1:2 ratio at 400^{o}C (Condition D). The d-spacings of Ni (111) and NiO (200) are 0.203 nm and 0.208 nm respectively, and are difficult to resolve in the diffraction pattern from nanoparticles. However, formation of Ni metal during reduction may be recognized from the appearance of Ni (200) reflections with d-spacing of 0.17 nm. Figure 3.13, shows an *in-situ* high resolution ETEM image along with the Fast Fourier Transforms (FFT) of Ni/SiO_2 during the initial stage of reduction in the presence of 0.1 Torr of CO and H_2 at 400^{o}C (Condition D). Lattice spacing on the surface of the nanoparticle matches with the NiO (200) spacing of 0.21 nm. FFT from core region near to the SiO_2 interface shows two fundamental

reflections from the lattice spacings that are very close to each other. These reflections match with the Ni (200) and Ni (111) spacings of 0.21 nm and 0.20 nm respectively, suggesting that Ni metal nucleates at the interface between NiO and SiO_2 during the reduction process giving a Ni-NiO core-shell structure.

As the O_2 partial pressure goes down in the later part of the catalyst bed, the main reducing gas exists in the reactor before the syngas formation was CH_4. Complete reduction of NiO to Ni took place when heated to 700^oC in the presence of CH_4 (Condition G). *In-situ* experiments were carried out in CH_4 at relatively low temperatures so that the intermediate morphologies could be determined. Figure 3.14 shows high resolution images along with their Fast Fourier Transforms (FFT) from particles observed in 0.3 Torr of CH_4 at 500^oC (Condition H) at different stages of the reduction process. During the early stage of reduction, some regions in the NiO particles may contain Ni nanodomains. If these domains contain crystalline metallic Ni, then a Moiré pattern may show in the HREM image due to the superposition of lattice fringes from the oxide and the metal. Several of these Moiré patterns are indicated in figure 3.14a.

The appearance of a Moiré pattern does not prove that Ni metal is present because Moiré patterns can also occur due to the superposition of two overlapping crystallites of NiO. To correctly interpret the Moiré pattern it is necessary to analyze the pattern in terms of the two fundamental periodicities. Full details of this procedure can be found in textbooks on TEM and involve expressing the reciprocal lattice vector for the Moiré reflection in terms of the reciprocal lattice vectors of the two fundamental reflections [20]. By knowing the Moiré reflection

and one of the fundamental reflections the other fundamental reflection can be obtained. The detailed approach of the Moiré analysis is discussed in Appendix I. FFT's were taken from different positions on the nanoparticle shown in Figure 3.14a and the local lattice parameter was determined using the Diffpack module for Gatan's Digital Micrograph software. The FFT from position 1 shows only one pair of spots with a lattice spacing of 0.24 nm corresponding to the NiO (111) plane. The FFT from position 2 shows two pairs of NiO (111) reflections from different lattice orientations along with the Moiré spacing of 1.48 nm. The Moiré was formed from the interference of two NiO (111) lattices. The FFT from position 3 shows only one pair of fundamental reflections corresponding to NiO (111) and two pairs of Moiré reflections with a spacing of 1.08 nm and 0.66 nm. In this case, the fundamental reflections can be found by expressing the unknown reciprocal lattice vector in terms of the Moiré and NiO (111) reciprocal lattice vectors. This analysis shows that both Moiré reflections are formed from the interference of NiO (111) with two different Ni (111) lattices oriented at different angles. The Ni (111) reflections do not appear in this image because of loss of resolution due to instabilities associated with the hot stage.

Figure 3.14b shows an example of a NiO particle with a void structure at a later stage of reduction. In this case a particle with dark contrast was observed at the interface of NiO and SiO_2. From the FFT's the surface lattice spacing was found to be 0.24 nm corresponding to the NiO (111), position 3, and the lattice spacing's in the dark particle are 0.20 nm and 0.17 nm corresponding to Ni (111) and Ni (200) respectively. Figure 3.14c, shows the core-shell structure formed at a

later stage of the reduction in CH_4. The FFT confirms the lattice spacing to be 0.24 nm corresponding to NiO (111) in the shell region and 0.20 nm corresponding to Ni (111) at the core region indicating a Ni core with NiO shell during the reduction. As the reduction continues, the NiO shell grows thinner and eventually a complete Ni metal particle remains.

In the CH_4 atmosphere, the primary thermodynamic driving force is to reduce the entire NiO particle to Ni metal (not just the particle surface). This means that oxygen from the NiO must be continually present on the particle surface so that it can react with CH_4. After the initial surface reduction of NiO, there are two possible transformation mechanisms for the oxide particle to completely reduce to metal involving either predominant diffusion of O anions (mechanism I) or predominant diffusion of metal cations (mechanism II). Figure 3.15, schematically represents the morphology of the particles that would form during the reduction process based on these two mechanisms.

If O anions are the primary diffusing species (Figure 3.15a), initially the top layer of the metal oxide will reduce to a metal-rich shell. O continues to diffuse through the metal-rich shell to react on the surface leaving oxygen vacancies in the oxide core. The reduction process continues until all the O is consumed creating a Kirkendall void at the centre of the metal particle. For example low temperature reduction of PdO results in a Pd metal shell with a void at the centre implying an O anion diffusion mechanism [21,22]. On the other hand, if metal is the primary diffusing species (Figure 3.15b), cations will diffuse away from the surface along defects and grain boundaries exposing fresh metal

oxide allowing reduction to continue. In this case, metal/metal oxide core-shell structures will form during the intermediate stage of reduction and eventually the oxide skin will vanish leaving a solid metal particle. For syngas production, the mechanism I involving the formation of an intermediate metal shell may be more desirable since it would mean that even partially reduced NiO would be active for the reaction.

Our observations collectively suggest that mechanism II is the main process for NiO reduction during ramp-up for POM. This interpretation is further reinforced by comparing the respective diffusion coefficients. The diffusion coefficient of Ni in NiO grain boundaries is ~10^{-12} cm^2 s^{-1} at 500^{o}C and is much greater than the value of 10^{-16} cm^2 s^{-1} at 500^{o}C [17,23] for O diffusing in Ni metal. For the experiments performed in pure CH_4, a clear indicator of metallic Ni on the surface is the formation of graphite which is easily observed in the HREM image. Thus the decomposition of CH_4 to graphite is a powerful tool for detecting metal species on the surface of the Ni particle at 500^{o}C. Figure 3.16, shows the *in-situ* ETEM image in presence of 0.3 Torr of CH_4 at 500^{o}C (Condition H) after the reduction of NiO showing graphite over layers formation on Ni surface by the dissociation of CH_4 on Ni surface according the reaction $CH_4 \rightarrow C + 2H_2$ [1]. All the above mentioned observations collectively show that, during the intermediate stage of reduction, NiO remains on the surface of the nanoparticle and the reduction process takes place via the diffusion of Ni cations along the grain boundaries in NiO shell (Reduction Mechanism II).

3.5. Structure-activity relationship for Ni/SiO_2 Catalyst

The observed particle reduction mechanism can allow us to interpret the sharp increase in syngas production observed in our reactor data at 775^{o}C. During the transformation of NiO to Ni, Ni cations will rapidly diffuse over the particle surface to extended defect sites and then move to subsurface sites exposing fresh NiO. The TEM images show that the average distance between grain boundaries and extended defects is on the order of 5 nm. At 500^{o}C, the diffusion coefficient for Ni diffusing on NiO is about 10^{-11} cm^2 s^{-1} suggesting that Ni species will remain on the surface for only a few hundredths of a second. Ni metal crystallites do not form on the surface and the catalyst surface remains predominantly NiO during this process and syngas production is suppressed. Only towards the end of the particle reduction process is there a significant increase in the Ni metal concentration on the surface as growing Ni metal nuclei break through giving a concomitant increase in syngas production.

The inactivity of the catalyst below 775^{o}C is in part caused by the difficulty in reducing the metal particle surface as described above. However, once the catalyst is activated, Ni remains as metallic during the temperature ramp-down favoring syngas formation. The lack of activity during most of the ramp-up is associated with the undesirable intermediate transformation of Ni metal to NiO. However, if the ramp-up is carried out in a reducing atmosphere, the metal to oxide transformation can be avoided in the downstream region of the bed and thermodynamically limited performance is achieved over an extended temperature range. The experimentally measured CH_4 conversion and CO selectivity for such

an experiment are shown in figure 3.17 on the same catalyst. In this case, the reactor was ramped to 600^{o}C in an H_2 flow and then the gas switched to the CH_4 and O_2 mixture. The catalyst immediately produced syngas with methane conversions near the thermodynamic limit of 60%. With continued ramping, the methane conversion (and syngas production) continued to rise in accordance with thermodynamic predictions approaching 99% at 900^{o}C.[2] The ramp-up procedure ensures that the entire catalyst bed contains only metallic Ni during the H_2 ramp-up to 600^{o}C. When CH_4 and O_2 are introduced, the Ni metal may initially oxidize (at least in region I of the reactor) but at 600^{o}C this oxide will rapidly convert the gas phase oxygen to CO_2 and H_2O via complete combustion of methane. Thus the oxygen partial pressure in the system will be dramatically lowered across most of the bed under our flow conditions allowing syngas formation to occur.

3.6. Effect of particle size on the catalyst performance

Partial oxidation of methane reaction was performed on higher loadings of Ni with 7.3 wt% Ni on SiO_2 support. Figure 3.18 shows the comparison between CH_4 conversion and CO selectivity for 2.5 wt% Ni and 7.3 wt% Ni for partial oxidation of methane during temperature ramp-up. Similar trends in the conversion and selectivity were observed for both catalysts until the CO formation; light-off temperature for both the catalyst is almost the same with 775^{o}C for 2.5 wt% loading sample and 795^{o}C for 7.3wt% sample. A sharp rise in the CH_4 conversion and CO selectivity was observed for 2.5 wt% loading at

775^{o}C. For 7.3wt% loading, CO selectivity increases gradually and a sharp rise in the CH_4 conversion took place at 850^{o}C, this sharp rise in the CH_4 conversion is 75^{o}C great for 7.3wt % loading compared to 2.5 wt% loading sample. Figure 3.19 (a-b) shows the particle size distribution and the total fractional surface area associated Ni particles of different sizes for 7.3 wt% sample. The 2.5 wt% sample has as average particles size of about 5.5 nm with 80% of the particles lying in the range 3 – 10 nm (figure 3.1). For the 7.3 wt% sample, the average particle size was also 5.5 nm but with 50% of the particles lying in the range 3 – 10 nm. Comparing the figure 3.19b with figure 3.11, it can be seen that the fractional surface associated with the big Ni particles is greater for 7.3 wt% sample than the 2.5 wt% sample.

The difference in the shift of sharp rise in CH_4 conversion to high temperatures 7.3 wt % can be explained as follows. During the temperature ramp-up the Ni metal nanoparticles are oxidized to NiO and the NiO nanoparticles have to reduce back to metallic Ni for producing syngas. During the reduction, NiO is the phase that exists on the surface of the nanoparticle with Ni in the core region (as discussed in section 3.4.3), syngas will form only when NiO completely reduces back to metallic Ni. The large NiO particles will take longer times or higher temperature for complete reduction compared to small NiO particles. For the 7.3 wt% sample, since the fractional surface area associated with the large Ni nanoparticles is higher, these large Ni nanoparticles will transform to larger NiO nanoparticles during the temperature ramp-up in CH_4 and O_2. During the reduction these large NiO particles will take longer time or higher temperatures

for the NiO to reduce back to Ni, which can explain the shift in the temperature for the sharp rise in CH_4 conversion for 7.3 wt % sample compared to 2.5 wt% sample. The 7.3 wt% sample still contains significant amount of small NiO nanoparticles which will completely reduce back to metallic Ni at lower temperatures, this explains the similar light-off temperature for CO formation for 7.3 wt% sample to that of 2.5 wt% sample.

Similar observations were found when two consecutive ramp-ups were performed on the same sample. Figure 3.20 shows the catalyst performance of 2.5 wt% Ni catalyst for the two consecutive runs (Run1 and Run2) showing CH_4 conversion and CO selectivity. Solid curves shows the catalytic data for Run1 and dotted curves shows the catalytic data for Run2. From the plot it can be seen that for the main rise in CH_4 conversion and the CO selectivity is shifted to higher temperatures (about 80^oC higher) for the Run2 relative to Run1. During Run1, Ni nanoparticles will sinter and the average particle size will increase and the fractional surface area associated with large Ni particles will also increase. During Run2 on the same sample the larger Ni nanoparticles will give large NiO particles which will require longer times or higher temperatures for the complete reduction.

3.7. Summary

In-situ ETEM was employed to develop an atomic level description of the structure, composition and morphologies that develop in model Ni/SiO_2 catalyst during ramp-up for partial oxidation of methane under high conversion conditions. The gas composition along the catalyst bed varies in space and time

during ramp-up. Essentially there is no single “reactor condition” in this case and the variation in the gas composition must be taken into account in the design of ETEM experiments so that the correct structure-property relations can be determined.

During the temperature ramp-up, the Ni metal particles transform to NiO at about 300^{o}C in the CH_4 and O_2 reacting gas mixture before any significant catalysis takes place. The void-like morphology present in NiO nanoparticle 5 nm is due to a Kirkendall process in which Ni cations preferentially diffuse along grain boundaries and extended defects presented in the initial oxide shell. The front of the catalyst bed always sees the reacting gases and the NiO particles present at temperatures above 300^{o}C favour complete oxidation of CH_4. As the temperature continues to increase, oxygen partial pressure in the later part (region II and III) of the catalyst bed goes down and the NiO in the later region of the bed transforms back to metallic Ni leading to syngas formation.

ETEM experiments were carried out in a variety of relevant reducing atmospheres and temperatures to investigate the NiO to Ni metal phase transformation. CH_4 is the main reducing gas that exists in the reactor before the syngas formation. In the CH_4 reducing atmosphere, the NiO reduction mechanism also involved diffusion of Ni cations along grain boundaries and extended defects giving rise to an intermediate catalyst state corresponding to Ni-NiO core-shell structures. NiO is the phase that exists on the surface of the nanoparticle until complete reduction takes place. Syngas formation will only take place during the later stages of NiO reduction when Ni metal nanoparticles break through the NiO

shell. This explains the sharp increase in CH_4 conversion and CO selectivity that is observed at 775^oC. Increasing the particle size of the Ni nanoparticles shifts the sharp rise in the CH_4 conversion to higher temperatures. Ramping of the catalyst in a reducing atmosphere avoids the syngas delay associated with NiO formation in the latter part of the bed and yields thermodynamically limited conversion over a wide temperature range.

References

1. Tsang, S. C., Claridge, J. B., Green, M. L. H. (1995). Recent advances in the conversion of methane to synthesis gas. Catalysis Today, 23, 3-15.

2. York, A. P. E., Xiao, T., & Green, M. L. H. (2003). Brief overview of the partial oxidation of methane to synthesis gas. *Topics in Catalysis*, 2003, 22(3-4), 345-358.

3. Vannice, M.A. (1976). Catalytic synthesis of hydrocarbons from carbon monoxide and hydrogen. *Catalysis Review: Science & Engineering*, 14, 153.

4. Bart, J. C. J., & Sneeden, R. P. A. (1987). Copper-zinc oxide-alumina methanol catalysts revisited. *Catalysis Today*, 2(1), 1-124.

5. Vernon, P. D. F., Green, M. L. H., Cheetham, A. K., Aschcroft, A. T. (1992). Partial oxidation of methane to synthesis gas, and carbon dioxide as an oxidising agent for methane conversion. *Catalysis Today*, 13(2-3), 417-426.

6. Enger, B. C., Lodeng, R., & Holmen, A. (2008). A review of catalytic partial oxidation of methane to synthesis gas with emphasis on reaction mechanisms over transition metal catalysts. *Applied Catalysis A: General*, 346, 1-27.

7. Wang, J.X., & Lunsford, J. H. (1986). Characterization of [Li+O] centers in lithium-doped magnesium oxide catalysts. Journal of Physical Chemistry, 90(22), 5883-5887.

8. Bartholomew, C. H. (2001). Mechanisms of catalyst deactivation. *Applied Catalysis A: General*, 212(1-2), 17-60.

9. Schaffer, B., Grogger, W., & Kothleitner, G. (2004). Automated spatial drift correction for EFTEM image series. *Ultramicroscopy*, 102, 27-36.

10. Crozier, P.A., & Chenna, S. (2011). *In-situ* analysis of gas composition by electron energy-loss spectroscopy for environmental transmission electron microscopy. *Ultramicroscopy*, 111, 177-185.

11. Gaskell, D. R. (2003). *Introduction to the thermodynamics of materials*. Taylor&-Francis.

12. Siegbahn, P.E.M., & Wahlgren, U. (1992). A theoretical study of atomic oxygen chemisorption on the Ni(100) and Ni (111) surfaces. *International Journal of Quantum Chemistry*, 42, 1149-1169.

13. Siegbahn, P.E.M., & Panas, I. (1990). A theoretical study of CHx chemisorption on the Ni(100) and Ni(111) surfaces. *Surface Science*, 240, 37-49.

14. Smigellkas, A.D., & Kirkendall, E.O. (1947). Zinc diffusion in alpha brass. *Transactions of the American Institute of Mining, Metallurgical and Petroleum Engineers*, 171, 130-134.

15. Atkinson, A., Moon, D.P., Smart, D.W., & Taylor, R.I. (1986). Tracer diffusion studies in NiO bicrystals and polycrystals. *Journal of Materials Science*, 21, 1747-1757.

16. Atkinson, A., & Taylor, R.I. (1978). The self-diffusion of Ni in NiO and its relevance to the oxidation of Ni. *Journal of Materials Science*, 13, 427-432.

17. Peraldi, R., Monceau, D., & Pieraggi, B. (2002). Correlations between growth kinetics and microstructure for scales formed by high-temperature oxidation of pure nickel. II. Growth kinetics. *Oxidation of Metals*, 58(3/4), 275-295.

18. Railsback, J. G., Johnston-Peck, A. C., Wang, J., & Tracy, J. B. (2010). Size-dependent nanoscale Kirkendall nanoparticles. *ACS Nano*, 4, 1913.

19. Nakamura, R., Lee, J. G., Mori, H., & Nakajima, H. (2008). Oxidation behaviour of Ni nanoparticles and formation process of hollow NiO. *Philosophical Magazine*, 88, 257.

20. D. B. Williams, C. B. Carter, Transmission Electron Microscopy Imaging III, Springer, 1996, p. 444.

21. Crozier, P. A., Sharma, R., & Datye, A. K. (1998) Oxidation and Reduction of Small. Palladium Particles on Silica. *Microscopy & Microanalysis*, 4, 278.

22. Crozier, P. A., & Datye, A.K. (2000). Direct Observation of Reduction of PdO to Pd Metal by *In-situ* Electron Microscopy. *Studies in Surface Science and Catalysis*, 130, 3119.

23. Lloyd, G.J., & Martin, J.W. (1972). The diffusivity of oxygen in nickel determined by internal oxidation of dilute Ni-Be alloys. *Material Science Journal*, 6, 7-11.

Table 3.1. Experimental conditions showing the gas environments, reaction temperatures and reaction times used during the *in-situ* ETEM studies

Experiment	Gas	Temperature Ramp (^{o}C)	Time (hr)	Comments
A	H_2	25-400	2	Initial Reduction
B	CH_4+0.5O_2	25-500	0.5-1	Ni Oxidation
C	CH_4+0.5O_2	25-800	2	Ni Oxidation
D	CO+2H_2	400	1-3	NiO Reduction
E	3CH_4+CO_2+2H_2O	400-700	1-3	NiO Reduction
F	CO+2H_2	400-800	1-3	NiO Reduction
G	CH_4	25-700	0.5-1	NiO Reduction
H	CH_4	25-500	1-3	NiO Reduction

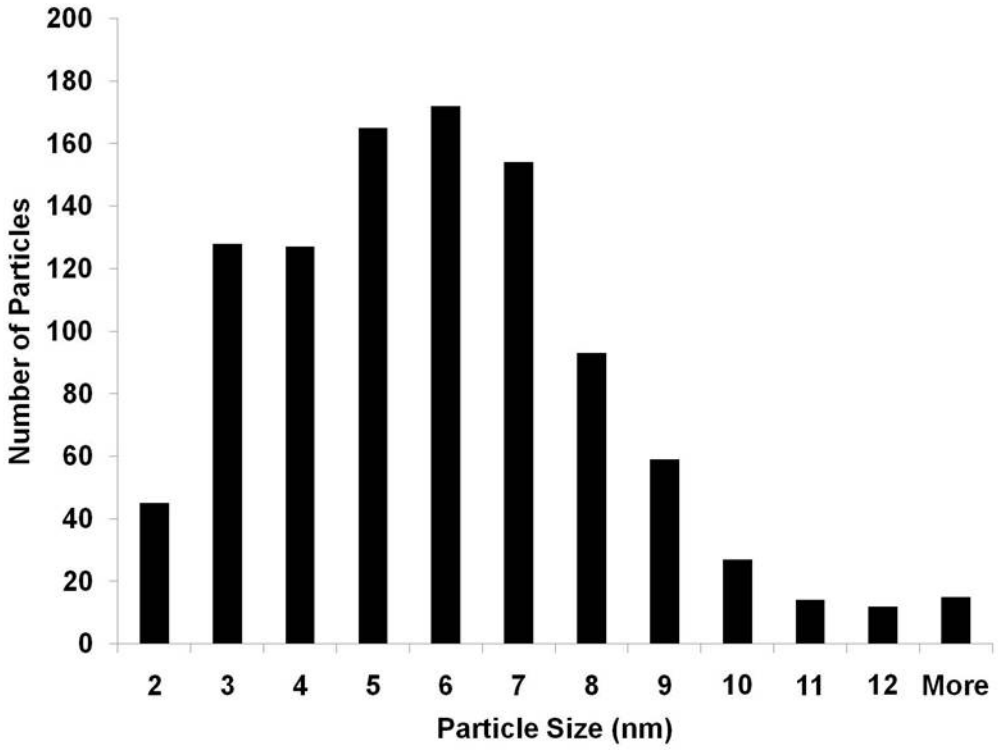

Figure 3.1. Ni particle size distribution for 2.5 wt% Ni/SiO_2 metal loading.

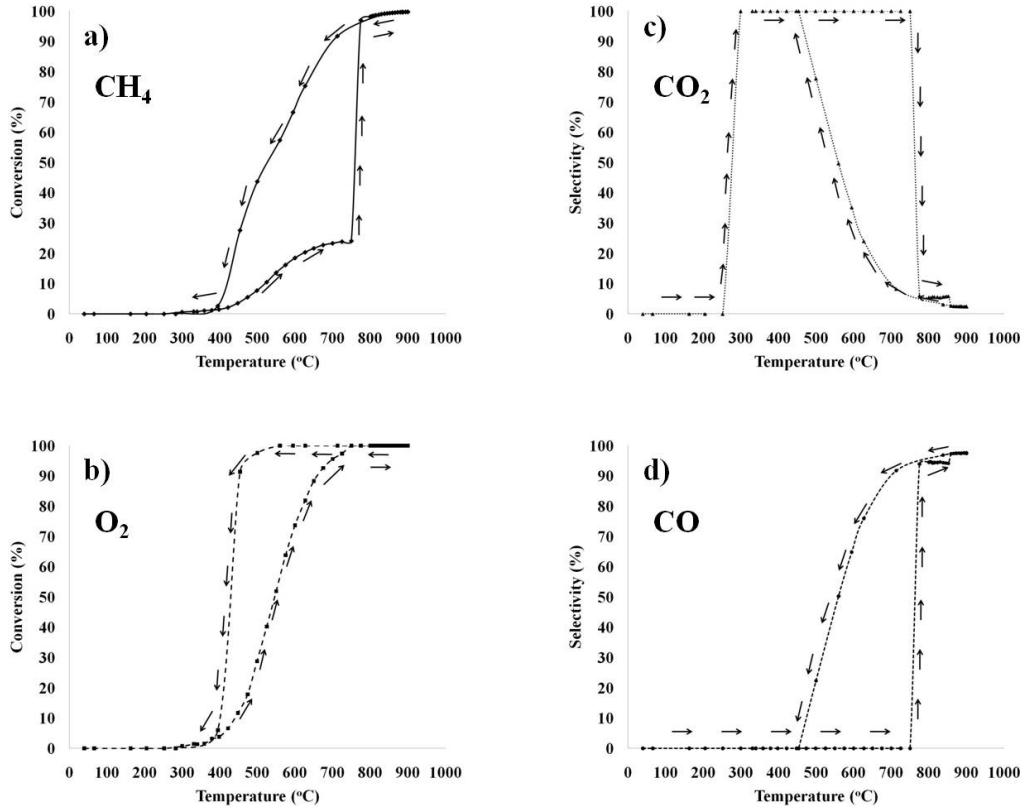

Figure 3.2. Plot showing conversion of CH_4 and O_2 and their selectivity towards CO_2 and CO during partial oxidation of methane over a model 2.5wt% Ni/SiO_2 catalyst.

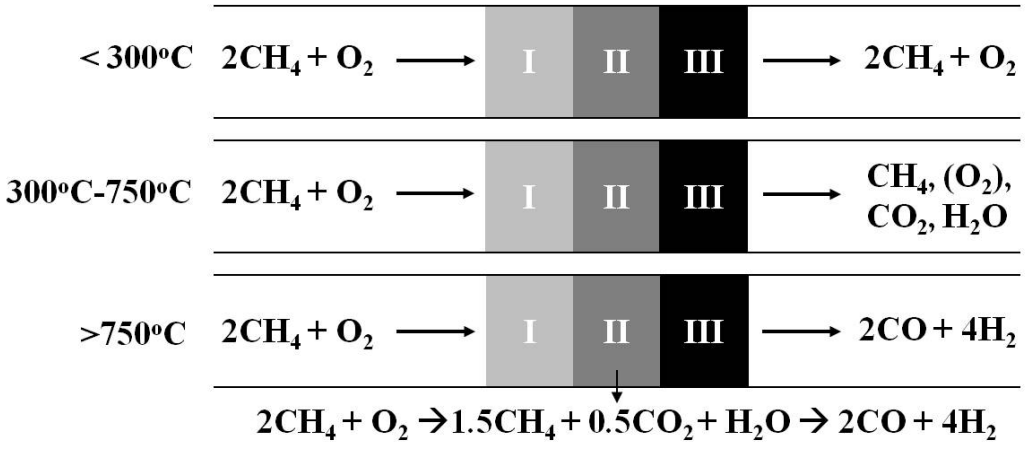

Figure 3.3. Variations in the gas composition along the catalyst bed (regions I, II and III) over different temperature ranges for 2.5 wt% Ni/SiO_2 catalyst.

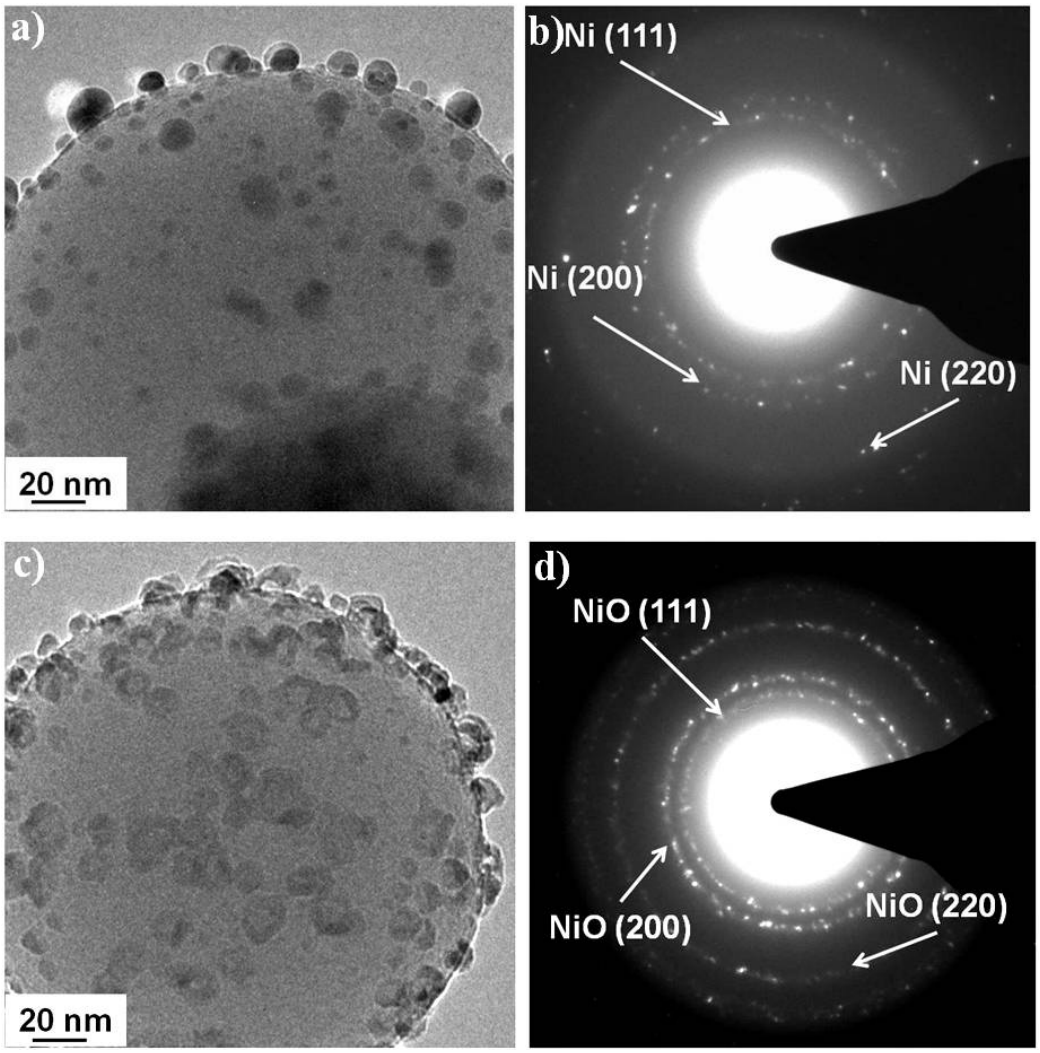

Figure 3.4. *In-situ* ETEM images and electron diffraction patterns of Ni/SiO_2 (a) in presence of 0.8 Torr of H_2 at 400^{o}C (Condition A) and (b) from the same region in presence of 0.8 Torr of mixture of CH_4 and O_2 in 2:1 ratio at 400^{o}C (Condition B).

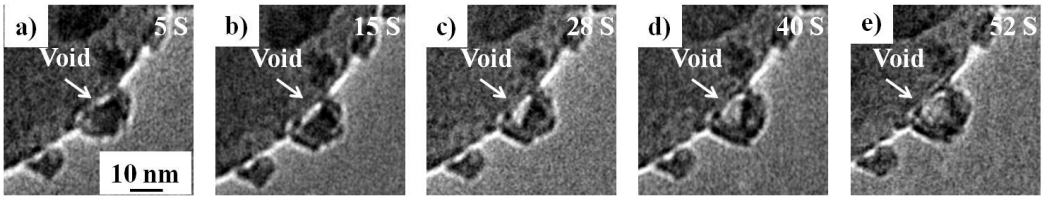

Figure 3.5. Sequential images of void formation in NiO in presence of CH_4 and O_2 (in 2:1 ratio).

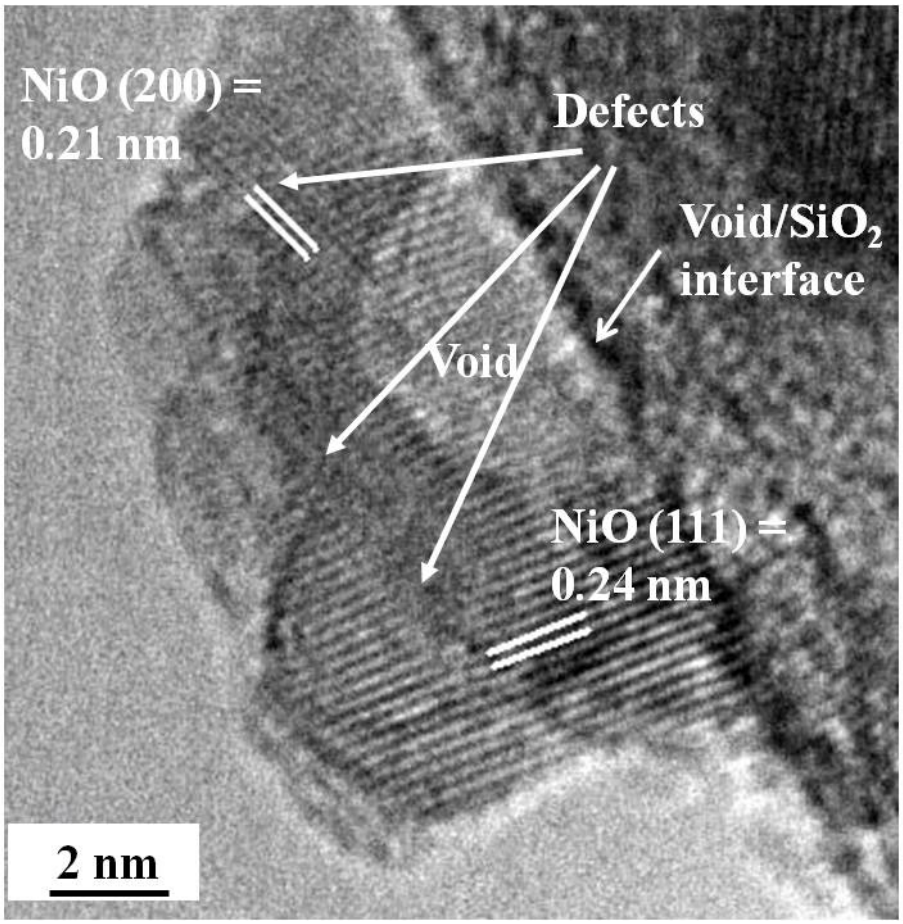

Figure 3.6. *In-situ* high resolution TEM image of void structured NiO/SiO_2 in presence of 0.8 Torr of CH_4 and O_2 in 2:1 ratio at 400^{o}C (Condition B).

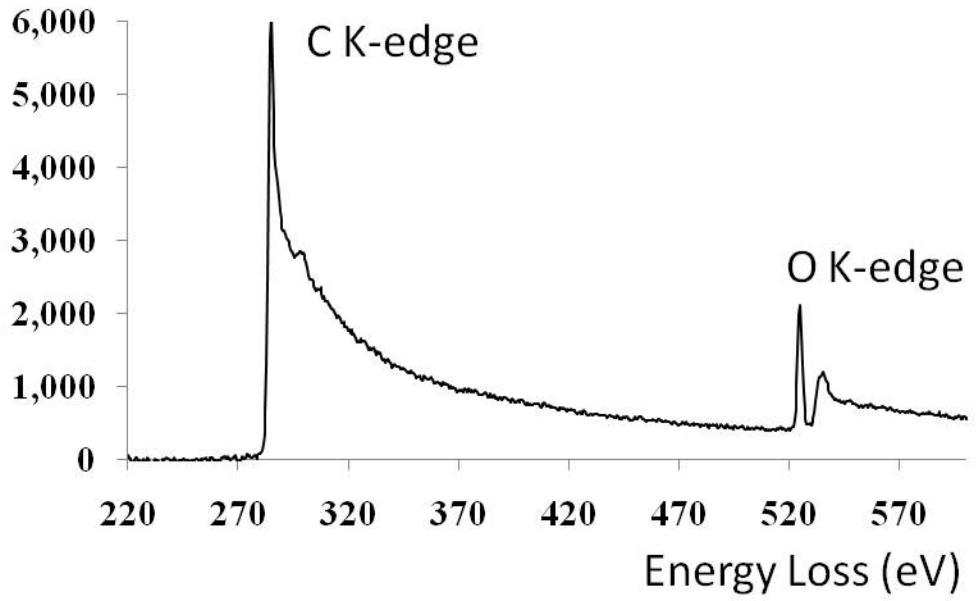

Figure 3.7. Background subtracted energy-loss spectrum from a mixture of 2.6 Torr CH_4 and O_2 in 2:1 ratio showing C and O K-edges.

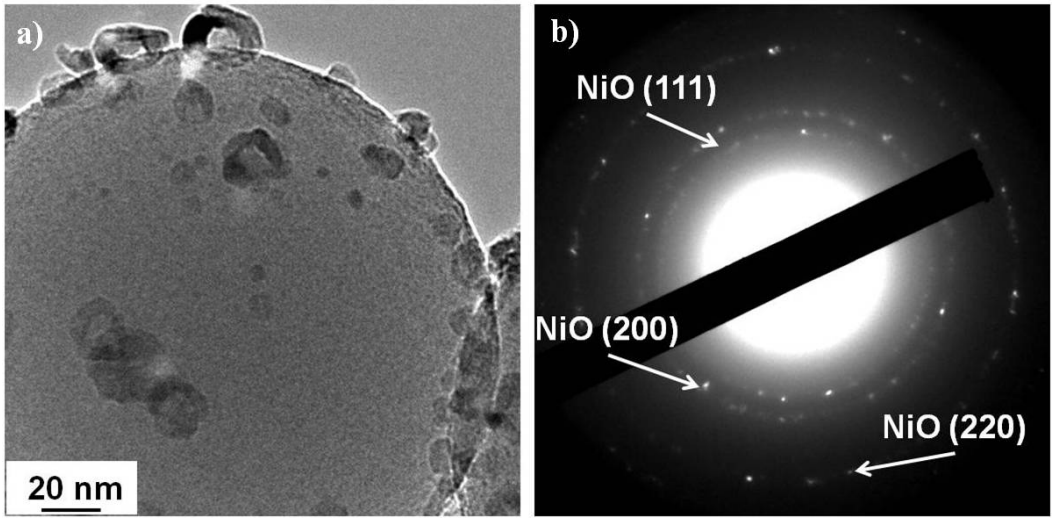

Figure 3.8. *Ex-situ* TEM image and electron diffraction of Ni/SiO_2 after ramping to 400^{o}C in CH_4 and O_2 and then cooling to room temperature in flowing He.

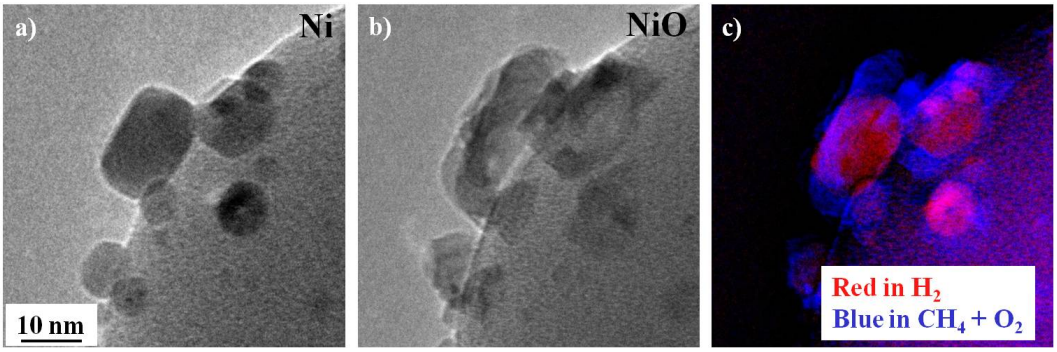

Figure 3.9. *In-situ* ETEM images of Ni/SiO_2 (a) in presence of 0.8 Torr of H_2 at 400^{o}C (Condition A) (b) from the same region in presence of 0.8 Torr of mixture of CH_4 and O_2 in 2:1 ratio at 400^{o}C (Condition B) (c) superposition of colorized images shown in a and b.

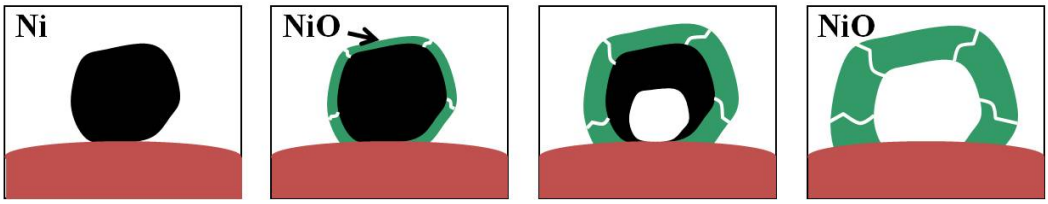

Figure 3.10. Schematic representation of NiO void formation by Kirkendall effect.

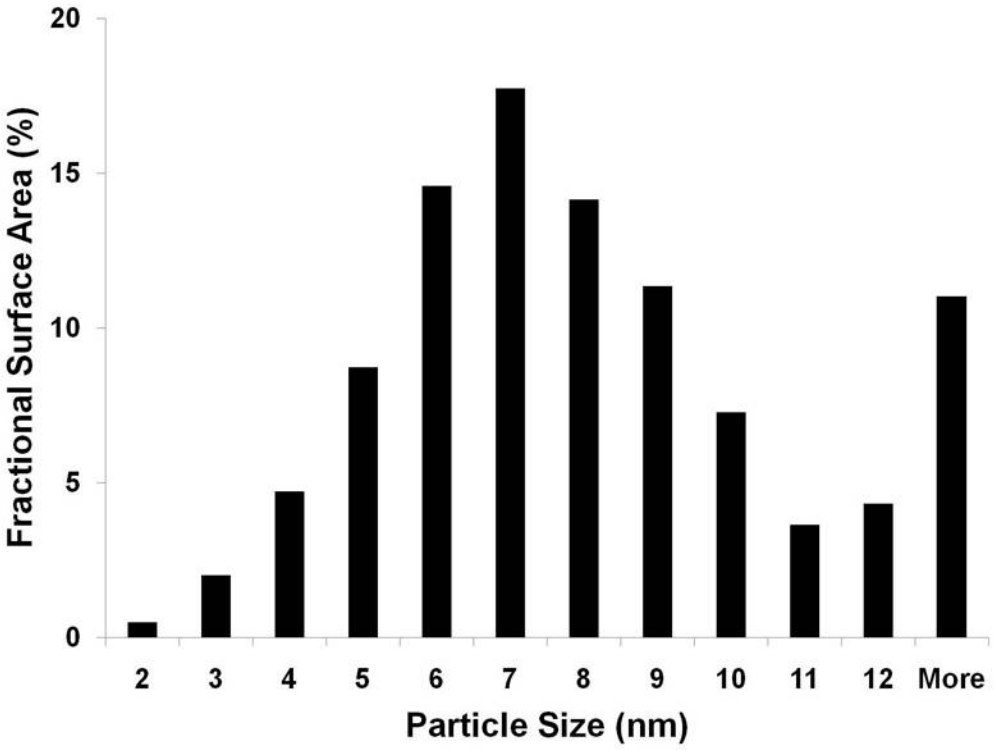

Figure 3.11. Fractional surface area associated with Ni particles of different sizes 2.5wt% Ni loading.

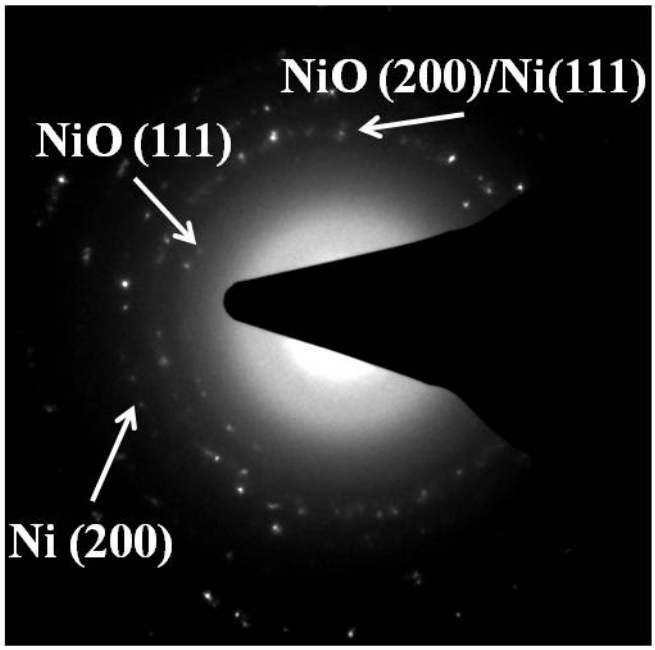

Figure 3.12. Electron diffraction pattern of Ni/SiO_2 during the reduction in presence of CO and H_2 (in 1:2 ratio) at 400^{o}C (Condition D).

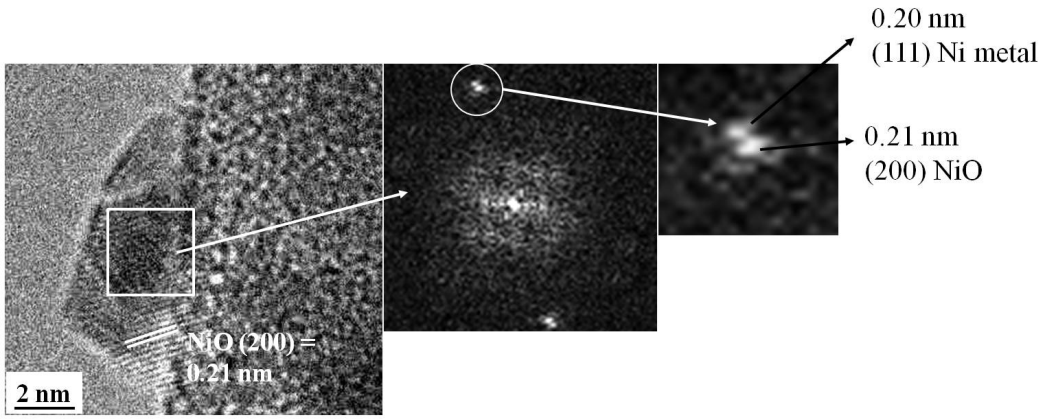

Figure 3.13. *In-situ* high resolution ETEM image along with the FFT's of Ni/SiO_2 during the reduction in presence of 0.1 Torr of CO and H_2 (in 1:2 ratio) at 400^{o}C (Condition D).

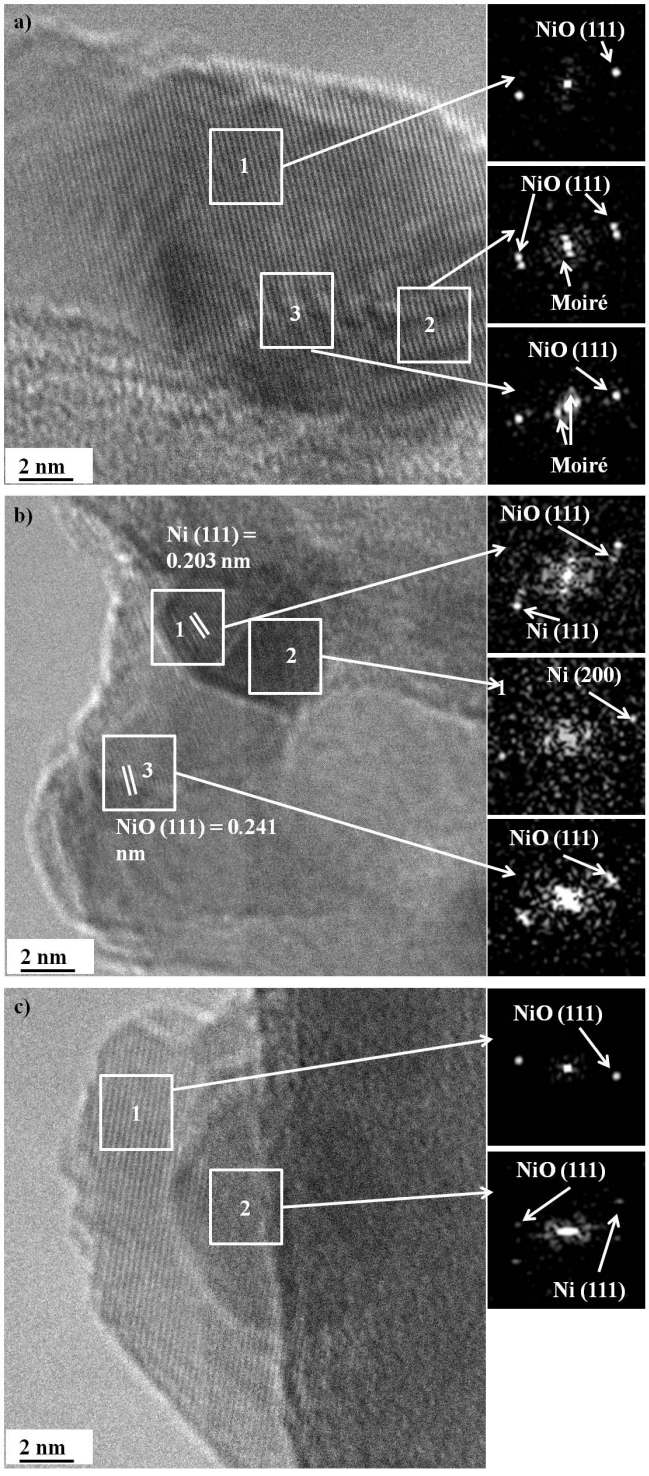

Figure 3.14. *In-situ* high resolution ETEM images along with FFT's of Ni/SiO_2 in presence of 0.3 Torr of CH_4 at 500^oC at different reduction times (Condition H). (a) and (b) shows the initial stage of reduction and c) intermediate stage of reduction.

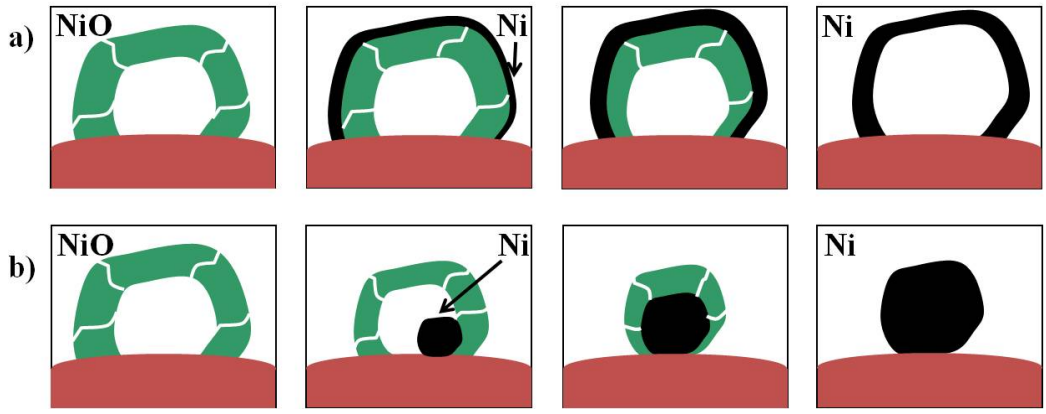

Figure 3.15. Schematic representation of NiO to Ni transformation under two different mechanisms (a) Mechanism I: O is the dominant diffusing species (b) Mechanism II: Ni is the dominant diffusing species.

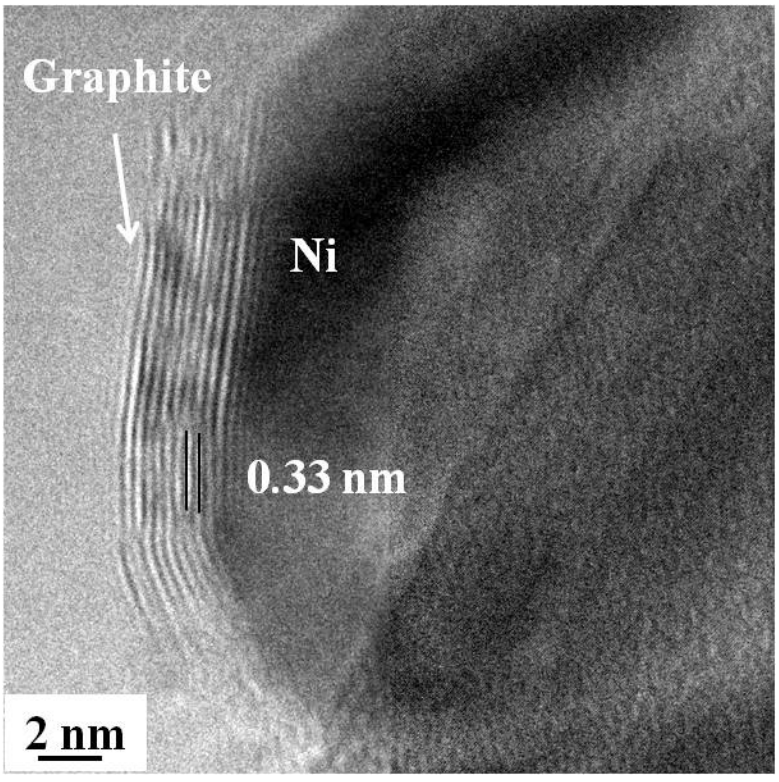

Figure 3.16. *In-situ* high resolution ETEM image of Ni/SiO_2 showing graphite formation of Ni after the complete reduction of NiO in presence of 0.3 Torr of CH_4 at 500^{o}C (Condition H).

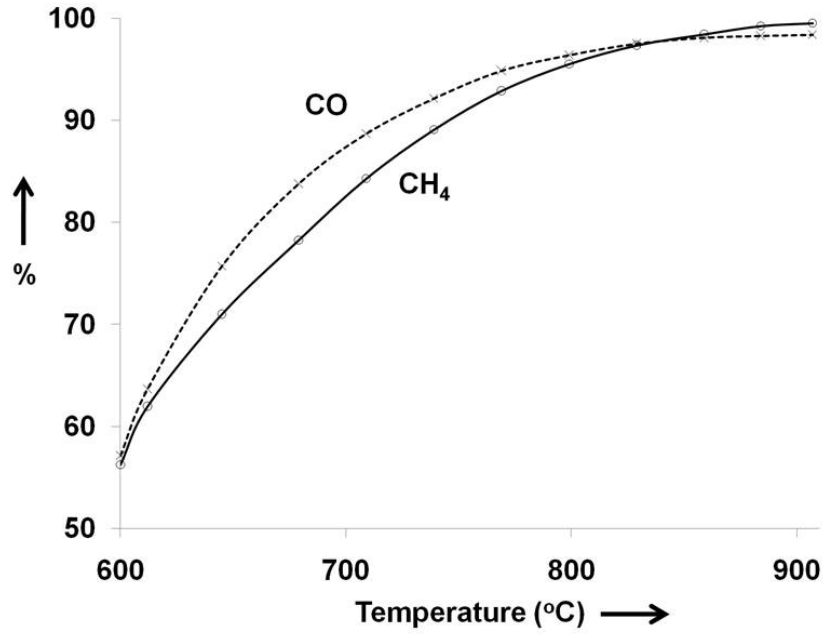

Figure 3.17. CH_4 conversion and CO selectivity of 2.5 wt% Ni/SiO_2 on showing the comparison between two consecutive runs on the same catalyst.

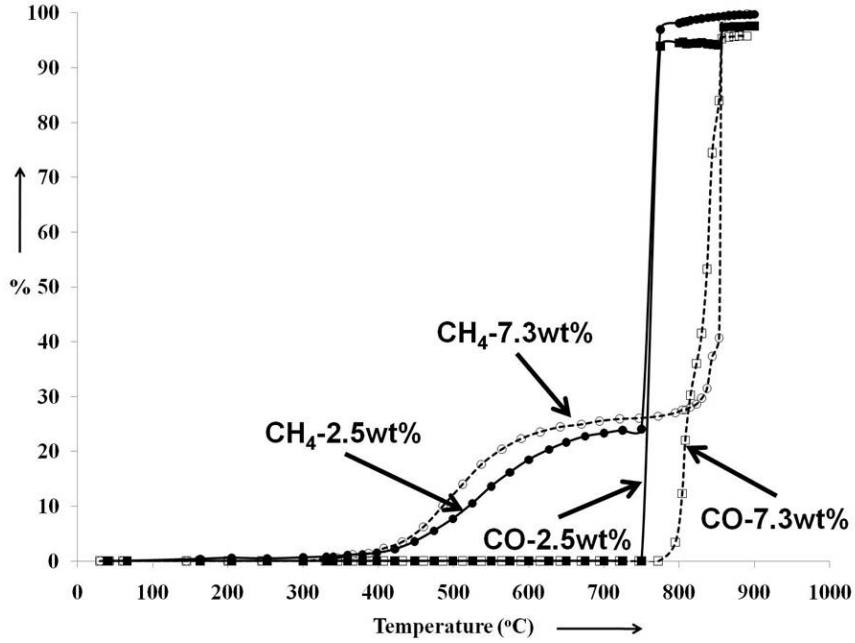

Figure 3.18. Plot showing CH_4 conversion and CO selectivity for partial oxidation of methane over a 2.5 wt% Ni/SiO_2 (solid curves) catalyst and 7.3wt% Ni/SiO_2 catalyst (dotted curves).

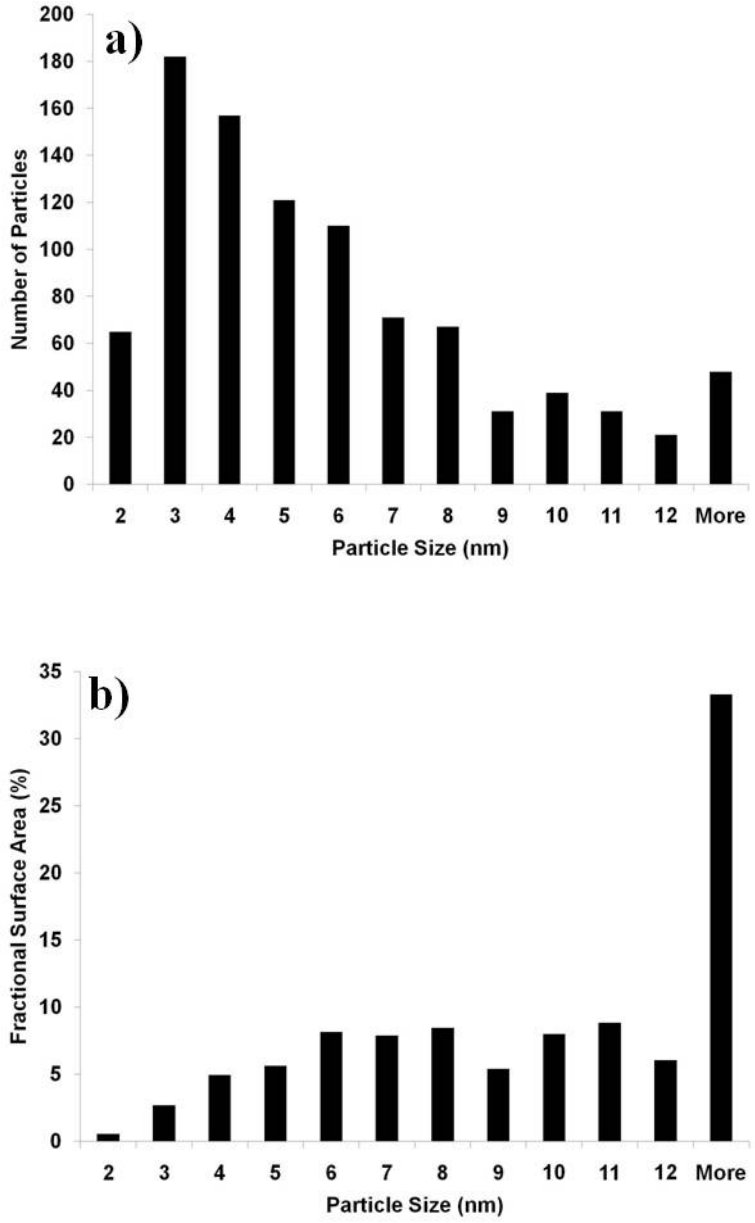

Figure 3.19. a) Ni particle size distribution and b) Fractional surface area associated with Ni particles of different sizes for 7.3. wt% Ni metal loading on SiO_2.

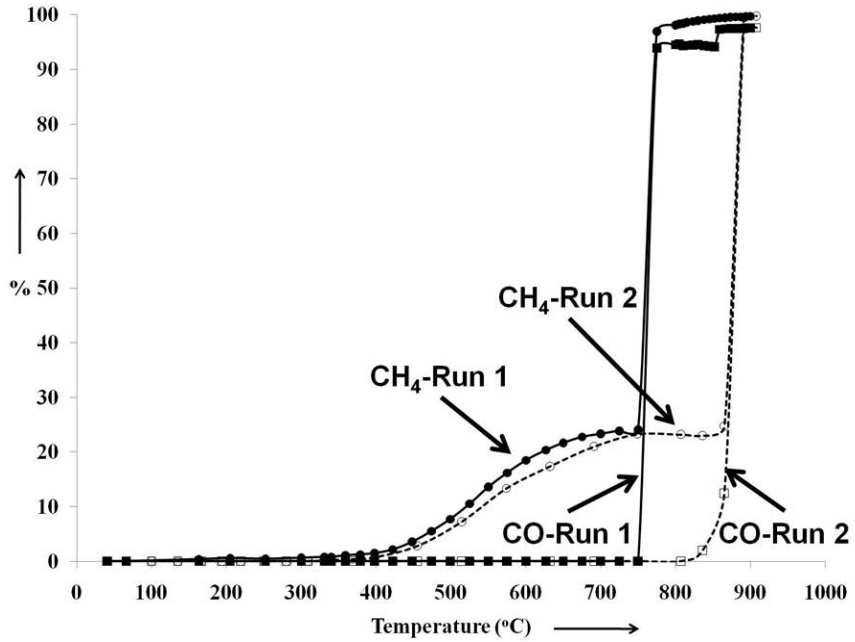

Figure 3.20. Plot showing CH_4 conversion and CO selectivity for partial oxidation of methane over a 2.5 wt% Ni/SiO_2 for the two consecutive runs Run1 (solid curves) and Run2 (dotted curves).

Chapter 4

IN-SITU ENVIRONMENTAL TEM STUDIES OF RU/SIO2 FOR PARTIAL OXIDATION OF METHANE

4.1. Introduction

Goal of this chapter is to understand structure-activity relationship in Ru/SiO_2 catalyst for partial oxidation of methane (POM) reaction. Catalytic performance for the POM reaction was performed on Ru/SiO_2 catalyst and *in-situ* ETEM experiments were performed to follow the nanostructural changes. *In-situ* ETEM experiments under oxidizing and reducing gas environments that are relevant to partial oxidation of methane were performed to follow the oxidation and reduction process in supported Ru nanoparticles and the observations are correlated with the catalytic performance. Ru is one of the most active catalysts for POM reaction [1,2], Ru is more expensive than Ni but reaches thermodynamic equilibrium conversions very fast and has higher resistance to poisoning from coke formation than Ni [3]. Experiments similar to Ni/SiO_2 were performed and the performance of Ru/SiO_2 is compared to Ni/SiO_2. The oxidation and reduction behaviors in Ru nanoparticles are compared with that of Ni and the differences in catalytic behavior is discussed.

4.2. Ru/SiO_2 catalyst preparation

2.5 wt% Ru/SiO_2 catalyst was prepared by impregnating SiO_2 spheres with ruthenium chloride hydrate ($RuCl_3.xH_2O$) solution using incipient wetness techniques. Ruthenium chloride hydrate solution was prepared by dissolving a

known amount of 99.98% $RuCl_3.xH_2O$ (obtained from Sigma Aldrich) using ethanol as a solvent. Incipient wetness impregnation was carried out in a mortar by drop wise addition of ruthenium chloride solution equivalent to the pore volume of the SiO_2 in a saturated ethanol atmosphere while mixing for 10 min. After impregnation, the sample was dried at 120^oC followed by reduction in 5%H_2/Ar atmosphere at 400^oC for 3 hours. Figure 4.1 shows a typical TEM image of Ru/SiO_2 catalyst after reduction.

4.3. Ru/SiO_2 catalyst performance

Catalytic measurements were performed in an *In-situ* Research Instruments RIG 150 reactor. For a typical reaction, 10 mg of catalyst was loaded into the reactor and initially reduced at 400^oC in 5% H_2/Ar. Reaction conditions for partial oxidation of methane on Ru/SiO_2 were the same as that of for Ni/SiO_2 catalyst. The effluent gas from the reactor outlet was analyzed with a Varian 3900 gas chromatography.

Figures 4.2, shows the measured catalytic conversion of CH_4 and O_2 and their selectivity towards CO_2 and CO on Ru/SiO_2 during partial oxidation of methane. During the temperature ramp up, no catalytic conversion of CH_4 took place at temperatures below 250^oC. Similar to the Ni catalyst, CO_2 is the initial product that was formed on Ru by complete combustion of CH_4, the light-off temperature for CO_2 formation is about 50^oC less in case of Ru compare to Ni. Complete combustion takes place in the temperature regime of 250^oC to 400^oC giving CO_2 and H_2O in 1:2 ratio. At 400^oC about 10% of CH_4 and 40% of O_2 is

converted giving CO_2 and H_2O, similar conversions happen on Ni catalyst at about 525^oC. A further increase in temperature to 425^oC results in a sharp rise in CH_4 conversion from 10% to 28% and also a sharp rise in O_2 conversion from 40% to almost 100%. CO also starts to form at this temperature. The light-off temperature for CO formation on Ru catalyst is about 350^oC lower than that of Ni catalyst under the same ramp-up conditions. With a further increase in temperature both CH_4 conversion and CO selectivity increases, following the thermodynamic limits of partial oxidation of methane [3]. A decrease in the O_2 conversion from 100% at 425^oC to 95% at 900^oC was observed.

Figure 4.3 schematically illustrates the possible variation in gas composition along the catalyst bed for three different temperature regimes. At temperatures below 250^oC, all regions of the bed are exposed to a mixture of CH_4 and O_2 (2:1). In the temperature range of 250^oC to 400^oC, region I at the front of the bed sees a reactant mixture of mostly CH_4 and O_2 whereas regions II and III are exposed to gas mixture containing CH_4, O_2, CO_2 and H_2O. The amount of O_2 in regions II and III of the catalyst bed decreases rapidly from 100 % to 0 % in a span of 150^oC. Above 400^oC, where CO formation starts to take place, region I is still exposed to the reactant gases CH_4 and O_2. Region II is exposed mostly to a mixture of CH_4, CO_2, H_2O, and very small concentrations of unreacted O_2. Reforming of methane with CO_2 and H_2O takes place in region II and region III is exposed to a mixture of unreacted gases CH_4, O_2, CO_2 and H_2O from region II and the product gases CO and H_2 (in 1:2 ratio). With increase in temperature,

more reforming of CH_4 takes place in region II, and the concentration of product gases CO and H_2 increases in region III.

4.4. Nanostructural characterization

Both *ex-situ* and *in-situ* nanoscale characterization was performed on the Ru/SiO_2 catalyst. For *in-situ* experiments, a series of ETEM experiments were performed under the reactant gases that are relevant to partial oxidation of methane and are listed in table 4.1.

Figure 4.4(a-b) shows the TEM image and electron diffraction of Ru/SiO_2 in the presence of 1 Torr of H_2 at 400^oC (condition A). Electron diffraction patterns confirm that the nanoparticles are metallic HCP Ru. A high resolution image from one of the nanoparticles in the presence of H_2 at 400^oC is shown in figure 4.5 with a lattice spacing of 0.235 +/- 0.014 nm corresponding to Ru (100). Figure 4.6a shows the TEM image from the same nanoparticle (as in figure 4.4a) in the presence of 1 Torr CH_4 and O_2 gas mixture in 2:1 ratio at 300^oC showing a formation of thin layer on the surface of the nanoparticle. Electron diffraction shows reflection of 0.318 nm corresponding to tetragonal RuO_2 (110) along with the Ru metal reflections, as shown in figure 4.6b. No change in the surface layer was observed even with the increase in temperature to 400^oC. Figure 4.7 shows the high resolution TEM image along with Fast Fourier Transforms (FFT) of Ru/SiO_2 in the presence of 1 Torr of CH_4 and O_2 gas mixture in 2:1 ratio at 400^oC. Lattice spacing from the core region (region I) measured from FFT gives a value of 0.217 +/- 0.016 nm corresponding to the HCP Ru (002). Lattice spacing

from the surface (region II and III) of the nanoparticle is 0.257 +/- 0.016 nm corresponding to RuO_2 (101).

In-situ electron energy-loss spectroscopy was also performed on these particles. Energy-loss from the surface of the nanoparticle shows O K-edge along with the Ru edges confirming that the surface of the nanoparticle is RuO_2 (figure 4.8a). Figure 4.8b shows the energy-loss spectra from the core region of the nanoparticle showing Ru M_{23} and M_{45} edges and small O K-edge is seen since the particle is surrounded by an oxide shell. Ru-RuO_2 core-shell structures were formed in the presence of CH_4 and O_2 gas mixture.

Ex-situ experiments were also performed to validate the *in-situ* observations. After the initial reduction step in H_2, the catalyst was heated to 400^{o}C in the *ex-situ* reactor in the presence of CH_4 and O_2 in a 2:1 ratio with He as a carrier gas. The sample was then cooled to room temperature and immediately transferred into a TEM for observation. TEM characterization was performed on JEOL JEM 2010 microscope. Figure 4.9 shows the STEM image of Ru/SiO_2 after the reaction in CH_4 and O_2 at 400^{o}C. Blow ups are shown from different areas from the image showing the presence of core-shell structure nanoparticles with a brighter core. Energy-loss spectra were collected from the surface and the core regions and are shown in figure 4.10 (a-b), clearly indicating that surface of the nanoparticle is RuO_2 and the core region is Ru metal. *Ex-situ* results are consistent with that of the *in-situ* data, validating the *in-situ* observations.

The formation of the oxide layer is due to the presence of high partial pressure of O_2 in the gas stream. The formation of the oxide layer even in the presence of reducing gas CH_4 is due to the higher chemisorption energies of O_2 on to the Ru surface compared to CH_4 (dissociative chemisorption energies of O_2 and CH_4 on the Ru (211) surface are -4.62 eV/molecule and -0.88 eV/molecule respectively) [4], which is the similar case observed in Ni. Complete oxidation of the Ni nanoparticle to NiO was observed for Ni, whereas in Ru only the surface of the nanoparticle is oxidized. This may be due to the kinetic limitations for O atoms to diffuse inwards and oxidize the Ru or for the Ru atoms to diffuse onto the surface of the nanoparticle and react with the O_2 gas. Mott et al., [5] proposed a theory for the formation of protective oxide films. Oxidation takes place by the ionic and electronic diffusion. An initial oxide layer will form when the metal surface is exposed to oxygen and the oxide layer grows as long as electrons from metal can diffuse through the oxide layer and reach the surface. Electrons can move through the oxide layer by tunneling or by thermionic emission. As the oxide layer grows, the film become too thick for the electron tunneling and if electron cannot move freely by thermionic emission the oxide layer stops growing. However RuO_2 can conduct electrons [6], and the Mott theory on protective oxide formation fails in this case. At this moment, the oxidation mechanism of Ru is not clearly understood. RuO_2 is the structure that exists on the nanoparticle surface up to 400^oC during the POM reaction and favors complete oxidation of methane to CO_2 and H_2O.

With increase in temperature, the partial pressure of O_2 goes down and the gas environment in the later part of the catalyst bed becomes reducing with CH_4 as the reducing gas. Figure 4.11 (a-b) shows the *in-situ* TEM images in the presence of 1 Torr of CH_4 and O_2 mixture (2:1 ratio) and in the presence of pure CH_4 at 400^oC from the same areas. From the images it is clear that the surface oxide layer present in the CH_4 and O_2 atmosphere is no longer present in the CH_4 atmosphere, Figure 4.12 shows the high resolution TEM image of Ru/SiO_2 in the presence of CH_4 at 400^oC with a lattice spacing of 0.235 +/- 0.011 nm corresponding to Ru (100). The reduction of RuO_2 to Ru metal was very fast and intermediate reduction steps were difficult to obtain. Once the RuO_2 surface layer reduces back to metallic Ru, reforming of CH_4 takes place with CO_2 and H_2O forming syngas and the CO selectivity increases with increasing temperature following the thermodynamic trends for partial oxidation of methane. Unlike Ni, there is no evidence for formation of graphite layers on the surface of the Ru metal. It is well known that Ni gets poisoned by the formation of coke on the surface, (one of the ways for coke formation on surface is due to the dissociation of methane) whereas Ru is much more resistant to the poisoning by coke [3]. Our observations also suggest that Ru has higher resistance for C poisoning than Ni.

In-situ reduction of RuO_2/SiO_2 in the presence of CH_4 was also performed to follow the reduction process in RuO_2 nanoparticles. RuO_2/SiO_2 samples were prepared by calcination of $RuCl_3.H_2O/SiO_2$ at 600^oC for 2 hours. $RuCl_3.xH_2O$ heated in the presence of air decomposes and forms RuO_2 [7]. Figure 4.13 (a-b) shows the *in-situ* TEM images of RuO_2/SiO_2 in the presence of vacuum at 200^oC

and the corresponding electron diffraction pattern confirming the nanoparticles are tetragonal RuO_2. Figure 4.13 (c-d) shows the *in-situ* TEM images from the same area in presence of 1 Torr of CH_4 at 400^oC and the corresponding electron diffraction pattern matches with the HCP Ru metal confirming the reduction. Figure 4.14 shows the *in-situ* high resolution TEM image of RuO_2/SiO_2 in the presence of 1 Torr of CH_4 at 400^oC. The nanoparticle consists of void like structures with several voids distributed within each the nanoparticle; this nanoparticle has lattice spacing of 0.23 nm corresponding to Ru (100). The presence of these void structures suggests that the reduction mechanism of RuO_2 is by the diffusion O-anions. The reduction process in RuO_2 is different from that of NiO. In the case of NiO, Ni cations are the faster diffusing species for the reduction process giving solid Ni particles after reduction (figure 3.15b)., whereas in RuO_2, O-anion is the main diffusing species which will give void like structures in the nanoparticle (figure 3.15a). Crozier et al., also observed void like structures during the reduction of PdO to Pd metal resulting in Pd metal shell. [8,9].

4.5. Summary

Both *in-situ* and *ex-situ* TEM experiments were performed on Ru/SiO_2 catalyst for partial oxidation of methane reaction. During the temperature ramp-up, the Ru metal particles transform to $Ru\text{-}RuO_2$ core-shell structures in the CH_4 and O_2 reacting gas mixture at 300^oC. RuO_2 is the species that exists on the surface of the nanoparticle when complete oxidation of methane takes place giving CO_2 and

H_2O as the main products. As the temperature increased to 425^oC almost all the O_2 is consumed in the region I of the catalyst bed and oxygen partial pressure in the later part (region II and III) of the catalyst bed goes down and the gas environment becomes reducing with CH_4 as the main reducing gas. From the *in-situ* data, RuO_2 surface layer back to metallic Ru in presence of CH_4 at 400^oC favoring reforming reactions to take place and produce syngas.

Both oxidation and reduction processes are different for Ru nanoparticles compared to Ni. In the case of Ni, complete oxidation of Ni nanoparticles was observed in presence of CH_4 and O_2 gas mixture (in 2:1 ratio) at 400^oC whereas for Ru only the surface of the nanoparticle is oxidized to RuO_2 forming Ru-RuO_2 core-shell structures. The kinetic limitation of diffusion of charged species through the oxide layer prevents the complete oxidation of Ru metal. During the reduction in CH_4, the NiO reduction mechanism involved diffusion of Ni cations along grain boundaries and extended defects giving raise Ni-NiO core-shell structures. NiO is the phase that is always exists on the surface of the nanoparticle until the complete reduction. In case of RuO_2, O-anion is the main diffusing species leaving void like structures in the nanoparticle after the complete reduction to Ru metal.

References

1. Tsang, S. C., Claridge, J. B., Green, M. L. H. (1995). Recent advances in the conversion of methane to synthesis gas. Catalysis Today, 23, 3-15.

2. Yan, Q. G., Wu, T. H., Weng, W. Z., Toghiani, H., Toghiani, R. K., Wan, H. L., & Pittman Jr, C. U. (2004). Partial oxidation of methane to H_2 and CO over Rh/SiO_2 and Ru/SiO_2 catalysts. *Journal of Catalysis*, 226, 247-259.

3. York, A. P. E., Xiao, T., & Green, M. L. H. (2003). Brief overview of the partial oxidation of methane to synthesis gas. *Topics in Catalysis*, 22(3-4), 345-358.

4. Bligaard, T., Nørskov, J. K., Dahl, S., Matthiesen, J., Christensen, C. H., & Sehested, J. (2004). The Brønsted–Evans–Polanyi relation and the volcano curve in heterogeneous catalysis, Journal of Catalysis, 224, 206–217.

5. Mott, N. F. (1940). Oxidation of metals and formation of protective films. Nature, 145, 996-1000.

6. Ryden, W. D., Lawson, A. W., & Sartain, C. C. (1970). Electrical transport properties of IrO2 and RuO2. *Physical Review B*, 1(4), 1494-1500.

7. Newkirk, A. E., & Mckee, D. W. (1968). Thermal decomposition of rhodium, iridium, and ruthenium chlorides. *Journal of Catalysis*, 11(4), 370-377.

8. Crozier, P. A., Sharma, R., & Datye, A. K. (1998) Oxidation and Reduction of Small. Palladium Particles on Silica. *Microscopy & Microanalysis*, 4, 278.

9. Crozier, P. A., & Datye, A. K. (2000). Direct Observation of Reduction of PdO to Pd Metal by *In-situ* Electron Microscopy. *Studies in Surface Science and Catalysis*, 130, 3119.

Table 4.1. Experimental conditions showing the gas environments, reaction temperatures during the *in-situ* ETEM studies.

Experiment	Gas	Temperature Ramp (^{o}C)	Comments
A	H_2	25-400	Initial Reduction
B	CH_4+0.5O_2	35-400	Oxidizing Condition
C	CH_4	25-450	Reducing Condition
D	CH_4	25-400	RuO_2 Reduction

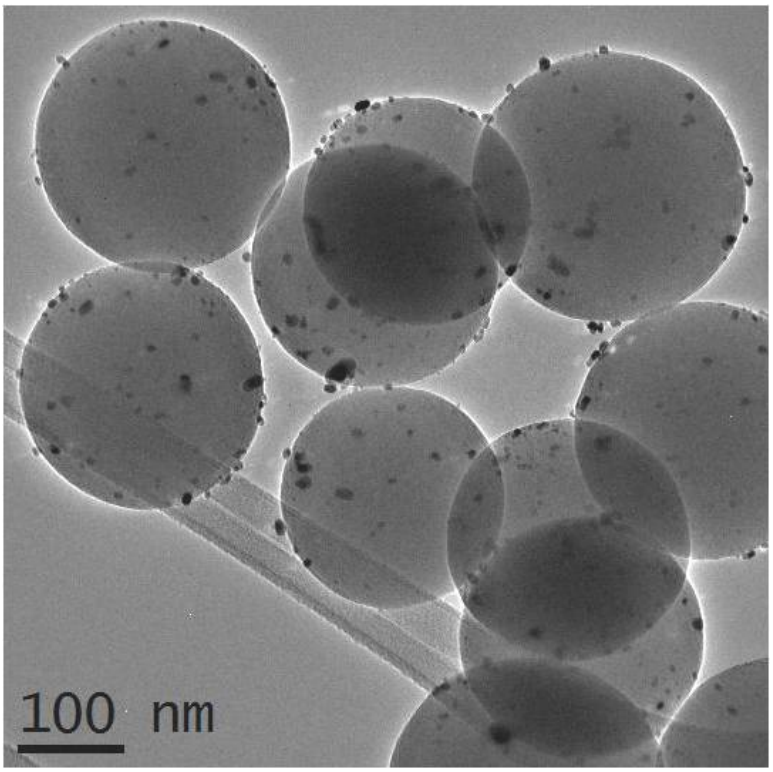

Figure 4.1. TEM image of 2.5wt% Ru/SiO2 catalyst.

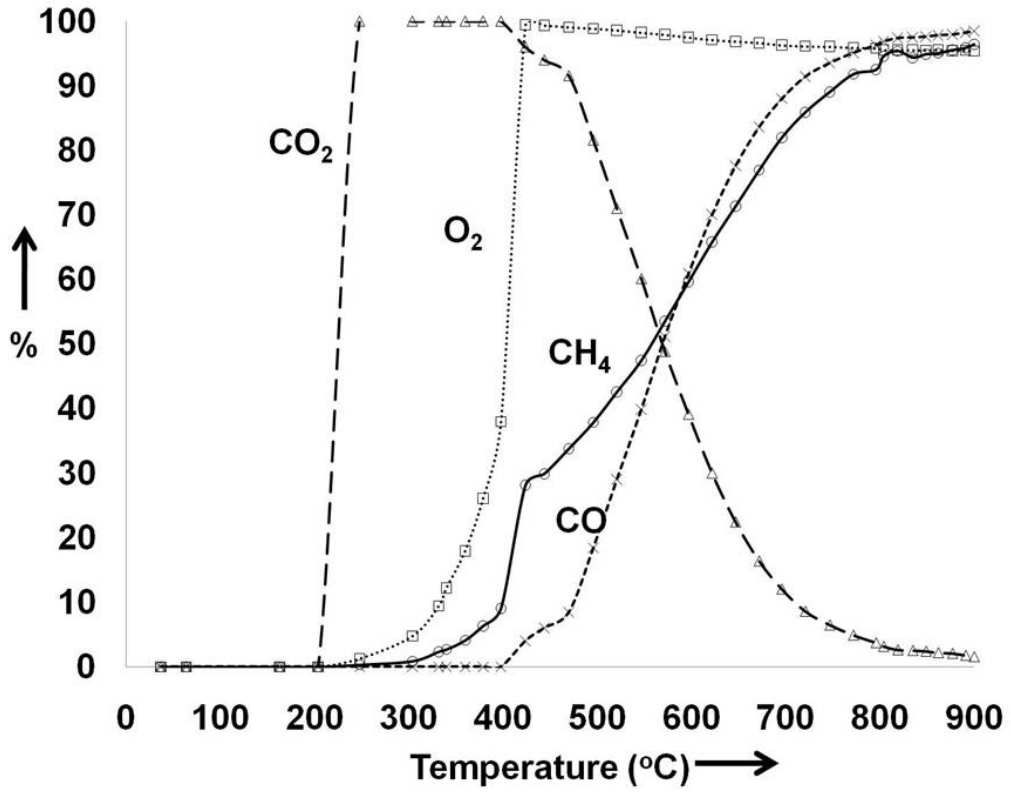

Figure 4.2. Plot showing the catalytic performance during partial oxidation of methane on 2.5 wt% Ru/SiO_2.

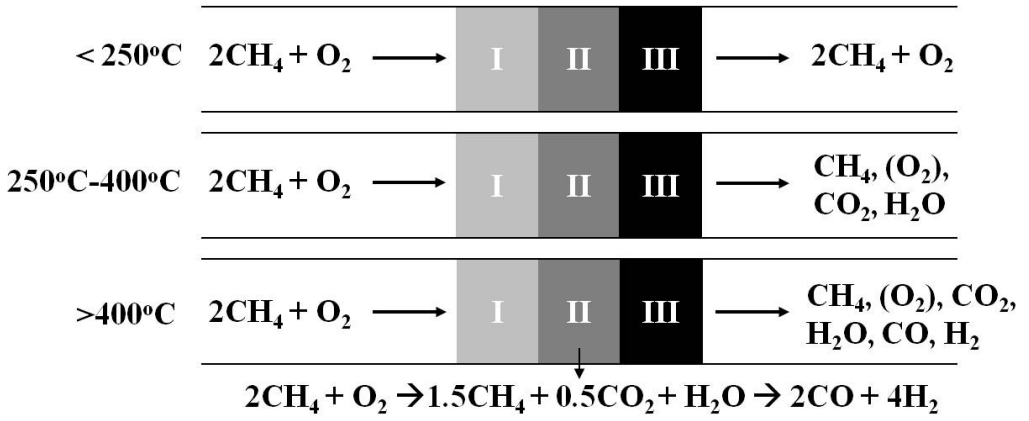

Figure 4.3. Variations in the gas composition along the catalyst bed (regions I, II and III) over different temperature ranges for 2.5 wt% Ru/SiO_2 catalyst.

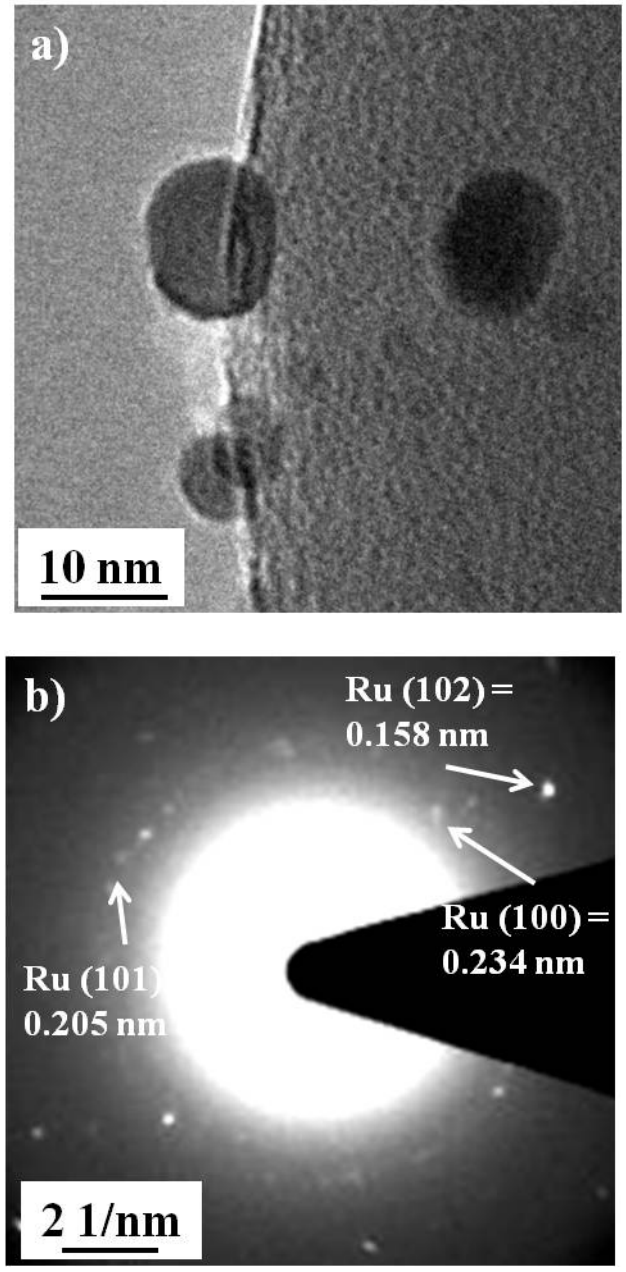

Figure 4.4. a) *In-situ* ETEM images in presence of Ru/SiO_2 1 Torr of H_2 at 400^{o}C and b) corresponding diffraction pattern.

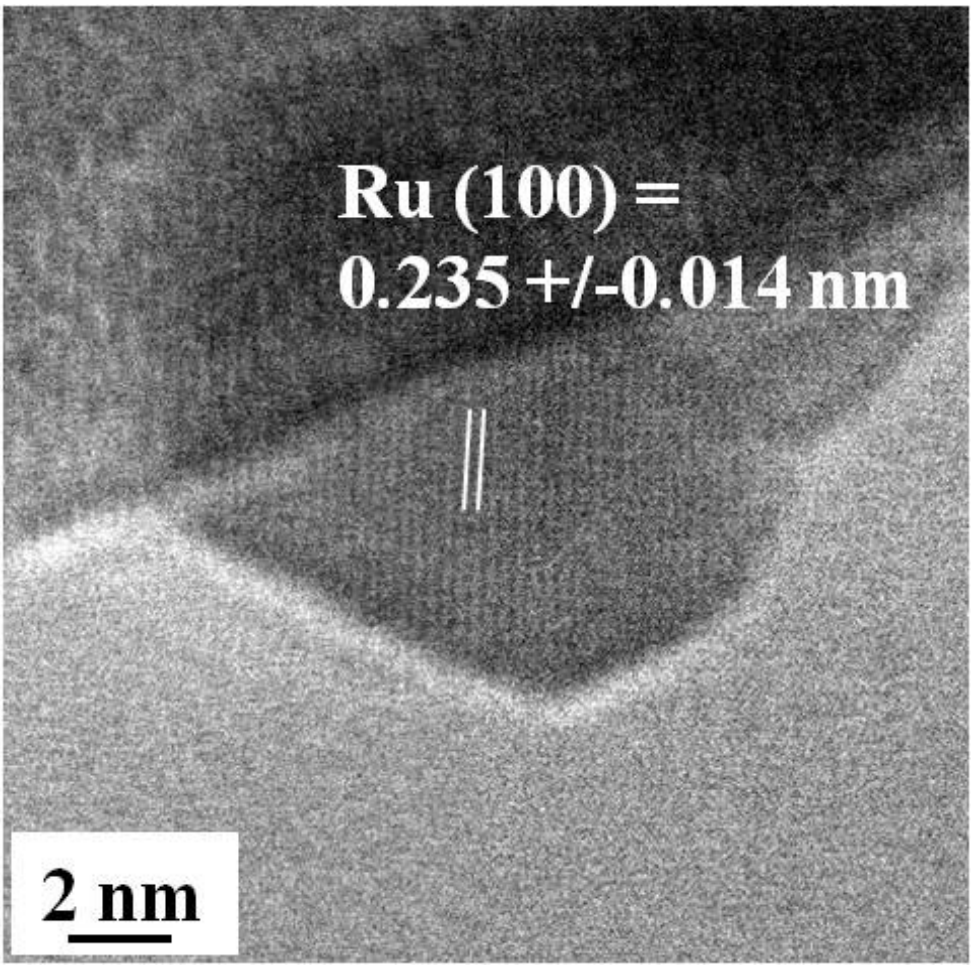

Figure 4.5. *In-situ* high resolution ETEM image of Ru/SiO_2 in presence of 1 Torr of H_2 at 400^oC.

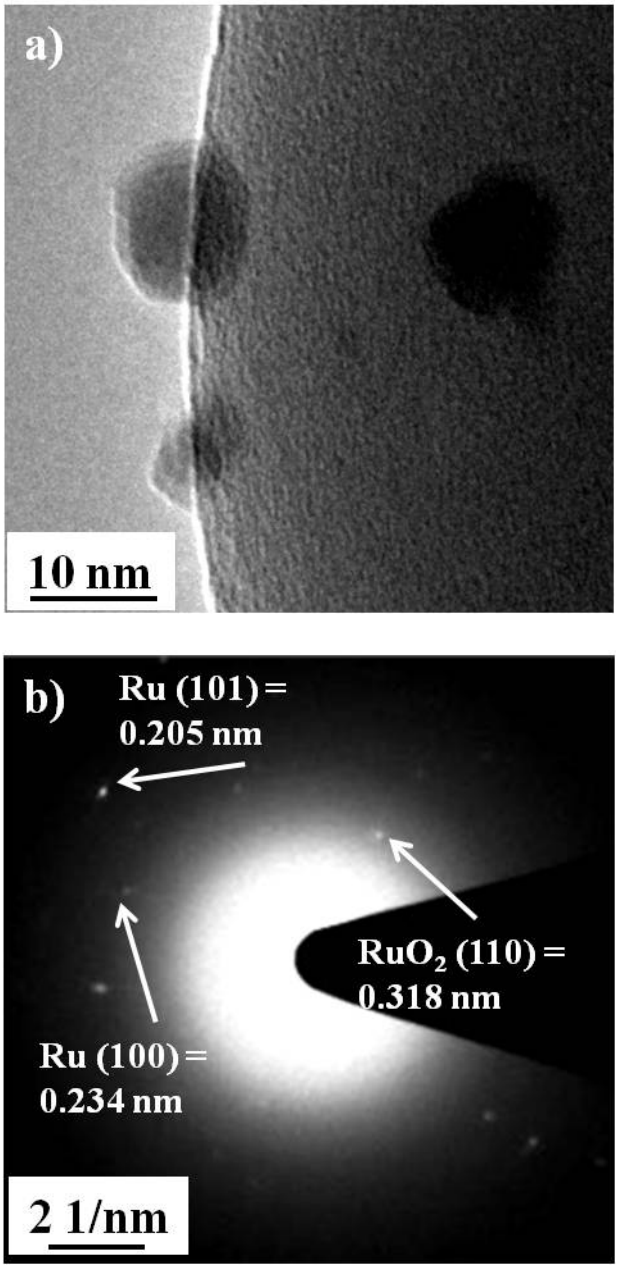

Figure 4.6. a) *In-situ* ETEM images from the same area in presence of 1 Torr of CH_4 and O_2 in 2:1 ratio at 300^{o}C and b) corresponding diffraction pattern.

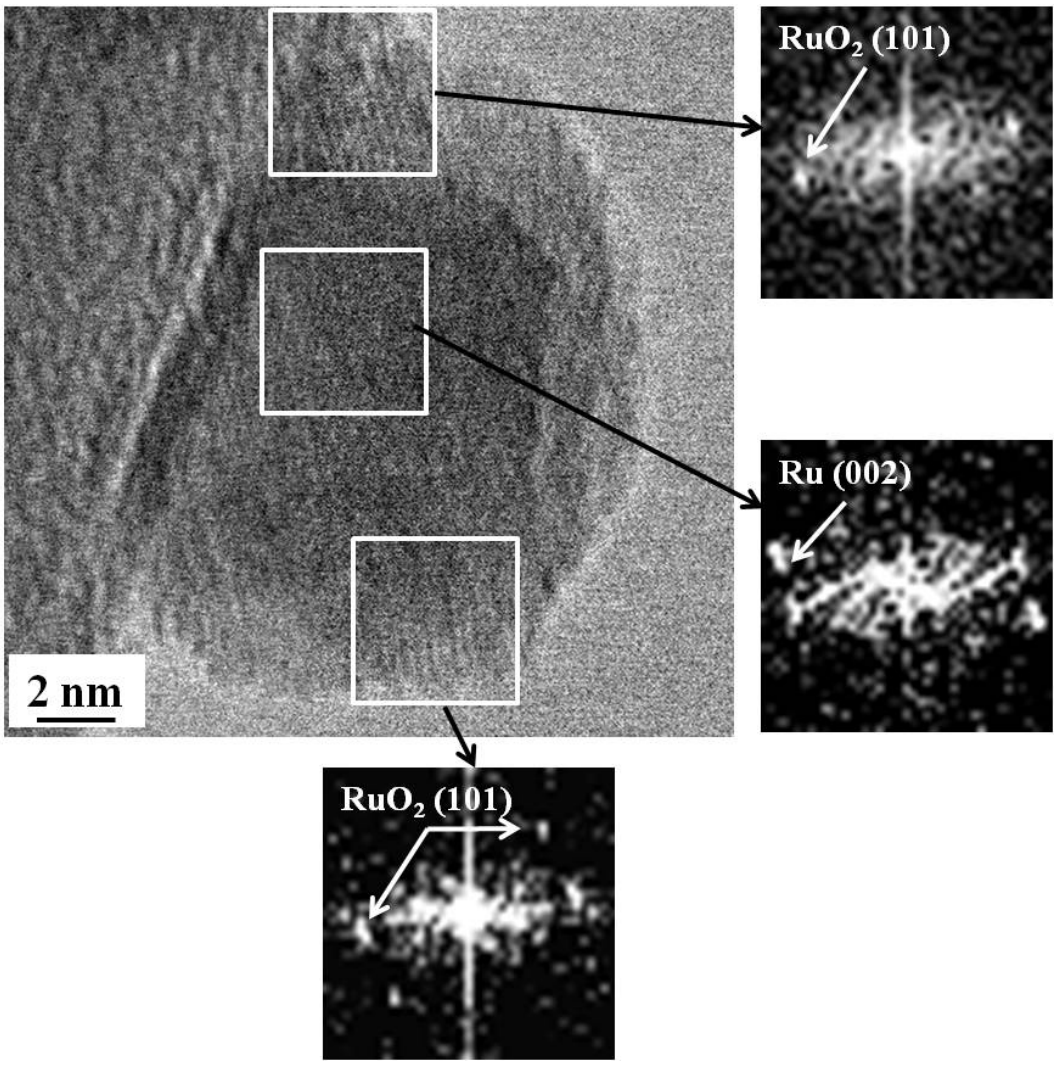

Figure 4.7. *In-situ* high-resolution ETEM image of Ru/SiO_2 in presence of 1 Torr of CH_4 and O_2 in 2:1 ratio at 400^oC.

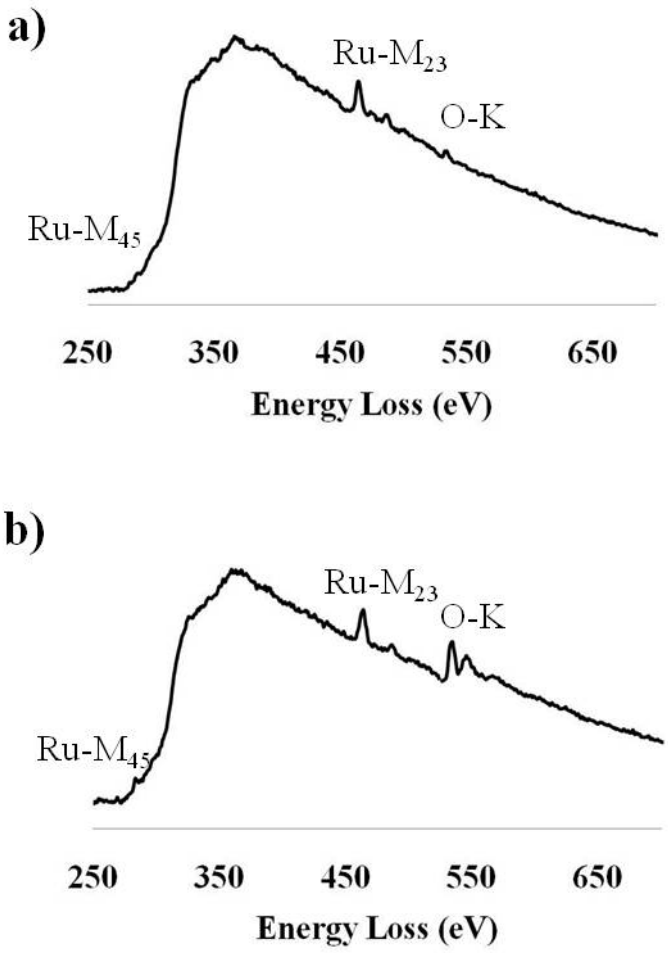

Figure 4.8. Background subtracted energy-loss spectrum in the presence of 1 Torr of CH_4 and O_2 at 300^{o}C a) from the core region of the nanoparticle b) from the surface of the nanoparticle.

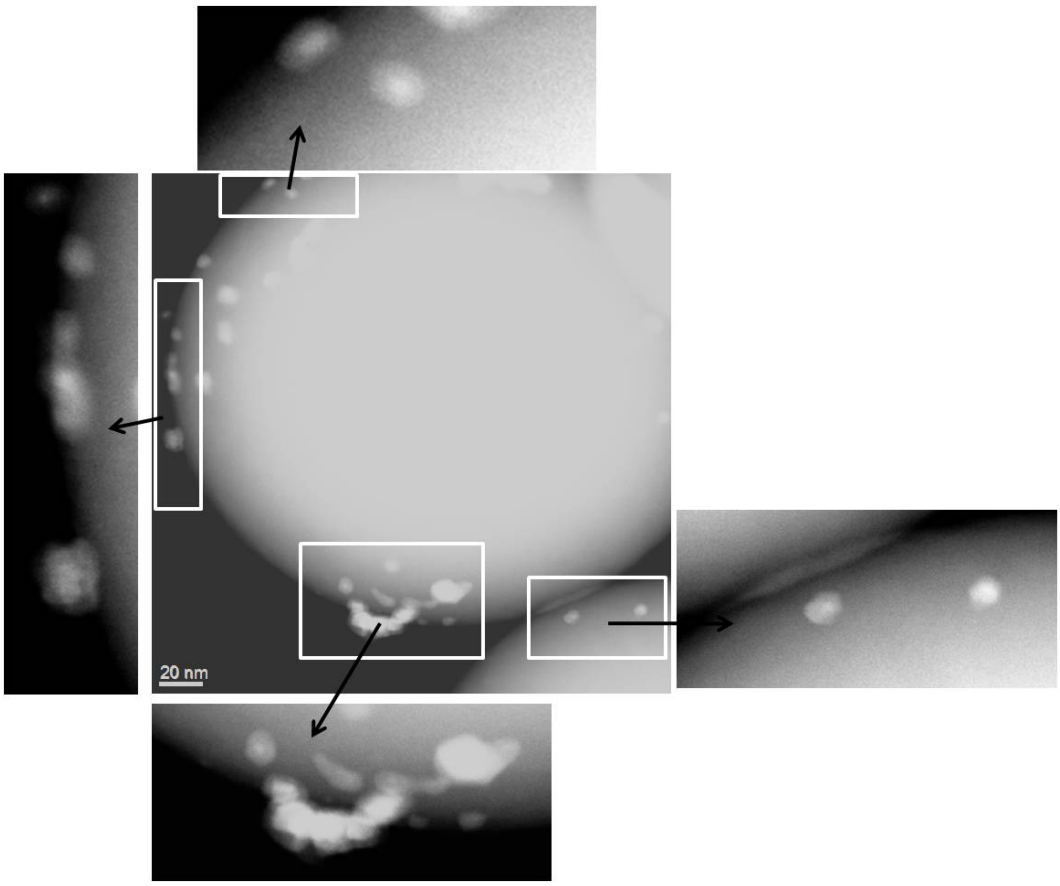

Figure 4.9. *Ex-situ* STEM image of Ru/SiO_2 after ramping to 400^{o}C in presence of CH_4 and O_2 in 2:1 ratio and cooling to room temperature in flowing He.

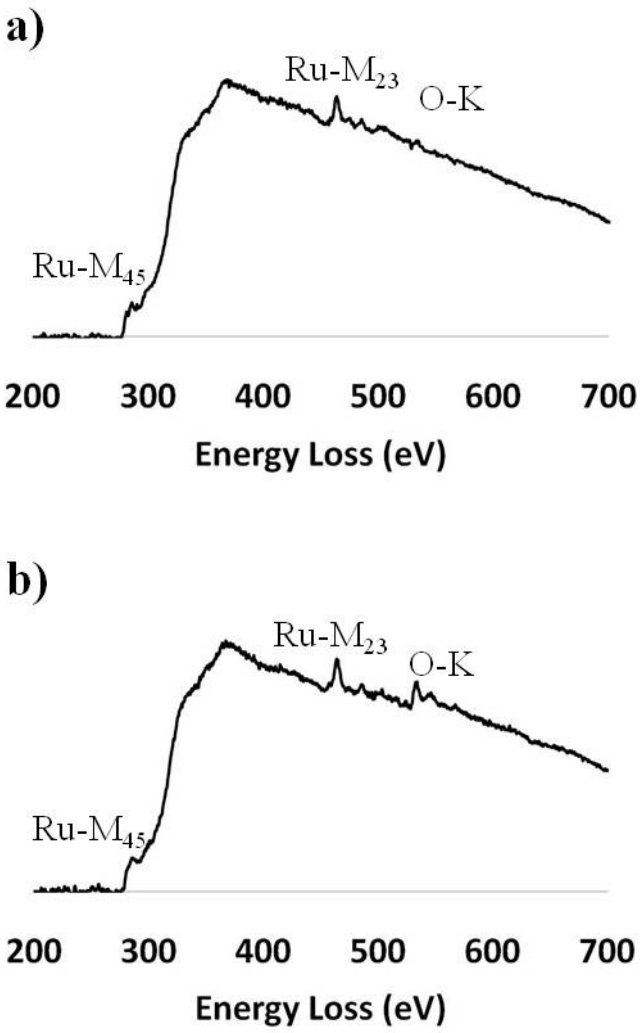

Figure 4.10. Background subtracted energy-loss spectrum from Ru/SiO_2 after ramping to 400^{o}C in presence of CH_4 and O_2 in 2:1 ratio and cooling to room temperature in flowing He. a) from the core region of the nanoparticle b) from the surface of the nanoparticle.

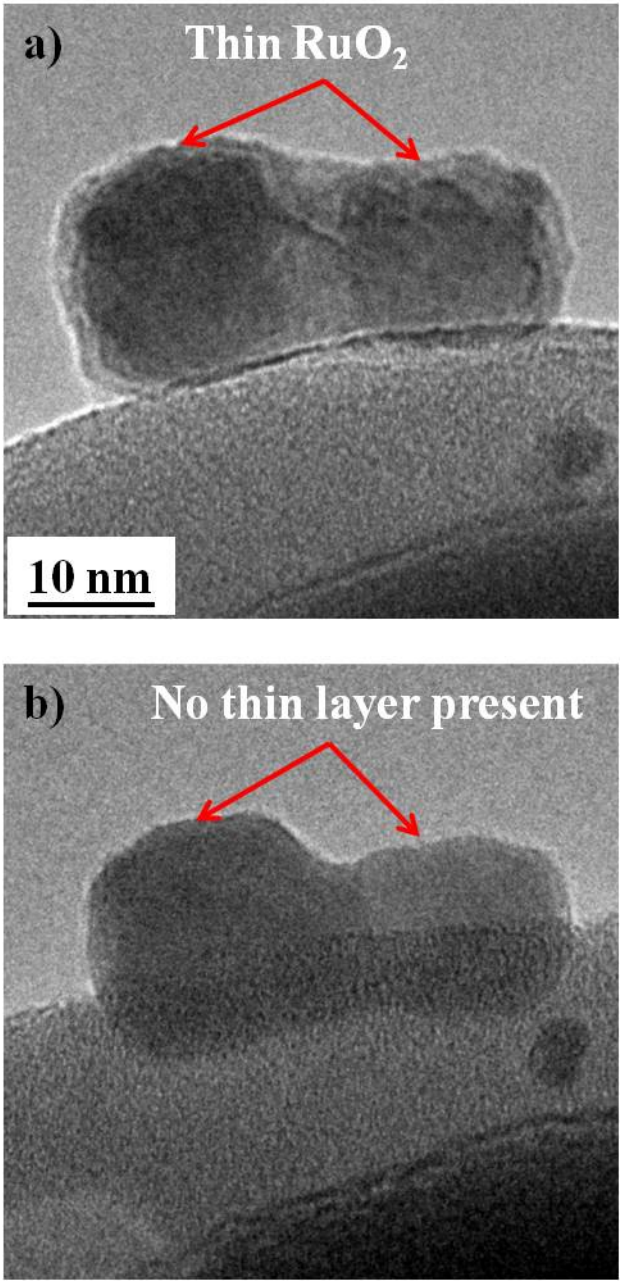

Figure 4.11. *In-situ* TEM images of Ru/SiO_2: a) In presence of 1 Torr of CH_2 and O_2 in 2:1 ratio at 400^oC and b) from the same region in presence of 1 Torr of mixture of CH_4 at 400^oC.

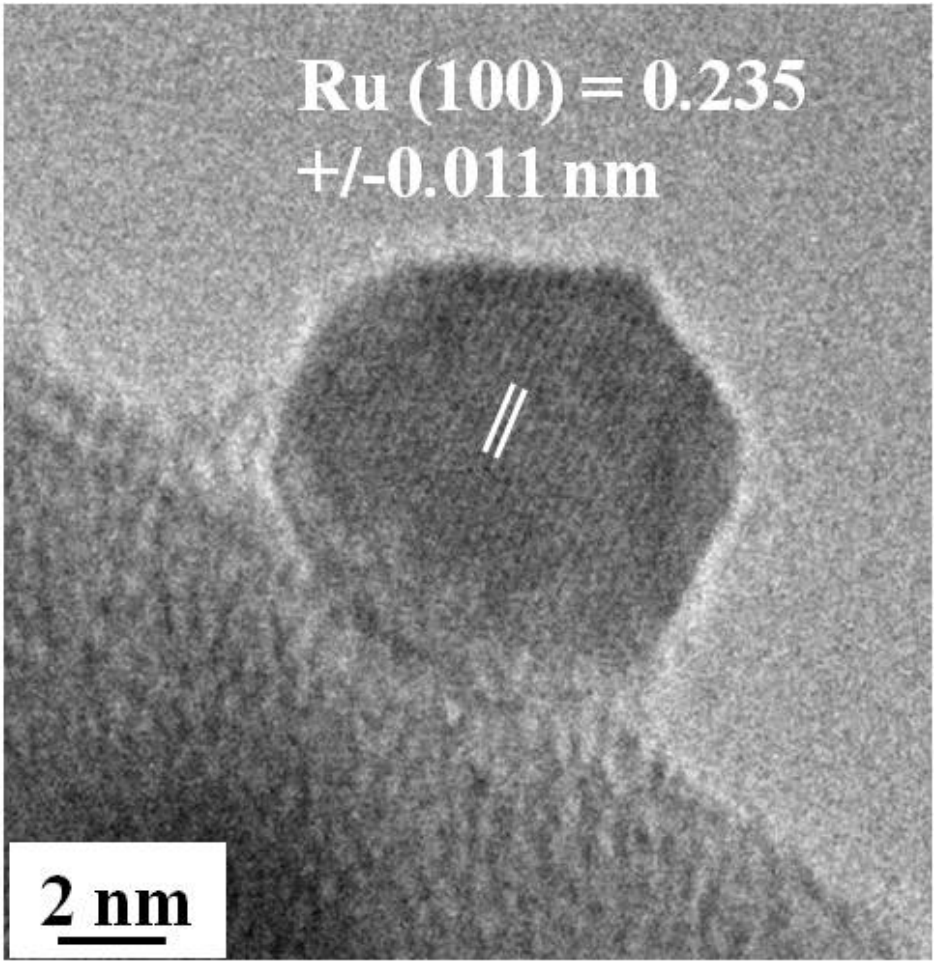

Figure 4.12. *In-situ* high-resolution ETEM image of Ru/SiO_2 in presence of 1 Torr of CH_4 at 400^{o}C.

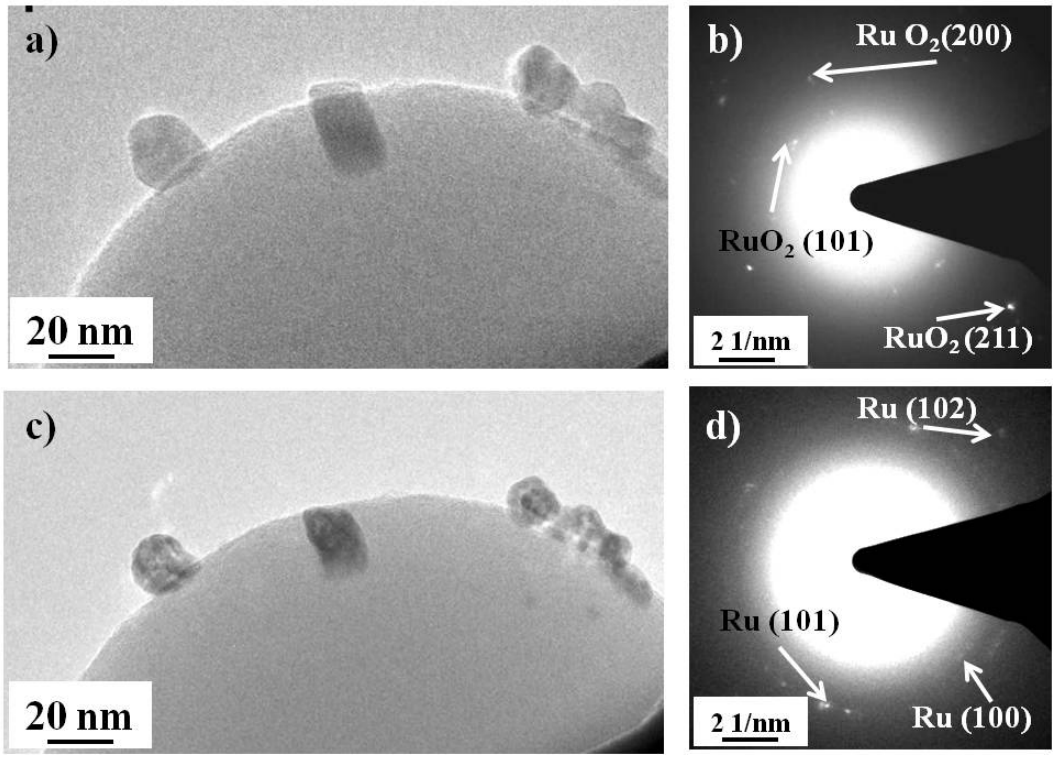

Figure 4.13. *In-situ* ETEM image and the electron diffraction pattern of RuO_2/SiO_2 a) in vacuum at 200^{o}C b) in presence of 1 Torr of CH_4 at 400^{o}C.

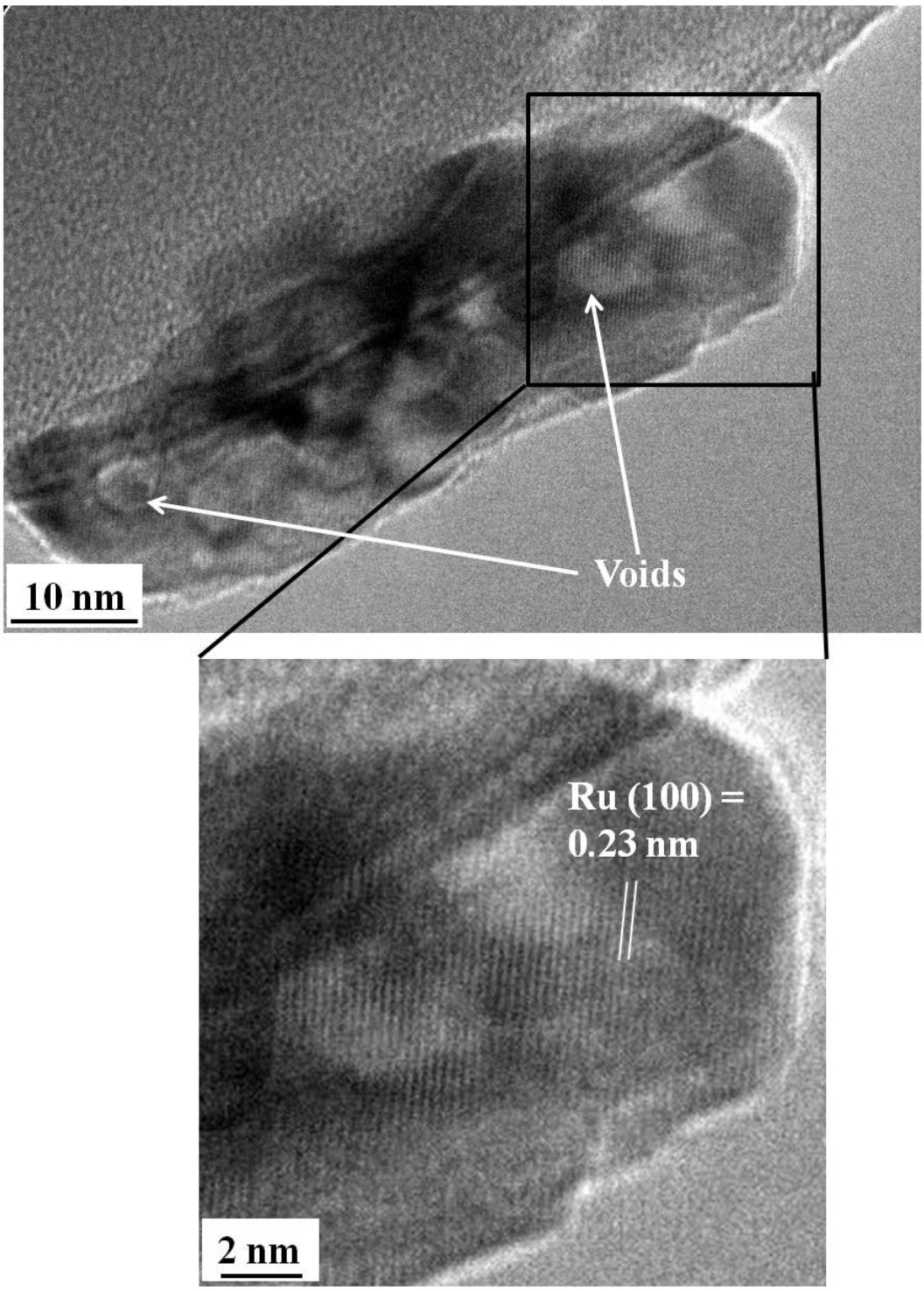

Figure 4.14. *In-situ* high-resolution ETEM image of RuO_2/SiO_2 in presence of 1 Torr of CH_4 at 400^{o}C.

Chapter 5

UNDERSTANDING THE EVOLUTION OF NI-RU BIMETALLIC NANOPARTICLES UNDER REACTING GAS CONDITIONS USING *IN-SITU* ENVIRONMENTAL TEM

5.1. Introduction

In the last two chapters, nanostructural changes in supported monometallic nanoparticles (Ni and Ru) and their effect on the catalytic performance was presented for partial oxidation (POM) of methane reaction. This chapter focuses on bimetallic nanoparticles (NiRu) for the POM reaction. Bimetallic catalysts sometimes exhibit superior activity, selectivity and resistance to deactivation [1]. In general noble metals are highly active for most of the chemical reactions, but are very expensive. A combination of a noble metal with an inexpensive metal is ideal for improving the catalyst performance and at the same time keeping material costs low. Ni and Ru were chosen to make bimetallic catalyst, where Ni is an inexpensive metal and Ru is a noble metal.

A major challenge in bimetallic catalysts lies in the synthesis of these particles, where the goal is to create a close interaction between the two metal species [2]. There are several possible interactions that can take place between the two metals during the preparation of these bimetallic nanoparticles as described in Figure 5.1 (a-e). There may be a possibility that the two metal species do not interact with each other (figure 5.1a) in which case the catalyst behaves as two individual monometallic catalysts with no synergetic effect of the two metals. Figure 5.1b and 5.1c shows the core-shell type structures that can form, and there

may be a possibility of phase separation in individual nanoparticles with non uniform metal distributions (figure 5.1d) or they can from complete solid solution with a uniform distribution (figure 5.1e). Moreover these nanostructures can undergo significant changes when they are exposed to reacting gas conditions at elevated temperatures.

In this chapter nanostructural changes in supported NiRu nanoparticles were studied under reacting gas conditions that are relevant to POM using *in-situ* environmental transmission electron microscopy (ETEM) and the effect of these nanostructural changes is correlated with the performance of the catalyst.

5.2. Ni-Ru/SiO_2 catalyst preparation

Supported NiRu bimetallic nanoparticles were prepared by co-impregnating SiO_2 spheres with the precursor solution of nickel nitrate hexahydrate ($(Ni(NO3)_2.6H_2O$) and ruthenium chloride ($RuCl_3.xH_2O$). Precursor solution was obtained by dissolving a known amount of 99.99% $Ni[NO_3]_2.6H_2O$ and 99.98% ($RuCl_3.xH_2O$) (obtained from Sigma Aldrich) together in a alcohol solvent. Incipient wetness impregnation was carried out in a mortar by drop wise addition of precursor solution equivalent to the pore volume of the SiO_2 in a saturated ethanol atmosphere while mixing for 10 min. The overall metal content in the catalyst is 2.5 wt% with 50 at% Ni and 50 at% Ru. After impregnation, the sample was dried at 120^oC followed by reduction in 5%H_2/Ar atmosphere at 400^oC for 3 hours.

5.3. EDX composition analysis of NiRu bimetallic nanoparticles

For determining the composition of the SiO_2 supported bimetallic NiRu nanoparticles, energy dispersive x-ray spectroscopy (EDX) was performed in a JEOL JEM 2010F transmission electron microscope with the microscope in STEM mode. Figure 5.2a shows the STEM image of 50Ni50Ru/SiO_2 and a typical EDX spectrum is shown in figure 5.2b. EDX spectra from individual nanoparticles was obtained in raster mode, where the beam is scanned across the entire particle this gives the average Ni and Ru composition in the individual nanoparticle. Spectra were collected for 60 to 120 seconds depending on the x-ray counts generated by the particle.

The Cliff-Lorimer method can be used to determine the composition of bimetallic nanoparticles by using the following equation [3]:

$$C_{Ni}/C_{Ru} = k_{Ni\text{-}Ru} * I_{Ni}/I_{Ru} \qquad (1)$$

where C_{Ni} and C_{Ru} are the atomic composition fractions of the elements Ni and Ru, I_{Ni} and I_{Ru} are the background subtracted intensities of Ni Kα and Ru Kα peaks respectively, $k_{Ni\text{-}Ru}$ is the sensitivity factor. For determining the k-factor, EDX spectra were collected from a standard sample. The standard sample was prepared as follows, a known amount of nickel nitrate hexahydrate and ruthenium chloride hydrate were mixed together to get a 50at% Ni and 50at% Ru metal concentrations and was dissolved in an ethanol solvent. The solution was ultrasonicated for 5 min to obtain a uniform mixing; a drop of this solution was placed onto a holy carbon TEM grid for EDX analysis. EDX spectra were collected from several areas and the ratio of intensities under the Ni Kα and Ru

Kα peaks was determined. Figure 5.3 shows the I_{Ni} and I_{Ru} ratio obtained from several regions, the ratio varies by only 7% from the average value, suggesting that a reasonably uniform composition of Ni, Ru is present in the standard sample. By knowing the initial composition ratio and the intensity ratios for the Ni and Ru, the k-factor can be determined by using equation 1. The k_{Ni-Ru} obtained from the standard is 0.33 with a standard deviation of 0.02. By knowing the k factor and the intensity ratio of Ni Kα and Ru Kα peaks, the composition in individual nanoparticles can be obtained. Figure 5.4 shows the composition distribution for 50Ni50Ru sample from several nanoparticles. The average composition obtained from the EDX analysis for 50Ni50Ru sample is 53.7 at% Ni and 46.3 at% with a standard deviation of 15 at%, which is close to the nominal bulk composition used for preparing this sample. From the plot it is clear that almost all the nanoparticles contain both Ni and Ru. EDX analysis shows that bimetallic nanoparticles of NiRu were successfully obtained by performing co-impregnation preparation technique.

5.4. Ni-Ru/SiO_2 catalyst performance

The catalytic reaction for partial oxidation of methane was performed in an *In-situ* Research Instruments RIG 150 reactor. Conditions for performing catalytic reactions are similar to that used for Ni/SiO_2 and Ru/SiO_2 catalysts. The effluent gas from the reactor outlet was analyzed with a Varian 3900 gas chromatography.

Figures 5.5 shows the measured catalytic conversion of CH_4 and O_2 and their selectivity towards CO_2 and CO on 50Ni50Ru/SiO_2 during partial oxidation

of methane. During the temperature ramp up, no catalytic conversion of CH_4 took place at temperatures below 300^oC. CO_2 is the initial product that was formed on NiRu bimetallic catalyst by complete combustion of CH_4, the light-off temperature for CO_2 formation (300^oC) was the same as that for the pure Ni catalyst and about 50^oC higher than that of pure Ru catalyst. Complete combustion takes place in the temperature range of 300^oC to 500^oC giving CO_2 and H_2O in 1:2 ratio. At 500^oC about 15% of CH_4 and 60% of O_2 is converted to CO_2 and H_2O, similar conversions happen on the Ni catalyst at about 575^oC. A further increase in temperature to 525^oC resulted in a sharp rise in CH_4 conversion from 15% to 50% and also a sharp rise in O_2 conversion from 60% to almost 100%. CO also started to form at this temperature. Under the same ramp-up conditions, the light-off temperature for CO formation on NiRu bimetallic catalyst is about 250^oC lower than that of pure Ni catalyst (775^oC) and about 100^oC higher than that of pure Ru catalyst (425^oC). With a further increase in temperature both CH_4 conversion and CO selectivity increased and reached the thermodynamic limits of partial oxidation of methane [4].

The performance of 50Ni50Ru catalyst has some similarities with that of pure Ru and pure Ni catalytic data. The conversion plots are more similar to Ru performance (chapter 4, figure 4.2), except there is a shift in the temperature to higher values. Sharp rise in the CO formation for 50Ni50Ru catalyst is similar to that observed in pure Ni (chapter 3, figure 3.2). The possible variation in gas composition along the catalyst bed for 50Ni50Ru catalyst was similar to that of

Ru (chapter 4, figure 4.3), however in case of 50Ni50Ru catalyst the temperature regimes are shifted to higher values.

5.5. Dynamic evolution of Ni-Ru bimetallic nanoparticles

5.5.1. Initial stage of ramp-up: NiO surface segregation

Figure 5.6a shows the *in-situ* TEM image of 50Ni50Ru bimetallic nanoparticle on SiO_2 support in the presence of 1 Torr of H_2 at 400^oC. A typical energy-loss spectrum from one of the nanoparticle in the presence of H_2 at 400^oC is shown in figure 5.6b confirming that both Ni and Ru are present in the nanoparticle. Figure 5.7a shows the same nanoparticle as that in figure 5.6a in the presence of CH_4 and O_2 (in 2:1 ratio) at 400^oC. The nanoparticle contains a dark core with a thin shell on the surface. Energy-loss spectrum from the surface of the nanoparticle (figure 5.7b) shows that the shell contains predominantly NiO with a slight hint of Ru. It is not clear at this moment whether Ru exists as metal or oxide because of the weak signal from Ru and the O edges of metals overlap. However based on the studies on pure Ru in chapter 4, Ru will form a layer of RuO_2 on the surface in the presence of CH_4 and O_2 (in 2:1 ratio). Hence it is reasonable to assume that any Ru that is present on the surface would exist as RuO_2. For all the energy-loss spectra discussed in this chapter, the background was removed from the Ru, O and Ni by fitting the power law to 60-80 eV pre-edge fitting windows before the Ru ionization edge.

Figure 5.8a shows the *in-situ* high resolution ETEM image of the 50Ni50Ru bimetallic nanoparticle in the presence of 1 Torr of H_2 at 400^oC. The

lattice spacing in the nanoparticle measures to be about 0.229 +/- 0.011 nm which does not belong to pure Ni or pure Ru within the error. According to the JCPDS data (PDF file number: 04-001-2915) this lattice spacing matches to the hexagonal NiRu (100) plane of 0.225 nm [5], with Ni to Ru atomic ratio of 1. Table 5.1 shows the lattice spacings of different planes for Ni, Ru and 50Ni50Ru obtained from JCPDS files.

Figure 5.8b shows the *in-situ* high resolution ETEM image of the same nanoparticle as in figure 5.8a in the presence of 1 Torr of CH_4 and O_2 (in 2:1 ratio) at 400^{o}C. A core-shell structure can clearly be seen in the nanoparticle. A Fast Fourier Transform (FFT) from the core region is shown in the figure, the lattice spacing measurement from the FFT is about 0.231 +/- 0.011 nm which matches with the lattice spacing of the HCP Ru (100). Coarse fringes were seen at the interface between the surface oxide layer and the core Ru particle. The lattice spacing of the coarse fringes measured from the FFT is about 0.322 +/- 0.009 nm which matches with the RuO_2 (110).

To further evaluate the compositional distribution along the nanoparticles, *in-situ* electron energy-loss spectroscopy (EELS) line scans in STEM mode were performed. A typical EELS line scan contains 20 spectra with a collection time of about 500 ms each. The gas pressure in the environmental cell was lowered to 0.3 Torr while collecting the EELS spectra to avoid the energy-loss signal from the gases. The EELS line scans in STEM mode under *in-situ* ETEM conditions is very difficult to perform due to drift associated with the sample holder at high temperatures. Figure 5.9 schematically illustrates the difficulty associated with

performing the EELS line scans in *in-situ* ETEM. Suppose an EELS line scan was performed along a nanoparticle; figure 5.9a represents the state of the supported nanoparticle image and a line profile was drawn for collecting the EELS spectra along this nanoparticle as shown. It takes about 10 seconds for all the spectra to be collected along the line profile. Within this time, the sample will drift away from the line profile as represented in figure 5.9b. This gives EELS spectra from the regions that are not of interest (i.e. not along the nanoparticle).

To overcome this issue, EELS line scans are carefully performed according to the following procedure. Initially an estimate of the sample drift was made by looking at a sequence of STEM images. Line scans are always started from the vacuum or from the SiO_2 surface. This will give two reference points, one from the vacuum with no signal in the EELS spectra and the other from the SiO_2 which gives an O K-edge in the EELS spectra. A complete scan along the nanoparticle is considered only if both the boundary points are seen while collecting the spectra. That is if the scan is performed from the vacuum, the first spectrum in the EELS line scan will have no peaks and the final spectrum will have an O-K edge signal from SiO_2. Similarly if the scan was performed from the SiO_2 surface, the first spectra in the EELS line scan will have an O-K edge signal from SiO_2 and the final spectra will have no peaks when the electron beam reaches the vacuum. The term “vacuum” in *in-situ* ETEM case is loosely used since the sample is surrounded by the reactant gas environment. Low gas pressures (0.3 Torr in this case) will not give enough signal in the STEM mode to be detectable by EELS.

Figure 5.10 (a-b) shows the STEM image and EELS line scan on the Ni-Ru bimetallic nanoparticle in the presence of 0.3 Torr H_2 at 400^{o}C. According to the bulk phase diagram (shown in figure 5.11) on Ni-Ru a complete phase separation of almost pure Ni and pure Ru regions should exist at this temperature (400^{o}C), this means the nanoparticle should contain regions with 100% Ni and 100% Ru. From the line scan in figure 5.10b some evidence for phase separation can be observed, however it is not as dramatic as the phase diagram prediction. From the composition profile in figure 5.10b, it can be observed that, the nanoparticle is more uniform towards the surface and rich in Ni towards the support-particle interface. These bulk phase diagram may not represent the actual Ni-Ru interaction for nanoparticles, moreover the presence of gas can also have effect on the composition distribution.

Figure 5.10 (c-d) shows the STEM image and EELS line scan from the same nanoparticle as that of figure 5.10a in the presence of 0.3 Torr CH_4 and O_2 (in 2:1 ratio) at 400^{o}C. The STEM image shows a bright core with a lighter shell on the nanoparticle, and EELS line scan shows preferential surface segregation of Ni onto the surface with Ru in the core region.

For obtaining the oxygen distribution along the nanoparticle, EELS line scans were taken across the nanoparticle parallel to the silica surface as shown in figure 5.12a. This geometry makes it is possible to avoid the O-K edge signal from the SiO_2. Figure 12b is the composition profile obtained from the EELS signal and shows a typical core-shell structure with Ni on both sides of the surface of the nanoparticle and Ru in the core. The oxygen profile almost matches the Ni

profile confirming that the nanoparticle is surrounded predominantly by the NiO shell. A dip in the oxygen profile in the core region suggests that Ru exist as metallic Ru. Oxygen is always seen because the Ru core is surrounded by an oxide shell, this oxide shell contributes oxygen signal in the EELS spectra even from the core region. Ru signal is always seen from the oxide shell (which is shown in figure 5.8, suggesting that the oxide shell consists of both Ni and Ru as oxides; however the shell predominantly consists of NiO.

The oxidation process in alloy nanoparticles can significantly vary depending on the metals that are forming the bimetallic system [6-10]. Figure 5.13 schematically shows the three possible mechanisms of oxidation behavior in two-phase alloys, adopted from Gesmundo et al. 1995 [6]. In the first case (mechanism I) (figure 5.12a), both the metals can undergo an oxidation process independently forming AO and BO. In the second case (mechanism II), the two metals can undergo oxidation process cooperatively forming a uniform oxide layer of (AB)O. In the third case (mechanism III), one metal undergoes an oxidation process and the other does not. From the *in-situ* ETEM observations, the oxidation process in Ni-Ru bimetallic nanoparticles is more close to mechanism III; however there is some presence of Ru oxide in the oxide shell.

Figure 5.14 schematically explains classic oxidation behavior of an alloy with a combination of a noble metal (Ru) and the metal that tends to undergo complete oxidation (Ni). To start it is assumed that the nanoparticle contains an almost uniform distribution of Ni and Ru (figure 5.14a). During the oxidation process, both Ni and Ru on the surface of the nanoparticle will get oxidized and

form a combination of NiO and RuO or (NiRu)O (figure 5.14b). From the previous observations on pure Ni (chapter 4) and pure Ru (chapter 5), both metal surfaces get oxidized when they are exposed to a gas mixture of CH_4 and O_2 in 2:1 ratio. Hence it is reasonable to assume that the initial oxidation process takes place by the formation of oxide scale formed by both Ni and Ru. The diffusion of Ni takes place from the alloy-oxide interface onto the surface of the nanoparticle and undergoes further oxidation. This will leave a Ni depletion region between the alloy and the oxide which is rich in Ru, as shown in figure 5.14c. This concentration gradient in the metallic core will lead to an inward diffusion of the Ru from the depletion region and outward diffusion of Ni from the core towards the interface. The driving force for Ni to form NiO in the presence of O_2 will lead to further diffusion of Ni from the depletion region onto the surface and undergoes oxidation. This process will continue eventually giving a nanoparticle with an oxide shell rich in Ni with Ru metal core and the interface contains aa mixed oxide layer (figure 5.14d). When metal species diffuses onto the surface this will leave a vacancy and can lead to the formation of voids at the interface between the oxide and the Ru metal core, these voids may not be stable and can collapse. The void structures are occasionally observed in the nanoparticles, an example is shown in figure 5.15.

The oxidation behavior does not exactly follow the mechanism as described above, since there is always some presence of Ru in the oxide layer as shown by EELS spectra in figure 5.7b. The surface oxide shell is a combination of Ni and Ru oxides with predominantly rich in NiO. This suggests that there may be

some diffusion of Ru is taking place on to the surface during the oxidation process. The oxidation mechanism described in figure 5.14 assumes that the bimetallic nanoparticles have a uniform composition to start with. However, the composition is not perfectly uniform for NiRu nanoparticles (as seen in figure 5.10 (a-b)) which can effect the composition distribution in the oxide scale during the oxidation.

5.5.2. Final stage ramp-up: NiRu formation

From the reactor data, as the temperature increases, the gas mixture in region II and region III of the catalyst bed becomes more reducing (as O_2 is consumed) with CH_4 as the main reducing gas. Eventually it becomes thermodynamically favourable for the oxide to transform back to metal at this point.

In-situ reduction was performed in the presence of CH_4. Figure 5.16 compares the STEM image and the EELS line scan profiles from the same nanoparticle in the presence of 0.3 Torr CH_4 and O_2 (in 1:2 ratio) at 400^oC and in the presence of 0.3 Torr CH_4 at 600^oC. Figure 5.16a in CH_4 and O_2 again shows the similar behaviour as before, with Ni rich on the surface (which is in the form of NiO) and Ru rich in the core. In the presence of CH_4 (figure5.16b), the oxide reduced back to metal and intermixing of Ni and Ru takes place. The EELS line scan profiles of Ni and Ru from several nanoparticles in the presence of 0.3 Torr CH_4 at 600^oC were shown in Appendix III. From these line scans it can be observed that there is a variation in the distribution of Ni and Ru from one nanoparticle to the other. Some nanoparticles show more or less uniform

distribution of Ni and Ru and some show an inhomogeneous distribution. Some nanoparticles contain Ru rich surface, which is in contrast with that of in the presence of CH_4 and O_2 gas mixture. A nanoparticle with Ni rich surface in the presence of CH_4 and O_2 mixture transforms into a Ru rich when the gas environment was switched to pure CH_4. (The apparent enrichment of Ru at the particle-silica interface is an artifact of the EELS background fitting caused by the presence of the silicon L_{23} edge). From chapter 3, it has been observed that Ni is the main diffusing species during the reduction of NiO. Since the oxide shell contains predominantly NiO, it is reasonable to assume that the dominant mechanism for the reduction to take place is by the diffusion of Ni cations to the subsurface during the reduction process. As the NiO reduces back to Ni metal, it will diffuse into the subsurface and the surface of the nanoparticle gets richer in Ru.

5.6. Low Ru composition sample

The above data is shown for a bimetallic catalyst containing 50% Ni and 50% Ru, high Ru content is used in this case to facilitate the easy detection of Ru while performing spectroscopic studies. However if the cost of the catalyst has to be lowered the use of noble metal (in this case Ru) should be much less. A very low Ru content NiRu bimetallic sample was prepared and tested for the catalytic performance for partial oxidation of methane. NiRu bimetallic catalyst was prepared with 95 at% Ni and 5 at% Ru on SiO_2 using the co-impregnation technique as described in section 5.2; the catalyst is labeled as 95Ni5Ru.

Figures 5.17, shows the measured catalytic conversion of CH_4 and O_2 and their selectivity towards CO_2 and CO on 95Ni5Ru/SiO_2 during partial oxidation of methane. During the temperature ramp up, no catalytic conversion of CH_4 take place at temperatures below 300^{o}C. CO_2 is the initial product that was formed on 95Ni5Ru bimetallic catalyst by complete combustion of CH_4. Complete combustion takes place in the temperature regime of 300^{o}C to 560^{o}C giving CO_2 and H_2O in 1:2 ratio. A further increase in temperature to 585^{o}C results in a sharp rise in CH_4 conversion from 19% to 62%, CO also starts to form at this temperature. Under the same ramp-up conditions, the light-off temperature for CO formation on 95Ni5Ru bimetallic catalyst is about 50^{o}C higher than that of 50Ni50Ru catalyst. However it is about 200^{o}C below the light-off temperature of pure Ni. Just by addition of 5 at% Ru to Ni there is dramatic decrease in the light-off temperature for CO production. With a further increase in temperature both CH_4 conversion and CO selectivity increases, following the thermodynamic limits of partial oxidation of methane [4].

Some preliminary *in-situ* ETEM experiments were performed on this sample. Figure 5.18a shows the *in-situ* ETEM image of 95Ni5Ru/SiO_2 catalyst in the presence of 1 Torr of H_2 at 400^{o}C. Figure 5.18b shows the *in-situ* ETEM image of 95Ni5Ru/SiO_2 catalyst in the presence of 1 Torr of CH_4 and O_2 in 2:1 ratio at 400^{o}C. A solid nanoparticle in the presence of H_2 has transformed to a void like structure when the gas composition is changed to CH_4 and O_2. This void structure formation is similar to that of the oxidation process in pure Ni, where the Ni cations can diffuse faster onto the surface than of the O anions and undergoes

oxidation process eventually leaving a void structure [11,12]. Figure 5.19 shows the *ex-situ* TEM image of the 95Ni5Ru/SiO_2 catalyst after the reaction in CH_4 and O_2 in a 2:1 ratio in an *ex-situ* reactor. Void structures are clearly seen in the low magnification image, a high resolution image from one of this particle shows the presence of NiO (111) and (200) lattice fringes confirming that the nanoparticles are NiO. More *in-situ* ETEM studies have to be performed under different reacting gas in order to understand the Ni and Ru distribution in this sample.

5.7. Structure-activity relationship

During the temperature ramp-up in CH_4 and O_2 for 50Ni50Ru catalyst, an oxide shell was formed on the surface of the nanoparticle containing predominantly NiO with some RuO_2. The surface oxide is an active phase for complete oxidation of methane given CO_2 and H_2O as the main product but not for syngas formation. On the NiO surface almost all the O_2 is converted at 775^oC, whereas on RuO_2 surface all the O_2 is converted at 425^oC. On the mixed oxide surface the O_2 conversion is 100% at 525^oC. Since the oxide layer contains both Ni and Ru oxides, this gives a synergetic effect and the temperature at which 100% O_2 conversion takes place lies in between that of the pure metals. Similar observation can be correlated to the 95Ni5Ru catalyst. The surface of the catalyst must contain a mixed oxide layer which can give a 100% conversion observed at 585^oC which is about 200^oC lower than that of on NiO.

Once the O_2 conversion is 100%, oxygen partial pressure goes down in the later part of the catalyst bed, with CH_4 as the main reducing gas. From the *in-situ*

ETEM data the oxide layer reduces back to metal which are active sites for CH_4 reforming reactions and favors the syngas formation.

5.8. Summary

SiO_2 supported Ni-Ru bimetallic nanoparticles were prepared by using co-impregnation technique. EDX data from 50Ni50Ru catalyst confirms that most of the nanoparticles contain both Ni and Ru and the composition variation among the nanoparticles is with the 15% of the nominal value used for preparing this sample . The performance of bimetallic 50Ni50Ru for partial oxidation of methane is better than that of pure Ni and slightly worse than the pure Ru. The light-off temperature for CO formation is lowered by about 250^{o}C for 50Ni50Ru bimetallic catalyst compared to pure Ni. The performance of 50Ni50Ru catalyst has some similarities with that of pure Ru and pure Ni catalytic performance. The conversion plots are more similar to Ru performance, except there is a shift in the temperature to higher values. Sharp rise in the CO formation for 50Ni50Ru catalyst is similar to that of observed in pure Ni.

In-situ environmental (TEM) experiments were performed under different gas environments that are relevant to partial oxidation of methane. In the presence of H_2 at 400^{o}C, *in-situ* EELS line scans shows that both Ni and Ru were present along the nanoparticle, with the uniform distribution of Ni and Ru towards the surface and Ni rich region from the core to the support-particle interface. During the temperature ramp-up in CH_4 and O_2, core-shell structures were observed from the *in-situ* data at 400^{o}C. EELS line scan along the nanoparticle suggest that the

surface of the nanoparticle is predominantly NiO with some RuO_2 in it and the core region is metallic Ru. The presence of mixed oxide layer on the surface of the nanoparticle gives 100% O_2 conversion at temperature lower than that of pure NiO and higher than that or RuO_2.

As the O_2 is consumed completely in the region I of the catalyst bed the oxygen partial pressure in the later part (region II and III) of the catalyst bed goes down and the gas environment becomes reducing with CH_4 as the main reducing gas. From the *in-situ* data, in the presence of CH_4 at 600^oC oxide layer reduces back to metal and intermixing of Ni and Ru takes place. The presence of NiRu metal on the surface is active for CH_4 reforming reactions giving syngas.

A low Ru (95 at%Ni and 5 at%Ru) composition bimetallic sample was also prepared and tested for the activity for partial oxidation of methane. A small addition of Ru lowered the light-off temperature for syngas production by about 200^oC. Preliminary TEM data on this sample suggest that void structures are formed in the bimetallic nanoparticles similar to that of the pure Ni. Further studies have to be performed on this sample in order to understand the compositional distribution of Ni and Ru in the nanoparticles under different reacting gas conditions.

References

1. Tsang, S. C., Claridge, J. B., Green, M. L. H. (1995). Recent advances in the conversion of methane to synthesis gas. Catalysis Today, 23, 3-15.

2. York, A. P. E., Xiao, T., & Green, M. L. H. (2003). Brief overview of the partial oxidation of methane to synthesis gas. *Topics in Catalysis*, 2003, 22(3-4), 345-358.

3. Ertl, G., Knozinger, H., & Weitkamp, J. (1997). *Handbook of heterogeneous catalysis* (Vol 1).

4. Garratt-Reed A. J., & Bell, D.C. (2003) *Energy-dispersive X-ray analysis in the electron microscope*. BIOS Scientific Publication: Limited.

5. Gesmundo, F., Niu, Y., & Viani, F. (1995). Possible scaling modes in high-temperature oxidation of two-phase binary alloys. II: Low oxidant pressures. *Oxidation of Metals*, 43(3/4), 379-394.

6. Gesmundo, F., Viani, F., Niu, Y., &.Douglass, D. L. (1993). The transition from the formation of mixed scales to the selective oxidation of the most-reactive component in the corrosion of single and two-phase binary alloys. *Oxidation of Metals*, 40(3/4), 373-393.

7. Gesmundo, F., & Gleeson, B. (1995). Oxidation of multicomponent two-phase alloys. *Oxidation of Metals*, 44(1/2), 211-237.

8. Gesmundo, F., & Viani, F. (1986). Transition from internal to external oxidation for binary alloys in the presence of an outer scale. *Oxidation of Metals*, 25(5/6), 269-282.

9. Wagner, C. (1952). Theoretical analysis of the diffusion processes determining the oxidation rate of alloys. *Journal of Electrochemical Society*, 369-380.

Table 5.1. d-spacings of Ni, Ru, 50Ni50Ru and RuO_2 obtained from JCPDS files.

Ni		**Ru**		**50Ni50Ru**		**RuO_2**	
a	3.523 Å	a	2.706 Å	a	2.607 Å	a	4.499 Å
b	3.523 Å	b	2.706 Å	b	2.607 Å	b	4.499 Å
c	3.523 Å	c	4.282 Å	c	4.198 Å	c	3.107 Å
Sp.gr	Fm3m	Sp.gr	P63/mmc	Sp.gr	P63/mmc	Sp. gr	P42/mnm
hkl	**d (nm)**	**hkl**	**d (nm)**	**hkl**	**d (nm)**	**hkl**	**d (nm)**
111	0.2034	100	0.2343	100	0.2257	110	0.3183
200	0.1762	002	0.2142	002	0.2099	101	0.2558
220	0.1246	101	0.2056	101	0.1988	200	0.2251
311	0.1062	102	0.1580	102	0.1537	111	0.2223
222	0.1017	110	0.1253	110	0.1303	210	0.2013
400	0.0881	103	0.1218	103	0.1189	211	0.1689

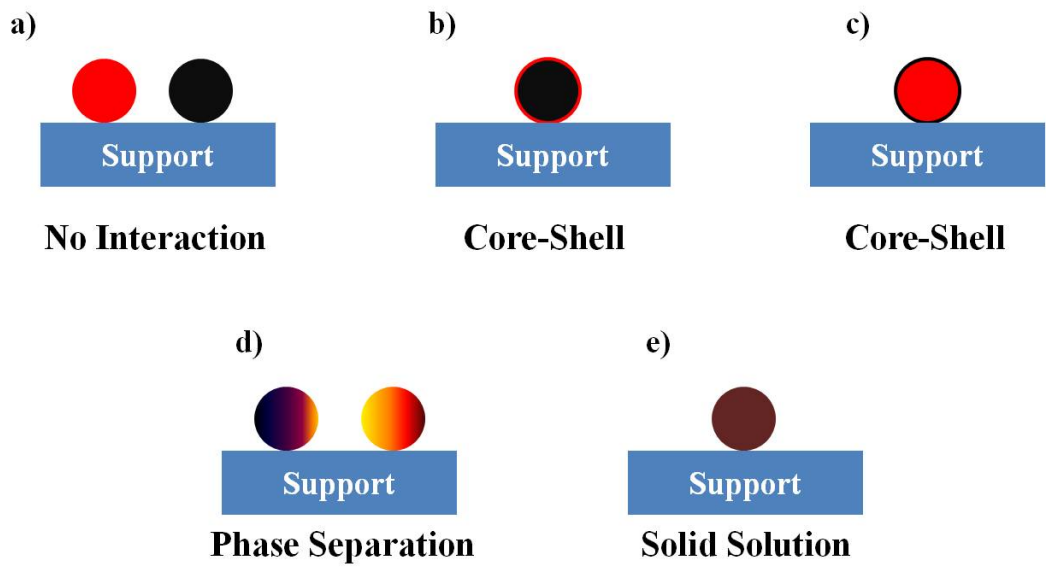

Figure 5.1. Schematic showing the different forms of interactions in bimetallic nanoparticles.

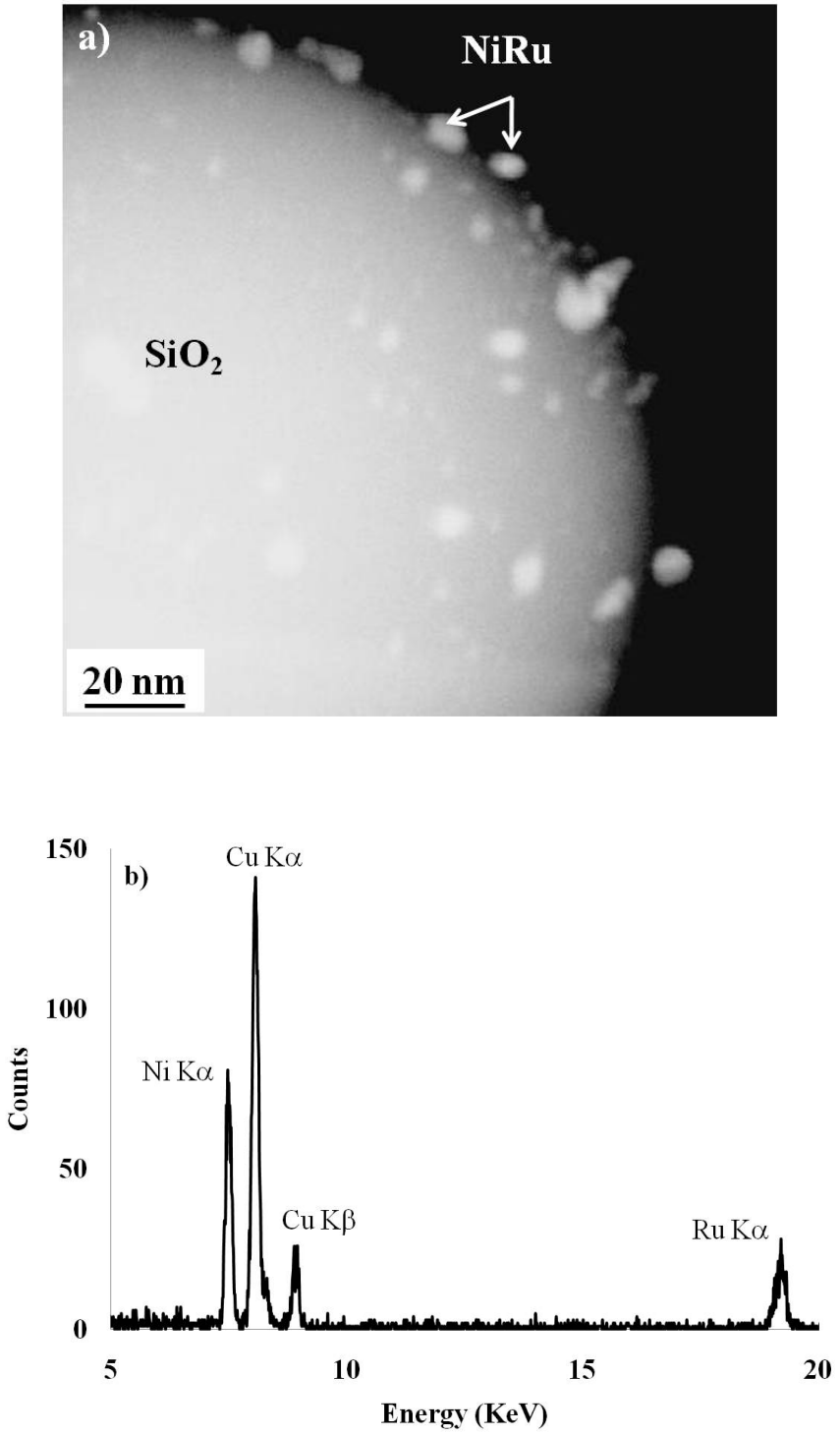

Figure 5.2. a) STEM image of $NiRu/SiO_2$, b) typical EDX spectra from one of the NiRu nanoparticle.

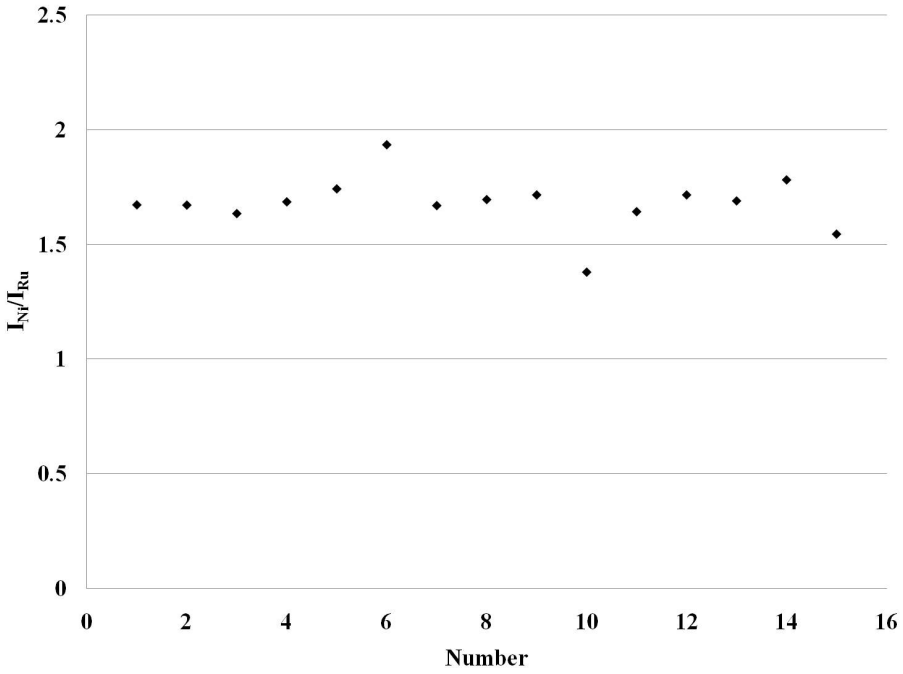

Figure 5.3. Compositional analysis from a NiRu standard showing the intensity ratio of Ni Kα to Ru Kα.

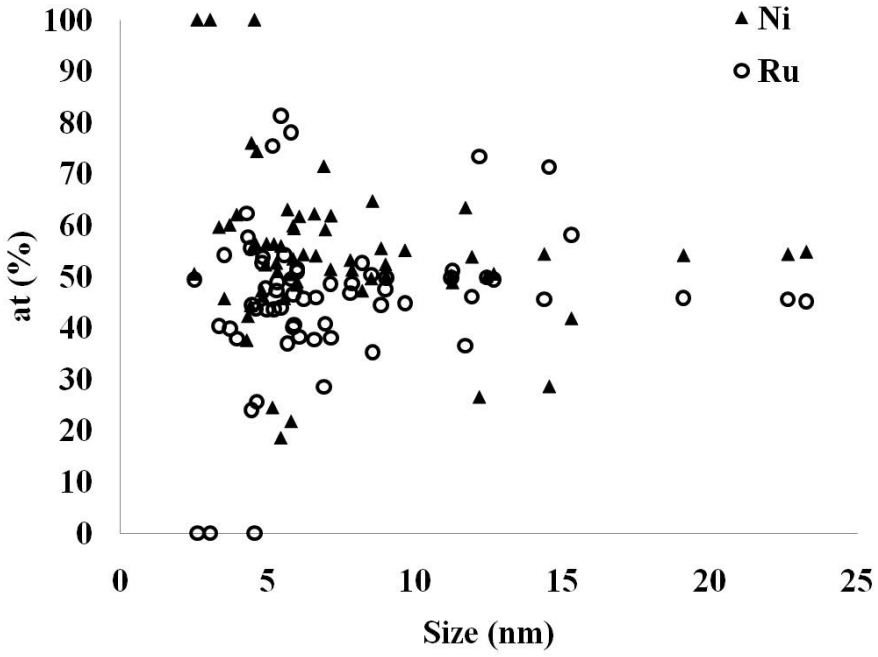

Figure 5.4. EDX composition analysis for 50Ni50Ru sample.

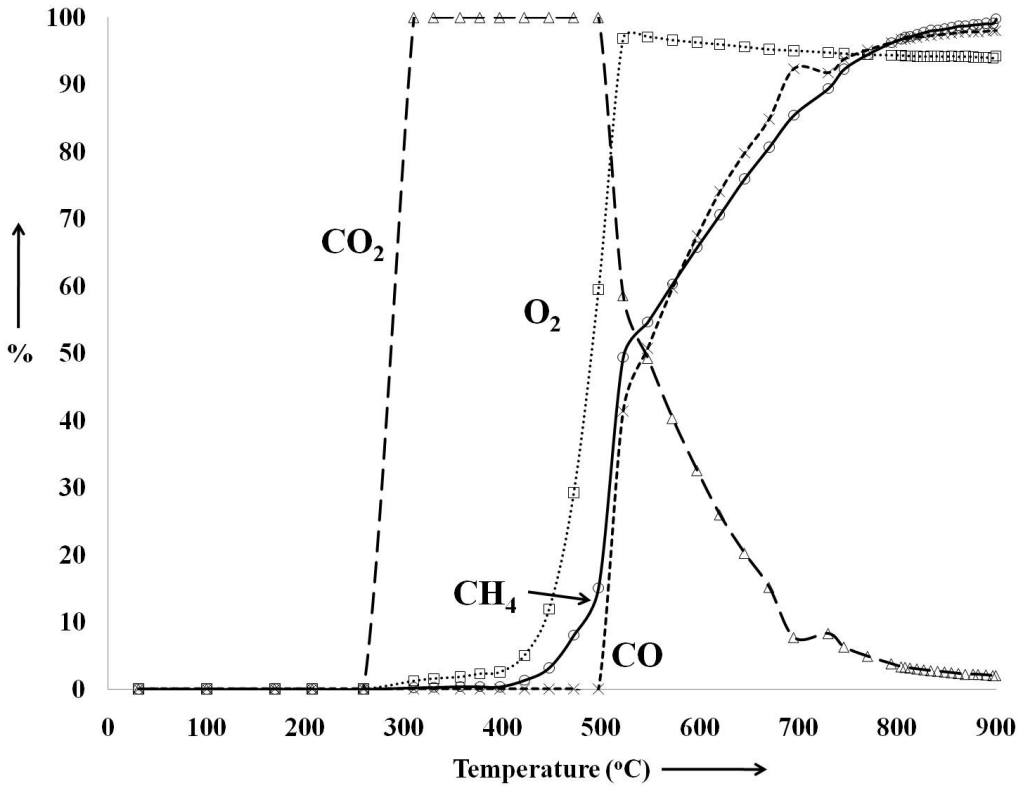

Figure 5.5. Plot showing the catalytic performance during partial oxidation of methane on 2.5 wt% 50Ni50Ru/SiO_2.

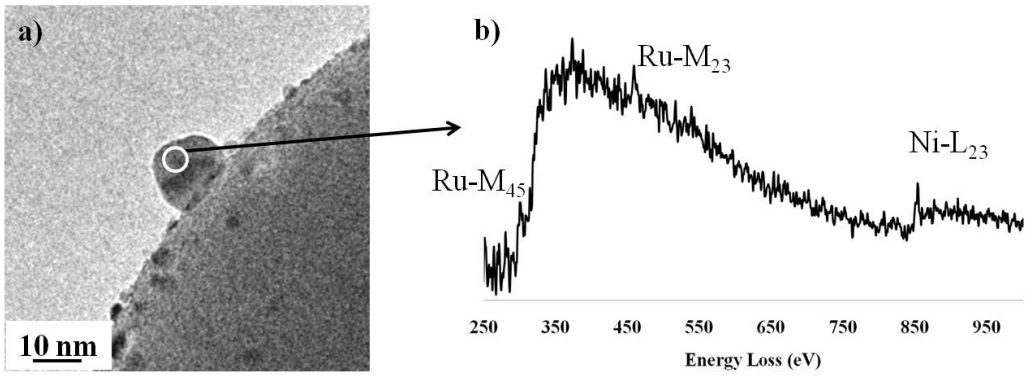

Figure 5.6. *In-situ* ETEM images and the corresponding EELS spectra from a 50Ni50Ru/SiO_2 catalyst in the presence of 1 Torr of H_2 at 400^{o}C.

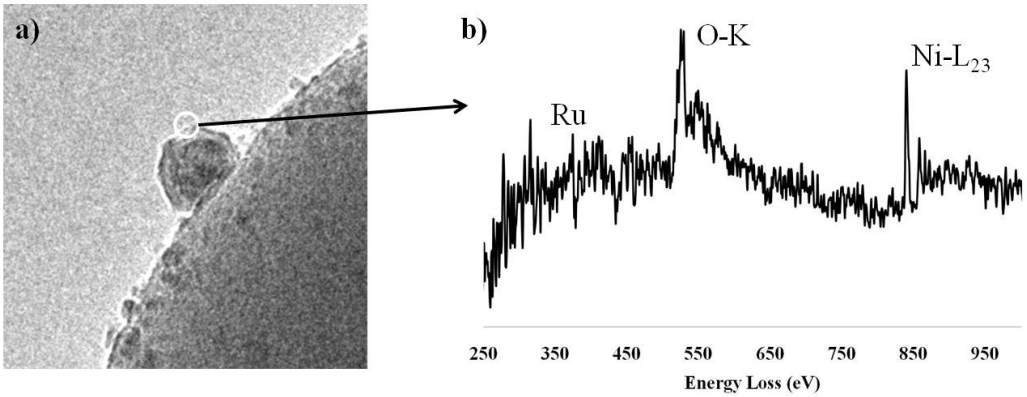

Figure 5.7. *In-situ* ETEM images and the corresponding EELS spectra from a 50Ni50Ru/SiO_2 catalyst in the presence of 1 Torr of mixture of CH_4 and O_2 in 2:1 ratio at 400^{o}C.

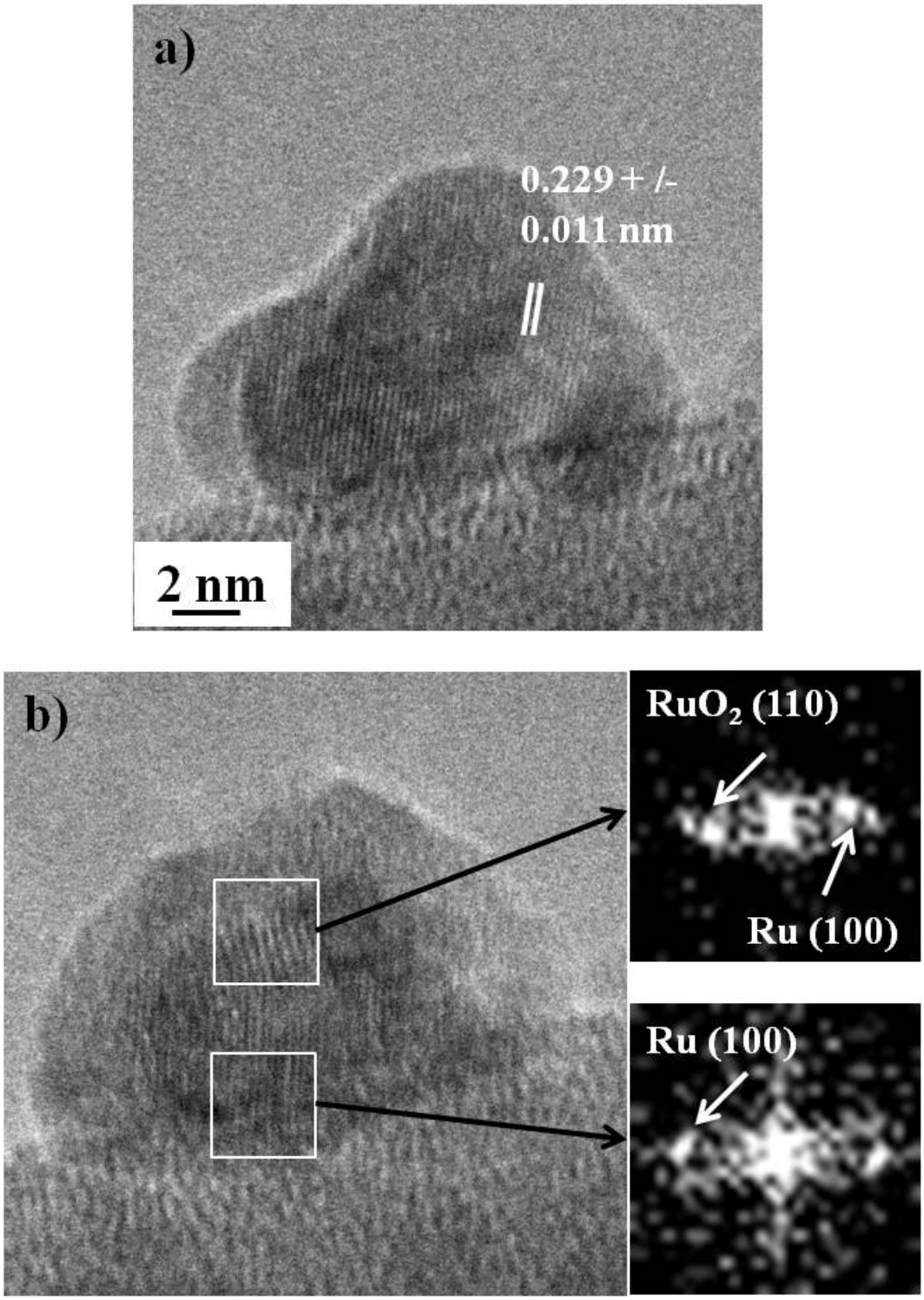

Figure 5.8. *In-situ* high-resolution ETEM images of 50Ni50Ru/SiO_2 a) In presence of 1 Torr of H_2 at 400^{o}C and b) from the same nanoparticle in presence of 1 Torr of mixture of CH_4 and O_2 in 2:1 ratio at 400^{o}C.

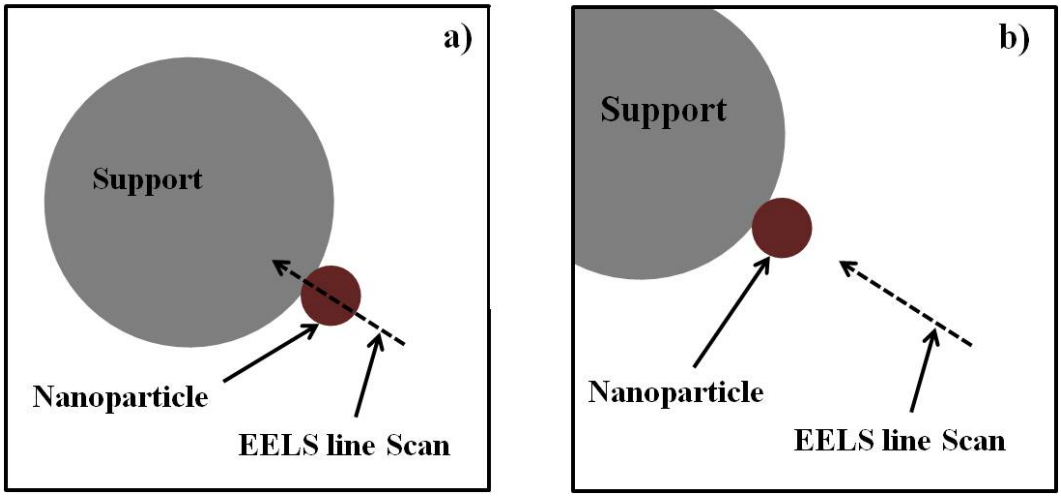

Figure 5.9. Schematic illustration of difficulties associated with sample drift during the collection of STEM EELS line scans.

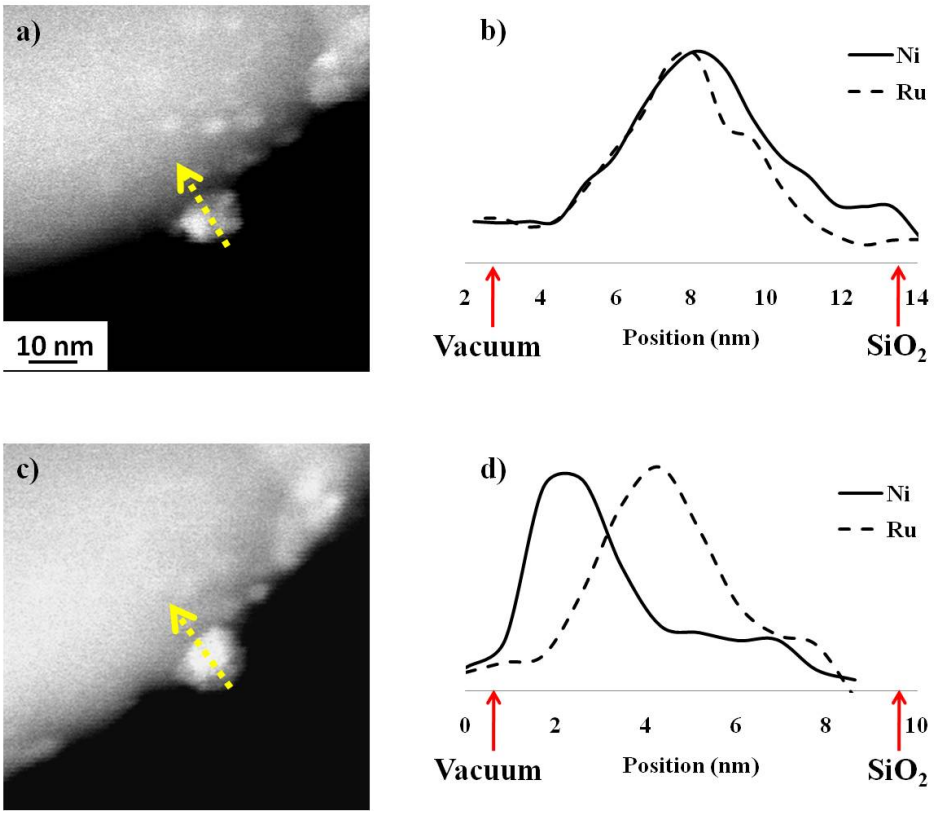

Figure 5.10. *In-situ* environmental STEM images and EELS line scans from 50NiRu50/SiO_2 a) In presence of 0.3 Torr of H_2 at 400^{o}C and b) from the same nanoparticle in presence of 0.3 Torr of mixture of CH_4 and O_2 in 2:1 ratio at 400^{o}C.

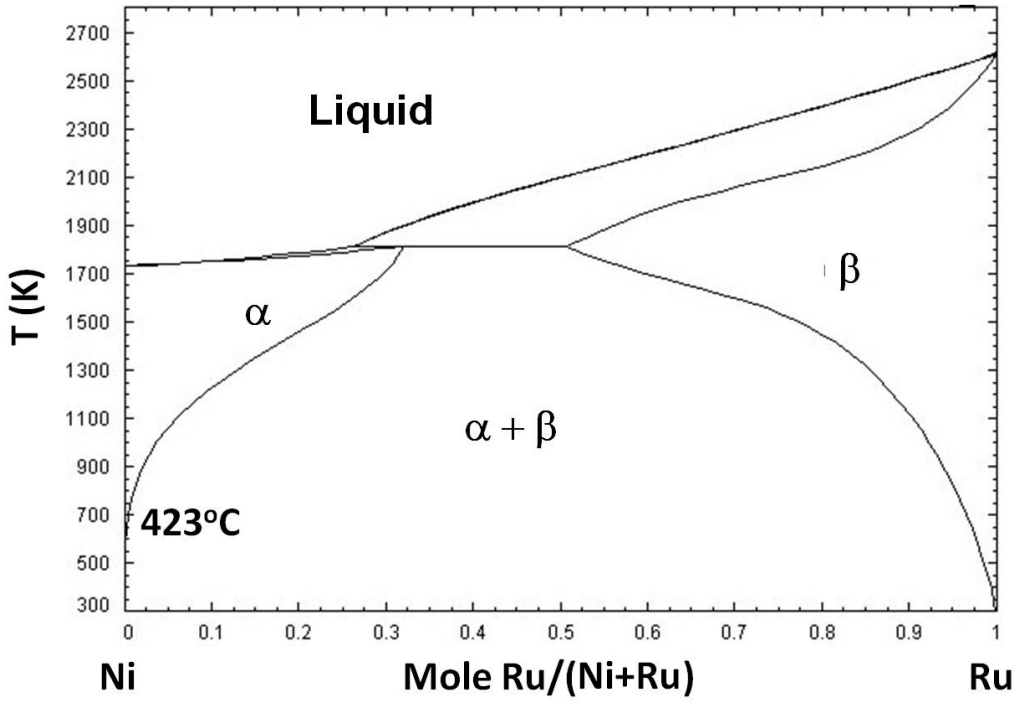

Figure 5.11. Ni-Ru phase diagram.

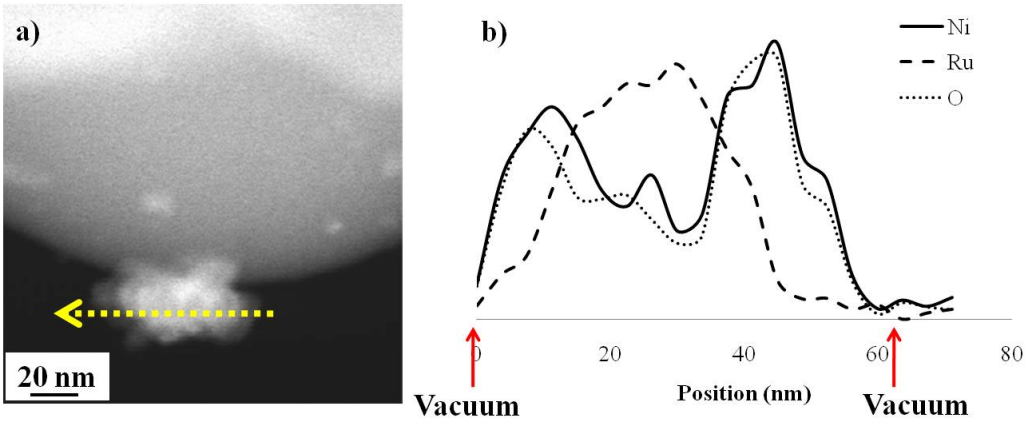

Figure 5.12. a) *In-situ* environmental STEM image and b) compositional profile obtained from EELS spectra from a 50Ni50Ru/SiO_2 in the presence of 0.3 Torr of mixture of CH_4 and O_2 in 2:1 ratio at 400°C.

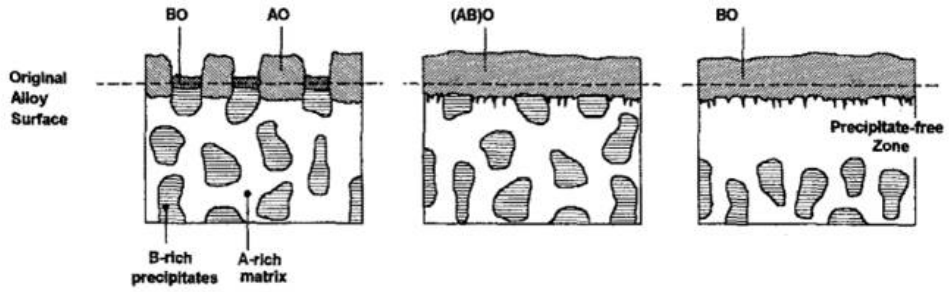

Figure 5.13. Schematic showing the various oxidation behaviors observed in two-phase alloys (a) the two metals oxidize independently to form a nonuniform scale (mechanism I) (b) the two metals oxidize cooperatively to form a uniform scale (mechanism II). (c) one metal oxidizes rapidly and protects the other metal from oxidation (mechanism III) [6].

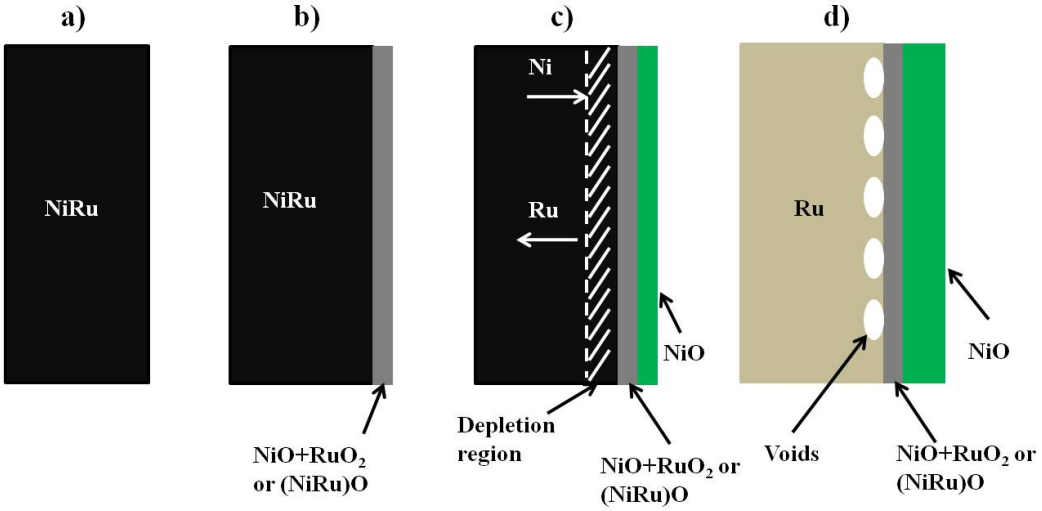

Figure 5.14. Schematic representation of possible oxidation behavior in 50Ni50Ru nanoparticles. a) showing a uniform NiRu alloy, b) initial oxidation of the ally surface forming both metal oxides, c) formation of depletion layer at the interface due to the preferential diffusion of Ni onto the surface d) after complete oxidation.

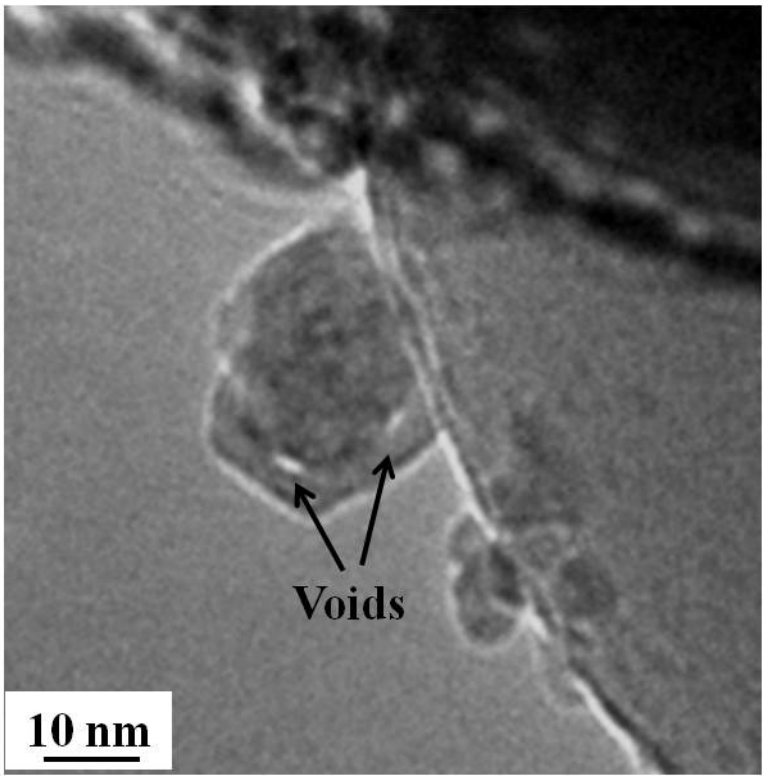

Figure 5.15. *In-situ* ETEM image of 50Ni50Ru/SiO_2 in the presence of 1 Torr of mixture of CH_4 and O_2 in 2:1 ratio at 400^{o}C, showing the formation of voids at the interface.

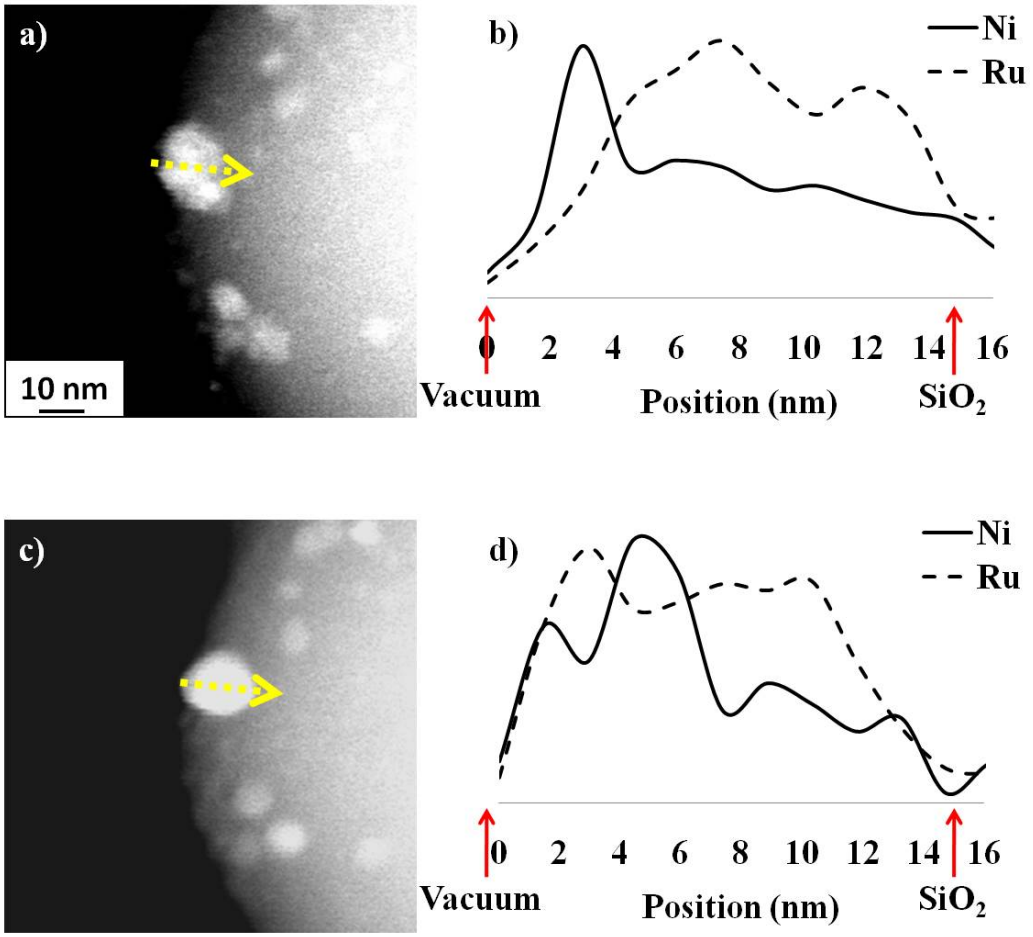

Figure 5.16. *In-situ* environmental STEM images and EELS line scans from 50Ni50Ru/SiO_2 a) in the presence of 0.3 Torr of CH_4 and O_2 in 2:1 ratio at 400^oC b) corresponding composition profile obtained from EELS c) from the same nanoparticle in the presence of 0.3 Torr of mixture of CH_4 at 600^oC d) corresponding composition profile obtained from EELS.

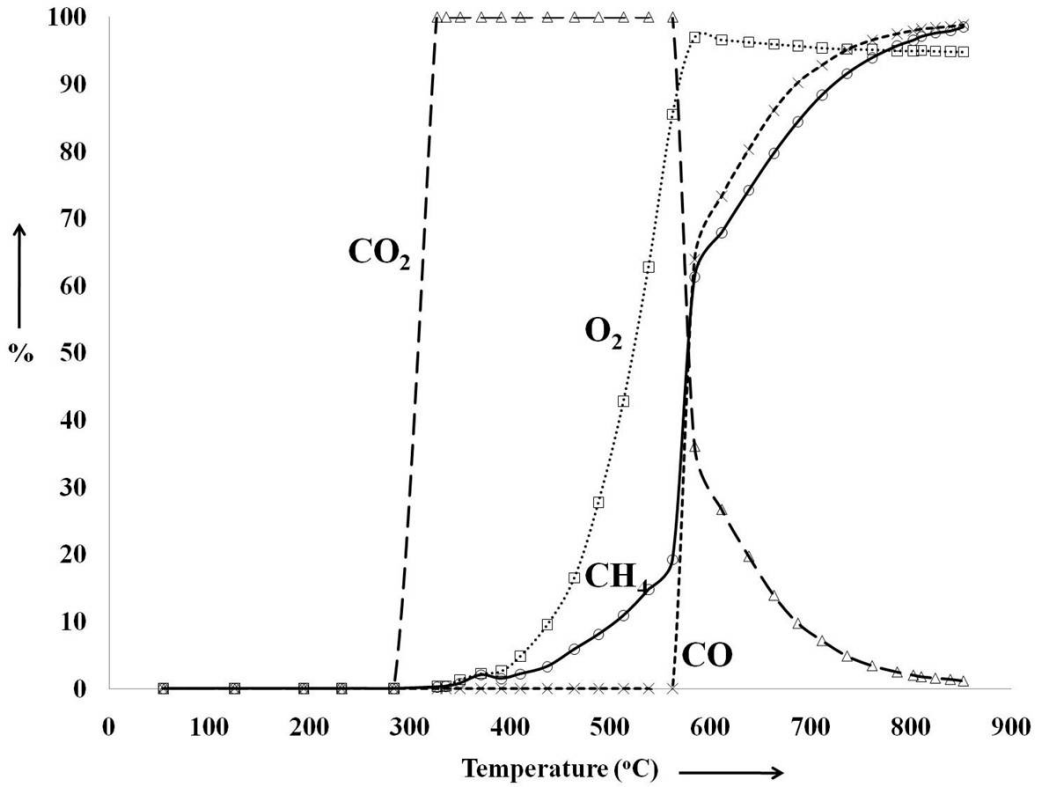

Figure 5.17. Plot showing the catalytic performance during partial oxidation of methane on 2.5 wt% 95Ni5Ru/SiO_2.

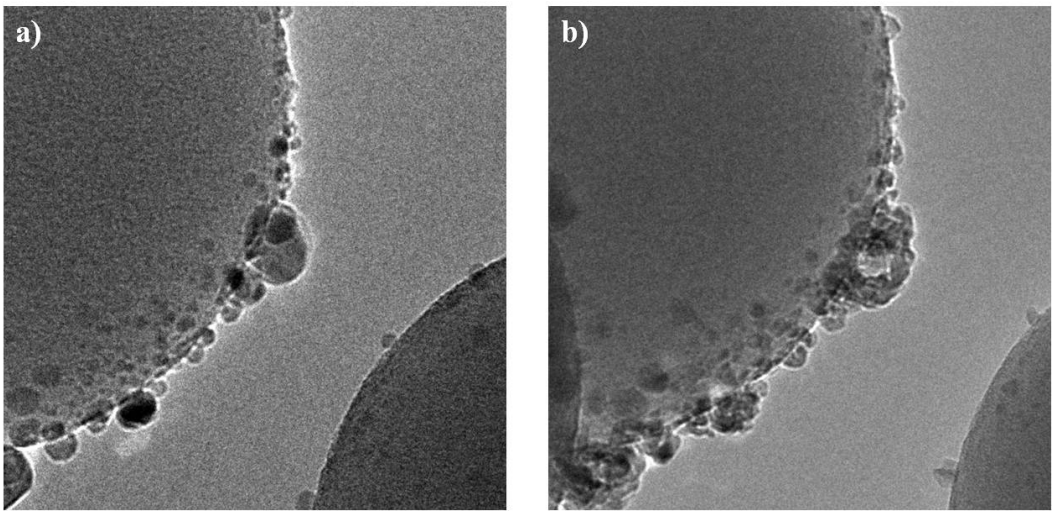

Figure 5.18. *In-situ* ETEM images of 95Ni5Ru/SiO_2: a) In presence of 1 Torr of H_2 at 400^{o}C and b) from the same region in presence of 1 Torr of mixture of CH_4 and O_2 in 2:1 ratio at 400^{o}C.

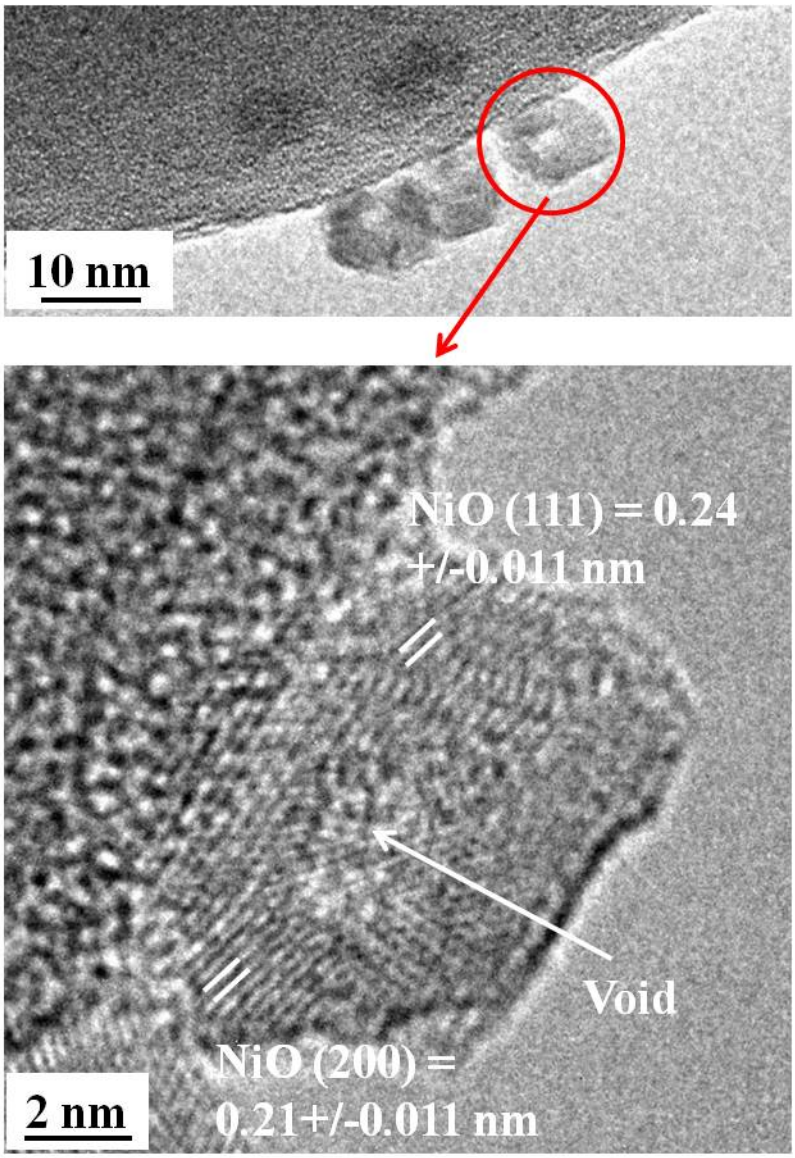

Figure 5.19. *Ex-situ* TEM image of 95Ni5Ru/SiO_2 sample after ramping to 400^{o}C in CH_4 and O_2 and then cooling to room temperature in flowing He.

Chapter 6

ELECTRON ENERGY LOSS SPECTROSCOPY OF GASES

6.1. Introduction

The goal of this chapter is to demonstrate the application of electron energy-loss spectroscopy (EELS) for determining the gas composition inside the environmental cell in a transmission electron microscope (TEM). In previous chapters, the importance of *in-situ* environmental TEM studies in understanding the structure-activity relationship in supported metal catalysts for heterogeneous catalysis application was presented. It has been shown that, the phase and structure of the catalyst can significantly vary based on the gas environment around the catalyst. The gas composition around the sample can also vary during an experiment due to the catalytic reactions that can take place on the surface of the catalysts. It is important to determine the dynamic gas composition changes near the sample region during an experiment for complete fundamental understanding of the gas-solid interactions. The composition of the gas in the environmental cell can be determined with residual gas analyzers and mass spectrometers. However, these gas analyzers are usually placed some distance away from the TEM because of space limitation and possible interference with electron optical performance. Use of EELS is a simple and efficient way to determine the gas composition directly in the environmental cell where the TEM sample is located.

Both inner-shell and valence-loss part of the EELS spectra can be used to determine the gas composition. The first part of the chapter is focused on using

inner-shell spectra for determining the gas composition. Inner-shell spectroscopy was initially performed on the reference gases, where the elemental composition is already known. This will help in identifying the potential artifacts and to develop suitable acquisition procedures. Once the technique is successfully developed for reference gases, inner-shell EELS quantification was performed on the gas mixtures. The later part of the chapter is focused on using the low-loss region of the EELS spectra for determining gas composition. One advantage of low-loss quantification is that it can be employed with gas mixtures containing hydrogen. Finally *in-situ* EELS gas analysis was used to identify and investigate the mass transport issues associated with the gas flow system. This is the first time that a detailed analysis of gas composition inside the environmental cell in a TEM is performed using EELS.

6.2. Experimental Approach

Electron energy-loss spectra from various gases were acquired on an FEI Tecnai F20 ETEM under gas pressures of about 1–3 Torr at room temperature. Energy-loss spectra were recorded with a typical energy resolution of about 1.2 eV and an acquisition time of between 0.1 and 4 s. Both inner-shell and low-loss spectra were collected from individual gases and gas mixtures. Conditions for recording the spectra for both inner-shell and low-loss are listed in table 6.1. Convergence and collection semi-angles were determined by taking the diffraction pattern from a known material at a given camera length and the details are discussed in Appendix II. Conditions A and C were chosen to get large signal intensities into

the spectrometer, and condition B was chosen to collect the inelastic signal close to the optic axis.

All gases (except lab air) were 99.999% pure and were admitted to the microscope via an external mixing tank as discussed in chapter 2. All the spectra are collected in a pressure range of 0.5 to 3 Torr. This pressure is large enough to give enough signal in the core-loss region of the spectrum and is also low enough to avoid plural scattering effects. At a few Torr of pressure, the ratio of the effective thickness of the gas column, t, to the inelastic mean free path, λ, is a measure of the importance of plural scattering (the so-called t/λ value or scattering parameter) [1]. The scattering parameters for different gases at a certain pressure were determined from the low loss spectra and are listed in table 6.2. Scattering parameter values are determined by taking the ratio of intensities under the inelastic part of the spectrum to the intensity under the zero-loss peak [2]. Since the intensity in the EELS spectrum falls rapidly with increasing energy loss, only the low loss portion of the spectrum (up to 50 eV) can be considered to calculate the inelastic intensity. EELS can be used to detect gases at pressures as low as 0.01 Torr.

6.3. Inner-shell spectroscopy

Inner-shell spectroscopy is a well established technique to determine the elemental composition in the solids [2,3]. The ratio of two elements A and B is given by:

$$N_A/N_B = I_A * \sigma_B/I_B * \sigma_A$$

where, I_A and I_B are the intensity under the peaks A and B, σ_A and σ_B are the ionization cross-sections for the elements A and B. Similar approach can be used for determining the gas composition inside the environmental cell. This equation assumes that the sample is very thin neglecting the backscattering and adsorption effects, and electrons contributing to the edge have undergone a single ionization event.

Initial quantification was done on CO and CO_2 reference gases to determine O/C concentration; the advantage of using these gases is O/C ratio is already known. Condition A in table 6.1 was used initially to collect the inner-shell spectra. Figure 6.1 shows the background subtracted inner-shell spectra from CO and at 3 Torr pressure recorder using condition A. The spectrum demonstrates the presence of large π^* peaks in front of the carbon K-edges in agreement with previously published data from Hitchcock et al. [4–6]. The background was removed from the C and O edges by fitting the form AE^{-r} (with E the energy loss and A and r constants) to 50–60 eV pre-edge fitting windows [2] before the C and O ionization edges. The background was extrapolated beyond the edges and the K-edge intensities were integrated over a 100 eV range, the large integration window averages out chemical bonding effects and maximizes the signal reference. Hartree Slater cross sections in Gatan's DigitalMicrograph software were used to convert the signal ratio to elemental ratio [7,8]. Several spectra (4 to 6) were collected with the same conditions and the average elemental composition was calculated. The resulting O/C ratio obtained for CO was 0.68+/-0.05, which is about 30% less than the actual value of 1. CO_2 was considered as another

reference gas to test the procedure; the O/C ratio should be 2 in this case. Figure 6.2 shows the inner-shell energy-loss spectra for CO_2 at 3.8 Torr pressure acquired using condition A. Similar quantification procedures to that of CO were used to calculate the O/C ratio. The O/C ratio for CO_2 was roughly twice the value obtained for CO but was still systematically low by at least 25%.

The systematic error in the elemental ratio obtained from these spectra suggests that there be may be an error with the quantification procedure or the acquisition conditions used to collect the spectra. The 1s ionization cross sections for light element are reasonably accurate [9-11] and should yield quantifications of 5% or better. Using Hydrogenic cross-sections in DigitalMicrograph did not make any difference in the result. The t/λ values for the gases are small (see table 6.2.) hence contribution from the plural scattering can be excluded.

The error may be from the acquisition procedures used for collecting the spectra for gases. To check the effect of acquisition conditions spectra were recorded from a hexagonal BN standard, where the B/N elemental ratio should be 1. Hexagonal BN sample was dispersed onto a holey C grid and energy-loss spectra were collected using the conditions A. Figure 6.3 is a typical spectrum from the BN sample and shows the classic near edge features found in this material at the B and N edges [12]**.** Similar quantification procedures to those of CO and CO_2 were employed and obtained a B/N ratio of 0.98+/-0.01, which is in good agreement with the nominal value, suggesting that EELS acquisition conditions are reasonably well defined for thin films analysis.

The convergence semi-angle, collection semi-angle and inelastic scattering angles are well defined for thin films but not for gases. Figure 6.4 schematically shows the difference in the scattering behavior between the solid and gases. The difference between these two is, for thin films signal is coming from a sample thickness of 5 nm which is at eucentric height, but for gases the signal is mostly coming from a gas path of about 5.4 mm (the distance between the objective pole pieces). The electrons that undergo similar inelastic scattering at the top and bottom of the gas cell may follow very different trajectories through the objective lens and the lower section of the TEM column. This will give rise to significant differences in the fraction of inelastically scattered electrons entering the spectrometer. To check this hypothesis, CO gas was admitted into the environmental cell by keeping the BN sample and the spectra were collected simultaneously for the BN sample and the gas. Similar quantification procedures as before gave a perfect match for B/N ratio but an error of about 30% low for O/C ratio. This confirms that there is no simple relationship between inelastic scattering angle and the convergence and collection semi-angle.

This difference in the collection efficiencies can be reduced by collecting signal scattering at low angles i.e. very near to the optic axes. This can be accomplished by using a lower convergence semi-angle and collection semi-angle. Condition B was used to collect the inner-loss spectra from CO and CO_2 and the quantification of O/C ratios of 0.94+/-0.02 and 1.95+/-0.05, respectively, which lie within 5% of the correct values for CO and CO_2. This suggests that the collection efficiency is different for different elements which can give errors in

the quantification. By going to lower convergence and collection angles the acquisition conditions are reasonably defined for the gases.

As a next step, spectra were collected from the gas mixtures and the gas composition was calculated from the spectra. Similar procedures were used to determine the gas composition from the gas mixture. First inner-shell analysis was tested on a gas samples from lab air where the O to N concentration ratio should be close to 0.268. Spectra were collected with convergence and collection semi-angles of 2.3 and 1.9 mrad, respectively (condition B). Figure 6.5 is a background subtracted spectrum from air showing prominent peaks at the front of the N K-edge at 400 eV and O K edge at 530 eV arising from transitions from the 1s state to the unoccupied π^* states. Similar quantification procedures were used as before. The results from quantification of 8 spectra gave a mean O/N ratio value of 0.25+/-0.01 which lies within 7% of the correct O/N ratio for air. No significant difference in the O/N ratio was observed in the spectra collected by using condition A and condition B. This suggests that there is not much difference in the collection efficiencies of the signal coming from O and N as they lie closer together in energy and have similar average scattering angles.

Once the procedure is well established to quantify the gas compositions inside the environmental cell in the TEM, composition analysis was performed on a gas mixture from mixing tank where they are manually premixed. Inner-shell analysis was performed on a gas mixture containing a mixture of CH_4 and O_2, mixed in 2:1 pressure ratio. Figure 6.6 shows the inner-shell spectrum from a gas mixture of CH_4 and O_2 at 2.6 Torr acquired using condition B. Similar

quantification procedures as that of air gave O/C ratio of 1.14+/-0.01 which is within 15% of the expected value of 1. Part of the discrepancy in this case may be associated with differential diffusion effects which will be discussed later in this chapter (section 6.5).

6.4. Low-loss spectroscopy

This section demonstrates the application of the low-loss part of the EELS spectrum to measure the gas compositions inside the environmental cell in a TEM. The advantage of the low-loss spectra is that H_2 can be detected, which has its first ionization at 12.5 eV. Figure 6.7 shows the valence loss spectra from different individual gas species. Molar concentrations of the gas mixture can be obtained by expressing valence loss spectra of gas mixtures as a linear combination of individual component valence loss spectra. Weighting coefficients can then be obtained from which gas compositions can be obtained. A linear fitting procedure is appropriate for gases because the intensity under the inelastic scattering spectrum is the sum of contributions from individual gases depending on the composition. There are no bonding effects between the gaseous species in the gas mixtures as in the case of solids. This procedure should be straightforward as the low-loss spectra from different gases in figure 6.7 have peak positions and shapes that are significantly different. The positions of gas peaks for different gas species are listed in table 6.3. The energy calibrations for peak positions were determined very carefully, first low-loss spectra from different gases are acquired including the zero-loss peak. Longer acquisition times cannot be used because of

the saturation of zero-loss peak; this will limit the intensity in the inelastic part of the spectra. Four of such spectra are added together to improve the signal intensity in the inelastic part. The positions for the strongest peaks were identified with respect to zero loss. The remaining peaks were identified from the spectra that were collected at longer acquisition times by excluding the zero-loss peak with respect to the calibrated peak. The collection efficiency problem associated with the inner-shell approach should be negligible for valence-loss spectroscopy because the energy losses and scattering angles are small.

To determine the relation between the valence loss spectra and the gas composition, let us consider a gas mixture composed of a homogeneous gas composition of two gases A and B. The gas in the environmental cell will have an effective thickness of t in the beam direction and a mean free path λ which depends on the pressure.

The intensity of the spectra undergoing inelastic scattering from gas A can be written as

$$J_A(E) = I_A N_A \sigma_A(E) \qquad (1)$$

where, I_A is the number of incident electrons which can be approximated to the number of electrons entering the spectrometer [13]. N_A is the number of gas molecules per unit area, which is related to partial pressure of gas ($N_A = kP_A$, k = constant). σ_A is the inelastic scattering cross section.

Similarly for gas B,

$$J_B(E) = I_B N_B \sigma_B(E) \qquad (2)$$

Now consider a homogeneous gas mixture of A and B with a fractional molar concentration of ‘a’ and ‘b’ and at a pressure of P_{AB}. Intensity of the spectra from the gas mixture will be the sum of the contributions from individual gases A and B which is given by

$$J_{AB}(E) = I_{AB}M_A\sigma_A(E) + I_{AB}M_B\sigma_B(E) \qquad (3)$$

where M_A and M_B are the number of gas molecules per unit area for gases A and B respectively, and

$$a = M_A/(M_A+M_B) \text{ and } b = M_B/(M_A+M_B) \qquad (4)$$

Considering that the inelastic scattering intensity is a linear combination of intensities from individual gas components, it can be written as

$$J_{AB}(E) = \alpha J_A(E) + \beta J_B(E) \qquad (5)$$

where ‘α’ and ‘β’ are the weighting coefficients of gases A and B to fit the signal from the gas mixture.

Substituting equations (1) (2) and (3) in (5) gives

$$I_{AB}M_A\sigma_A(E) + I_{AB}M_B\sigma_B(E) = \alpha I_A N_A\sigma_A(E) + \beta I_B N_B\sigma_B(E) \qquad (6)$$

For the above equation, the coefficients of $\sigma_A(E)$ and $\sigma_B(E)$ are equal, hence

$$I_{AB}M_A = \alpha I_A N_A \qquad (7)$$

$$I_{AB}M_B = \beta I_B N_B \qquad (8)$$

Taking the ratio of equations (7) and (8) gives,

$$M_A/M_B = \alpha I_A N_A/\beta I_B N_B \qquad (9)$$

Substituting equation (4) in equation (9) and $N_A = kP_A$ and $N_B = kP_B$, equation 9 becomes,

$$a/b = \alpha I_A P_A / \beta I_B P_B \qquad (10)$$

In the above equation, I_A and I_B are the total intensities of the spectra including zero loss peak and inelastic part. In practice, to achieve the best fit between the spectrum from the gas mixture and the pure gas components it is desirable to measure the low-loss part of the spectrum with high counting statistics. The zero loss peak is often saturated when a spectra with high counts in the inelastic part is acquired because of the weak scattering parameters of the gases. To get a spectrum with high counts it is desirable to avoid the zero loss peak so that larger times can be used to get a better signal. Hence it is convenient to develop an equation in terms of inelastic scattering intensities.

From Poisson statistics [2],

$$I_{tot}/I_o = e^{t/\lambda}$$

where I_o is the zero-loss peak intensity and I_{tot} (= I_A, I_B) is the sum of intensities from zero-loss and inelastic-part of the spectrum. Expanding the exponential to first order and putting $I_{tot} = I_o$ allows us to write

$$I_{tot} = (\lambda/t) I_{in}$$

Therefore,

$$I_A = (\lambda/t)_A I_{in}{}^A \text{ and}$$

$$I_B = (\lambda/t)_B I_{in}{}^B$$

Equation (10) can be written as

$$a/b = \alpha(\lambda/t)_B I_{in}{}^A P_A / \beta(\lambda/t)_B I_{in}{}^B P_B \qquad (11)$$

The molar concentration ratio from a gas mixture can be determined by linear coefficients by knowing the individual gas pressures and there scattering

parameters. The equation is independent of the pressure of the gas mixture in the environmental cell. The above equation can be simplified by normalizing the inelastic area under individual spectra to unity before determining the linear coefficients. Therefore the simplified equation will be

$$a/b = \alpha(\lambda/t)_B P_A/\beta(\lambda/t)_B P_B \qquad (12)$$

This equation is valid provided the scattering parameters are small and plural scattering is similar in all the spectra employed for the analysis.

In order to test this method, low-loss spectra were acquired from lab air for which O/N molar ratio should be 0.268. Figure 6.8 (solid curve) shows the typical low-loss spectra from lab air at 2.8 Torr. Reference spectra from individual gases N_2 and O_2 are acquired at 3.2 Torr and 2 Torr respectively. For quantifying the gas composition, first the energy calibration was done for the reference spectra and the spectra from the gas mixture according to their peak positions (by using the values mention in table 6.3). All the spectra were normalized to unity. The weighting coefficients α and β are obtained by fitting a composite spectrum from individual gases to the experimental air spectrum. The dotted curve in figure 6.8 shows the fitted composite spectrum from reference gases. The air spectrum and the composite spectrum are almost indistinguishable indicating that a good fit has been achieved over the range 5–50 eV. The quality of the fit between the air spectrum and the component spectrum suggests that plural scattering effects are negligible. The average O/N molar concentration ratio from several measurements combining different spectra was 0.28+/-0.01 which is

within 4% of the expected value of 0.268. The integration to determine I_{in} was performed over the range of 6.5–50 eV.

This method was also tested for a gas mixture of CH_4 and O_2 mixed in 2:1 pressure ratio in the mixing tank. Figure 6.9 shows the low-loss spectra from the mixture of CH_4 and O_2 (solid curve). The dotted curve shows the composite spectrum obtained by adding the reference spectra CH_4 and O_2; again the fit is indistinguishable from the experimental spectrum suggesting a good fit has been obtained. The molar O_2/CH_4 ratio was determined to be about 0.6+/-0.02 and a corresponding O/C ratio of 1.2. This is with 5% of the O/C elemental ratio of 1.14 determined with the K-shell approach. These quantification procedures can be employed for spectra containing more than two gases.

6.5. Gas diffusion issues

During our initial experiments inconsistencies in the gas compositions in the environmental cell were observed using the same acquisition and quantification procedures. Later it was found that the difference in gas composition observed was due to the mixing procedures employed in combining the gases in the mixing tank. From the figure 2.11 (chapter 2), the gas handling system, gas enters into the microscope from the mixing tank through a stainless tube of about 1 m in length with an internal diameter of about 10 mm. In our initial experiments, if two gases A and B have to mixed, first all the gases were pumped out from the mixing tank and fill with gas A first and later with gas B. By using this procedure it has been found that, the stainless steel pipe is first filled with gas A and acts as a diffusion

barrier for the gas B. This will create an inhomogeneous gas distribution along the stainless steel pipe and the mixing tank. The gas that enters initially into the environmental cell will be rich in gas A, with time there will be an increase in the concentration of gas B.

EELS was used to monitor the change in the gas composition in the environmental cell with time. Figure 6.10 illustrates the effect of the gas diffusion barrier in the stainless steel pipe for a gas mixture of O_2 and H_2 in 2:1 ratio. Initially the tank was filled with O_2 gas of about 500 Torr followed by adding 250 Torr of H_2. Gas was leaked into the microscope and the gas composition was monitored at different times using low-loss spectroscopy. Figure 6.10 shows the spectra collected at different times. Figure 6.10a, immediately after sending the gases into the column, figure 6.10b after 30 min and figure 6.11c after 60 min. Figure 6.10a looks similar to the low-loss spectra taken from pure oxygen. After 30 min there is a small increase in the peak at 12.5 eV which corresponds to the H_2 signal and it continues to increase with time. At about 60 min the peak remains the same implying that the equilibrium gas composition was reached. Similar observations were observed for other gas mixtures.

The gas that was added first will act as a diffusion barrier for the second gas which gives inconsistencies in the gas compositions in the environmental cell, which is essentially referred to as a “plug flow regime”. Under plug flow conditions, the gas flowing in the line can be visualized as cylindrical slices of mass moving along the line with relatively little mixing occurs between adjacent slices [14]. To get around this problem, a valve was installed in between the

mixing tank and the stainless steel tubing. This valve is closed while adding to the mixing tank, which stops the gas to flow into the stainless steel during gas mixing. The way of adding gases into the mixing tank was also modified; instead of adding full quantities of gas A followed by gas B, gases were added alternatively in small quantities to get homogeneous gas mixture in the mixing tank. The valve between the mixing tank and the stainless steel tube is opened after mixing the gases in the mixing tank. By these modifications, gas composition changes in the environmental cell were no longer observed. This apparently simple example illustrates the power of being able to measure the gas composition in the immediate vicinity of the TEM sample.

6.6. H_2 quantification

Even with the modified gas handling system, still some diffusion related issues were observed during the quantification of gas mixtures containing H_2. Figure 6.11 shows the low-loss spectra acquired from a gas mixture of CO and H_2 in 1:2 pressure ratio (solid curve). Individual gas spectra for CO and H_2 were collected at 1.8 and 2.8 Torr respectively. The dotted curve in figure 6.11 is the composite spectra obtained from the linear combination of reference spectra of CO and H_2. The composite spectrum is indistinguishable from the experimental spectrum suggesting a good fit. The CO/H_2 ratio obtained from this spectrum was about 0.9 which is much higher than the nominal molar ratio of 0.5. Several spectra were acquired from this composition with different mixing procedures, but still a large discrepancy in the calculated value with that of the expected value was observed.

To explore the error associated with H_2, several spectra were collected from a mixture of CO and H_2 with varying CO to H_2 ratio. Table 6.4 shows the nominal compositions used and the quantification results along with the systematic percentage error. In all cases, the fit between the gas mixture and the composite spectra was similar to that of figure 6.11 demonstrating that fitting artifacts and plural scattering effects were not the source of the observed discrepancy. From the table 6.4 it is clear that the systematic percentage error increases with increase in the H_2 content in the gas mixture. The error is smallest for the higher CO/H_2 ratio and increase with decrease in the CO/H_2 ratio.

The systematic discrepancy between the EELS measurement and the mixing tank composition is associated with the differential diffusion rate of H_2 relative to CO. From the kinetic theory of gases the average speeds of the H_2 and CO molecules are 1900 and 500 m/s respectively at room temperature. Hence, the diffusion rate for H_2 is faster than that of for CO. Consideration of the mass transport through the external gas handling system and ETEM is useful to interpret the EELS observations. Consider that the gas is flowing in two steps, in the first step it flows from the external gas handling system into the environmental cell and in the second step it is pumped out from the environmental cell to the external pumping system. Let's consider the first case and assume that a uniform gas composition of CO to H_2 ratio of 1 was filled in the mixing tank pressurized to 1 atmosphere. When the leak valve is opened gas enters into the environmental cell. Graham's law states that the rate of effusion of a gas is inversely proportional to the square root of its molecular weight. Hence the rate at

which H_2 entering into the environmental cell is 4 times faster than that of the CO this gives a CO rich gas at the entrance of the leak valve. As discussed earlier, now the CO rich mixture at the entrance of the leak valve will act as a diffusion barrier for the H_2 that is the stainless steel line and the mixing tank. With time there will a uniform gas composition in the gas line equivalent to the mixing tank.

Similar arguments can be made for the second case, for gas pumping from the environmental cell. The environmental cell is equipped with a differential pumping system with the differential pumping apertures size of 100 μm. With the same Graham's law argument, as the gas enters into the environmental cell, H_2 escapes faster into the pumping system than that of CO. This means that the amount of time spent for H_2 is less than that of CO, which will decrease the probability of inelastic scattering from H_2 giving lower H_2 EELS signal. This explains the large error in composition determination for H_2 gas. In the case of a higher CO/H_2 ratio, the CO acts as a diffusion barrier for the H_2 while pumping from the environmental cell which lowers the systematic percentage error observed in table 6.4.

Quantification of the O_2/H_2 ratio from figure 6.10c also showed a similar result. Even after reaching equilibrium, the O_2/H_2 ratio obtained was about 2.8 which is 40% low in H_2 to the actual value of 2. Similar evidence were observed with CH_4 and O_2 mixtures (figures 6.6 and 6.9), however the effect is smaller in this case. This may be due to the fact of this faster diffusion rate of one gas relative to the other. CH_4 is a lighter molecule than O_2. According to Graham's law, CH_4 would diffuse 40% faster than that of O_2 giving enrichment in O_2. From

the results also a higher value in O_2 was obtained suggesting that CH_4 does diffuse faster through the environmental cell.

The above observations show the importance of EELS in determining the gas composition in the environmental cell near the sample region. Use of gas analyzers or mass spectrometers, which are usually far away from the environmental cell, may not provide accurate gas compositions near the sample region.

6.7. Summary

Electron energy-loss spectroscopy was used to determine the gas composition in the environmental cell in a TEM for *in-situ* applications. The approach was developed for quantification in a differential pumping environmental TEM, however the same approach can also be used to determine gas composition in windowed cells. Techniques were developed to identify the gas composition using both inner-shell and low-loss spectroscopy of EELS. The advantage of using low-loss spectroscopy is to detect the H_2 which has first ionization at 12.5 eV. A systematic error in inner-shell quantifications was observed which are associated with the inelastic scattering of the electron along the entire gas path of 5.4 mm (gap between the two pole pieces). Convergence semi-angle, collection semi-angle and inelastic scattering angles are well-defined for thin films but not for gases. These systematic errors can be minimized by using small convergence semi-angle and collection semi-angle. The inner-shell approach requires only

knowledge of the ionization cross sections and provided compositional analysis with an accuracy of better than 15% for the cases investigated here.

Molar concentrations of the gas mixture can be determined from low-loss spectra by expressing valence loss spectra of gas mixtures as a linear combination of individual component valance loss spectra. The molar fraction of the gas compositions can be obtained by knowing the gas pressures from the individual reference gases, scattering parameters and the linear coefficients of the composite spectra. The method gives results that agree with the inner-shell method and also appears to have an accuracy of better than 15%. *In-situ* EELS will give the accurate gas composition in the environmental cell and can follow real time changes in the gas composition. It helped in improving the gas handling system to get accurate gas compositions into the environmental cell. It also helped in revealing the mass transport issues and diffusion barrier effects.

References

1. Johnson, D., & Spence, J. (1974). Determination of the single-scattering probability distribution from plural-scattering data. *Journal of Physics D*, 7, 771-780.

2. Egerton, R. F. (1996). *Electron energy-loss spectroscopy in the electron microscope* (2nd Ed.). New York, NY: Plenum Press.

3. Egerton, R. F. (2009). Electron energy-loss spectroscopy in the TEM. *Reports on Progress in Physics*, 72, 016502-016526.

4. Hitchcock, A. P. (2000) Inner shell excitation spectroscopy of molecules using inelastic electron scattering. *Journal of Electron Spectroscopy & Related Phenomena*, 112(1-3), 9-29.

5. Hitchcock, A. P., & Brion, C.E. (1980). K-shell excitation spectra of CO, N_2 & O_2. *Journal of Electron Spectroscopy & Related Phenomena*, 18(1-2), 1-21.

6. Hitchcock, A., & Mancini, D.C. (1994). Bibliography & database of inner-shell excitation spectra of gas phase atoms & molecules. *Journal of Electron Spectroscopy & Related Phenomena*, 67(1), 1-132.

7. Leapman, R. D., Rez, P., & Meyers, D.F. (1980). K, L & M shell generalized oscillator strengths & ionization cross sections for fast electron collisions. *Journal of Chemical Physics*, 72, 11-29.

8. Ahn, C. C., & Rez, P. (1985) Inner shell edge profiles in electron energy loss spectroscopy. *Ultramicroscopy*, 17, 105.

9. Crozier, P.A. (1990). Measurement of inelastic electron scattering cross sections by electron energy-loss spectroscopy. *Philosophical Magazine B-Physics of Condensed Matter Statistical Mechanics Electronic Optical & Magnetic Properties*, 61(3), 311-336.

10. Hofer, F., & Golob, P. (1988). Quantification of electron energy-loss spectra with K-shell & L-shell ionization cross sections *Micron & Microscopica Acta*, 19(2), 73-86.

11. Hofer, F. (1991). Determination of inner-shell cross section for EELS quantification. *Microscopy Microanalysis Microstructures*, 2(2-3), 215-230.

12. Leapman, R. D., Fejes, P. L., & Silcox, J. (1983). Orientation dependence of core edges from anisotropic materials determined by inelastic scattering of fast electrons *Physical Review B*, 28(5), 2361-2373.

13. Egerton, R. F. (1978). Formulae for light element microanalysis by electron energy-loss spectroscopy. *Ultramicroscopy*, 3, 243-251

14. Fogler, H.S., (2002). Elements of chemical reaction engineering (3rd ed.). Upper Saddle River, NJ, USA: Prentice Hall PTR.

Table 6.1. List of conditions used of EELS spectra acquisitions

Condition	TEM Mode	Dispersion (eV)	Convergence semi-angle (mrad)	Collection semi-angle (mrad)
A	Diffraction	0.5	1	8
B	Diffraction	0.5	2.3	1.9
C	EFTEM-Image	0.05	1	50

Table 6.2. Scattering parameter (t/λ) values for different gases at a given pressure

Gas	**Pressure (Torr)**	**Scattering Parameter (t/λ)**
N_2	2.1	0.115 +/- 0.003
O_2	2	0.092 +/- 0.003
CH_4	2	0.082 +/- 0.002
CO_2	2.2	0.192 +/- 0.004
CO	4	0.184 +/- 0.007
H_2	3.8	0.049 +/- 0.001
H_2O	2.4	0.078 +/- 0.002

Table 6.3. Low-loss peak positions for different gas species

Gas	**Peak 1**	**Peak 2**	**Peak 3**	**Peak 4**	**Peak 5**	**Peak 6**
H_2	12.5					
N_2	12.8	15.8				
O_2	18.45	13	15.35	17.05	19.75	21.8
CO	8.4	11.4	13.4	16.95		
CO_2	11.2	13.25	16.05			
CH_4	9.7	12.90				
H_2O	7.25	9.8	10.9	13.2	16.8	

Table 6.4. Nominal and measured CO/H_2 molar concentrations in a variety of different CO/H_2 mixtures

Gas Mixture	**Nominal CO/H_2 ratio**	**Measured CO/H_2 ratio**	**Percentage systematic error**
$2CO + 8H_2$	0.25	0.51+/-0.05	100
$CO + 2H_2$	0.5	0.82+/-0.05	64
$CO + H_2$	1	1.52+/-0.07	52
$2CO + H_2$	2	2.4+/-0.1	19
$8CO + 2H_2$	4	3.6+/-0.2	-10

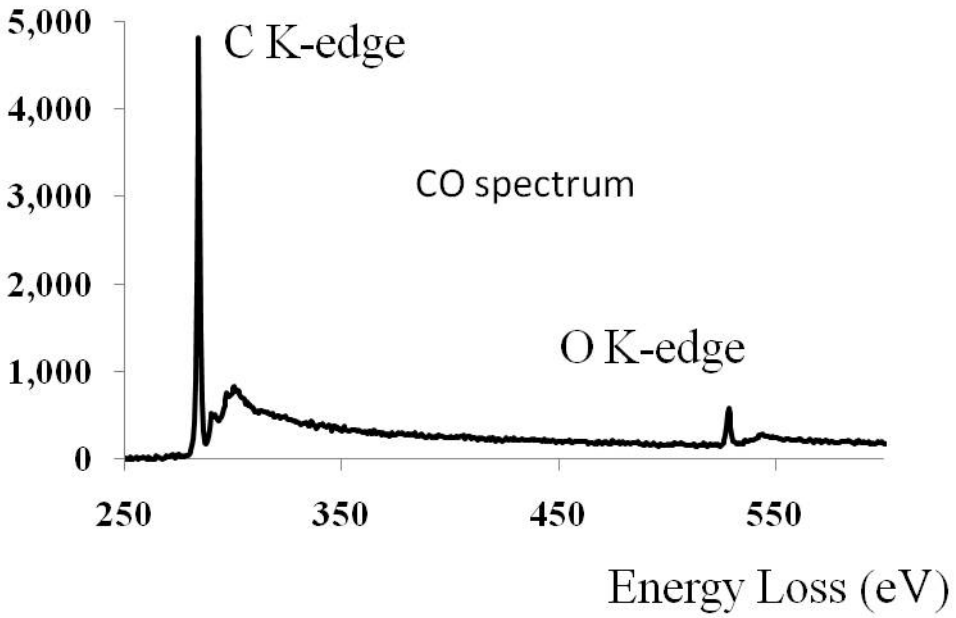

Figure 6.1. Energy loss spectrum from CO at 3 Torr pressure showing K-edges from C and O (condition A). The background before the carbon edge has been extrapolated and removed from each spectrum for clarity.

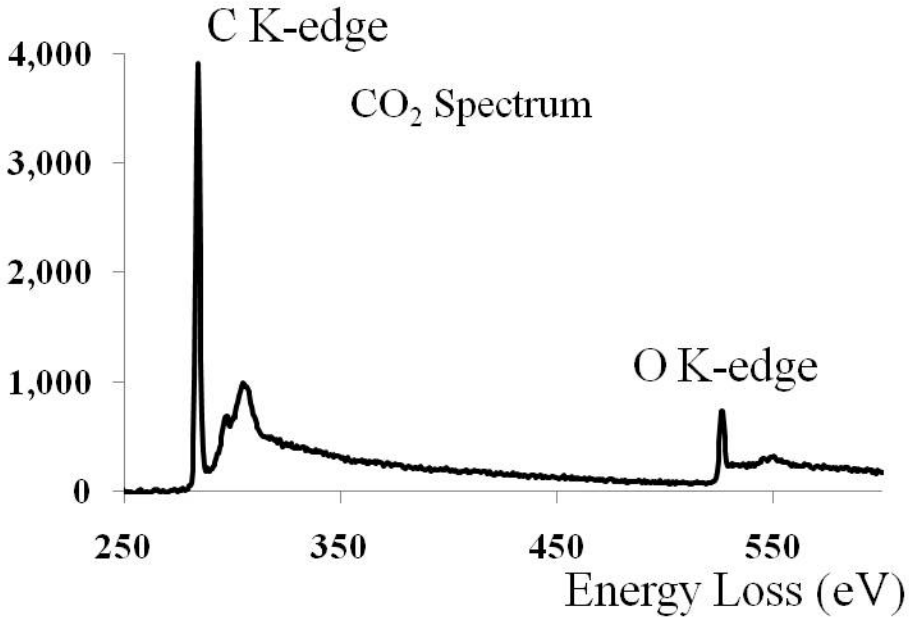

Figure 6.2. Energy loss spectrum CO_2 at 3.8 Torr pressure showing K-edges from C and O (condition A). The background before the carbon edge has been extrapolated and removed from the spectrum.

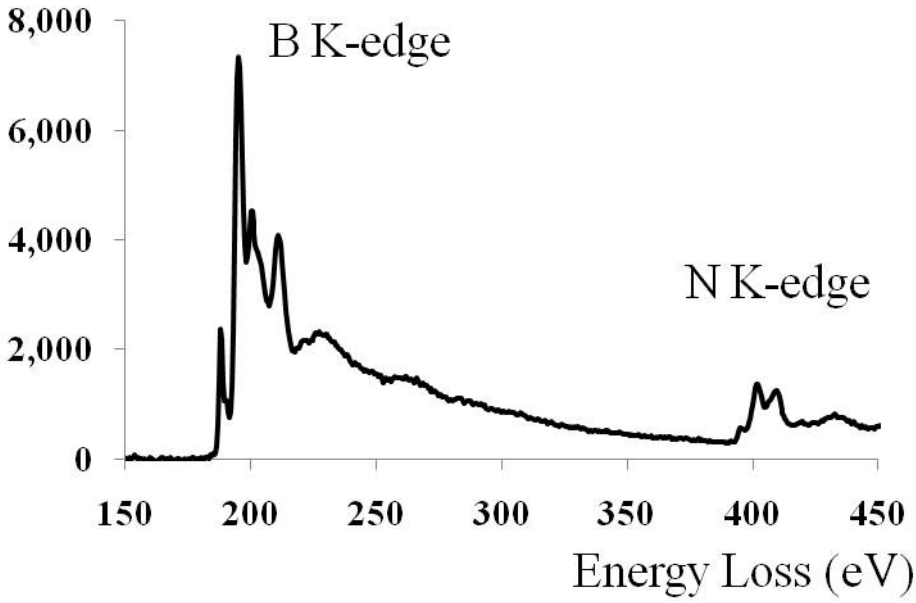

Figure 6.3. Background subtracted energy loss spectrum from BN showing K-edges from B and N (condition A). The background before the boron edge has been extrapolated and removed from the spectrum.

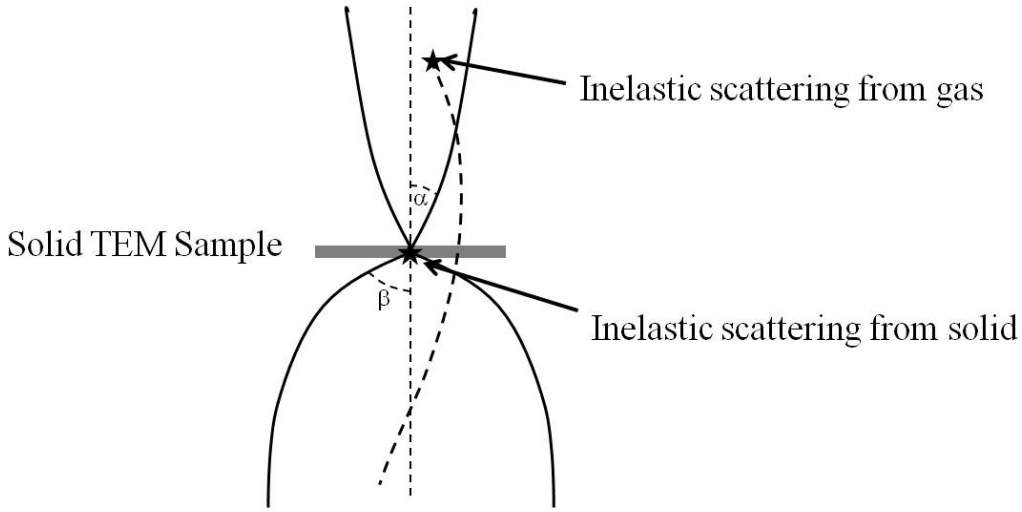

Figure 6.4. Schematic showing the differences in the inelastic scattering behavior from a solid and the gas.

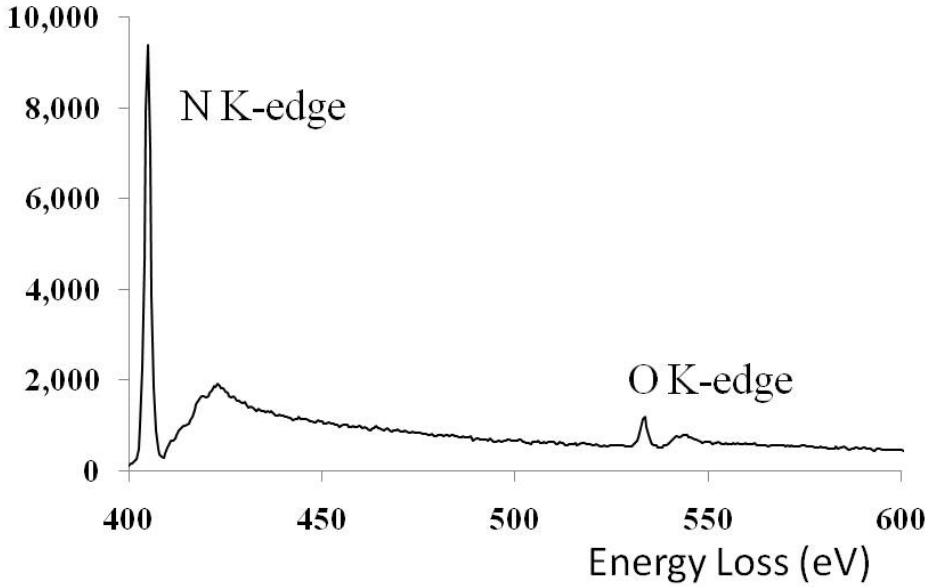

Figure 6.5. Background subtracted energy loss spectrum from 2.6 Torr of air showing K-edges from N_2 and O_2 (condition B).

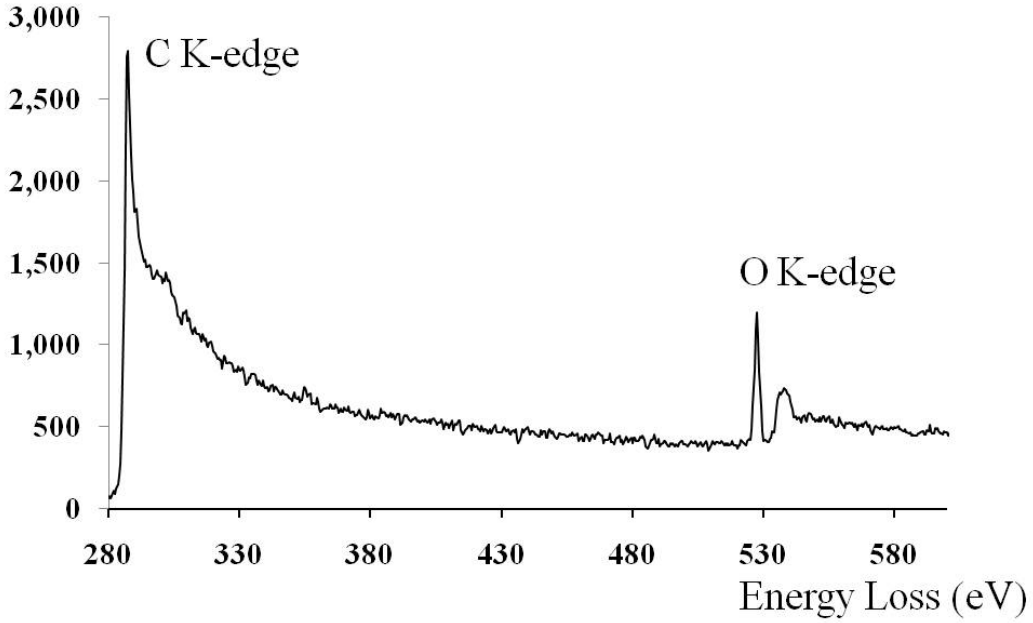

Figure 6.6. Background subtracted energy loss spectrum from 2.6 Torr of mixture of $2CH_4$ and O_2 showing C and O K-edges (condition B).

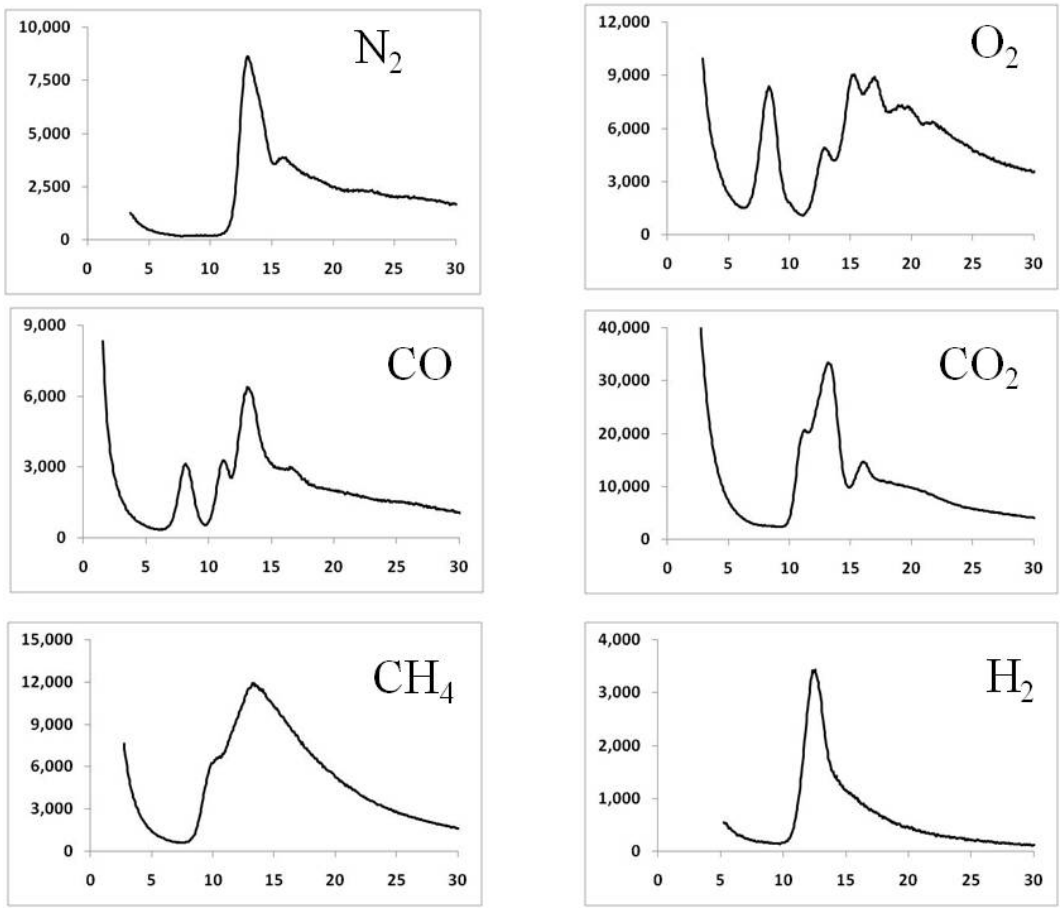

Figure 6.7. Low-loss spectra from a variety of gases recorded at a few Torr.

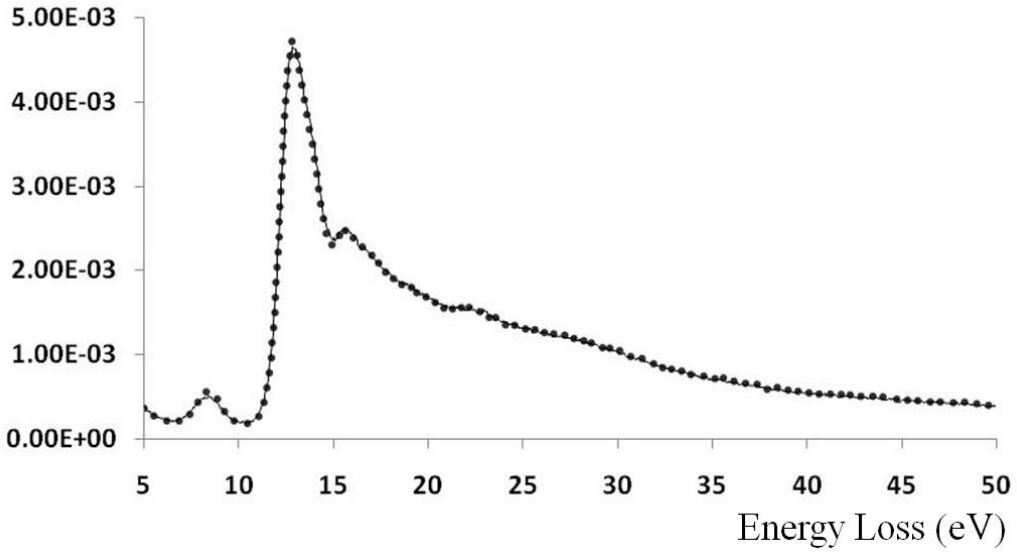

Figure 6.8. Normalized low-loss spectra from air at about 2.8 Torr pressure (solid curve). The dotted curve is the linear combination of the individual spectra from O_2 and N_2 recorded at 2 Torr and 2.1 Torr, respectively. The t/λ values for these three spectra were 0.13, 0.115 and 0.09 for air, N_2 and O_2 , respectively.

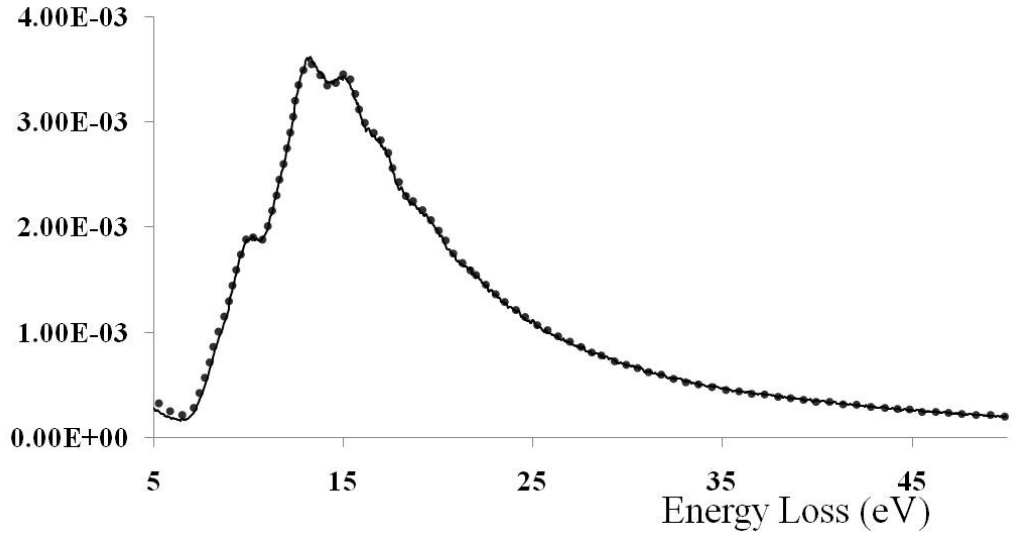

Figure 6.9. Normalized low-loss spectra from mixture of $2CH_4 + O_2$ at about 2.6 Torr pressure (solid curve). The dotted curve is the linear combination of the individual spectra from CH_4 and O_2 both recorded at 2 Torr. The t/λ values for these three spectra were 0.11, 0.08, 0.09 for ($2CH_4 + O_2$), CH_4 and O_2 , respectively.

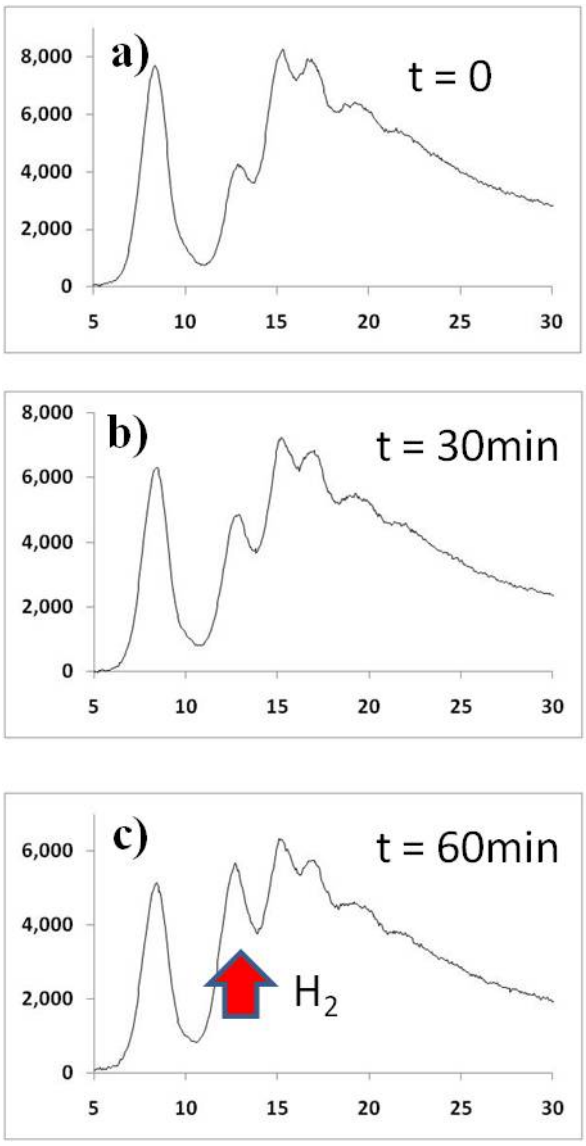

Figure 6.10. Evolution of energy loss spectrum in reaction cell with time after charging the mixing tank with $2O_2 + H_2$, adding O_2 to the mixing tank first. (a) Immediately after changing gas mixture, (b) after 30 m and (c) after 1 h (cell pressure = 2.5 Torr).

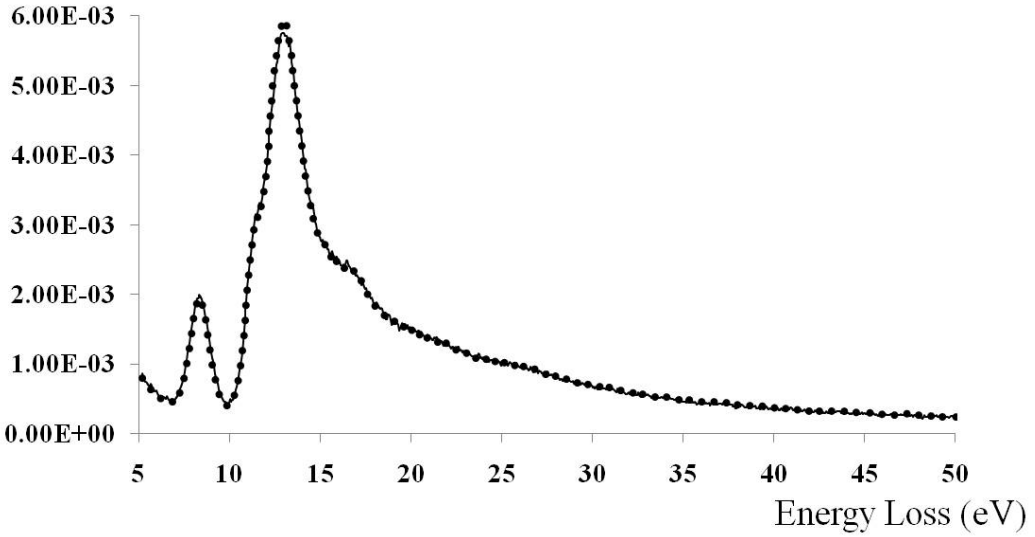

Figure 6.11. Normalized low-loss spectra from a nominal mixture of $2H_2$ +CO at about 2.9 Torr pressure (solid curve). The dotted curve is the linear combination of the individual spectra from H_2 and CO recorded at 3.8 and 1.8 Torr, respectively. The t/λ values for these three spectra were 0.06, 0.05, 0.08 for ($2H_4$ +CO), H_2 and CO, respectively.

Chapter 7

OPERANDO TEM - DETECTION OF GAS PHASE CATALYSIS IN AN ENVIRONMENTAL TEM WITH EELS

7.1. Introduction

The surface structure of catalyst depends on several factors, such as temperature, pressure, reactant gases, product gases, and concentration of different gas species on the surface of the catalyst. Thus, in order to obtain information on the active state of a catalyst, it is important to apply techniques that allow a study of catalyst structure while catalytic reactions are taking place i.e. under the working conditions of the catalyst. Chapters 3, 4 and 5 have shown the significance of *in-situ* environmental transmission electron microscopy (ETEM) studies in developing the structure-activity relationship in supported metal catalysts for heterogeneous catalysis application. However in this case, the catalytic measurements were performed in an *ex-situ* reactor and the nanostructural information is obtained from *in-situ* ETEM studies. For determining the direct structure-activity relationship, a measure of the catalyst performance should preferably be obtained simultaneously with the structural information. An "*Operando* TEM" technique was developed for the first time that combines the nanostructural characterization of the catalyst material during the reaction with the simultaneously measurement of the catalyst performance.

In Latin, *operando* means "working" or "operating", since structural studies are performed simultaneously with the catalytic measurements the technique was called as "*Operando* TEM". The composition of the gas in the

environmental cell of the TEM can be determined with residual gas analyzers and mass spectrometers; however this will require an extra cost for the instrumentation. In chapter 6 it was demonstrated that electron energy-loss spectroscopy (EELS) can be used to measure gas composition around the sample in the environmental cell. In this chapter, EELS has been used to detect the product gases that are formed during the catalytic reactions. In general, most of the microscopes are equipped with EELS detectors and do not require any additional cost. It may seem trivial to measure the product gas formation in the environmental cell, but there are several challenges in approaching this technique. This thesis chapter demonstrates the considerations for developing the *operando* TEM methodology and will show the first attempts of this technique in performing catalytic activity measurements in the environmental cell in the TEM using EELS.

7.2. ISRI RIG-150 reactor vs. ETEM reactor

Figure 7.1 (a-b) shows the schematics of the *in-situ* research instruments (ISRI) RIG-150 reactor bed and the Tecnai F20 ETEM reactor. In RIG-150 reactor gas flows from the top of the reactor tube along the catalyst bed and the product gas coming out of the reactor is analyzed by the gas chromatography. The flow rate of the gases is controlled by the mass flow controllers. In ETEM reactor, gas mixtures for the reaction are premixed in mixing tank and were introduced into the environmental cell through the leak valve. Gas that has been admitted into the environmental cell diffuses through the differential pumping apertures and was

pumped by molecular pumps [1]. The gas composition in the environmental cell is detected by EELS. In RIG-150 reactor, most of the gas molecules will be in contact with the catalyst surface before exiting the bed, whereas in ETEM it is not the case. The gas that is admitted into the environmental cell can escape through the differential pumping apertures before interacting with the catalyst surface.

The RIG-150 reactor works at 1 atmosphere with reactant gas partial pressures typically ranging from 50 to 200 Torr and the rest is He carrier gas. The ETEM reactor experiments are typically performed at reactant gas pressures of about 1 Torr and no carrier gas is used. In the RIG-150 reactor almost all the length of the reactor tube is heated. The gas that is coming from the top of the reactor tube will be at the reaction temperature by the time it contacts with the catalyst surface. A small volume of the furnace, attached to the holder, is heated in the ETEM reactor. The gas admitted into the environmental cell is at room temperature and will reach the reaction temperature only when it is in contact with the sample.

One of the challenges in developing an *operando* TEM technique is associated with the TEM sample preparation. In RIG-150 reactor, the amount of catalyst used will be in milligrams, which gives reasonable amounts of product gases that can be detectable by gas chromatography. Whereas the amount of sample present on a TEM sample is typically less than a microgram, this may give some product gases but they cannot be detected by EELS. The challenge here is to prepare a TEM sample with a large amount of catalyst sample, so that high

catalytic conversions can take place giving significant amount of product gases that can be detectable by EELS.

7.3. CO oxidation on Pt mesh

To solve the issues related to TEM sample preparation to get high catalytic loadings, initial proof of concept experiments were performed on a Pt mesh. CO oxidation (given by equation 1) on Pt mesh was chosen as a test reaction for performing *operando* TEM experiments. Pt is one of the active catalysts for this reaction [2].

$$CO + ½O_2 \rightarrow CO_2 \qquad (1)$$

CO oxidation is an easy reaction in terms of detecting the gas phase catalysis by using EELS. Figure 7.2a and 7.2b, shows the background subtracted inner-shell spectra from pure CO and pure CO_2 respectively at 1 Torr pressure showing the presence of large π^* peaks in front of the carbon K-edges [3-5]. All the inner shell energy-loss spectra were recorded with the microscope in diffraction mode with an energy dispersion of 0.1 eV.

The π^* peak positions are calibrated with the C K-edge from an amorphous carbon film (284 eV). The C π^* peaks are at 286.4 eV for CO and 289.7 eV for CO_2. The difference of 3.3 eV between the two C π^* peaks is useful for differentiating CO_2 from CO using EELS in an *in-situ* ETEM. During CO oxidation, if there is any formation of CO_2, a peak will be seen at 289.7 eV corresponding to C π^* peak from CO_2. Energy-loss spectra were acquired from a mixture of CO and CO_2 in 1:1 ratio and the background subtracted spectra is

shown in figure 7.2c. From the figure it is clearly seen that the C π* peaks of CO and CO_2 are very sharp and easily resolved.

The CO oxidation reaction was initially performed on a Pt mesh (a typical TEM grid of 3mm diameter) in an RIG-150 reactor to test its activity. Pt mesh was initially reduced at 400^{o}C in the presence of 5%H_2/Ar for 3 hours. CO oxidation reaction was performed by flowing He:CO:O_2 in 50:8:4 ratio. Figure 7.3 shows the catalytic performance on Pt mesh for CO oxidation reaction. CO conversions to CO_2 start to take place at about 200^{o}C. CO conversion reaches about 7% at 305^{o}C, above 305^{o}C CO conversion increases rapidly with increase in the temperature with almost all the CO converted to CO_2 by 465^{o}C.

For performing *operando* TEM experiments, Pt mesh was loaded onto a heating holder and the gas mixture containing CO and O_2 (in 2:1 ratio) was admitted to the environmental cell of the TEM while gradually increasing the temperature. Figure 7.4, shows the background subtracted energy-loss spectra of C π* peaks obtained while heating the Pt mesh inside the environmental cell in the presence of CO and O_2 (2:1) mixture at 1 Torr pressure. No catalytic conversion of CO was observed below 400^{o}C. A small peak started to appear at 289.7 eV at 400^{o}C corresponding to C π* peak from CO_2, indicating the formation of CO_2 by the CO oxidation reaction. This observation confirms that catalysis has been detected inside the TEM. The π* peak at 289.7 eV gradually increases with increasing temperature. In order to exclude a possible catalytic effect from the inconel furnace, similar experiments were performed on the holder without the presence of Pt mesh. Figure 7.5 shows the background subtracted

energy-loss spectrum of C K-edge from CO and O_2 (2:1) mixture at 500^oC performed on inconel holder. The absence of C π^* peak at 289.7 eV suggests that no CO_2 has formed even at 500^oC on the inconel furnace indicating that the product gas measured is due to the catalytic activity of Pt for CO oxidation to CO_2.

Quantification of the catalytic conversions was performed by fitting the energy loss spectra as a linear combination of individual component reference spectra from CO and CO_2. All the spectra are normalized to unity before performing the fitting. Weighting coefficients were determined by fitting the composite spectrum with the experimental spectrum from which catalytic conversions can be obtained. Initially an EELS spectrum was collected from a known mixture of CO and CO_2 and the ratio of fitting coefficients were obtained by performing fitting with the composite spectrum of CO and CO_2. Figure 7.6, shows the normalized reference spectrum from a mixture of CO and CO_2 in 1:1 ratio (solid curve). The dotted curve shows the fitted composite spectra from the linear combination of CO and CO_2 reference spectra. The spectra from the gas mixture and the composite spectra are almost indistinguishable indicating that a good fit has been achieved. The ratio of linear coefficients for CO_2 to CO from the curve fitting was obtained to be about 0.95. Since a 1:1 ratio of CO to CO_2 was used, this ratio corresponds to a CO conversion of 50%. This ratio is taken as a calibration for calculating the CO conversion on Pt mesh in an *in-situ* ETEM.

Figure 7.7 shows the corresponding plot of CO conversion during catalysis at different temperatures, obtained from quantification procedures as

described above. This demonstrates that EELS can be used to detect and measure the gas phase catalysis inside the environmental TEM. The difference in the catalytic CO conversions obtained from the RIG-150 reactor and the ETEM reactor are due to the difference in the design of these reactors as discussed in section 7.2. In the RIG-150 reactor, the reactant gases are forced to go through the catalyst bed and almost all the reactant gas is in contact with the catalyst during the reaction. In the ETEM reactor, not all the reactant gases will be in contact with the catalyst surface, hence conversion values are lower in this case compared to RIG-150 reactor. To perform similar experiments on a metal supported catalyst, TEM sample preparation techniques were developed for getting high catalyst loadings which is discussed in the next section.

7.4. TEM sample preparation for *operando* TEM

A 2.5 wt% Ru/SiO_2 sample was used a catalyst. The catalyst sample was prepared using the impregnation techniques in the same way as described in chapter 5. Two different techniques were tested for getting a high catalyst loading onto a TEM sample. In the first technique (Method A), quartz wool was used as a support to hold the catalyst sample. A large quantity of catalyst sample was dispersed onto the quartz wool and a 3mm diameter sample was made out of the wool. The quartz wool with the catalyst sample on it was placed onto an inconel heating holder by placing it between the inconel washers and secured with the hexring. A small hole was made at the center of the sample with the help of tweezers; the hole allowed electrons to pass through and it left some dangling quartz fibers with

catalyst sample on them for TEM characterization. Figure 7.8 shows the low magnification TEM image of Ru/SiO_2 sticking on to the surface of the quartz fiber.

In the second technique (Method B), catalyst was dispersed onto glass wool and was heated to 600^oC in air for about 30 minutes. Glass wool was chosen over quartz wool because of its lower softening temperature. At 600^oC, the glass fibers will just start to flow and fuse at the contacts forming a network of fibers. From this a 3 mm disk was cut using a razor blade and used as a TEM sample. Both procedures were quite successful in getting high loadings of catalyst onto a TEM sample. However the sample prepared by method B was mechanically more rigid than the sample prepared by method A.

7.5. CO oxidation on Ru/SiO_2

CO oxidation was performed on a Ru/SiO_2 catalyst. Ru is an active catalysts for this reaction. There is an extensive debate in the catalysis community to understand whether metallic ruthenium or ruthenium oxide that is responsible for the activity for CO oxidation reaction [6-11]. "*Operando* TEM" is ideal to understand the surface structure under reacting gas conditions since structural changes and catalytic measurements are determined together.

Catalytic activity of Ru/SiO_2 catalyst for CO oxidation was tested initially in a RIG-150 reactor. Figure 7.9 shows the performance of the Ru/SiO_2 catalyst for the CO oxidation reaction performed in a RIG-150 reactor. CO conversion to CO_2 starts to take place 60^oC, however the amount of conversions are very low at

temperatures below 150^{o}C. Above 150^{o}C, CO conversion increases rapidly with increase in temperature with almost all the CO converted to CO_2 at 280^{o}C.

In-situ catalytic activity measurements in an environmental TEM were performed on a Ru/SiO_2 catalyst by preparing a TEM sample made of quartz wool (Method A). Ru/SiO_2 was initially reduced in 1 Torr of H_2 at 400^{o}C for 3 hours. After the reduction step, the reactant gas mixture for CO oxidation (CO and O_2 in 2:1 ratio) was admitted to the environmental cell and the pressure was maintained at 1 Torr. Inner-shell energy-loss spectra were collected at different temperatures by slowly ramping up. Figure 7.10 shows the background subtracted energy-loss spectra of C π^* peaks obtained while heating the Ru/SiO_2 catalyst inside the environmental cell in the presence of CO and O_2 (2:1) mixture at 1 Torr pressure. No catalytic conversion of CO was observed until 150^{o}C. A very small peak started to appear at 289.7 eV at 150^{o}C corresponding to C π^* peak from CO_2, this temperature is 250^{o}C less than that observed on the Pt mesh. As the temperature increases, the C π^* peak from CO_2 also increases. Figure 7.11 shows the corresponding CO conversion to CO_2 on Ru/SiO_2 during catalysis at different temperatures using a spectral quantification method identical to that described in the previous section. Catalytic conversions of about 1% can be detected with this approach.

7.6. Carbonyl contamination issues

Figure 7.12 (a-b) shows TEM images of Ru/SiO_2 catalyst at 80^{o}C and 300^{o}C respectively. A dark layer was formed around the SiO_2 sphere at 300^{o}C (figure

7.12b), these dark layers started to appear at about 200^{o}C. An energy loss spectrum from these regions showed the presence of Fe and Ni (figure 7.13). There can be several possible sources from which the contamination can occur. To determine the source of contamination, several heating experiments were performed on pure SiO_2 spheres with no metal loading.

The inconel heating holder can be a potential contamination source which contains significant amount of Fe and Ni. A Gatan holder with a furnace made of tantalum was used instead of inconel. Fe and Ni contamination was still seen within 10 minutes when the sample temperature reached 200^{o}C in the presence of CO and O_2 in 2:1 ratio. To test the effect of gas, samples were heated to 200^{o}C in pure O_2; no contamination was seen in this case. When the gas was switched to pure CO, contamination started to appear again. Fe and Ni contamination was always seen in the presence of CO. Figure 7.14 shows the TEM image of SiO_2 sphere in the presence of CO at 200^{o}C clearly showing the contamination as a dark layer around the sphere. EELS confirm that the contamination seen is of Fe and Ni.

The other source of contamination could be the stainless steel tubing used for gas handling system that connects the mixing tank and the environmental cell (chapter 2, figure 2.11). CO when contacted with stainless steel can react to form Fe and Ni carbonyls; however the concentration of carbonyls will be very low at room temperature [12]. These carbonyls can interact with the sample at 200^{o}C and decompose on the surface of the sample, decomposition temperatures for Fe and Ni carbonyls is about 180^{o}C [13, 14]. The CO gas tank was directly connected to

the environmental cell to reduce contact of CO gas with the stainless steel tubing. Fe and Ni contamination is still seen in this case, suggesting that the stainless steel may not be the source of contamination. The only other source of contamination is the CO gas cylinder itself which is made of steel. CO reacts with the cylinder forming Fe and Ni carbonyls. The presence of Fe and Ni carbonyls in the gas mixture is the source of contamination which is always seen in the presence of CO.

The contamination issues in the presence of CO gas limits the surface characterization of Ru catalyst. The catalysis that has been observed can be from Ru/SiO_2 or from the Fe and Ni contamination that has formed all over the sample. If the catalytic activity is due to the Fe and Ni contamination, CO_2 would have been detected while performing EELS measurement on the bare inconel holder. No CO_2 was detected on inconel holder even at 500^oC (figure 6.5), suggest that the gas phase catalysis detected in the environmental cell was from the Ru catalyst.

It has been observed that some of the quartz fibers fell into the TEM column and blocked the electron beam when the TEM sample was prepared by method A. This was not good for the microscope, so as an alternative TEM sample prepared by method B was used for further experiments.

7.7. CO_2 methanation on Ru/SiO_2

To avoid contamination problems associated with the use of CO, a reaction has to be chosen that does not involve CO as one of the reactant gas. CO_2 methanation

(given by equation 2) was chosen for performing *operando* TEM experiments on Ru/SiO_2 catalyst. Several catalysts were tested for this reaction [15, 16]; Ru is one of the most efficient catalysts [17, 22].

$$CO_2 + 4H_2 \rightarrow CH_4 + 2H_2O \qquad (2)$$

Before performing the *operando* TEM, the Ru/SiO_2 catalyst was tested for CO_2 methanation. Figure 7.15 shows the catalyst performance of 2.5 wt% Ru/SiO_2 for CO_2 methanation. CO_2 conversion starts to take place about 290^oC and increases gradually with increase in temperature and reaches to 47% at 430^oC. The increase in conversion with temperature was not much in the temperature range of 430^oC to 550^oC. Above 550^oC the CO_2 conversion increased slowly and reached 75% at 800^oC. CH_4 is the initial product that formed at 290^oC during CO_2 methanation; above 290^oC small quantities of CO was started to from along with the CH_4. Up to 490^oC the main product gas formed is CH_4 with small quantities of CO. Above 490^oC, CO selectivity started to increase gradually with decrease in CH_4 selectivity, and almost all the CO_2 that has been converted produced CO at 800^oC. Two different products, CH_4 and CO, can form during CO_2 methanation reaction depending on the reaction temperature. From a fundamental point of view, it is interesting to follow the evolution of catalyst surface structure under different product gas formation.

In-situ catalytic measurements were performed on Ru/SiO_2 catalyst for CO_2 methanation by preparing the sample using Method B and loading onto the Gatan heating holder. TEM sample prepared by method B has a network of glass fibers that are fused at the contacts; this will help the fibers to hold with each

other and not to fall in the TEM column. A CO_2 and H_2 gas mixture was admitted to the environmental cell of the TEM in 1:4 pressure ratio and EELS spectra were collected at different temperatures. *In-situ* ETEM experiments were performed up to a temperature of 500^oC; from the reactor data CH_4 is the main product gases that is formed up to this temperature (Figure 7.15). Inner-shell energy loss peaks positions of C K-edge from CO_2, CO and CH_4 are 289.7 eV, 286.4 eV and 287.9 eV and this difference in peak position can be used to detect and differentiate between different gas products.

Figure 7.16 shows the background subtracted C K-edge spectra in the presence of CO_2 and H_2 (in 1:4 ratio) at different temperatures. No change in the spectra was observed below 400^oC. A shoulder peak started to appear at 400^oC at about 286.4 eV corresponding to the CO formation. The shoulder peak increases with increase in temperature as shown in figure 7.16. It was surprising to see the formation of CO instead of CH_4 which was the main product gas that formed at this temperature from the *ex-situ* reactor data. The difference between the reactor experiments and the *in-situ* experiments is the pressures of the reactant gases. In the reactor, experiments were performed at 1 atmosphere by flowing He:CO_2:H_2 in 50:4:16 (partial pressure of CO_2 and H_2 in the gas feed 43 Torr and 172 Torr respectively). In the *in-situ* ETEM, experiments were performed at 1 Torr of gas pressure with partial of CO_2 and H_2 at 0.25 Torr and 0.75 Torr respectively. This pressure differences can have effect on the product gas formation.

To check the effect of pressure, thermodynamic calculations were performed for this reaction using FACTSAGE program [19]. Figure 7.17a and

7.17b shows the plots for CO_2 conversion to CH_4 and CO obtained from the FACTSAGE program for CO_2 methanation reaction at 1 atmosphere and 1 Torr respectively. From this thermodynamic data, the main product gas in the temperature range of 400^{o}C to 500^{o}C at 1 atmosphere is CH_4 which is similar to the reactor data and at 1 Torr it is CO which is consistent with the *in-situ* ETEM data. These experimental observations demonstrate the importance of *operando* TEM studies. In order to develop direct structure-activity relationships, structural characterization of the catalyst must be performed while simultaneously measuring the catalytic performance. Quantification of CO_2 conversion to CO during the catalysis can be obtained using the similar procedures used for calculating CO conversions for CO oxidation reaction in sections 7.3 and 7.4. Figure 7.18 shows the plot of CO_2 conversion to CO in the presence of 1 Torr of CO_2 and H_2 mixture (in 1:4 ratio) at different temperatures performed in an *in-situ* ETEM.

The low-loss region of the energy-loss spectrum can also be used to detect product gas formation. Figure 7.19 shows the low-loss reference spectra from individual gases CO_2, H_2, CO, CH_4 and H_2O that are relevant to CO_2 methanation reaction. The formation of CO and H_2O can be identified by the presence of peaks at 8.4 eV for CO and 7.25 eV for H_2O, as pointed in the figure 7.19. Figure 7.20 shows the low-loss spectra in the presence of CO_2 and H_2 (in 1:4 ratio) at 500^{o}C and clearly shows the presence of peak at about 8.4 eV corresponding to formation of CO. No peak was observed at 7.25 eV for H_2O. From the thermodynamic data there should be an almost equal amount of H_2O and CO

formation at 500^{o}C at 1 Torr of pressure during the CO_2 methanation. It is not clear why there is no peak at 7.25 eV corresponding to the formation of H_2O. Further studies are required to clarify this issue. Figure 7.21 shows the TEM image of Ru/SiO_2 catalyst in the presence of CO_2 and H_2 in 1:4 ratio at 500^{o}C taken in parallel while measuring the catalytic performance. High resolution microscopy studies were difficult to perform on this sample because of the instabilities caused by the dangling fibers.

7.8. Summary

"*Operando* TEM" methodology was successfully developed for heterogeneous catalysis by applying EELS to detect the product gases inside the environmental TEM. One of the challenges in developing an *operando* TEM technique is associated with the TEM sample preparation. In RIG-150 reactor, the amount of catalyst used will be in milligrams, which gives reasonable amount of product gases that can be detectable by gas chromatography. Whereas the amount of catalyst sample used for TEM studies is much less (less than micrograms) compared to the catalyst used in the RIG-150 reactor.

As a proof of concept initial experiment were performed on a Pt mesh (usual TEM sample) for CO oxidation reaction, and it has been successfully demonstrated that it is possible to detect product gases using EELS in the *in-situ* environmental TEM. To perform similar experiments on supported metal catalysts, two different techniques were developed for preparing a TEM sample with high catalyst loadings. A TEM sample was prepared from quartz/glass wool

by dispersing catalyst sample onto the wool. Product gas analysis was successfully detected by EELS for CO oxidation and CO_2 methanation reactions on Ru/SiO_2 catalyst. The amount of catalytic conversions in the ETEM reactor as a function of temperature was also calculated with the help of reference spectra from standard gas mixture. The catalytic conversions obtained in the ETEM reactor are less compared to the RIG-150 reactor due to the differences in the reactor design.

During CO oxidation, Fe and Ni contamination was observed due to the presence of metal carbonyls in the CO cylinder. The contamination issues in the presence of CO gas limits the surface characterization of Ru catalyst. For the CO_2 methanation reaction, a difference in the product gas formation was observed the ETEM reactor compared to RIG-150 reactor. CH_4 was the main product formed in the RIG-150 reactor up to 500^oC, whereas CO is the main product observed in the ETEM reactor. This difference in the product gas formation is attributed to the pressure gap that exists between the RIG-150 reactor and ETEM reactor. The CO_2 methanation reaction further emphasized the importance of "*operando* TEM" studies. In order to develop direct structure-activity relationships, structural characterization of the catalyst must be performed while simultaneously measuring the catalytic performance.

References

1. Sharma, R. (2005). An environmental transmission electron microscope for *in-situ* synthesis and characterization of nanomaterials. *Journal of Materials Research,* 20(7), 1695-1707.

2. McClure, S. M., & Goodman, D. W. (2009). New insights into catalytic CO oxidation on Pt-group metals at elevated pressures. *Chemical Physics Letters* 469 (2009) 1–13.

3. Hitchcock, A. P. (2000) Inner shell excitation spectroscopy of molecules using inelastic electron scattering. *Journal of Electron Spectroscopy & Related Phenomena,* 112(1-3), 9-29.

4. Hitchcock, A. P., & Brion, C.E. (1980). K-shell excitation spectra of CO, N2 & O2. *Journal of Electron Spectroscopy & Related Phenomena,* 18(1-2), 1-21.

5. Hitchcock, A., & Mancini, D.C. (1994). Bibliography & database of inner-shell excitation spectra of gas phase atoms & molecules. *Journal of Electron Spectroscopy & Related Phenomena,* 67(1), 1-132.

6. Wendt, S., Seitsonen, A. P., Kim, Y. D., Knapp, M., Idriss, H., & Over, H. (2002). Complex redox chemistry on the RuO_2 (110) surface: experiment and theory. *Surface Science,* 505, 137–152.

7. Goodman, D.W., Peden, C. H. F., & Chen, M.S. (2007). CO oxidation on ruthenium: The nature of the active catalytic surface. *Surface Science,* 601, L124–L126.

8. Over, H., Muhler, M., & Seitsonen, A.P. (2007). Comment on ‘‘CO oxidation on ruthenium: The nature of the active catalytic surface’’ by D.W. Goodman, C.H.F. Peden, M.S. Chen. *Surface Science,* 601, 5659–5662.

9. Goodman, D.W., Peden, C. H. F., & Chen, M.S. (2007). Reply to comment on ‘‘CO oxidation on ruthenium: The nature of the active catalytic surface’’ by H. Over, M. Muhler, A.P. Seitsonen. *Surface Science,* 601, 5663–5665.

10. Over, H., Balmes, O., & Lundgren, E. (2009). *In-situ* structure–activity correlation experiments of the ruthenium catalyzed CO oxidation reaction. *Catalysis Today*, 145, 236–242.

11. Over, H., Kim, Y. D., Seitsonen, A. P., Wendt, S., Lundgren, E., Schmid, M., Varga, P., Morgante, A & Ertl, G. (2000). Atomic-scale structure and catalytic reactivity of the RuO_2 (110) surface, *Science*, 287, 1474-1476.

12. Brynestd, J. (1976). Iron and nickel carbonyl formation in steel pipes and its prevention: Literature survey. *Metals and Ceramic Division*, Oak Ridge National Lab.

13. Hui-ping, S., Hyo-Sook, L., Yong-Jae, S., Jong-Hee, K., Ying, Li., & Chong-Oh, K. *Proceedings of 19th International Workshop of Rare Earth Permanent Magnets & their Application*, 205-208.

14. Elschenbroich, C., & Salzer, A. (1992). *Organometallics:A Concise Introduction* (2nd Ed). Weinheim: Wiley-VCH. ("Retrieved from http://en.wikipedia.org/wiki/Nickel_carbonyl").

15. Bowker, M., Cassidy, T. J., Ashcroft, A. T., & Cheetham, A. K. (1993). The Methanation of CO and CO_2 over a Rh/Al_2O_3 Catalyst Using a Pulsed-Flow Microreactor. *Journal of Catalysis*, 143, 308-313.

16. Park, J. N., & McFarland, E. W. (2009). A highly dispersed $Pd\text{-}Mg/SiO_2$ catalyst active for methanation of CO_2. *Journal of Catalysis*, 266, 92-97.

17. Sharma, S., Hu, Z., Zhang, P., McFarland, E. W., & Metiu, H. (2011). CO_2 methanation on Ru-doped ceria. *Journal of Catalysis*, 278, 297–309.

18. Mori, S., Xu, W. C., Ishidzuki, T., Ogasawara, N., Imai, J., & Kobayashi, K. (1996) *Applied Catalysis A: General*, 137, 255-268.

19. Bale, C. W., Chartrand, P., Degterov, S. A., Eriksson, G., Hack, K., Ben Mahfound, R., Melancon, J., Pelton, A. D., & Petersen, S. (2002). Factsage thermochemical software and databases. Calphad, 26(2), 189-228.

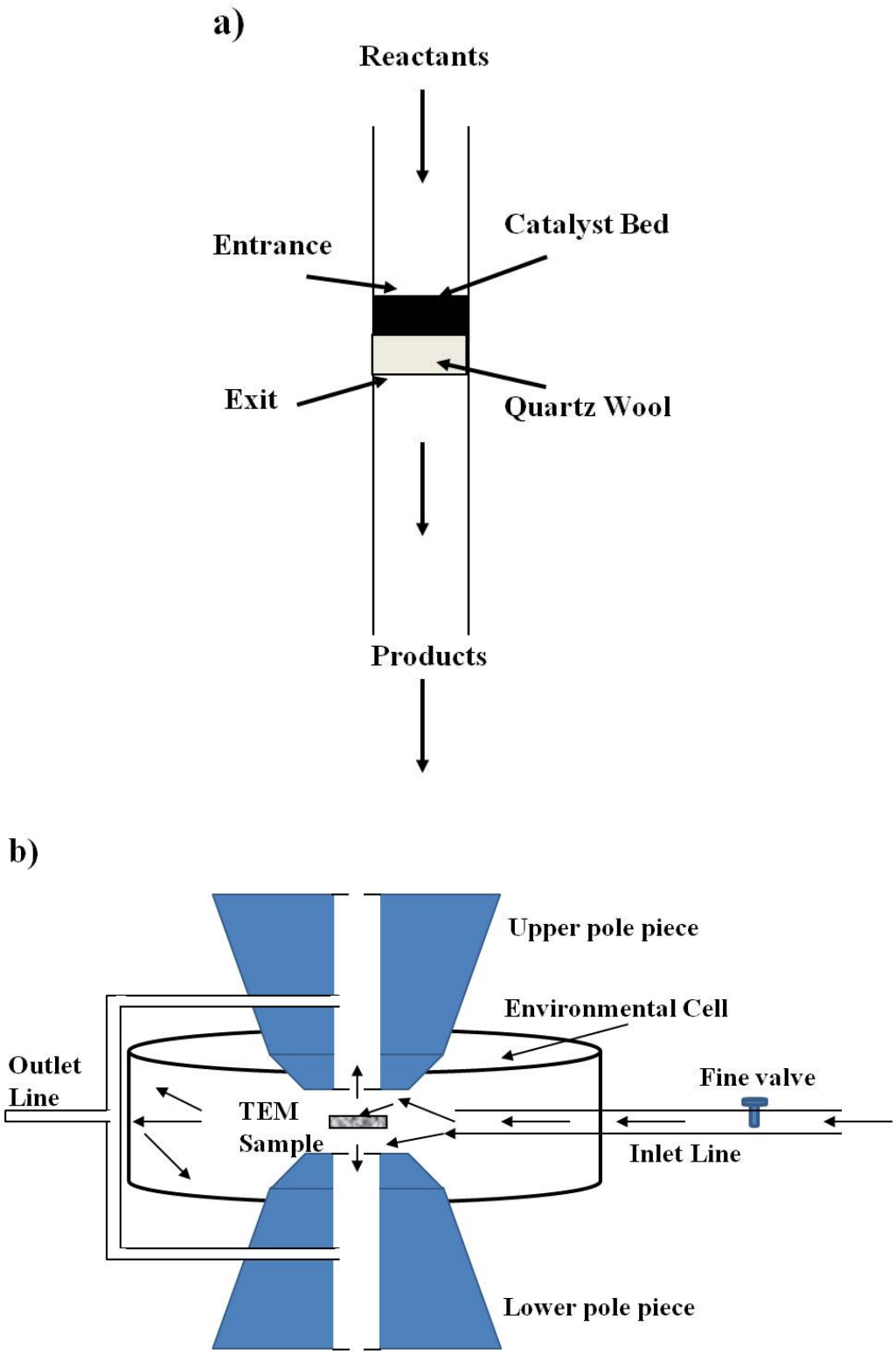

Figure 7.1. Schematic representation of the ISRI RIG-150 reactor bed and the ETEM reactor.

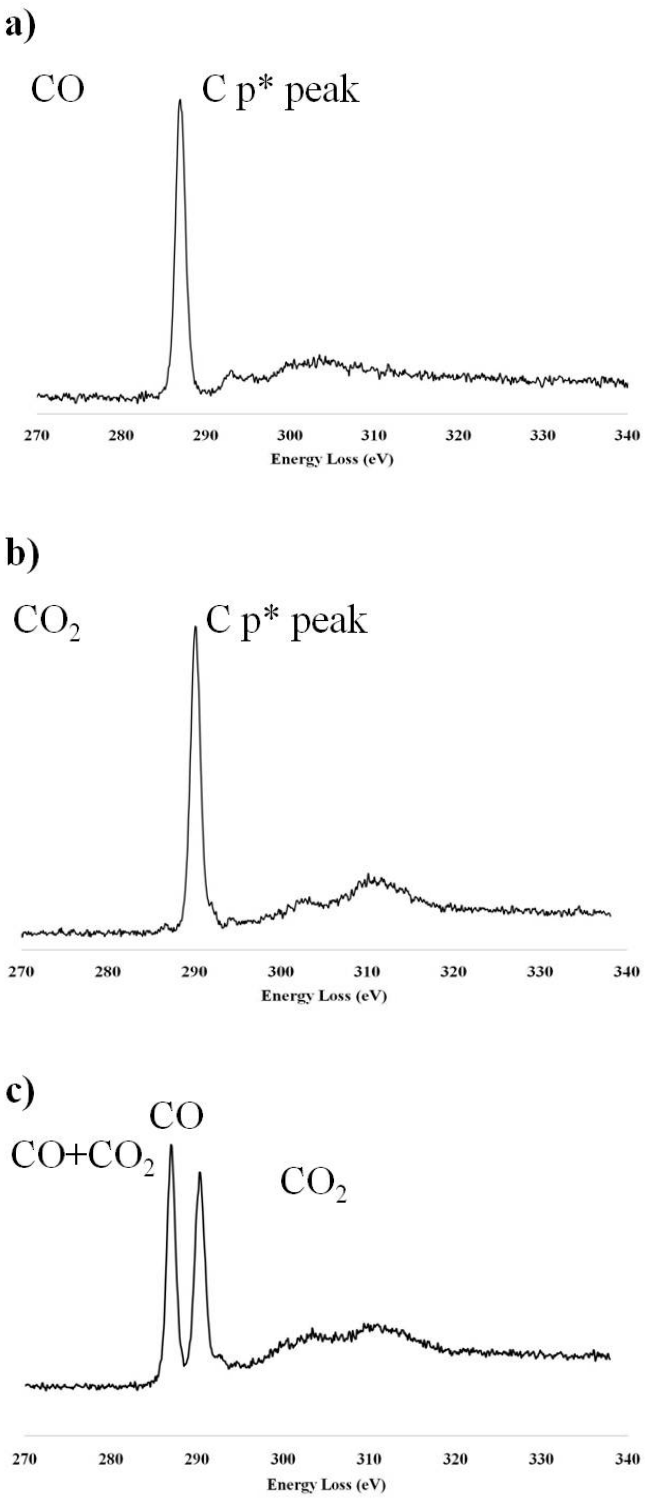

Figure 7.2. Background subtracted energy-loss spectra from a) 1 Torr of CO and b) 1 Torr of CO_2 and c) normalized EELS spectra from a mixture of CO and CO_2 in 1:1 ratio at 1 Torr pressure.

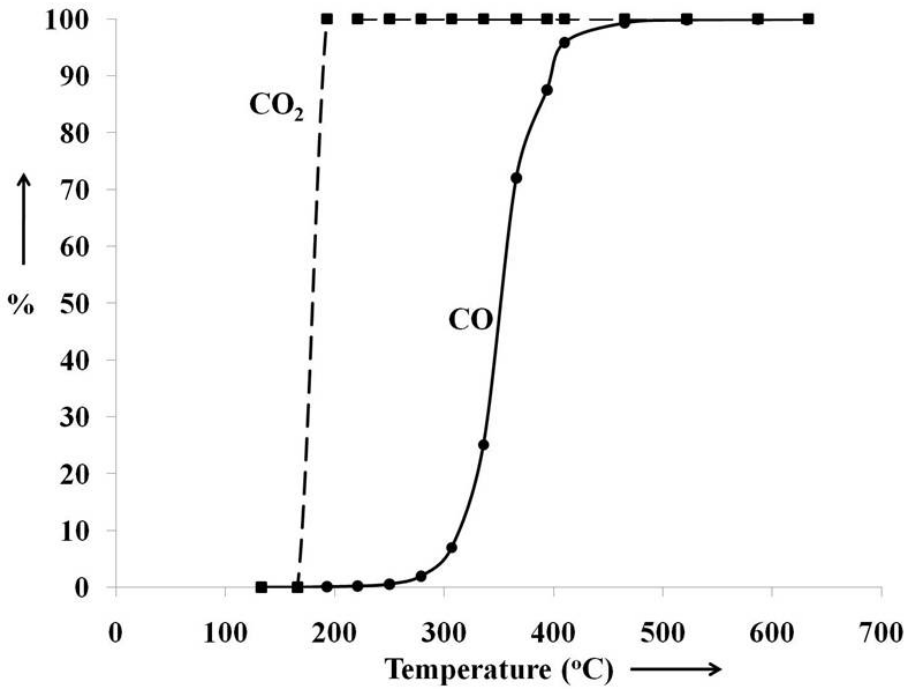

Figure 7.3. Plot showing the CO oxidation reaction on a Pt mesh performed in an RIG-150 reactor.

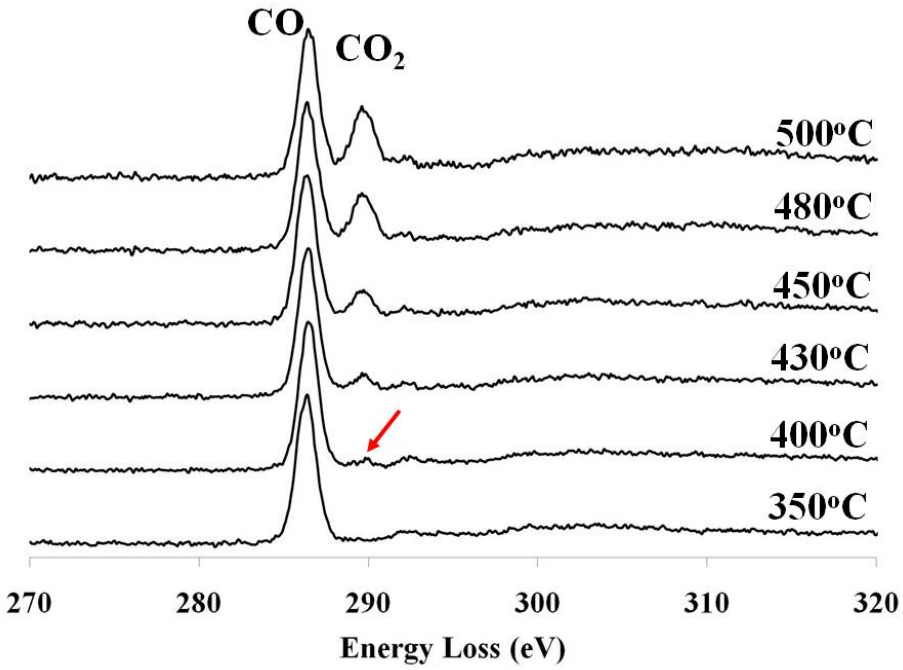

Figure 7.4. Background subtracted energy-loss spectra acquired at different temperatures during CO oxidation on Pt mesh in an ETEM reactor.

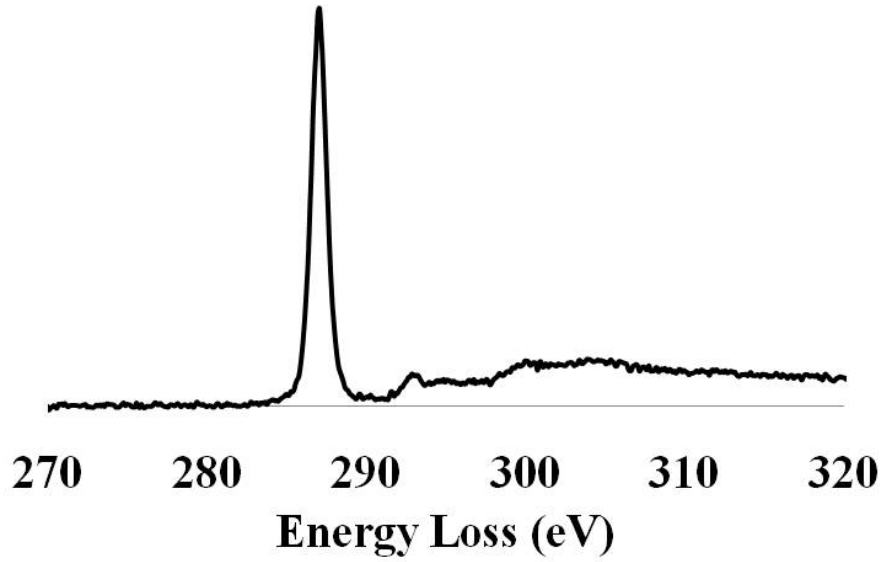

Figure 7.5. Background subtracted energy-loss spectra acquired at 500^{o}C during CO oxidation on inconel heating holder.

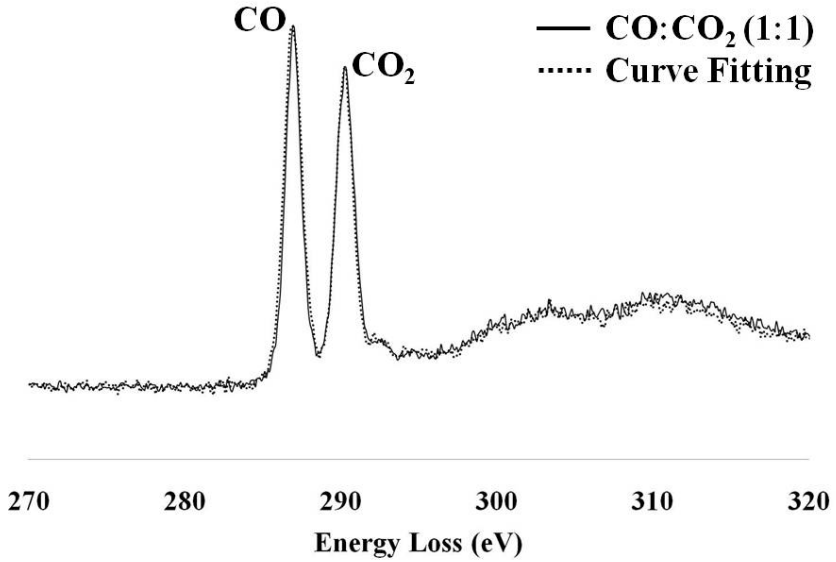

Figure 7.6. Normalized EELS spectra from a mixture of CO and CO_2 in 1:1 ratio at 1 Torr pressure (solid curve). The dotted curve is the linear combination of the individual spectra from both CO and CO_2.

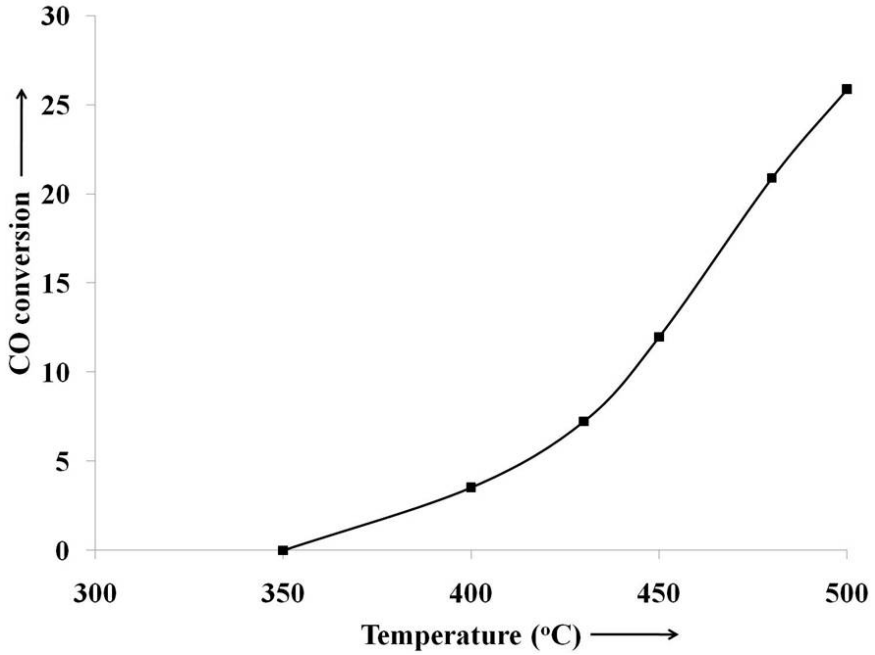

Figure 7.7. Plot showing the CO conversion with increase in temperature on Pt mesh measured from *in-situ* energy-loss spectroscopy.

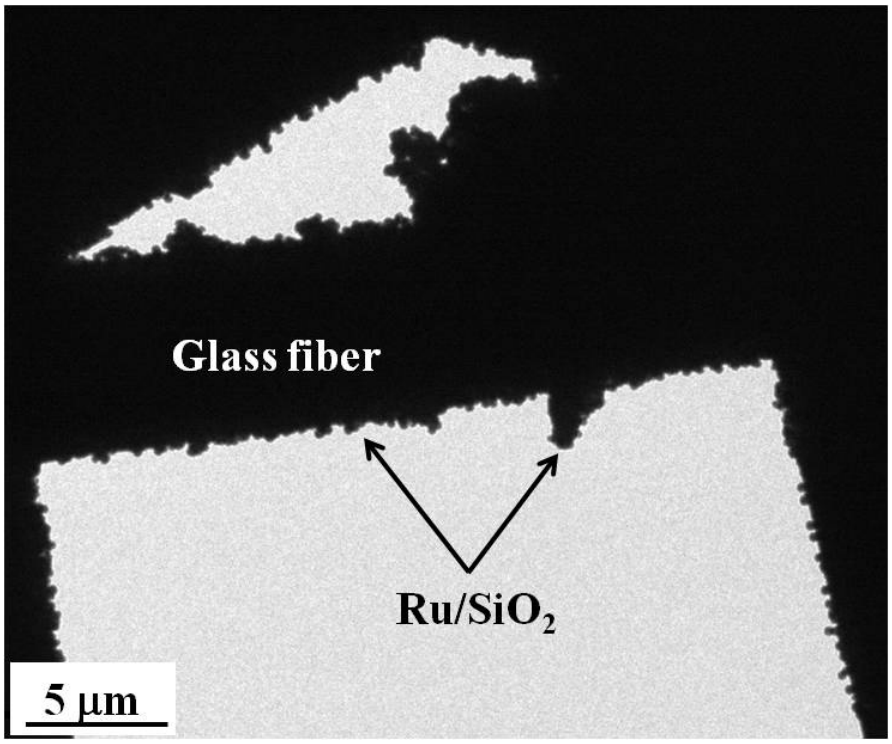

Figure 7.8. TEM image of glass fiber with Ru/SiO_2 sample loaded.

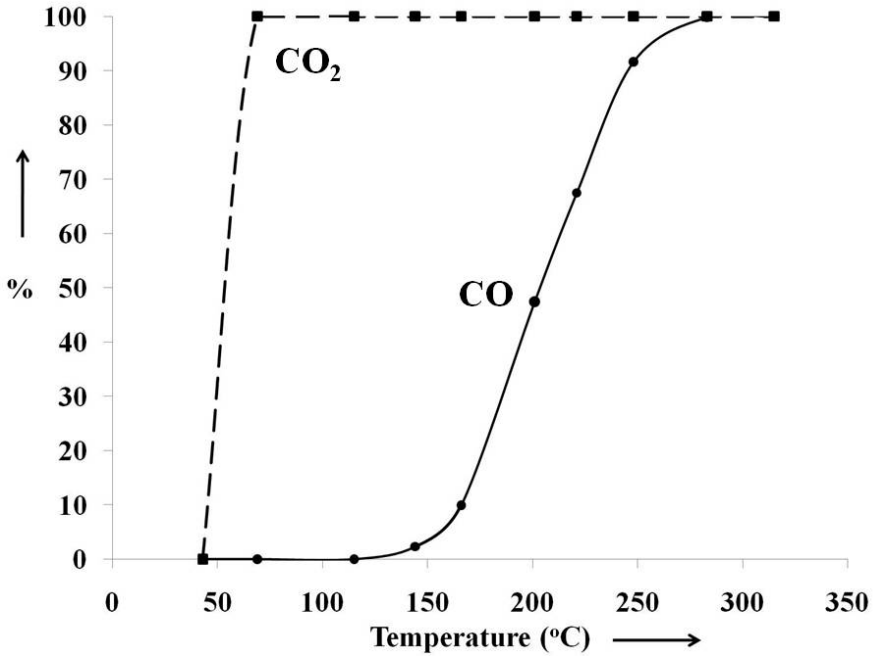

Figure 7.9. Plot showing the CO oxidation reaction on a Pt mesh performed in an RIG-150 reactor.

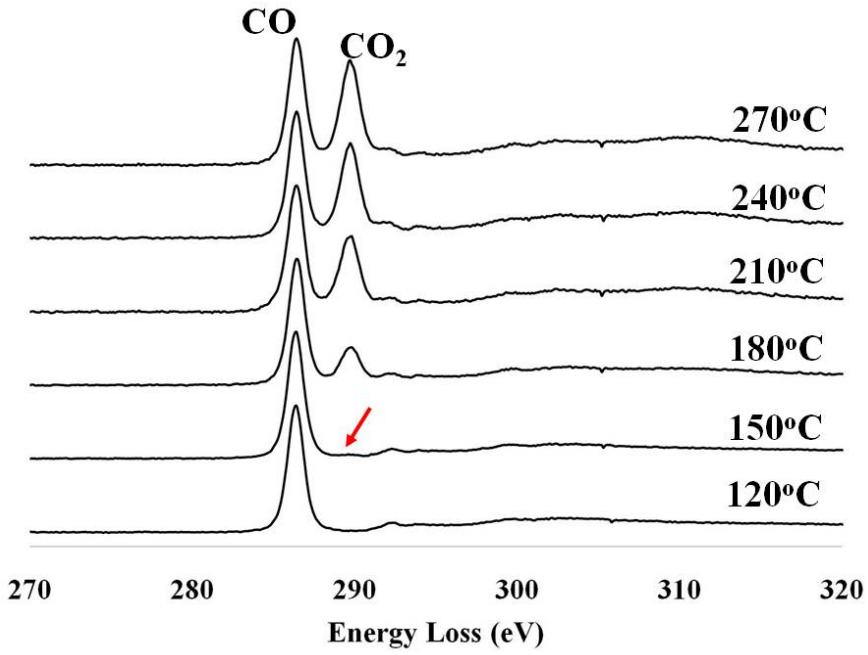

Figure 7.10. Background subtracted energy-loss spectra acquired at different temperatures during CO oxidation on Ru/SiO_2 catalyst in a ETEM reactor.

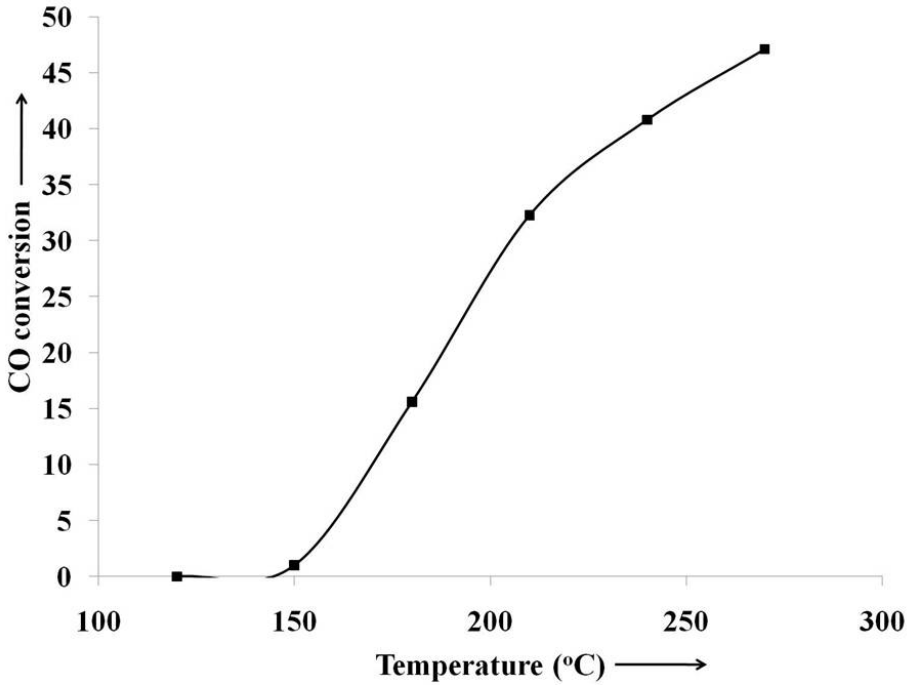

Figure 7.11. Plot showing the CO conversion with increase in temperature on Ru/SiO_2 catalyst measured from *in-situ* energy-loss spectroscopy.

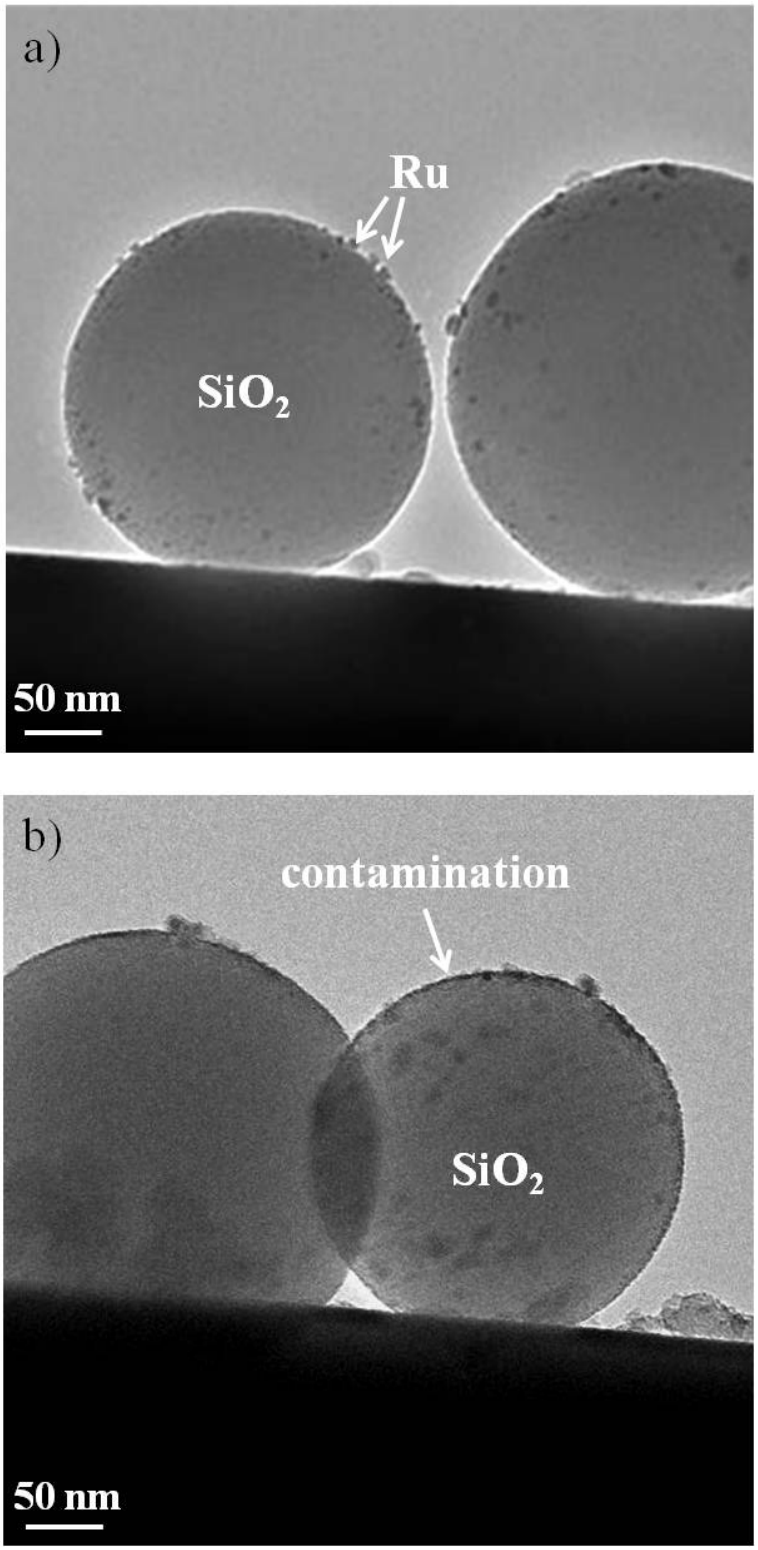

Figure 7.12. *In-situ* TEM images of Ru/SiO_2 in the presence of CO and O_2 gas mixture in 2:1 ratio at a) 80^oC, b) 300^oC.

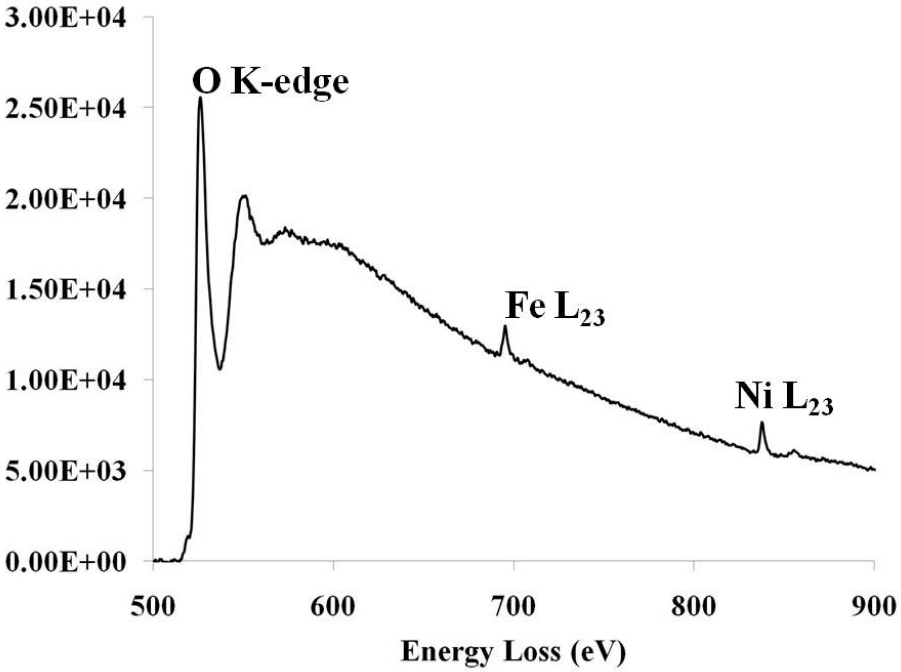

Figure 7.13. Background subtracted energy loss spectrum from Ru/SiO_2 catalyst at 300^{o}C, showing the presence of Fe and Ni contamination along with O K-edge from the SiO_2 substrate.

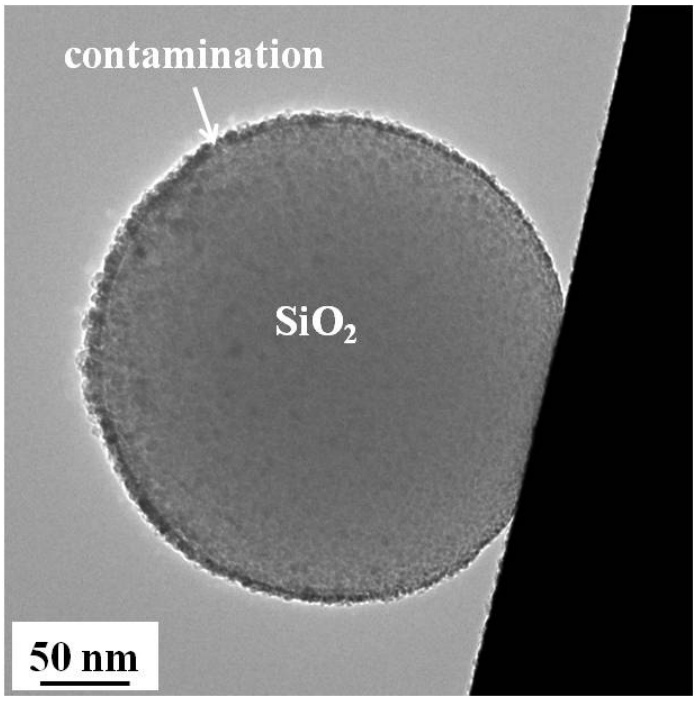

Figure 7.14. TEM image of SiO_2 sphere in the presence of CO at 200^{o}C.

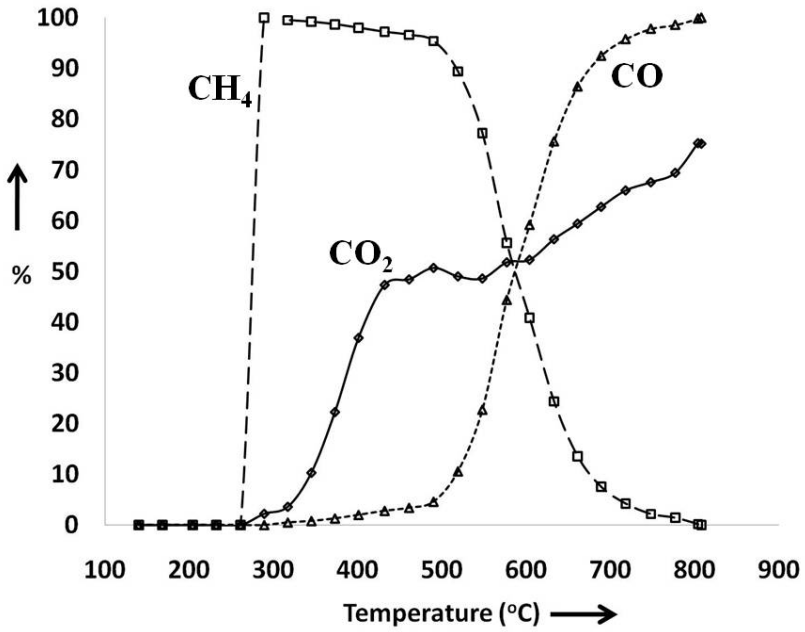

Figure 7.15. Plot showing the CO_2 conversion and its selectivity to CH_4 and CO with increase in temperature during CO_2 methanation on 2.5Wt% Ru/SiO_2 catalyst in RIG-150 reactor.

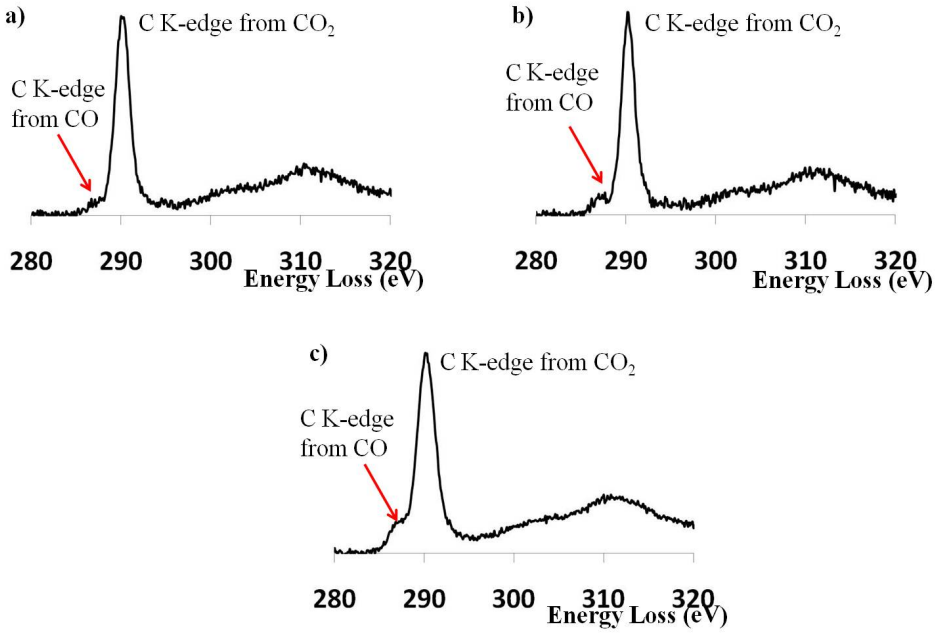

Figure 7.16. Background subtracted energy-loss spectra of C K-edge acquired at different temperatures during CO_2 methanation on Ru/SiO_2 catalyst in a ETEM reactor.

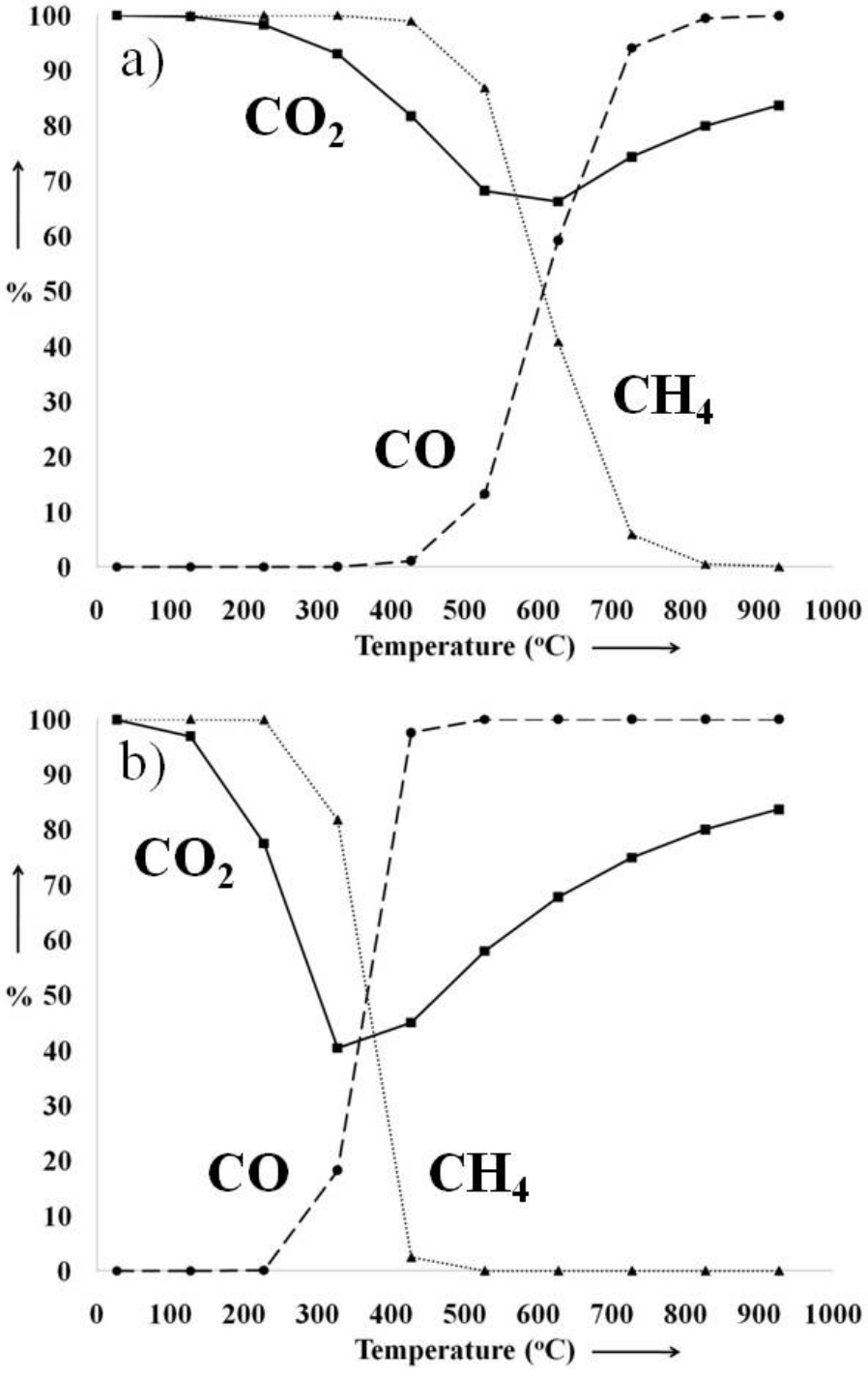

Figure 7.17. Plot showing the thermodynamic equilibrium calculations of CO_2 conversion to CH_4 and CO at a) 1 atmosphere and b) 1 Torr [19].

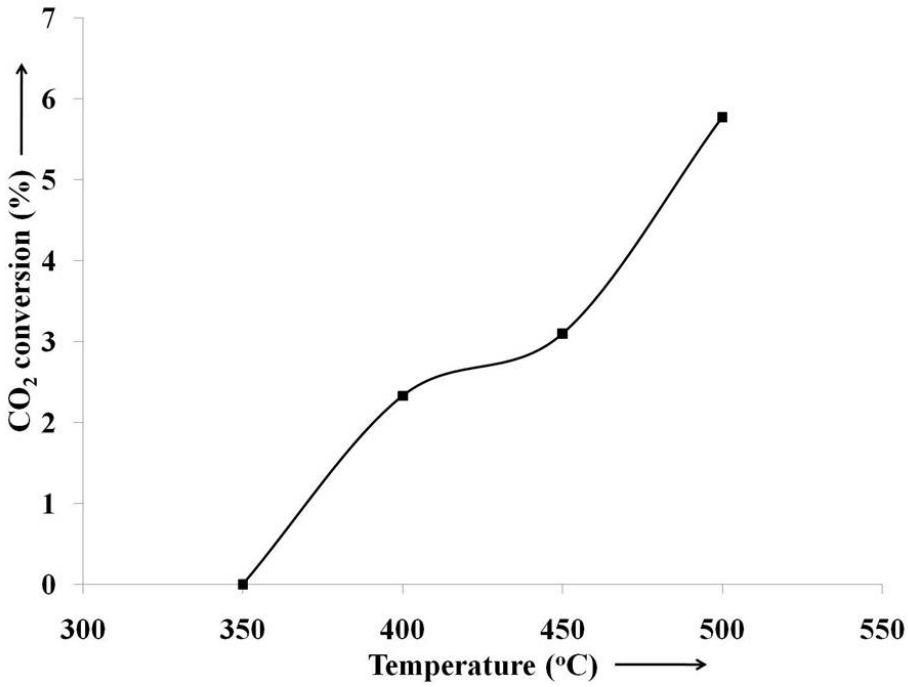

Figure 7.18. Plot showing the amount of CO_2 conversion to CO with increase in temperature during CO_2 methanation on Ru/SiO_2 catalyst measured from *in-situ* energy-loss spectroscopy.

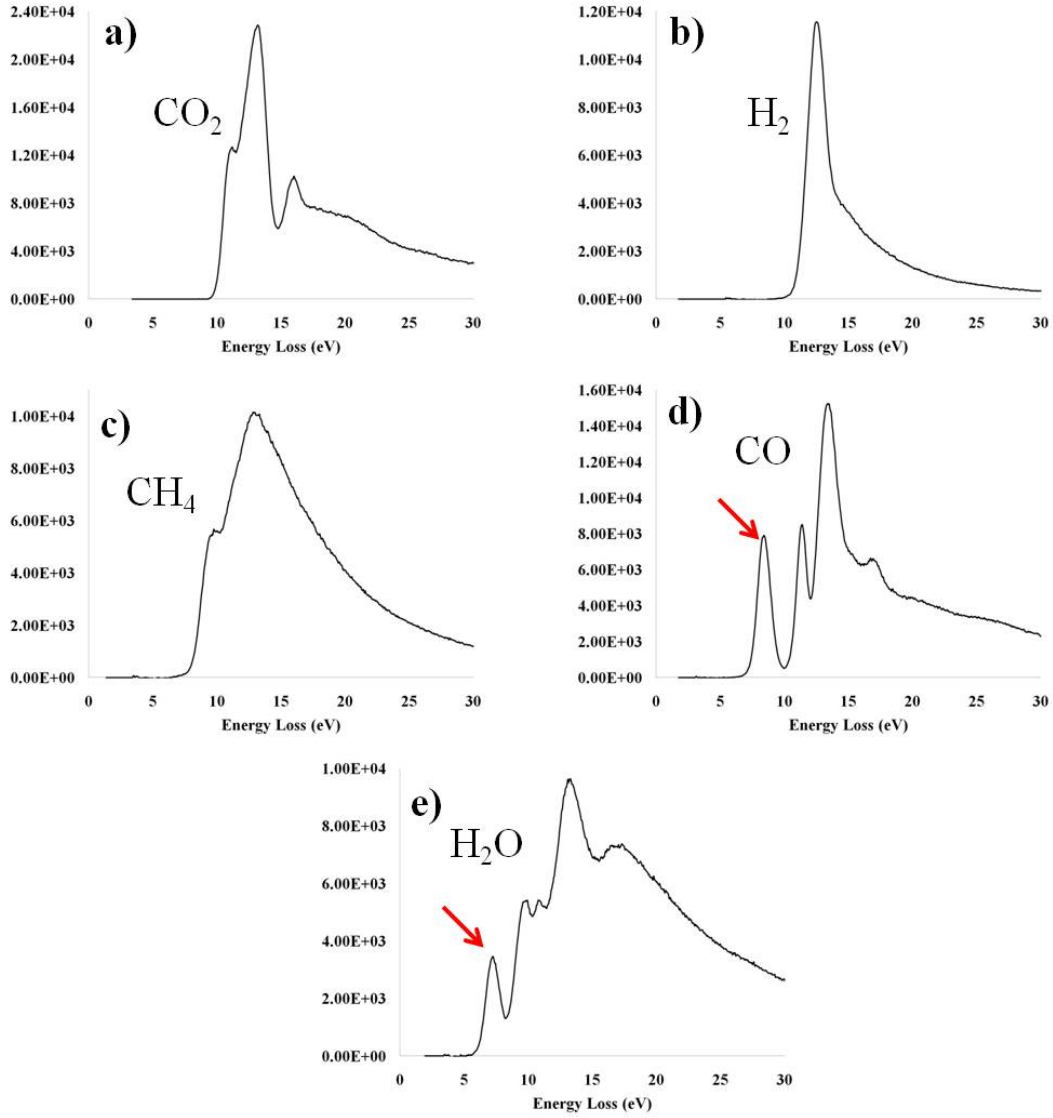

Figure 7.19. Background subtracted low-loss reference spectra from individual gases a) CO_2, b) H_2, C) CH_4, d) CO and e) H_2O.

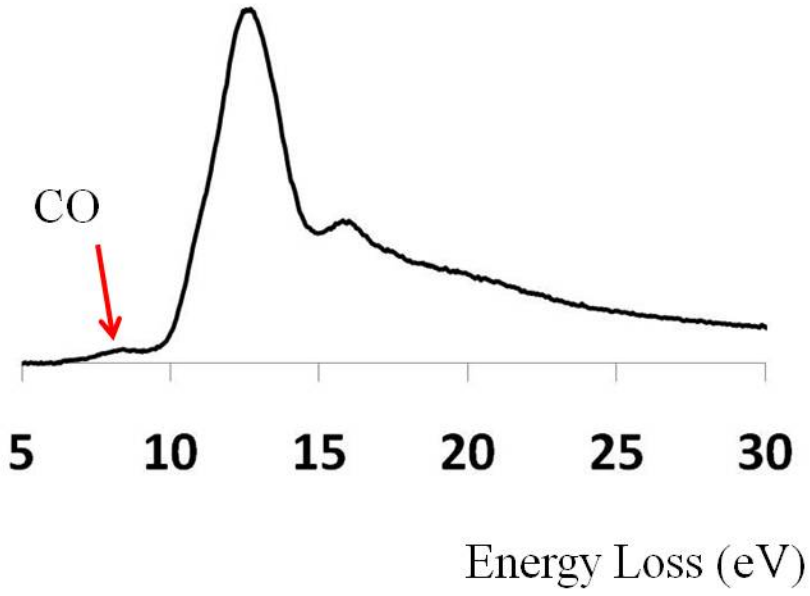

Figure 7.20. Background subtracted low-loss spectra acquired at 500^{o}C during CO_2 methanation on Ru/SiO_2 catalyst.

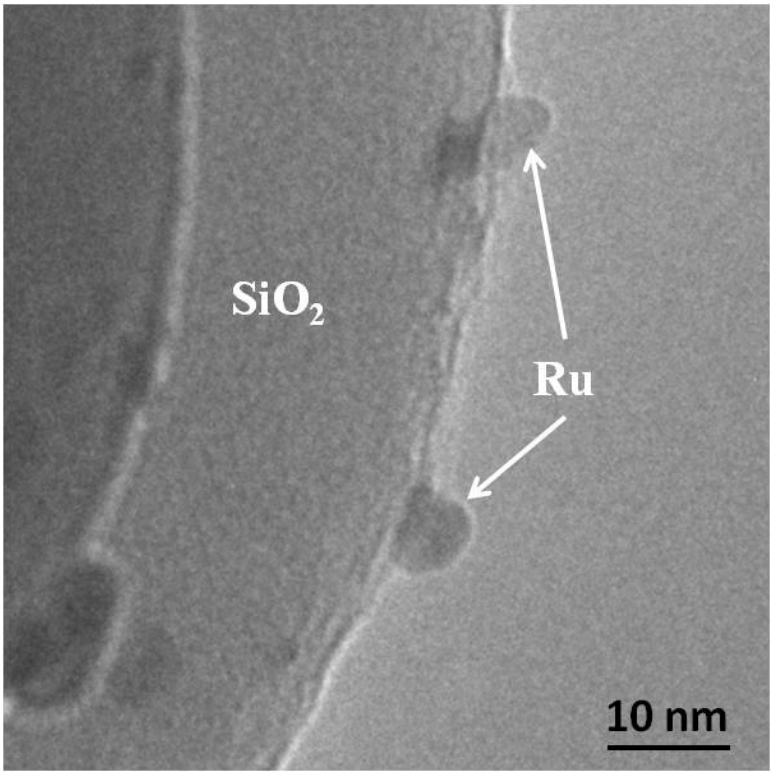

Figure 7.21. TEM image of Ru/SiO_2 during CO_2 methanation in an *in-situ* ETEM.

Chapter 8

SUMMARY AND FUTURE WORK

8.1. Summary

The research described in this thesis can be divided into two parts. The first part of the thesis (chapter 3, 4 and 5) covers the application of *in-situ* environmental TEM (ETEM) to understanding the structure-activity relationship in supported metal catalysts. And the second part (chapter 6 and 7) involves the development of the electron energy-loss spectroscopy (EELS) technique for determining the gas composition and detecting the gas phase catalysis inside environmental cell in the ETEM.

8.1.1. Structure-activity relationship

In-situ ETEM studies on nanostructures in parallel with *ex-situ* reactor studies of conversions and selectivities were performed on monometallic Ni, Ru and bimetallic NiRu supported catalysts for partial oxidation of methane (POM) in order to develop structure-activity relationships. SiO_2 spheres were chosen as a model support; the advantage of the SiO_2 spheres is that they have a well-defined morphology which is very helpful in following the nanoparticles evolution under dynamic gas reacting conditions in the *in-situ* ETEM. Supported metal nanoparticles were synthesized using incipient impregnation techniques. Co-impregnation technique were used form preparing NiRu bimetallic catalyst. EDX analysis confirms that almost all the nanoparticles contain both Ni and Ru.

From the catalytic data, during the temperature ramp-up in CH_4 and O_2, CO_2 is the main product that forms initially at low temperatures for all the three (Ni, Ru, NiRu) catalysts. The light-off temperature for CO formation was different for different catalysts. Ru has the lowest light-off temperature of 425^oC for CO formation and Ni as the highest light-off temperature of 775^oC. NiRu (50Ni50Ru) has an intermediate light-off temperature of 525^oC. A sharp rise in the CH_4 conversion and CO selectivity was observed for Ni and NiRu catalyst at the light-off temperature. For Ru, there was also a sharp rise in CH_4 conversion at CO formation temperature, however this sharp rise is relatively small compared that of observed for Ni and NiRu catalytic data.

From the catalytic data it can be observed that the gas composition along the catalyst bed varies in space and time during the temperature ramp-up. Essentially there is no single "reactor condition" in this case and the variation in the gas composition must be taken into account in the design of ETEM experiments so that the correct structure-property relations can be determined. *In-situ* ETEM experiments were performed mainly under two different gas environments, one was in the presence of CH_4 and O_2 gas in 2:1 ratio (which is reactant gas composition ratio for POM reaction) and the other gas is pure CH_4 (reducing gas component before the syngas formation).

During the temperature ramp-up in CH_4 and O_2 (in 2:1 ratio), both monometallic and bimetallic nanoparticles undergo oxidation processes and the oxidation behaviors are quite different for Ni and Ru. In case of Ni, the Ni metal nanoparticles transform completely to NiO forming void-like structures at

temperatures above 300^{o}C in the presence of CH_4 and O_2. The void-like structures are formed due to the preferential migration of Ni cations along grain boundaries and extended defects. For Ru metal nanoparticles, a thin layer of RuO_2 shell was formed on the surface at 300^{o}C in the presence of CH_4 and O_2 with Ru metal at the core region. The RuO_2 layer acts as a barrier for the diffusion of electrons onto the surface and protects the metal core from further oxidation. These metal oxides are active for complete combustion of methane giving CO_2 and H_2O (in 1:2 ratio) as the main product gases. RuO_2 is more active for CH_4 and O_2 conversions that NiO. Almost all the O_2 is consumed during complete oxidation of CH_4 on RuO_2 surface at about 425^{o}C, whereas on NiO surface it was below 10%. 100% O_2 conversion on NiO took place only at 775^{o}C.

In 50Ni50Ru bimetallic nanoparticle case, a fairly uniform NiRu nanoparticle in the presence of H_2 at 400^{o}C was transformed to core-shell structures, forming a mixed oxide shell with a Ru metal core when the gas composition is switched to CH_4 and O_2 (in 2:1 ratio). The oxide shell predominantly contained NiO along with some RuO_2. The presence of mixed oxide layers on the surface of the nanoparticle has a synergetic effect for the complete oxidation of CH_4 reaction. Almost all the O_2 is converted on 50Ni50Ru catalyst at 525^{o}C.

With increase in temperature, the oxygen partial pressure in the later part (region II and III) of the catalyst bed goes down and the oxide transforms back to metal leading to syngas formation. During the reduction in CH_4, the NiO reduction mechanism involved diffusion of Ni cations along grain boundaries and

extended defects giving raise Ni-NiO core-shell structures. NiO is the phase that always exists on the surface of the nanoparticle until reduction completes. As the last layer of NiO reduces back to metallic Ni, the gas environment is suddenly exposed to metallic Ni and reforming reactions take place on metalic Ni giving a sharp increase in CH_4 conversion and CO selectivity at 775^oC observed in the catalytic performance data. In case of RuO_2, the RuO_2 surface layer reduces back to metallic Ru in presence of CH_4 at 400^oC favoring reforming reactions to take place and produce syngas at lower temperatures. In case of Ni, formation of NiO at intermediate temperatures inhibits syngas formation at lower temperatures. It has been proven that if Ni exists in metallic form during the temperature ramp-up, syngas formation can take place at lower temperatures.

In case of 50Ni50Ru bimetallic nanoparticle, the reduction process is more complex. From the *in-situ* data, in the presence of CH_4 at 600^oC, the surface oxide layer reduces back to metal and intermixing of Ni and Ru takes place. As the oxide layer reduces back to metal, syngas formation starts to take place.

8.1.2. Electron energy-loss spectroscopy of gases

Electron energy-loss spectroscopy was used for the first time to determine the gas composition in the environmental cell in a TEM for *in-situ* applications. The approach was developed for quantification in a differential pumping environmental TEM, however the same approach can also be used to determine gas composition in windowed cells. Techniques were developed to identify the gas composition using both the inner-shell and low-loss regions of the spectrum.

The inelastic scattering for the gases is different compared to that of thin films. In the case of thin films, the inelastic scattering of the electron beam is coming from a thin (about 50 nm) region and the relations between convergence semi-angle, collection-semi angle and scattering angles are well defined. For gases, inelastic scattering of electrons takes place along the entire gas path of 5.4 mm (gap between the two pole pieces), and there is not a straight forward relationship between the convergence semi-angle, collection semi-angle and the scattering angle. This difference in the inelastic scattering gave a systematic error in inner-shell quantifications. These systematic errors can be minimized by using small convergence semi-angle and collection semi-angle. Molar concentrations of the gas mixture can be determined from low-loss spectra by expressing valence loss spectra of gas mixtures as a linear combination of individual component valance loss spectra.

An "*Operando* TEM" technique was demonstrated for the first time, where the catalyst nanostructres can be studied while simultaneously measuring the catalytic performance. EELS was used to determine the gas products in the environmental cell formed due to the catalytic reactions that take place on the surface of the catalyst. One of the challenges in developing an *operando* TEM technique is associated with the TEM sample preparation. In the RIG-150 reactor, the amount of catalyst used will be in milligrams, which gives reasonable quantities of product gases that can be detectable by gas chromatography. However, the amount of catalyst sample used for TEM studies is much less (less than micrograms) compared to the catalyst used in the RIG-150 reactor. A sample

preparation technique was developed to get high catalytic loadings onto a TEM sample and product gases from this catalyst was succesfully detected using EELS. Catalytic conversions as low as 1% were detected for CO oxidation to CO_2 on a Ru/SiO_2 catalyst using EELS.

8.2. Future work

8.2.1. Effect of catalyst support

In this thesis, model amorphous SiO_2 spheres were used as a support, which are not the usual catalyst supports used for heterogeneous catalysis application. Most supports have very high surface area and are crystalline with multiple facets. The use of model SiO_2 spheres demonstrates the application of *in-situ* ETEM studies in understanding the structure-activity relationship in supported metal catalysts. Similar experiments can be performed on high surface area SiO_2 and other oxide supports such as CeO_2, TiO_2, and Al_2O_3 which are the usual oxide supports used in heterogeneous catalysis.

8.2.2. NiRu bimetallic catalysts

During the oxidation process of 50Ni50Ru catalyst an oxide layer contains both NiO and RuO_2. Further studies on this sample can give more information on how the Ni and Ru were distributed along the oxide scale, from which oxidation mechanisms in nanoparticles can be obtained. Similarly, following the intermediate reduction stages of this catalyst is useful in understanding the reaction mechanism. More studies have to be performed on low Ru content

bimetallic catalyst (95Ni5Ru) to understand the distribution of Ni and Ru along the nanoparticles.

8.2.3. *Operando* TEM

This thesis successfully demonstrated the detection of gas phase catalysis using EELS. However the surface structure of the catalyst was not determined while measuring the catalytic performance. A better sample preparation technique has to be developed to obtain stable imaging conditions in the *in-situ* environmental TEM. Two reactions (CO oxidation and CO_2 methanation) were used to demonstrate the application of EELS in detecting gas phase catalysis. By careful studies this technique can be used for any gas phase catalytic reaction.

APPENDIX I

MOIRE ANALYSIS

Figure 1 explains the determination of the unknown reflection by knowing Moiré reflection and a known reflection in terms of the reciprocal lattice vectors.

Consider a vector OA representing the Moiré reflection (g_m) and vector OB representing the known fundamental reflection (g_1) and θ is the angle between them. Unknown reflection (g_2) can be determined by drawing a vector from A to B, and β is the angle between g_1 and g_2.

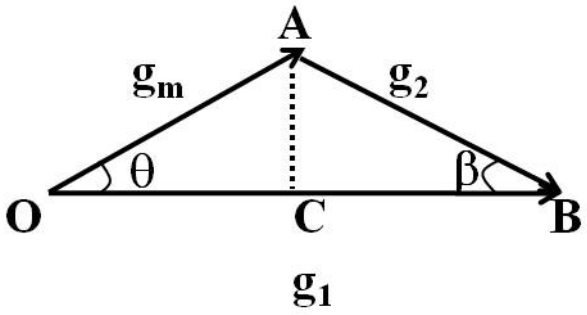

g_2 can be determined from the following equations:

$$OC = |g_m| \cos\theta$$
$$AC = |g_m| \sin\theta$$
$$BC = |g_1| - |g_m| \cos\theta$$
$$\beta = \tan^{-1}(AC/BC)$$
$$|g_2| = AC/\sin\beta$$

APPENDIX II

DETERMINATION OF CONVERGENCE AND COLLECTION SEMI-ANGLES FOR EELS

Determination of convergence semi-angle:

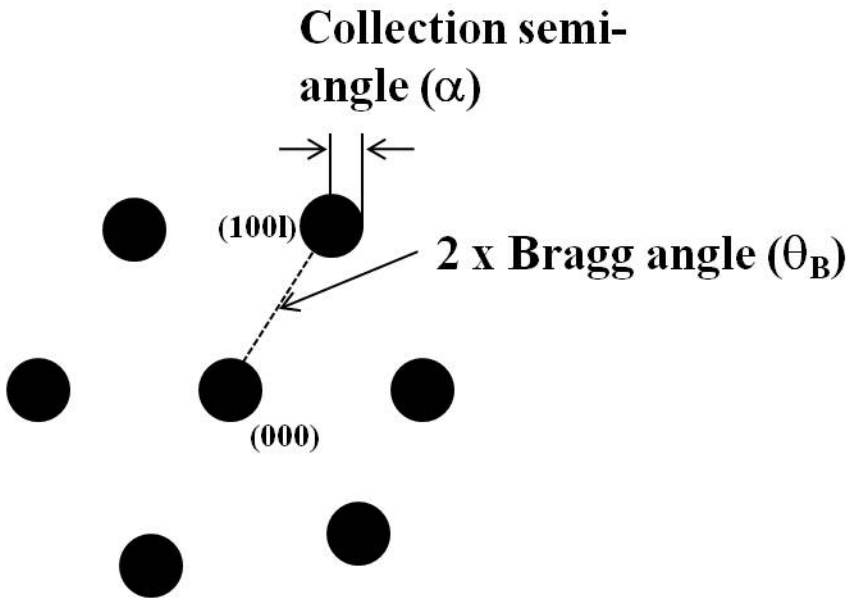

Above schematic explains the determination of collection semi-angle and convergence semi-angle for electron energy-loss spectroscopy. An electron diffraction pattern was initially obtained from a BN sample, which gives a first reflection of (100) with a d-spacing of 2.173 Å.

The distance between the (000) and (100) is equivalent to $2\theta_B = \lambda/d$

where, λ is the wavelength of the electron beam, for a 200kV electron beam λ = 0.0251 A^o and d is the lattice spacing of hexagonal BN (100) which is equal to 2.173 A^o. By measuring the distance between the (000) and (100) reflection and the disk diameter of the (100), convergence semi-angle can be obtained.

Determination of collection semi-angle:

Again a diffraction pattern from a BN sample was obtained initially on a Gatan camera and the entrance aperture of the energy-loss spectrometer was placed on to the diffraction pattern to cover both (000) beam and at least one of the (100) reflection of BN, as shown in the following schematic.

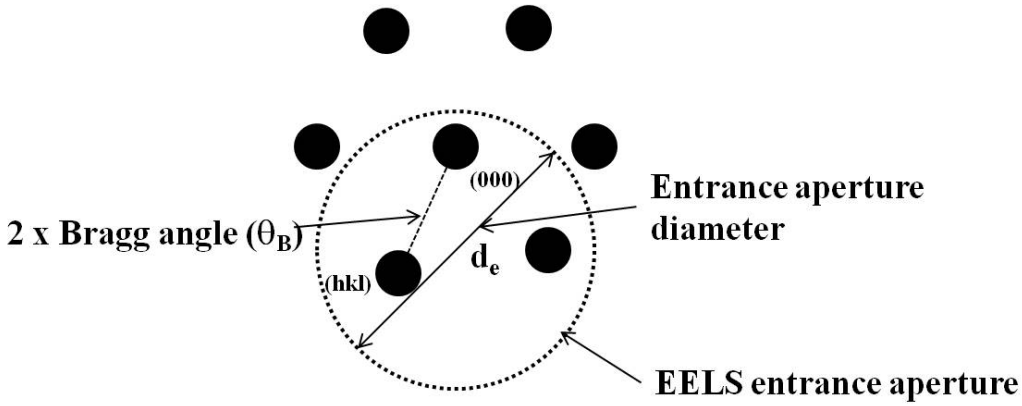

The distance between the (000) and (100) is equivalent to $2\theta_B = \lambda/d$

By knowing the diameter of the entrance aperture (d_e) and the distance between the 000 and (100), collection semi-angle can be obtained.

APPENDIX III

EELS LINE SCAN PROFILES FROM 50NI50RU BIMETTALIC NANOAPRTICLES IN THE PRESENCE OF CH4

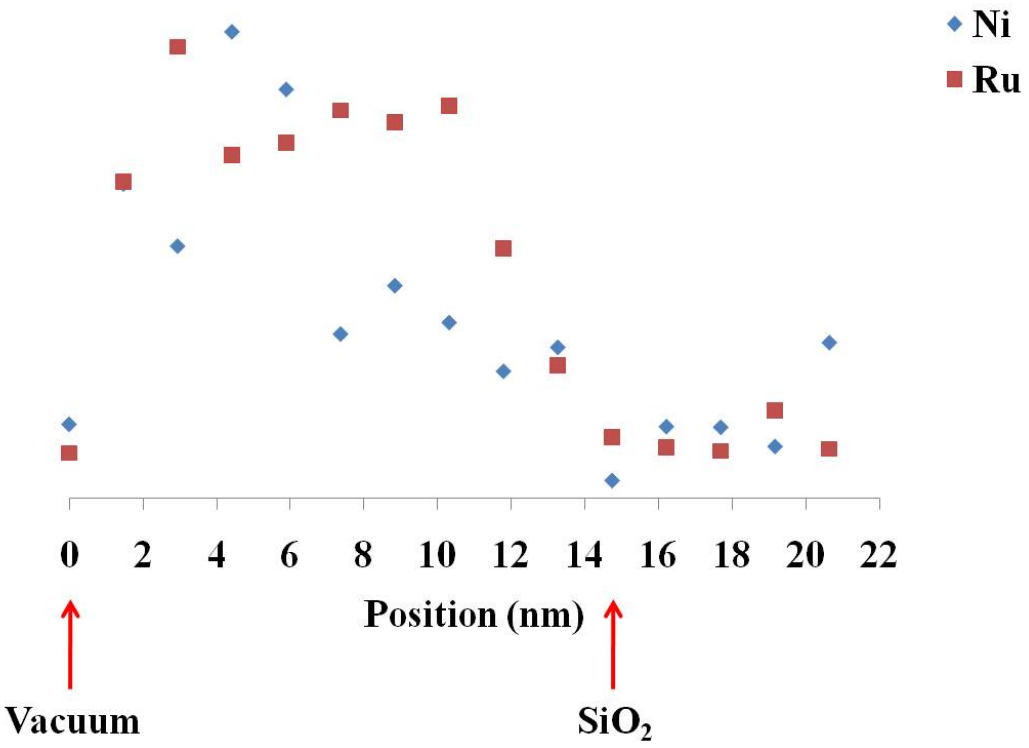
Ni
Ru
0
2
4
6
8
10
12
14
16
18
20
22
Position (nm)
Vacuum
SiO2

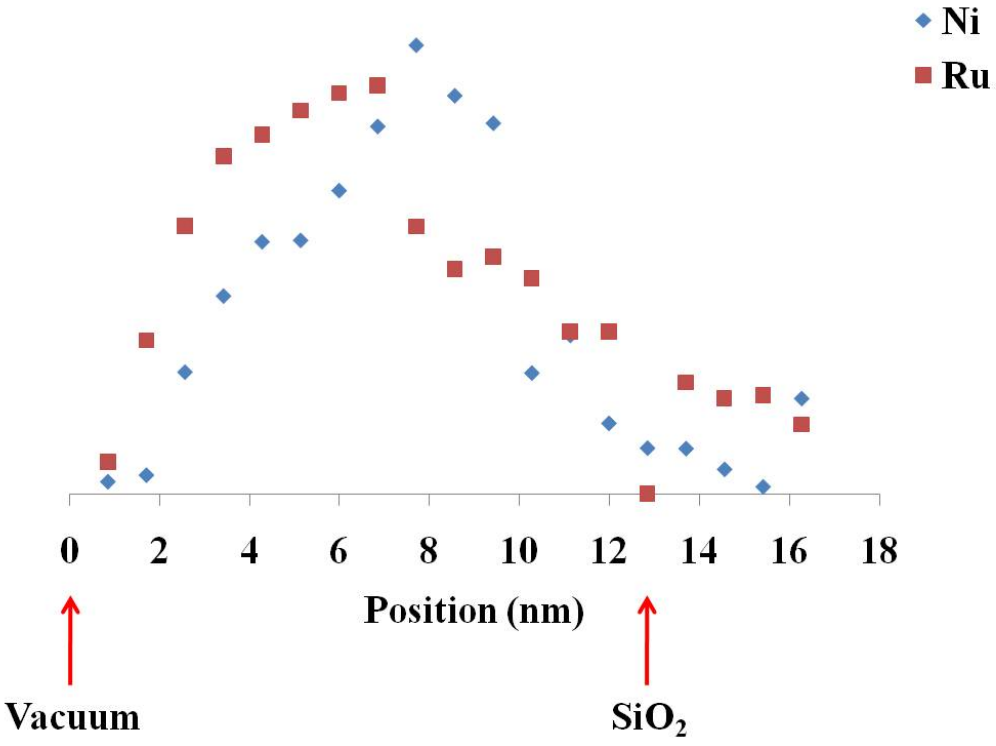
Ni
Ru
0
2
4
6
8
10
12
14
16
18
Position (nm)
Vacuum
SiO2

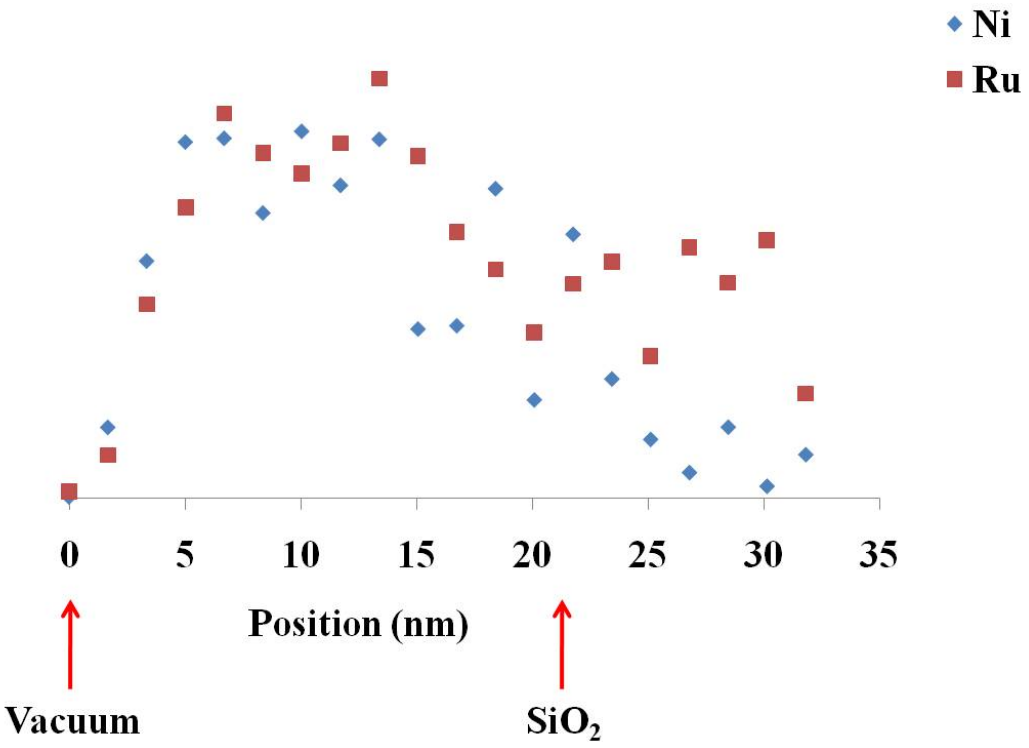
Ni
Ru
0
5
10
15
20
25
30
35
Position (nm)
Vacuum
SiO2

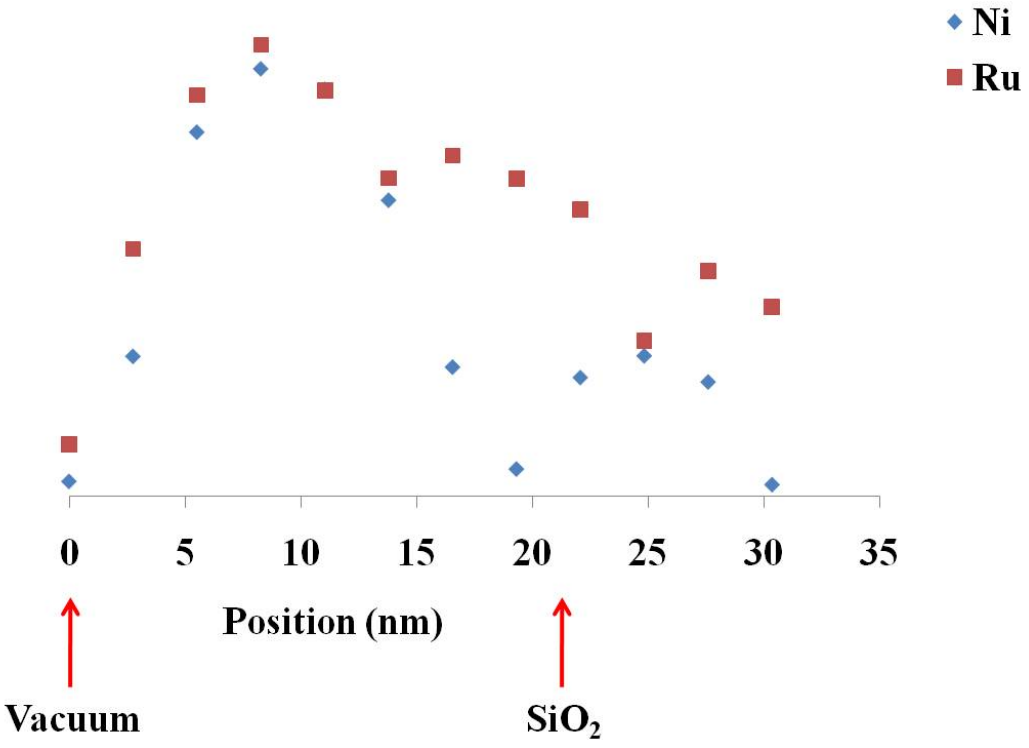
Ni
Ru
0
5
10
15
20
25
30
35
Position (nm)
Vacuum
SiO2

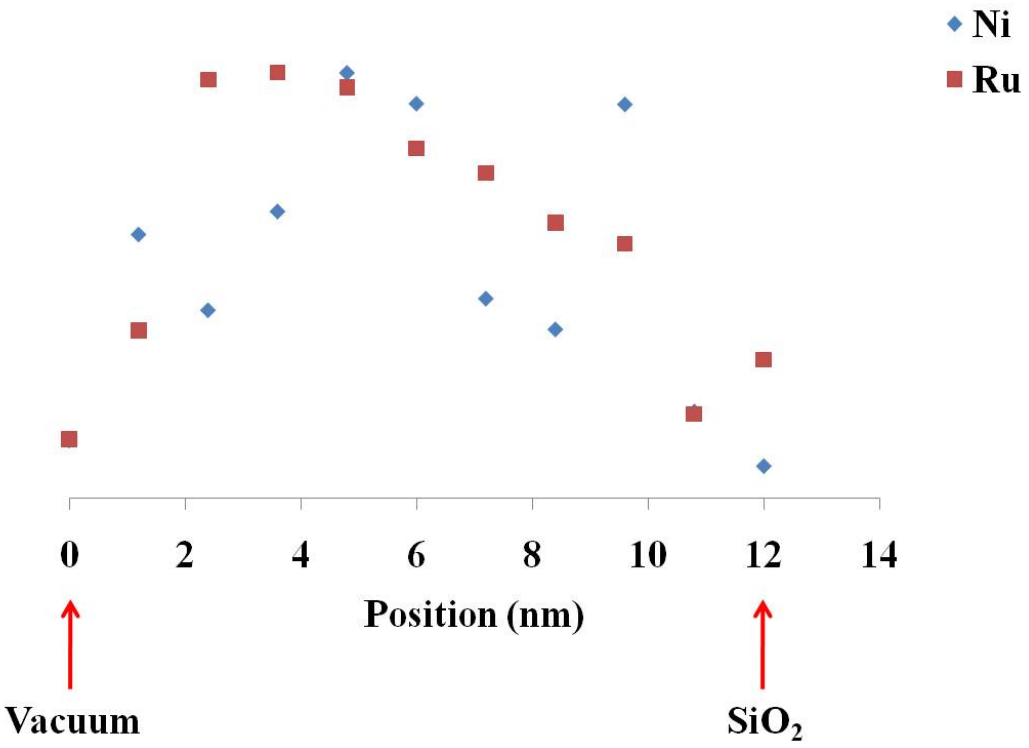
Ni
Ru
0
2
4
6
8
10
12
14
Position (nm)
Vacuum
SiO2

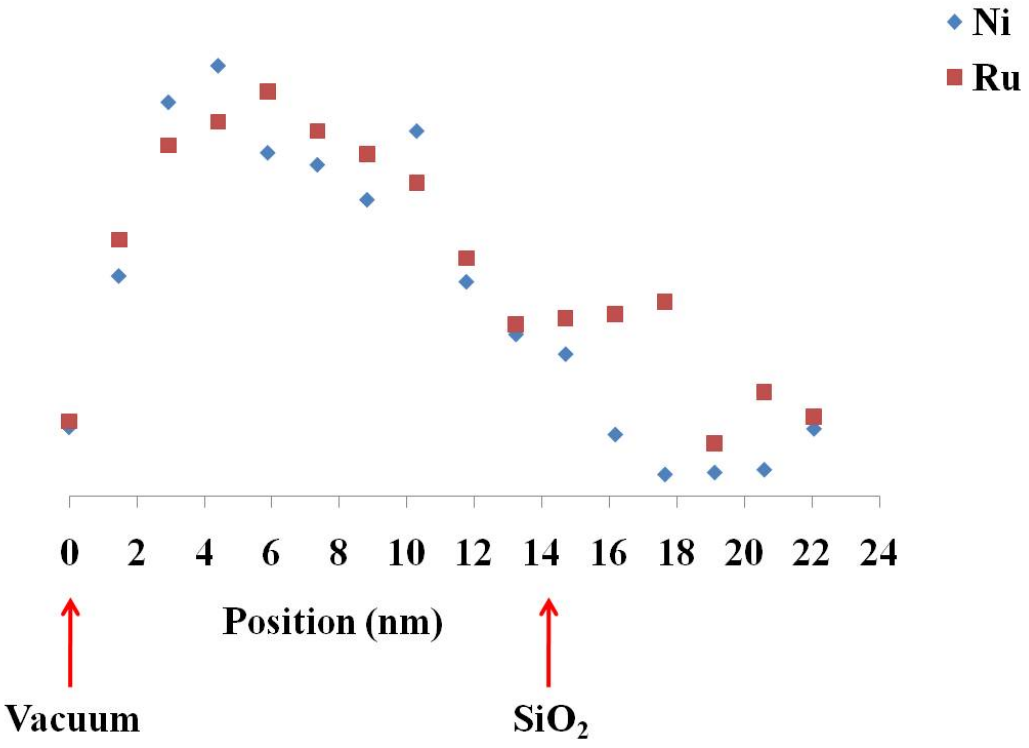
Ni
Ru
0
2
4
6
8
10
12
14
16
18
20
22
24
Position (nm)
Vacuum
SiO2